Étude du ^{3}Ca : structure nucléaire et implications astrophysiques

Louis Lalanne

université
PARIS-SACLAY

Study of ^{36}Ca: nuclear structure and astrophysical implications

Étude du ^{36}Ca : structure nucléaire et implications astrophysiques

Thèse de doctorat de l'Université Paris-Saclay

École doctorale n°576 Particules, Hadrons, Énergie, Noyau, Instrumentation, Imagerie, Cosmos et Simulation (PHENIICS)
Spécialité de doctorat: Structure et réactions nucléaires
Unité de recherche: Université Paris-Saclay, CNRS, IJCLab, 91405, Orsay, France
Référent : Faculté des sciences d'Orsay

Thèse présentée et soutenue à Orsay, le 24 Septembre 2021, par

Louis Lalanne

Composition du jury:

Dr David Verney Directeur de recherche, IJCLab	Président
Pr Beatriz Fernández-Dominguez Professeure, Université de Saint-Jacques-de-Compostelle	Rapporteur & Examinatrice
Dr Stéphane Grévy Directeur de recherche, CENBG	Rapporteur & Examinateur
Pr Alison Laird Professeure, Université de York	Examinatrice
Pr Alfredo Poves Professeur, Université autonome de Madrid	Examinateur

Direction de la thèse:

Dr Olivier Sorlin Directeur de recherche, GANIL	Directeur de thèse
Dr Marlène Assié Chargée de recherche, IJCLab	Co-Encadrante de thèse
Dr Fairouz Hammache Directrice de recherche, IJCLab	Co-Directrice de thèse

Thèse de doctorat
NNT: 2021UPASP077

Acknowledgements

J'ai vécu durant mes trois années de thèse une aventure fantastique, et si j'ai pu traverser cette expérience exceptionnelle avec autant de bonheur, c'est grâce à toutes les personnes formidables que j'ai rencontré le long de mon chemin. Je vais essayer en quelques lignes de leur rendre l'hommage qu'elles méritent.

Mes premiers mots de remerciements iront à mes encadrants : Olivier, Marlène et Faïrouz. On ne peut rêver meilleur encadrement de thèse que celui que j'ai eu avec vous trois. Merci infiniment pour tout ce que vous m'avez apporté. Olivier, ta passion, ta vision de la physique et ta culture scientifique gargantuesque m'ont fasciné. Merci d'avoir accepté de me prendre en thèse et de m'avoir transmis tes connaissances, tu seras tout au long de ma carrière de physicien l'exemple que je m'efforcerai de suivre. Avec toi Marlène, je me suis senti en confiance dès notre première rencontre. Merci infiniment pour ta bienveillance et l'écoute dont tu as fait preuve tout au long de ma thèse. Merci également de m'avoir guidé avec patience dans les méandres de l'analyse de données des réactions de transfert. Sans toi, je n'y serais jamais parvenu. Quant à toi, Faïrouz, non seulement tu as toujours été là pour m'aider dans les interprétations d'astrophysique, mais tu m'as également soutenu dans les périodes de doutes. Je te remercie pour la gentillesse et l'attention dont tu as fait preuve envers moi au cours de ces années. Pour tout cela et pour beaucoup d'autres choses je vous remercie tous les trois du plus profond de mon cœur.

Je tiens également à remercier les membres de mon jury. David Verney d'abord, mon président et collègue avec lequel j'ai eu de nombreuses interactions durant ma thèse. Merci pour nos échanges toujours très fructueux, j'ai énormément appris à tes côtés. Merci à mes deux rapporteurs Stéphane Grévy et Beatriz Fernandez-Domingez ; pour les discussions que nous avons eues, pour les lectures attentives de mon manuscrit et pour les commentaires très constructifs qui ont apporté des éclairages nouveaux sur mon travail. Merci à mes examinateurs Alison Laird et Alfredo Poves pour leurs questions et leurs commentaires avisés. Un merci supplémentaire à Alfredo et beaucoup de reconnaissance, les réunions d'interprétations effectuées avec Olivier resteront à jamais gravées dans ma mémoire.

En plus d'une équipe d'encadrants fantastiques j'ai bénéficié durant ma thèse de l'aide et de l'enseignement de nombreuses autres personnes. Un grand merci à la NPTeam Freddy, Nicolas et Adrien pour votre aide avec NPTool et l'analyse. J'ai adoré travailler avec vous et vous côtoyer pendant les manips MUST2 et MUGAST. Vous êtes tous les trois des exemples pour moi et j'espère suivre votre chemin dans les prochaines années. Merci beaucoup à tous mes collègues de l'IJCLab, du GANIL et de RIKEN : Didier, Yorik, Iulian, Franco, Jacques, François, Carole, Matthieu, Clément, Marion, Vladimir, Iolanda, Serge, Antoine, Thomas, Jean-Charles, François, Lucia, Pierre, Shumpei

et Daisuke... je m'excuse d'oublis éventuels. J'ai adoré passer ces années auprès de vous, j'ai adoré travailler avec vous, à votre contact je me suis enrichi, je ne l'oublierai pas. Tous mes remerciements également aux directeurs d'IJCLab Achille, Sébastien et Fadi pour nous avoir permis d'organiser une vie étudiante au labo et au bureau des étudiants Eli, Guillem, Remy, Cloé et Léo avec qui on a essayé de la créer.

Merci à tous mes collègues thésards d'IJCLab et de Caen (même si certains sont Docteurs maintenant) pour le travail et les rigolades que nous avons partagés. Ces moments de détentes sont indispensables au bon déroulement d'une thèse. Pour n'en citer que quelques-uns : Damien, Sarah, Lama, Anahi, Ren, Anne, Wenling, Alessendro, Cyrile, Armel, Chloé, Nishu, Valérian, Benoit, Julien, Joel, Blaise... Mention spéciale à Rems et Guigui. Ces trois années passées dans le même bureau ont tissé entre nous des liens indéfectibles.

Merci également à tous mes amis pour leur soutien permanent et pour tout ces moments qui m'ont permis de déconnecter et de garder un bon équilibre. Merci pour les sessions d'escalade into apéro. Merci pour les soirées de vrille. Merci pour les barbuc en terrasse. Merci pour les weekend en van. Merci pour les déjeuners alsaciens. Merci pour les sessions musique. Merci pour les soirées à Mouffetard. Merci pour les voyages en montagne. Merci pour les concerts a Paris. Merci pour les soirées Catan. Merci pour les dîners algériens. Merci à vous tous pour tout ça et bien plus encore.

Je dois aussi ajouter que je n'aurai jamais commencé cette thèse sans l'appui de ma mère et de mon père. Même s'ils n'ont pas toujours été d'accord avec mes choix, ils les ont respectés et ils m'ont accompagné avec enthousiasme tout au long de mon parcours. Merci mes parents pour votre aide, votre écoute, votre confiance, et votre amour.

Mon tout dernier message sera pour toi Eli. Merci pour ton soutien inconditionnel, ta bonne humeur, ton écoute et ton énergie. Tu m'as donné de la force dans les moments difficiles et tu m'as aidé à me relever lorsque face aux épreuves j'avais l'impression de ne plus avancer. Je n'y serais jamais arrivé sans toi. Merci d'illuminer ma vie.

Un grand merci à vous tous, à ceux que j'ai cité, à ceux que j'ai peut-être oublié et auxquels je présente mes excuses. Sans vous ce manuscrit n'aurait jamais existé.

J'espère que vous trouverez dans ce manuscrit ce que vous êtes venus chercher. Je vous souhaite une très bonne lecture.

"Ca valait le coup de persévérer,
de passer quelques années à errer pour déterrer la voie d'accès à ses rêves."[1]

Louis Lalanne

[1] Louis Lalanne, *Le vent se lève*, Album: *Empreinte*, 2020.

Contents

Introduction

The world we live is made of matter composed of very tiny elements called molecules and atoms. For centuries, scientists thought that atoms were the most elementary bricks from which our universe was built up. Thanks to pioneers such as Rutherford, Bohr or Curie, we now know that an atom consists of a cloud of negatively charged particles, electrons, orbiting around a positively charged nucleus. The atomic nucleus itself is composed of two kind of particles: the proton, which has a positive charge and the neutron which is neutral. These particles are bound together by the strong interaction to form a nucleus. Nuclear physics is the science that study this complex object, its behavior and its fundamental properties.

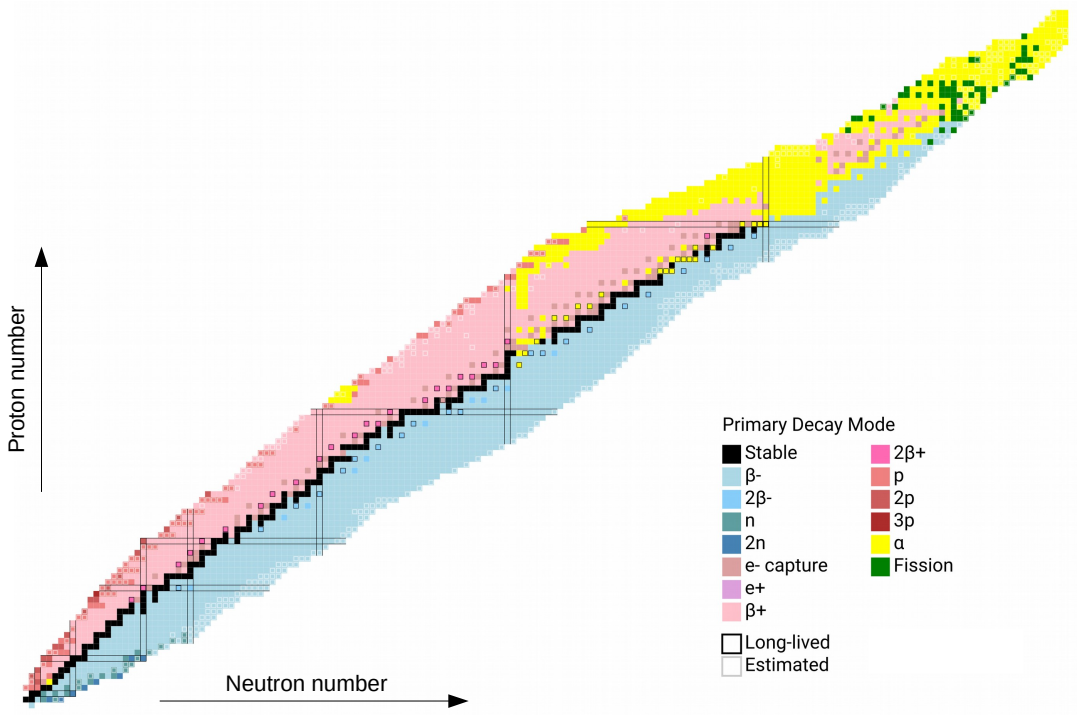

Figure 1: The nuclear chart of isotopes according to their primary decay modes. Figure adapted from Ref. [1]

Nuclei are usualy represented in the chart of nuclides which is shown in Fig. 1. In this chart, each box represents a nucleus, which is ordered as a function of its proton and neutron number Z and N, respectively. Today, 3314 nuclei are known experimentaly [2] with elements going from Hydrogen

($Z = 1$) to Oganesson ($Z = 118$). Only 288 of these nuclei are stable, forming the so-called "valley of stability", the others being radioactive due to an excess of protons and/or neutrons. Nowadays, in laboratories, one can study experimentally very exotic nuclei, going far from the valley of stability, with large proton-neutron asymmetry. Understand the evolution of fundamental nuclear properties such as masses, radius or excitation energies, when going from stable to exotic nuclei, is at the heart of nuclear structure studies.

Exotic nuclei are also very interesting for nuclear astrophysics. Indeed, explosive nucleosynthesis processes occurring in classical novae, core-collapse supernovae, X-ray bursts or neutron star mergers, consist of chains of nuclear reactions passing through very exotic regions of the nuclear chart. Studying experimentally exotic nuclei provides data on their nuclear properties which allows to better understand these explosive stellar processes.

The nucleus of ^{36}Ca is a fascinating nucleus in which many nuclear physics fields meet. It is a very exotic nucleus, with four neutrons less than its lightest stable isotope ^{40}Ca, its first excited state is already unbound. It is key nucleus to understand the evolution of nuclear structure when going from stable to proton-rich nuclei and to probe fundamental symmetries of the nucleus such as the isospin symmetry (which exchanges the number of protons and neutrons). At the same time, ^{36}Ca sits on the *rp*-process path which is an explosive nucleosynthesis process occurring in X-ray burst. The study of its nuclear properties allows to better understand how this process occurs and more specifically, it allows to better understand the main observable of X-ray burst: the X-ray light curve.

In this manuscript, the experimental study of the ^{36}Ca nucleus will be presented together with its nuclear structure and astrophysical implications. In the first part, the nuclear structure context and motivations will be discussed as well as the experimental tool used to produce and study ^{36}Ca: the ^{37}Ca(p,d)^{36}Ca and ^{38}Ca(p,t)^{36}Ca transfer reactions. Then, the experiment performed at GANIL, will be presented with the production of the radioactive beams and the experimental set-up composed of tracking detectors, a cryogenic target, charged-particle detectors and a zero degree detection. The method to go from raw data, provided by the detectors, to physical observables, will be detailed before presenting the results obtained about the nuclear properties of ^{36}Ca. The very first study of the ^{35}Ca nucleus will also be presented. The nuclear structure implications of these results will then be discussed. In the second part, the astrophysical motivation of this work will be presented. Additional results about ^{36}Ca, relevant for the astrophysical part, will be shown before to present the calculation of the reaction rate of interest, ^{35}K(p,γ)^{36}Ca, and its implications.

Part I

Nuclear Structure

1 Context and Motivations

Sommaire

This chapter presents the context in which this nuclear structure study is performed and the physics motivations we have to study ^{36}Ca. First, the structure of the atomic nucleus will be discussed in the framework of nuclear shell model. Then, a fundamental symmetry of the nucleus, the isospin symmetry, will be presented and mechanisms that can destroy it will be discussed. Afterwards, the physics case of ^{36}Ca will be presented in details before giving an overview of the experimental method that we used to produce and study this nucleus.

1 The Nuclear Shell Model

The atomic nucleus is a quantum system composed of protons and neutrons (collectively called nucleons) bound by the nuclear force. The understanding of the nuclear force has been at the heart of nuclear physics since the born of the field. The first historical model describing the nuclear force was proposed by Yukawa in a paper of 1935 in which he proposed the pion (π) exchange process as the origin of the nuclear force [3]. Since then, enormous efforts have been devoted to understand the nucleon-nucleon (NN) interaction both from theory and experimental side. Fig. 1.1 shows typical examples of the NN interaction computed in the ^{1}S$_0$ channel by modern calculations. The NN interaction is characterized by three different regimes: at long range, ($r > 2$ fm) the NN interaction is weakly attractive and is dominated by one pion exchange. In the medium range ($r \sim 1$ fm) it is attractive and received contributions from multi-pion (2π) and heavy meson (ρ, ω, σ) exchange [4]. At short range ($r < 1$ fm), the NN interaction is empirically known to be strongly repulsive.

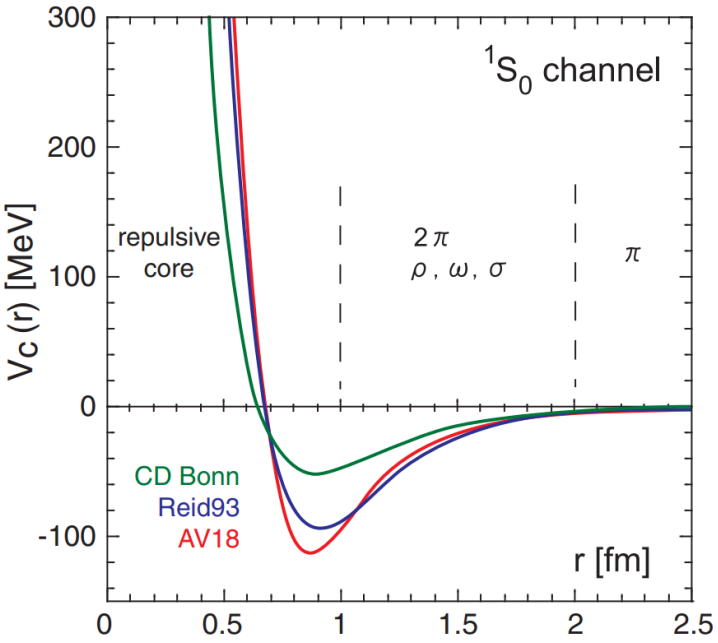

Figure 1.1: Three examples of NN interactions in the ^{1}S$_0$ channel. Figure from from Ref. [4].

The properties of the nuclear force are such as the distance between two nucleons is approximately constant (being about 0.7 fm) leading to a constant density (of about $\rho_f = 0.16$ nucleon fm^{-3}) in the inner part of the atomic nucleus. Since the density of a nucleus is constant, the volume of an atomic

nucleus increases linearly with its number of constituants. Furthermore, the NN interaction being negligible at long range, one can consider that a nucleon only interacts with its immediate neighbors which lead to a saturation of the binding energy [5]. Fig. 1.2 shows the density profile of some nuclei. One can see that they have an almost uniform density at the interior that can be approximated to ρ_f, independently of their masses. One can also see that the radius of nuclei increases with the mass following $R = r_0 A^{1/3}$ (with $r_0 \sim 1.25$ fm).

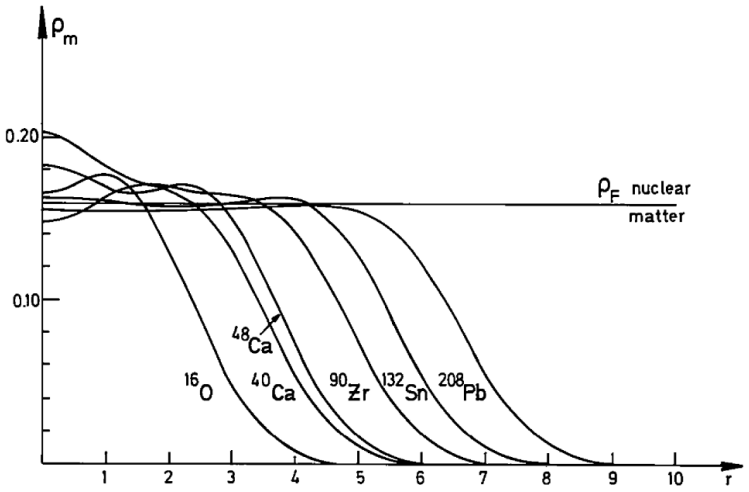

Figure 1.2: Combination of nuclear matter densities ρ_m (fm^{-3}) for a set of nuclei. The nuclear matter density $\rho_f = 0.16$ fm^{-3} is given for comparison. Figure from Ref. [6].

In order to completely determine the wave function Ψ_A of a nucleus composed of A nucleons one have to solve its Schrodinger equation:

$$H\Psi_A = E\Psi_A. \tag{1.1}$$

Taking only two-body forces into account, the Hamiltonian of the system can be written:

$$H = \sum_{i=1}^{A} T_i + \sum_{1=i<j}^{A} V_{ij}, \tag{1.2}$$

where $T_i = -\frac{\hbar^2}{2m}\Delta_i$ is the kinetic energy term of the nucleon i [7] and V_{ij} is the two-body NN interaction term. To solve exactly Eq. 1.2 is an extremely challenging many-body problem, complicated even further by the fact that the details of the interaction term V_{ij} are not known. For instance, three body forces can have non-negligible effects (*e.g.* take into account three body forces is needed to reproduce the position of the neutron drip-line along the oxygen isotopic chain [8]). Therefore, in general, the interaction term V_{ij} used in the calculations corresponds to an effective NN interaction. Exact solution of Eq. 1.2 can be found using *ab initio* calculations for very light nuclei (A<12 see Ref. [9]). For heavier system, approximations have to be made in order to get an approximate solution for the wave function of the system.

A first step towards an approximate solution is to introduce a central single-particle mean field

potential $U(r)$. Using the central potential, one can re-write the Hamiltonian of the nucleus as [10]:

$$H = \sum_{i=1}^{A}(T_i + U(r_i)) + \left(\sum_{1=i<j}^{A} V_{ij} - \sum_{i=1}^{A} U(r_i) \right) = H_0 + H_{res}, \tag{1.3}$$

where H_0 is the Independant Particle Model Hamiltonian, describing an ensemble of independent particles in a central mean potential U. H_{res} corresponds to the residual interaction between the nucleons. Then the Schrodinger equation can be solved by either neglecting the residual interaction or by treating it as a perturbation.

1.1 The Independent Particle Model

The Independent Particle Model (IPM) assumes that each nucleon interacts with a central mean field potential $U(r)$ generated by the sum of all the other nucleons of the nucleus, neglecting the residual interactions between them. In this approximation, the Hamiltonian can be written as:

$$H = \sum_{i=1}^{A}(T_i + U(r_i)), \tag{1.4}$$

allowing to reduce the N-body problem to N one-body problems.

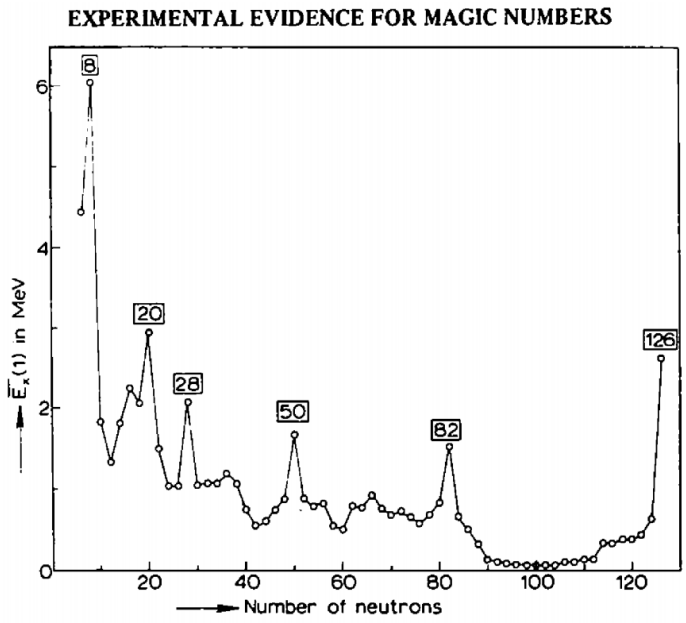

Figure 1.3: The occurrence of magic numbers as demonstrated by the average excitation energy of the first excited state in doubly-even nuclei, as a function of neutron number N. Figure from Ref. [6]

Historically, the first success of the IPM was to describe the sequence of the experimentally observed magic numbers. Magic numbers are special numbers of proton Z or neutron N for which the nucleus has a particularly stable configuration. Fig. 1.3 shows the average excitation energy of the first excited state in doubly-even nuclei as a function of the number of neutron N. One can see that for N= 8, 20, 50, 82 and 126, the first excited state is at particularly high energy as compared to its neighbors

indicating a very stable configuration.

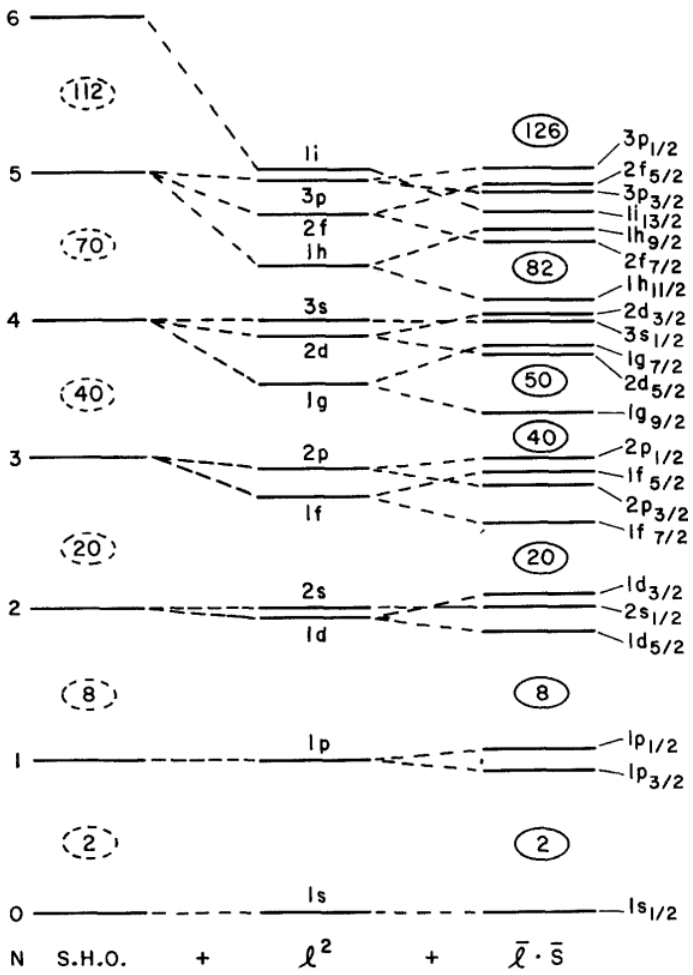

Figure 1.4: Single-particle energies for a simple harmonic oscillator (S.H.O.), a modified harmonic oscillator with a $\vec{l^2}$ term, and a realistic shell model potential with $\vec{l^2}$ and spin-orbit $\vec{l}\cdot\vec{s}$ terms. Figure from Ref. [11].

In 1949, Mayer [12] and Haxel [13] introduced a spherical mean field consisting in an isotropic harmonic oscillator in addition to a strongly attractive spin-orbit potential and an angular momentum term:

$$U(r) = \frac{1}{2}m\omega^2 r^2 + \alpha(\vec{l^2}) + \beta(\vec{l}\cdot\vec{s}), \tag{1.5}$$

where m is the mass of the nucleon, ω is the frequency of the harmonic oscillator, r is the distance of the nucleon to the center of the nucleus and $\vec{l}$ and $\vec{s}$ are its orbital angular momentum and its intrinsic spin (of value $||\vec{s}||=\frac{1}{2}$ for nucleons), respectively. The single particle energies (which correspond to the eigenvalues of the Hamiltonian) and the orbits (which correspond to the eigenstates of the Hamiltonian) obtained using this potential are shown in Fig. 1.4. The single-particle states are classified by the radial (or principal) quantum number n, the orbital angular momentum l, and the total angular momentum j and noted nl_j. The single-particle states are grouped according to n (corresponding to the eigenvalues

of the harmonic oscillator, see the extreme left of Fig. 5.1), forming shells (*e.g.* the *sd* shell which corresponds to $n = 2$). Shells are separated by shell gaps. If two orbitals are separated by a large energy gap, the number of protons or neutrons needed to completely fill the lower orbital defines a magic number.

Magic numbers can have two different origins, either from the harmonic oscillator (which is the case for 2, 8 and 20 for instance) or from the spin-orbit splitting (like 28, 50 or 82). Indeed, the spin-orbit coupling induces splitting between $j_> = l + 1/2$ and $j_< = l - 1/2$ orbits and can generate large gaps between orbitals (see for instance the large 28 gap between the $1f_{7/2}$ and the $2p_{3/2}$ orbitals, arising from the strong $1f_{7/2} - 1f_{5/2}$ spin-orbit splitting). The magic numbers emerging from the potential described by Eq. 1.5, reproduces very well the observed binding energy of stable nuclei along the nuclear chart. This discovery made Maria Goeppert-Mayer and Hans Daniel Jensen earn the Nobel Prize of Physics in 1963.

Since the NN interaction acts at small range, the intensity of the mean potential U should be directly linked to the nuclear density, which is not the case for the harmonic oscillator. Therefore, latter, a more realistic potential, as compared to the harmonic oscillator one, was adopted. It is known as the Wood-Saxon (WS) potential and is expressed in terms of three parameter (its depth V_0, its radius R and its diffusivity a) as:

$$V(r) = V_0(1 + e^{\frac{r-R}{a}})^{-1}. \tag{1.6}$$

A comparison between the harmonic oscillator and the (WS) potential is shown in Fig. 1.5. This potential better reflects the form of the nuclear density (shown in Fig. 1.2) with a flat bottom. It has also a more realistic asymptotic behavior with flatten behavior at the surface of the nucleus and which tend to zero at large distance.

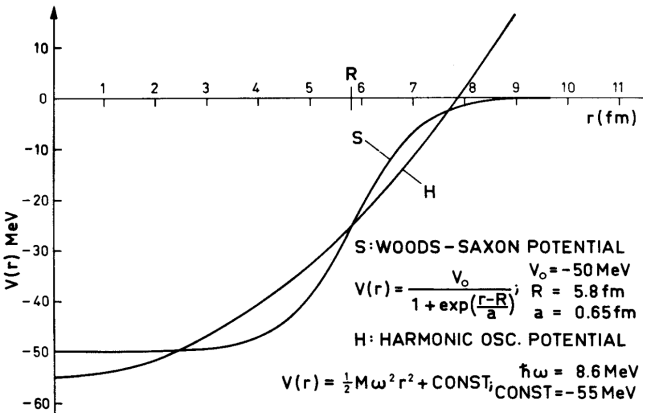

Figure 1.5: Comparison between a Wood-Saxon and a harmonic oscillator potential. Figure from Ref. [14].

The IPM composed of a central WS potential, an angular momentum term and a strongly attractive spin-orbit potential successfully described numerous of nuclei close to the valley of stability and was an enormous success for the understanding of nuclear structure. The permanence of the nuclear magic numbers which the IPM describes, remained a 'dogma' for many years. However, progress in experimental techniques allowed to explore new regions of the nuclear chart. First evidences about

the disappearance of magic numbers were provided and triggered a large number of experimental and theoretical works devoted to study shell structure evolution.

1.2 The Interacting Shell Model and shell evolution

In the previous section we saw how to describe the nucleus as a sum of nucleon interacting with a central field. In the IPM picture, the size of the shell gaps are fixed all along the nuclear chart. However, many evidences of the disappearance of magic numbers and of the appearance of new magic numbers have been provided in the last decades such as the disappearance of the $N = 20$ and the $N = 28$ gaps when going toward very neutron rich nuclei. Indeed, as more nucleons are added to a nucleus, the single-particle energies of the valence orbits may change significantly, due to the interaction between the valence nucleons. This implies some changes of shell structure, called shell evolution. In order to describe these shell evolutions, one has to consider the nucleon-nucleon interaction between the valence nucleons.

The Shell model Hamiltonian can be decomposed in a monopole H_m and a multipole H_M part [15]:

$$H = H_m + H_M. \tag{1.7}$$

The monopole part represents the average effect of the NN interaction over all possible orientations of two nucleons in the orbits j_1 and j_2. It is responsible for the drift of the Single Particle Energies (SPE) of the proton and neutron orbitals. The remaining part of the interaction is represented by the multipole part. It contains the J-dependent part of the NN interaction. It includes, in particular, the pairing term and the quadrupole correlations which are responsible for the configuration mixing and the deformation of nuclei.

The Two Body Matrix Element (TBME) of the monopole term, for two nucleons 1 and 2 on the single particle orbitals j_1 and j_2, are defined as the mean of the possible orientations m_1 and m_2 and are defined by [5]:

$$V_{12}^{m}(j_1, j_2) = \frac{\sum_{m_1,m_2} \langle j_1, m_1; j_2, m_2 | V_{12} | j_1, m_1; j_2, m_2 \rangle}{\sum_{m_1,m_2}} \tag{1.8}$$

The monopole interaction changes the SPE of the orbital when adding more nucleons on top of a core. The so-called Effective Single Particle Energies (ESPE) can be expressed in term of the monopole TBME. Considering the addition of $n_{j'}^{p}$ protons on the proton orbital j' and $n_{j'}^{n}$ neutrons on the neutron orbital j' the shift of the ESPE of the proton orbital j $\Delta\epsilon_j^p$ is then given by [5]:

$$\Delta\epsilon_j^p = V_{pp}^{m}(j, j') n_{j'}^{p} + V_{pn}^{m}(j, j') n_{j'}^{n}, \tag{1.9}$$

and the shift of the ESPE of the neutron orbital j $\Delta\epsilon_j^n$ is then given by [5]:

$$\Delta\epsilon_j^n = V_{pn}^{m}(j, j') n_{j'}^{p} + V_{nn}^{m}(j, j') n_{j'}^{n}. \tag{1.10}$$

This ESPE drift can cause the disappearance of the known magic numbers or the appearance of new sizable shell gaps when going far from stability (*i.e.* when adding more and more nucleons to a core). The more the wave functions of the two orbitals j and j' overlap, the stronger is the coupling.

The V^m are phenomenologically known to be stronger for a proton-neutron ($T=0$) coupling than for a proton-proton or a neutron-neutron ($T=1$) coupling. Moreover, the V^m strongly decreases with increasing mass since the probability to find a pair of interacting nucleons in the interaction range is inversely proportional to the nuclear volume [5].

Based of the spin-tensor decomposition, the TBME can be separated into three contributions which are the central, vector and tensor components [16]. The central force component is the main driving force of the shell evolution. It always acts attractively, bringing binding energy to the system. The central force decreases as the difference Δn between the radial number of the interacting orbital increases.

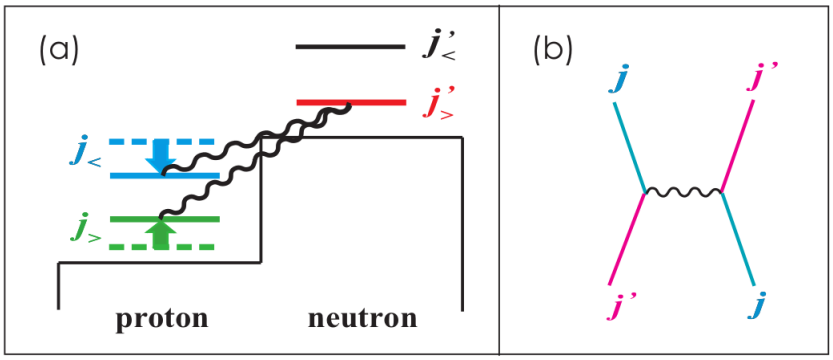

Figure 1.6: (a) Schematic picture of the monopole interaction produced by the tensor force between a proton in $j_{>,<} = l \pm 1/2$ and a neutron in $j'_{>,<} = l' \pm 1/2$. (b) Exchange processes contributing to the monopole interaction of the tensor force. Figure from Ref. [17].

In the past decades, numerous theoretical and experimental studies have been carried to better understand the tensor part of the monopole interaction. Otsuka *et al.* showed that many features of the shell evolution can be attributed to the tensor force [18, 17, 8]. The tensor force arises from the exchange of ρ and π mesons which process is shown in the right part of Fig. 1.6. The tensor force acts only on orbitals which have a non zero orbital angular momentum ($l > 0$) and its intensity decreases when the difference of orbital angular momentum Δl between the two orbits increases. The main feature of the tensor force is that it is attractive between spin-orbit partners $j_>$ and $j_<$ and repulsive between $j_>$ and $j_>$ or $j_<$ and $j_<$ orbits which have their intrinsic spins aligned or anti-aligned with the orbital momenta. This is schematically shown in the left part of Fig. 1.6 in which the proton-neutron tensor force of the neutron orbital $j'_>$ brings binding energy to the proton orbital $j_<$ while it makes the proton orbital $j_>$ less bound. The tensor force can therefore significantly change the spin-orbit splitting of the single particle orbitals and leads to the disappearance of magic numbers or to the appearance of new ones when going far from the stability (*e.g* the collapse of the $N=28$ magic number when going from the stable ^{48}Ca to the very exotic ^{42}Si [19]).

1.3 The N=20 Island of Inversion

One of the most famous and studied case of shell evolution among the nuclear chart is the $N=20$ Island of Inversion (IoI). Historically, the IoI referred to a group of neutron-rich nuclei in a region of

the nuclear chart centered around ^{31}Na [20]. In this region, instead of occupying the orbitals in the classical IPM ordering, the neutrons partly occupy the orbitals involved in the next shell, across the $N = 20$ shell gap, leading to a deformed ground state configurations.

Near stability, the ground state of an even-even magic nuclei corresponds to a spherical, closed shell configuration. The main configuration of the second 0^+_2 state usually corresponds to the promotion of a pair of nucleons to the upper shell. In the case of the $N = 20$ isotones, the ground state configuration corresponds to a filled neutron $d_{3/2}$ orbital while the 0^+_2 configuration corresponds to the promotion of a pair of neutron from the $d_{3/2}$ to the $f_{7/2}$ orbital, across the $N = 20$ gap (see extreme left part of Fig. 1.7). This type of configuration, which implies the next higher main shell, is usually referred as intruder configuration. The excitation energy of this state is therefore directly linked to the size of the $N = 20$ shell gap.

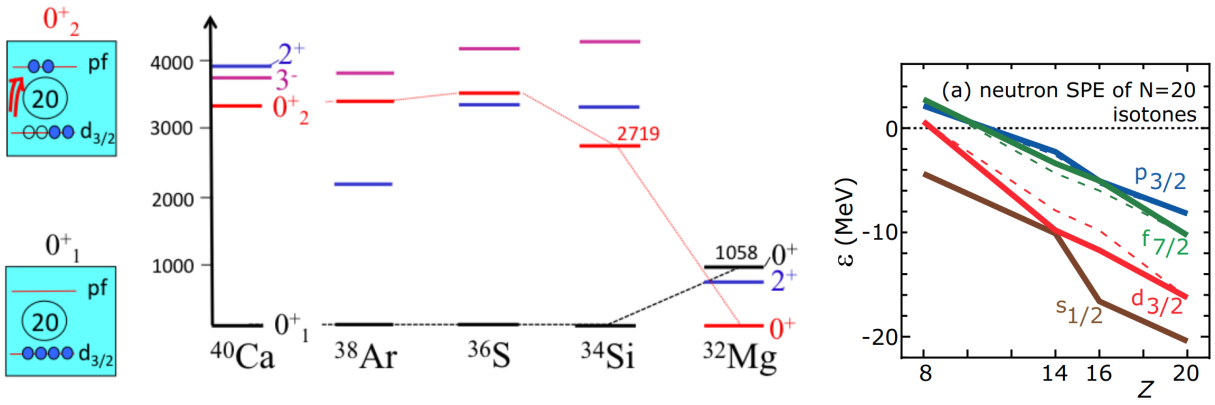

Figure 1.7: Left: Evolution of the 2^+_1 and 0^+_2 energies in the N=20 isotones from ^{40}Ca (Z=20) to ^{32}Mg (Z=12). Adapted from Ref. [21]. Right: Single-particle energies of the N=20 isotones calculated by VMU interaction. The dashed lines are obtained by the central force only, while the solid lines include both the central force and the tensor force. Adapted from Ref. [8].

The left part of Fig. 1.7 shows the evolution of the excitation energy of the 0^+_2 state along the $N = 20$ isotones. Its energy stays almost constant from $Z = 20$ (^{40}Ca) to $Z = 16$ (^{36}S) when emptying the proton $d_{3/2}$ orbital. When going from ^{34}Si to ^{32}Mg, one starts to empty the proton $d_{5/2}$ orbital which strongly reduces the size of the $N = 20$ gap. Indeed the TBME $V_{pn}(d_{5/2}, d_{3/2})$ is very large since it acts between spin-orbit partner of same orbital angular momentum. The TBME $V_{pn}(d_{5/2}, f_{7/2})$ is relatively smaller since it contains repulsive tensor force [8]. This is shown in the right part of Fig. 1.7 where the evolution of the ESPE along N=20 is presented. In this figure, the slope of the variation of the ESPE expresses the attractive power of a monopole. Therefore, one can see the reduction of the $N = 20$ shell gap, below Z=14, due to a stronger increase of the ESPE of the $d_{3/2}$ as compared to the one $f_{7/2}$ orbital. This evolution is associated with the emergence of a new shell gap at N=16.

Furthermore, when going from ^{34}Si to ^{32}Mg, the proton configuration changes from closed to open shell. This leads to an enhancement of the quadrupole proton-neutron interactions and therefore to the deformation of the nucleus [22]. The interplay of shell evolution, driven by the monopole proton-neutron interaction and the deformation induced by the quadrupole interaction leads to a deformed ground state to ^{32}Mg and to all the nuclei belonging to the Island of Inversion region.

2 The Isospin symmetry

The isospin quantum number was initially introduced by Heisenberg [23], soon after the discovery of the neutron by Chadwick [24] in 1932. Given that the proton and the neutron have very similar masses, he proposed to treat them as two different quantum states of the same particle, the nucleon. The isospin value of 1/2 was proposed for the nucleon (by analogy with the spin) and its projection on the z-axis characterizes the two different states: $t_z = -1/2$ for the proton and $t_z = 1/2$ for the neutron.

The strong interaction is, within a good approximation, invariant under a rotation by 180° in the isospin space. This property is called the charge symmetry and means that, once the coulomb effects are removed, the interaction between two protons or between two neutrons is identical ($V_{pp} = V_{nn}$). At a higher order of approximation, the strong interaction can be considered as invariant under any rotation in the isospin space. This is related to the charge independence of the strong interaction and implies that $V_{pp} + V_{nn} = 2V_{np}$ [25].

One can consider that the mirror symmetry, that exchanges the number of protons and neutrons in a nucleus as a good symmetry for a nuclear system. With the charge independent and charge symmetric properties of the strong interaction, if one can neglect the coulomb effects, the level schemes of mirror nuclei (with exchanged number of protons and neutrons) should be identical. Fig 1.8 shows a typical example of very similar level schemes in a mirror pair. In this figure, the level schemes of the mirror nuclei ^{23}Na and ^{23}Mg are compared for positive parity states up to 3 MeV. One can see that the level schemes are almost identical with very small energy differences between the analogue states.

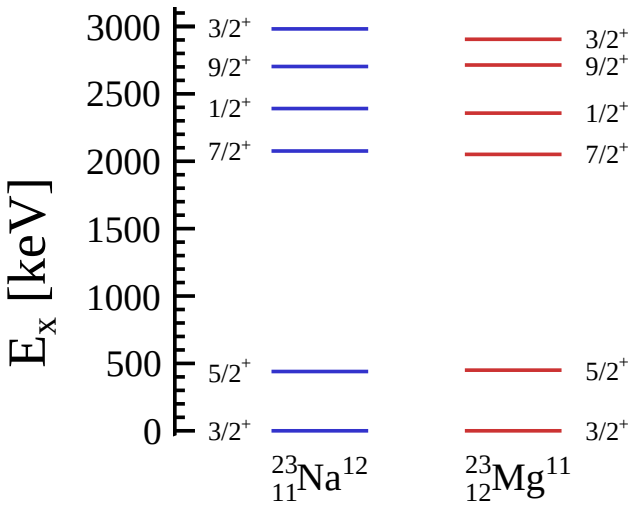

Figure 1.8: Comparison of the level schemes of the mirror nuclei ^{23}Na and ^{23}Mg. Only the positive parity levels up to 3 MeV are shown in this figure.

The Coulomb interaction breaks isospin symmetry since it acts only between protons. Since the Coulomb potential is inversely related to the distance of the charged particles to the core, the study of displacements in excitation energies between mirror nuclei is a very powerful and sensible probe to nuclear structure. In general, the effects of the Coulomb interaction are very small in the nucleus, arising from the strength of the electromagnetic interaction of 1/137 relatively to the strong interaction.

In some cases, electromagnetic effects are significant and induce differences in mirror spectra. In these cases, the energy displacement acts as a magnifying glass of the structure of the states.

The difference in excitation energy between analogue states in mirror nuclei is usually referred as Mirror Energy Differences defined as:

$$MED(J) = E_x^{T,T_z}(J) - E_x^{T,-T_z}(J), \tag{1.11}$$

where $E_x^{T,T_z}(J)$ is the excitation energy of state of spin J in the nucleus of total isospin T with its projection $T_z = \frac{N-Z}{2}$ while $E_x^{T,-T_z}(J)$ is the excitation energy of the analogue state in the mirror nucleus.

As for the Shell-Model Hamiltonian, the Coulomb potential V_C can be separated into a monopole V_{Cm} and a multipole component V_{CM} such as $V_C = V_{Cm} + V_{CM}$ [26]. The monopole part determines the effect of the Coulomb interaction on the single particle energies while the multipole one determines the effects on collectivity and configuration mixing. In Ref. [26], the authors have shown that, in order to reproduce the MED observed in the lower half of the pf region (such as in the ^{47}V-^{47}Cr or the ^{51}Mn-^{51}Fe mirror pair), an isospin non-conserving nuclear interaction V_B has to be introduced. They found that its contribution is at least as important as the Coulomb potential. Therefore, the MED can be fully described by three components [26]:

$$MED(j) = \Delta_M\langle V_{Cm}(J)\rangle + \Delta_M\langle V_{CM}(J)\rangle + \Delta_M\langle V_B(J)\rangle, \tag{1.12}$$

where $\Delta_M\langle V_{Cm}(J)\rangle$, $\Delta_M\langle V_{CM}(J)\rangle$, $\Delta_M\langle V_B(J)\rangle$ are the difference between the mirror nuclei due to the monopole Coulomb, multipole Coulomb and isospin non-conserving nuclear interaction, respectively.

The monopole component accounts for differences of charge radii between analogue states in mirror nuclei. When going from the ground state to an excited state configuration in a given nucleus, the occupancies of the orbitals may change as well as the resulting radius of the nucleus. Since Coulomb acts only on the protons, a change in the proton configuration induces a change of Coulomb energy which will not be felt by the mirror neutron configuration, inducing a MED between analogue states in mirror nuclei. The monopole Coulomb contribution to the MED can therefore be deduced from the difference of radius between the ground state and the exctited state J considered. Considering the Coulomb energy of an uniformly charged sphere, one can obtain [27]:

$$\Delta_M\langle V_{Cm}(J)\rangle = -\frac{3}{5}k(2Z-k)e^2\frac{\Delta R(J)}{R_C^2}, \tag{1.13}$$

where k is the number of nucleon inverted in the mirror pair such as the mirror nuclei have $T_z = \pm\frac{k}{2}$, Z is the number of protons of the nuclei which has the more protons among the mirror pair, R_C is the radius of the ground state and $\Delta R(J) = R_C(J) - R_C(g.s)$ is the difference of radius between the excited state J and the ground state.

The effect of the monopole term has been put in evidence in the rotational band of the mirror pair ^{48}Mn-^{48}V [28]. The mean radius of a single particle orbital increases with increasing value of n and l [6]. In the fp shell, the $2p$-orbits ($n=2$, $l=1$) have slightly larger radii than the $1f$-orbits ($n=1$, $l=3$)

arising from its larger number of nodes. In a rotational band, as the nuclear spin increases it becomes energetically favorable to couple pairs of particles to maximum angular momentum, corresponding to an alignment of their respective angular momentum. Alignment of nucleons along the rotational band will make the occupation of the $p_{3/2}$ orbital decrease and so the radius. This leads to an increase of the Coulomb repulsion and therefore of the MED. Therefore, it appears that the MED are directly sensitive to the variation of shell occupancy between ground and excited state, which is very interesting to probe the single particle configuration of excited states.

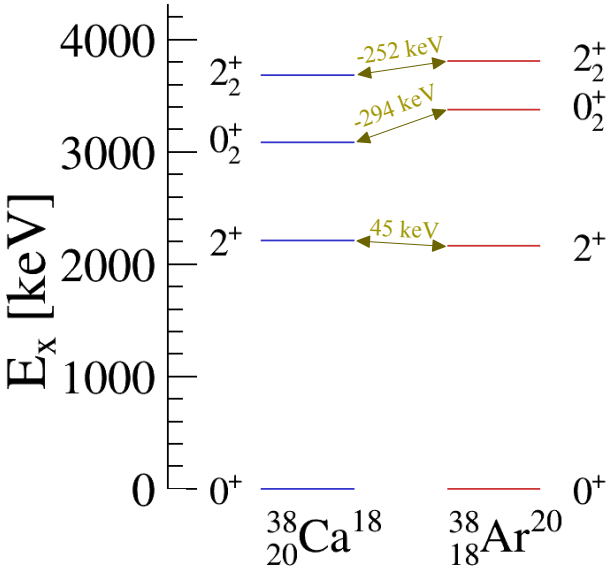

Figure 1.9: Comparison of the level schemes of the mirror nuclei ^{38}Ca and ^{38}Ar. Only the positive parity levels up to 4 MeV are shown in this figure. The corresponding MED are given in yellow.

MED have been extensively studied in the fp shell where the states are known to be very collective. Therefore, no strong impact of the monopole Coulomb interaction has been identified. Stronger influences of the monopole Coulomb interaction are expected to be seen when studying excitation energies of *sd* nuclei. Indeed in the *sd* shell, excited states can have a very pure single-particle nature. The difference of radius between s d and f orbitals, therefore, induces MED that can be used to probe the occupancies of the single particle orbitals.

Fig. 1.9 shows the partial level scheme of the mirror nuclei ^{38}Ca and ^{38}Ar, for positive parity levels up to 4 MeV. The ground state configuration of ^{38}Ar (^{38}Ca) consists mainly in two protons (neutrons) in the $d_{3/2}$ orbital coupled to $J = 0$ while the first 2^+ state corresponds to two protons (neutrons) in the $d_{3/2}$ orbital coupled to $J = 2$ [29]. The overlap of the wave functions of identical particles on the same orbital is reduced with increasing J [11]. This leads to a smaller Coulomb repulsion (in the case of ^{38}Ar) between the protons coupled to $J = 2$ than to $J = 0$ leading to a more bound configuration and therefore to a lower excitation energy of this state in ^{38}Ar as compared to ^{38}Ca. Still, this effect is small and leads to an observed positive MED of 45 keV.

The main configuration of the second 0_2^+ and 2_2^+ states corresponds to an intruder $2p-2h$ configuration with the promotion of a pair of proton (neutron) from the $d_{3/2}$ to the $f_{7/2}$ orbital in ^{38}Ca (^{38}Ar). This is known from the strong population of these states in the ^{36}Ar(^{3}He,n)^{38}Ca and the ^{36}Ar(t,p)^{38}Ar

reactions that populate excited states by addition of a pair of nucleons to non-occupied orbits and therefore, favor the population of intruder configurations. The increase of radius between $d_{3/2}$ and the $f_{7/2}$ ($n = 1$, $l = 3$) orbits combined with the large difference of their occupancies relatively to the ground state configuration leads to a smaller Coulomb repulsion (in the case of ^{38}Ca) and therefore, to large MED of -294 and -253 keV, respectively. The sign is in line with an increase of the radius (see Eq. 1.13) of ^{38}Ca when going from the ground to the intruder configuration. This is a nice illustration of a strong effect of the monopole Coulomb interaction on the MED.

3 The case of ^{36}Ca

In Section 1.3, we saw that the N=20 magic number disappears when going from ^{40}Ca ($Z = 20$) to ^{32}Mg ($Z = 12$), leading to the Island of Inversion centered around ^{31}Na. This shell evolution is driven by the monopole part of the NN interaction. If the isospin symmetry holds, the same scenario is expected to occur in the mirror region, leading to a strong reduction of the $Z = 20$ shell gap when going from ^{40}Ca ($N = 20$) to ^{32}Ca ($N = 12$). In the previous section, we saw that the MED reflects the structural properties of the excited states such as orbital radii or occupancies. The proton rich Ca isotopes are located close to the proton drip-line (^{35}Ca being the last bound Ca isotope) and the increasing influence of the continuum may further destroy the mirror symmetry. Therefore, the proton rich Ca isotopes are of special interest both for shell structure evolution driven by the monopole forces and for the study of the mirror symmetry.

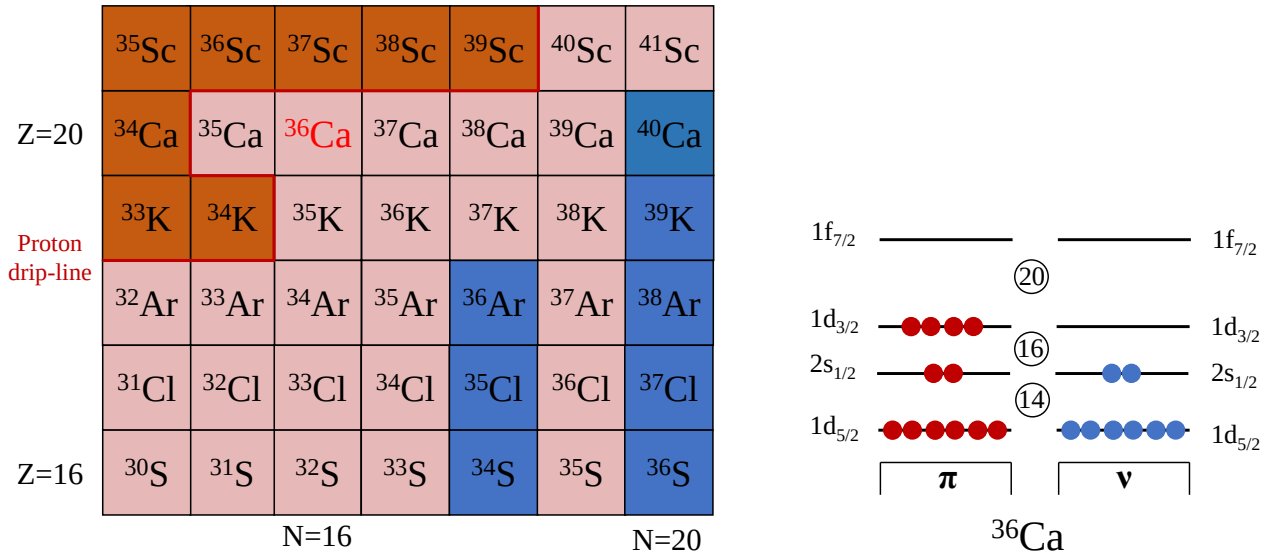

Figure 1.10: Left: The nuclear chart zoomed around ^{36}Ca . Stable, unstable and unbound nuclei are in blue, pink and brown respectively. Right: single particle structure of the ground state of ^{36}Ca .

^{36}Ca is a key nucleus to understand the physics of the region. It has 20 protons and 16 neutrons filling, in its ground state configuration (shown in the right part of Fig. 1.10), the proton and neutron orbits up to the $1d_{3/2}$ and the $2s_{1/2}$ orbital, respectively, leading to a spin-parity of $J^\pi = 0^+$. The first observation of ^{36}Ca was reported in 1976 by Tribble *et al.* [30], using the ^{40}Ca(^{4}He,^{8}He)^{36}Ca reaction to produce ^{36}Ca. From the measurement of the reaction Q-values, they performed its first

mass measurement with a mass excess of $\Delta M = -6440(40)$ keV. The second mass measurement of ^{36}Ca has been performed very recently (2021) by Penning trap mass spectroscopy [31]. The authors of Ref. [31] obtained a mass excess of $\Delta M = -6483.6(56)$ keV, improving by a factor 6 the precision. The first estimation of its life-time was performed in 1981 via β-decay measurement and was found to be about 100 ms [32]. The ^{36}Ca half-life has been remeasured in 1997 leading to a value of 102(1) ms [33].

The first observation of an excited state in ^{36}Ca was performed in 2007 both at GSI [34] and GANIL [35] by using a one-neutron knock-out reaction from a secondary beam of ^{37}Ca. Both experiments observed a single γ-ray at 3015(16) keV and 3036(11) keV, respectively. From the comparasion with the mirror nucleus ^{36}S, a spin parity $J^\pi = 2^+$ was proposed for this state. It is important to note that this 2^+ excited state is already unbound through proton emission since the one-proton separation energy of ^{36}Ca is $S_p = 2599.6(61)$ keV. The width of the momentum distributions measured in the GANIL experiment has shown a pure $l = 2$ distribution (from the removal of the $1d_{3/2}$ neutron in ^{37}Ca) for the ground state and a pure $l = 0$ distribution (from the removal of the $s_{1/2}$ neutron) for the 2^+ state. This is in line with a pure $1p-1h$ neutron configuration for the 2^+ state with the promotion of a neutron from the $2s_{1/2}$ to the $1d_{3/2}$ orbital. The energy of the first 2^+ excited state has been remeasured more precisely few years later at NSCL leading to an energy of 3045.0(25) keV [36]. The high excitation energy of the 2^+ state indicates a large $N = 16$ sub-shell gap which is supported by the pure $l = 0$ distribution obtained for this state in the GANIL experiment [35].

The strong $Z = 16$ sub-shell closure was known in the mirror nucleus ^{36}S and was interpreted as an effect of the tensor force. Indeed, ^{36}S has four neutrons filling the $d_{3/2}$ orbital. Due to the tensor interaction of the $d_{3/2}$ neutrons with the protons, the proton $1d_{5/2}$ orbital, becomes more bound whereas the proton $d_{3/2}$ orbital becomes less bound than for nuclei where the $\nu d_{3/2}$ shell is not completely filled. Tensor force does not act on s orbits, thefore, the $Z = 16$ gap bewteen the $\pi s_{1/2}$ and the $\pi d_{3/2}$ is enlarged, leading to high excitation energy for the first 2^+ excited state in ^{36}S of 3.291 MeV. The same picture holds for ^{36}Ca with exchanged numbers of protons and neutrons, which indicates the isospin independence of the tensor force.

Still, a large MED of $MED(2^+) = -276(16)$ keV (taking the value of Ref. [34]) is found in the 2^+ excitation energy when comparing to the mirror nucleus ^{36}S. This value is the largest MED observed in $T = 2$ mirror pair in the sd shell. This can be understood as an effect of the monopole Coulomb interaction. Indeed, both 2^+ states have a rather pure $1p-1h$ $d_{3/2}-s_{1/2}$ configuration. The large of radius of the $2s_{1/2}$ orbital as compared to the one of the $1d_{3/2}$ orbital makes the $2s_{1/2}$ slightly more bound relatively to the $1d_{3/2}$ in the case of the proton orbits as compared to the neutron ones. This effect, enlarges effectively the $Z = 16$ sub-shell closure leading to a higher excitation energy of the 2^+ in ^{36}S (with proton excitation) than in ^{36}Ca (with neutron excitation).

This large MED has been succesfully reproduced by the SM calculations of Ref. [37] (performed in $sdpf$ valence space with the SDPFU-M plus Coulomb effective interaction) with the mechanism described above. With the model constructed in Ref. [37], the authors predict that the first excited state of ^{36}Ca should be a 0^+_2 intruder state. Indeed, the 0^+_2 intruder state should have a $2p-2h$ configuration with the promotion of a pair of protons from the $d_{3/2}$ orbital to the $f_{7/2}$ orbital. As for ^{38}Ca, the large difference of radii between d and f orbits combined with the large difference of their

occupancies relatively to the ground state configuration should, therefore, generate a very large MED of $MED(0_2^+,^{36}\text{Ca}-^{36}\text{S}) = -720$ keV, called in Ref. [37] Colossal Mirror Energy Difference (CMED).

Therefore, additional spectroscopic information about ^{36}Ca is highly desired. It will allow to probe the nuclear structure of Ca isotopes when going toward the proton drip line. The identification of higher excited state in ^{36}Ca will allow to continue the study of the MED at higher excitation energies and eventually to identity CMED generated from the monopole part of the Coulomb interaction, which have never been observed up to now.

4 Experimental overview

To produce ^{36}Ca and populate its excited states, we used (p,d) and (p,t) transfer reactions in inverse kinematic induced by radioactive beams of ^{37}Ca and ^{38}Ca impinging on a liquid hydrogen target. As ^{37}Ca and ^{38}Ca are unstable nuclei, they cannot be used as targets due to their short lifetime of 181 ms [33] and 443 ms [38] respectively. Direct transfer reactions are direct mechanisms where one or a few nucleons are exchanged between the target and the projectile, without perturbation of the core. Fig.1.11 shows a schematic picture of the transfer of one and two neutrons via (p,d) and (p,t) transfer reactions to produce ^{36}Ca.

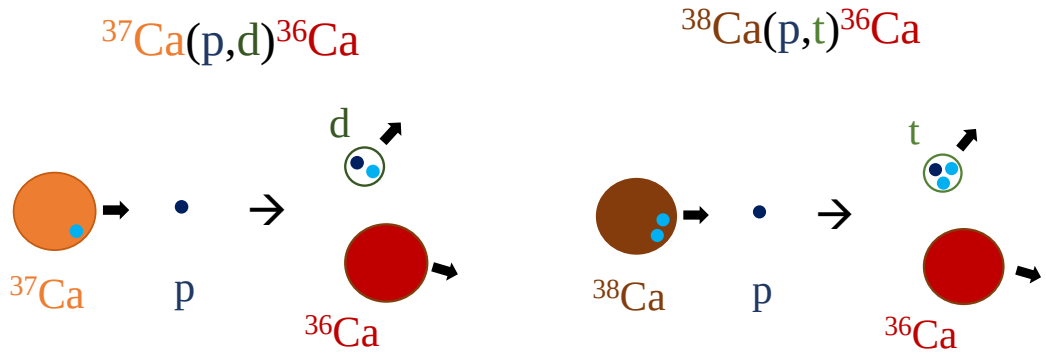

Figure 1.11: Schematic picture of the ^{37}Ca(p,d)^{36}Ca and ^{38}Ca(p,t)^{36}Ca transfer reactions.

This type of reaction is a very powerful probe to study nuclear structure. It allows to populate single-particle orbitals from or to which the nucleons are transferred. An intuitive picture of how single particle states are populated in ^{36}Ca via the ^{37}Ca(p,d)^{36}Ca reaction is shown in Fig.1.12. Here the removal of the $1d_{3/2}$ (L=2) neutron in ^{37}Ca produces the ^{36}Ca nucleus in its ground state. The removal of a $2s_{1/2}$ (L=0) neutron produces ^{36}Ca in the $\nu(2s_{1/2})^{-1}\nu(1d_{3/2})^1$ particle-hole excited configuration which generates two excited states of spin-parities $J^\pi = 2^+$ and 1^+. Finally, the removal of a $1d_{5/2}$ (L=2) neutron produces ^{36}Ca in the $\nu(1d_{5/2})^{-1}\nu(1d_{3/2})^1$ particle-hole excited configuration generating 4 states: 4^+, 3^+, 2^+ and 1^+.

Transfer reactions are governed by the two-body kinematics allowing indirect measurement of the spectroscopy of the outgoing heavy nuclei. Indeed, the knowledge of the energy and angle of the incoming projectile and of the light outgoing particle will allow us to reconstruct the excitation energy of the populated states in ^{36}Ca using the missing mass method. The kinematic lines of the ^{37}Ca(p,d)^{36}Ca reactions populating the ground and the first 2^+ excited state at 3 MeV in ^{36}Ca are

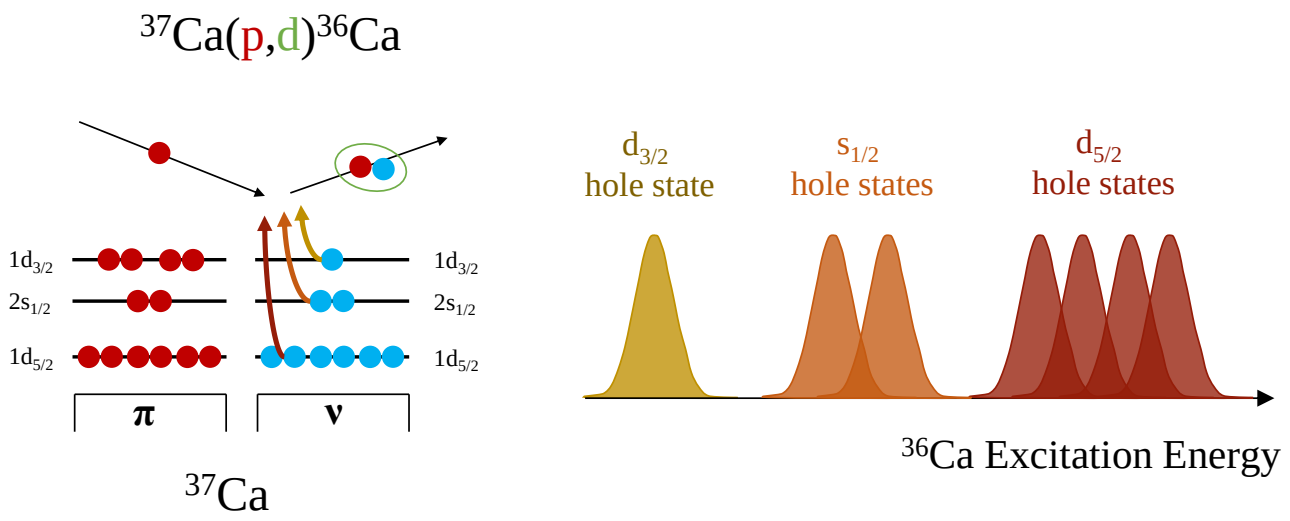

Figure 1.12: Left: The shell structure of ^{37}Ca is shown with protons in red and neutron in blue. The reaction is represented by a proton incoming and a deuterium outgoing. Right: Expected excitation energy spectrum in ^{36}Ca obtained with the ^{37}Ca(p,d)^{36}Ca transfer reaction.

shown in Fig.1.13. They display the relation between the energy and the angle of the light outgoing particle, in the laboratory frame for a given excitation energy. The corresponding angles in the center-of-mass frame are represented by dots on this figure.

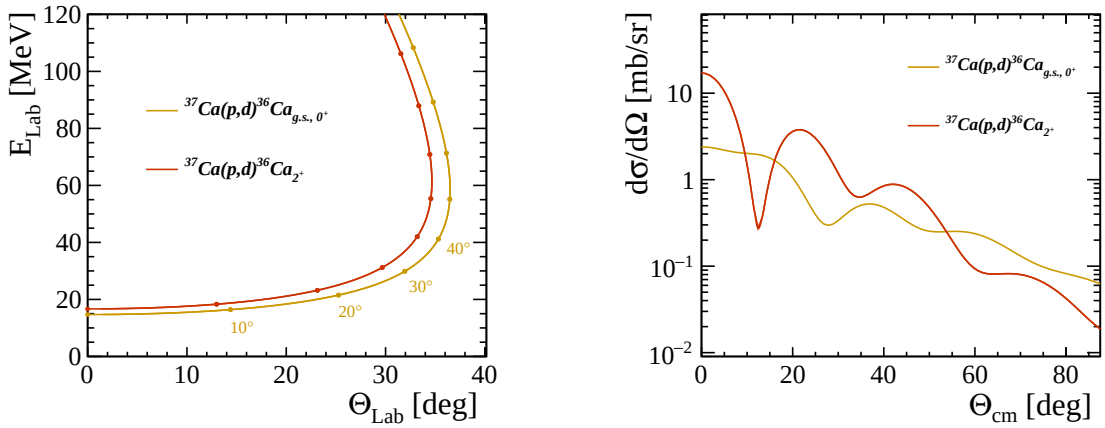

Figure 1.13: Left: Kinematic lines of the ^{37}Ca(p,d)^{36}Ca reactions at 48 MeV/nucleons for the 0^+ ground state (yellow) and the first 2^+ excited state at 3 MeV (red), which correspond, as explained in Fig. 1.12 to L=2 and L=0 transfer reactions, respectively. The corresponding theoretical angular distributions are shown in the right part. Dots on the lines indicate the corresponding angles in the center-of-mass frame.

The right part of Fig.1.13 shows the evolution of the cross section as a function of the center-of-mass angle of the light outgoing particles for the ground and the first 2^+ state. The differences in the shape of the cross sections between the two states arise from the orbitals from which the nucleon are removed in ^{37}Ca. As explained in Fig. 1.12, the ground state of ^{36}Ca is populated from the removal of an L=2, $1d_{3/2}$ neutron and the first 2^+ excited state from the removal of an L=0, $2s_{1/2}$ neutron. One

can see the main differences between the two angular distributions are at small center-of-mass angles. Indeed, an L=0 distribution displays a strong maximum at 0° while the L=2 distribution is rather flat between 0° and 20°. Hence, from the comparison of the shape of the measured angular distribution to the predicted one, one can deduce the transferred angular momentum L and then constrain the spin-parity of the populated state. The measurement of the light particles at small angles is, therefore, crucial for our study.

Another advantage of direct reactions is that it allows to extract the spectroscopic factors corresponding to the populated states in ^{36}Ca. The spectroscopic factor is a direct measurement of the single-particle purity of a given state. It is obtained from the ratio between experimental differential cross section and the calculated ones using Distorded Wave Born Approximation (DWBA) formalism. Usually, theoretical cross sections calculations are performed considering that the occupancies of the orbitals are the ones of the single-particle picture (*e.g.* in the case of the ^{37}Ca(p,d)^{36}Ca reaction, we consider an occupancy equals to 1 for the neutron $d_{3/2}$ orbital). Therefore, spectroscopic factors evaluate how a given state is represented by the single particle picture and is proportional to the occupancy of the orbital from which the nucleon is removed. More details can be found in Appendix A.

In the case of a one-nucleon transfer, the shape of the angular distribution is determined by the transferred angular momentum L which is given by the angular orbital momentum of the orbital from which the nucleon is removed (in the case of a stripping reaction). In the case of two-nucleon transfer, the transferred angular momentum L also characterizes the shape of the angular distribution but it is carried by the pair of nucleons. In this case, an L=0 distribution is obtained from the removal of a pair of nucleon from the same orbital while a L=2 angular distribution is obtained from the removal of the two neutrons in two different orbitals. Two-nucleon transfer reactions from even-even to even-even nuclei are especially well adapted to populate 0^+ excited states since it is very selective for $2p-2h$ configurations. Furthermore, if the ground state of the initial nucleus is mixed with other 0^+ excited configurations, the corresponding excited 0^+ states are expected to be populated together with the ground state in the final nucleus.

2 Experimental set-up

Sommaire

This chapter will presents the experimental method used to study the ^{37}Ca(p,d)^{36}Ca and the ^{38}Ca(p,t)^{36}Ca reactions. The production of the ^{37}Ca and ^{38}Ca radioactive beams will be detailed in Section 1. Prior to their interaction with the LH_2 target (see Section 2.2), the incoming nuclei are tracked by two CATS[1] (see Section 2.1) which allows the determination of the interaction point at the target in the directions perpendicular to the beam direction. To select the reaction of interest, we need first to identify the light ejectile of the transfer reaction and secondly to measure its energy and angle with high precision in order to reconstruct the kinematics of the reaction. This information is provided by a set of 6 MUST2[2] telescopes placed downstream of the target. Those detectors will be used as well to detect the protons emitted during the one-proton and two-proton decays from the one- and two-particle unbound states in ^{36}Ca or ^{35}Ca. The MUST2 telescopes will be presented in Section 2.3. Finally, to identify the heavy residue of the transfer reaction, we use a third stage of detection: the Zero Degree Detection (ZDD) system, composed of an ionization chamber, a set of two drift chambers and a plastic scintillator. As we are dealing with proton-rich nuclei that can decay by emission of one or two protons, the ZDD will allow us to identify the outgoing nuclei and to make a selection either on a Ca, K or Ar outgoing to study γ, one-proton and two-proton decays, respectively. All the detectors composing the ZDD will be presented in detail in Section 2.4. Furthermore, the combination of the identification of the incoming ^{37}Ca, the use of a liquid Hydrogen target, the identification of the deuterium (or tritium) from the transfer reaction and of the outgoing nucleus reject most of the background.

1 Beam production

1.1 Radioactive beams production

There are mainly two ways to produce radioactive beams: the isotope separation on line (ISOL) method and the in-flight separation method. The first one produces radioactive ions using spallation, fragmentation or fission induced by a light projectile (mainly photon, proton or neutron) on a thick target (mainly Uranium) [39]. The exotic ions produced are stopped in the target and have to diffuse to the surface to be collected. The chemical properties of the elements to be exctracted and the ones of the target play an important role. The ions of interest are then ionized and extracted to produce a beam suitable for nuclear physics experiments. This beam can be used at low energy (at about fex tens of keV) or post-accelerated at higher energies to induce secondary reactions. By using the ISOL technique, one can access to beam with high purity but some regions of the chart of nuclei are unattainable. Especialy, the proton-rich region is very difficult to access due to very short lifetimes ($<$ 100 ms). The ISOL method is used in many facilities around the world: SPIRAL at GANIL (France), ALTO at IJCLab (France), CARIBU at ANL (USA), ISOLDE at CERN (Swizerland), ISAAC at TRIUMF (Canada) and IGISOL at Jyväskylä (Finland)... Those facilities produce large variety of beams including fission fragments with energy going from few keV up to 25 MeV/nucleon (at GANIL, for the ligher nuclei)[40, 41] .

[1] Chambre A Trajectoire de Saclay
[2] MUr à STrip 2

The second method produces radioactive beams using projectile fragmentations. A primary stable beam is first accelerated up to few tens to hundreds of MeV/nucleon [40]. This primary beam impinges on a relatively thin target and the fragmentation products are then selected in mass and in charge using a spectrometer called fragment separator. This method provides beams at high energy (typically 2/3 on the incoming beam energy) and it very efficient to produce exotic nuclei with short half lives. Despite the use of a fragment separator, in most of the cases, the so-called "cocktail" beam is not pure. It contains many isotopes from different elements that can be identified by means of their energies and/or time-of-flights. The radioactive beams that can be produced with this technique depend mainly of the presence of a stable projectile-nucleus close to the nuclei of interest. For more than one nucleon removed, the fragmentation cross section loses one order of magnitude for each removed nucleon from the primary stable beam (e.g. for a primary beam of ^{40}Ca at $\sim 10^{10}$ pps we get for our experiment a secondary beam of ^{38}Ca at $\sim 10^{5}$ pps and of ^{37}Ca at $\sim 10^{4}$ pps). Again, many facilities around the world use this method to produce radioactive beam: GANIL (France), GSI (Germany), NSCL (USA) and RIKEN (Japan).

The choice of the facility for an experiment depends on many parameters: nuclei of interest, required energy, intensity, purity... In the case of the ^{37}Ca(p,d)^{36}Ca reaction, the Q-value of -12.5 MeV requires a ^{37}Ca beam of few tenth of MeV/nucleon. Therefore, we choose to produce the ^{37}Ca radioactive beam at GANIL using the "in-flight" method and the LISE spectrometer. Furthermore, the momentum matching for the pick-up reactions (*e.g.* (p,d) and (p,t)) is ideal at the typical beam energies provided by the LISE spectrometer. The next part details the production method of the radioactive cocktail beam of ^{37}Ca and ^{38}Ca.

1.2 Production of ^{37}Ca and ^{38}Ca nuclei at the LISE spectrometer

The E755 experiment was performed during summer 2018 at GANIL. The ^{37}Ca and ^{38}Ca nuclei were produced, in two different settings, using a primary beam of $^{40}Ca^{20+}$. A schematic layout of GANIL is shown in Fig.2.1. The ^{40}Ca is first ionized and extracted from the ion source. The primary beam pre-accelerated by the C01 cyclotron and then accelerated by the two cyclotrons CSS1 and CSS2 up to 95 MeV/nucleon with an average intensity of $\sim$ 2 μAe. It is then guided to the LISE spectrometer [42] to produce the radioactive cocktail beam from the fragmentation products of the ^{40}Ca on a 2 mm thick ^{9}Be target.

The LISE[1] spectrometer is operational at GANIL since 1984 and was the first spectrometer of its generation. The pioneer work of Remy Anne, the "father of LISE", has inspired many other works such as A1200 at NSCL, FRS at GSI and RIPS at RIKEN [43]. A schematic view of the LISE spectrometer is shown in Fig.2.2. It is composed of two main magnetic dipoles used to separate the different isotopes of the beam, several quadrupole magnets to focus the beam, an achromatic degrader and a Wien filter. First the beam is deflected by the first magnetic dipole. The curvature of the trajectory of each ion is defined by the magnetic rigidity of the dipole:

$$B\rho = \frac{\gamma m v}{q},$$

[1] Ligne d'Ion Super Epluché

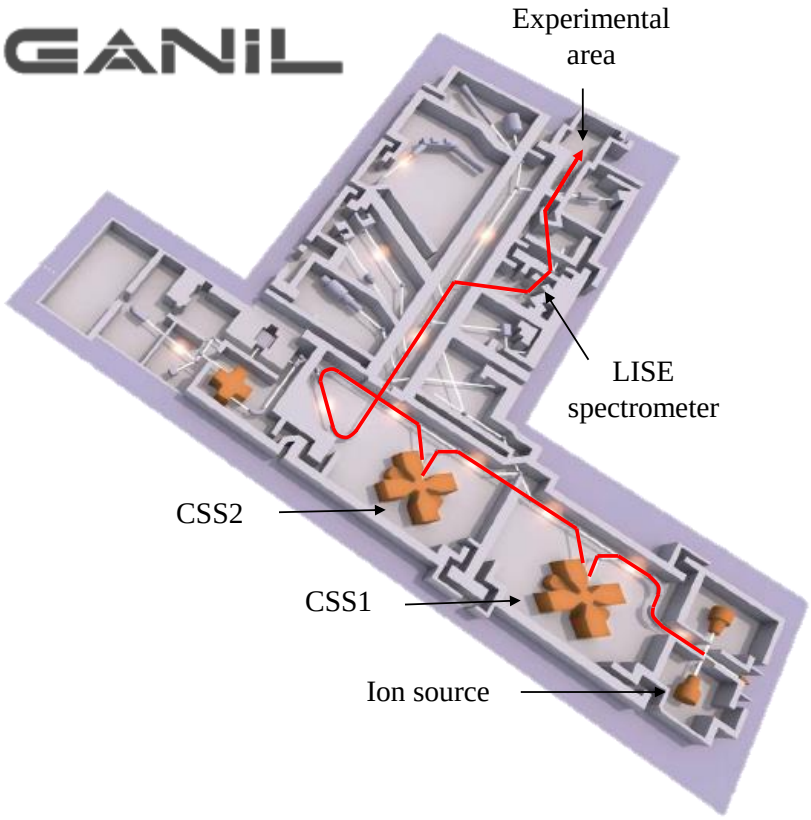

Figure 2.1: Schematic layout of the GANIL facility. The path of the beam for the E755 experiment is highlighted in red.

where B is the magnetic field of the dipole, ρ the radius of curvature of the ion and γ, m, v and q, the Lorentz factor, the mass, the velocity and the charge of the ion. Since all the ions have very similar velocities, each ion will be deflected differently depending on its $\frac{m}{q}$ ratio. Then, the beam is focused by a set of quadrupoles on the first dispersive focal plane where a first set of slits (FH31) is placed. Ions with different $B\rho$ are focused at different positions in the dispersive focal plan. The first set of slits induces a first selection in $B\rho$ on the fragmentation products and defines the $B\rho$ acceptance of the setting. If the ions are fully stripped, this is equivalent to an A/Z selection, where A and Z are the mass and charge number of the ions [44].

To achieve a better selection on the fragmentation products, a Be achromatic degrader is inserted at the first dispersive focal plane (slits FH31). This degrader induces an energy loss ΔE selection, which, according to the Bethe-Bloch formula, is proportional in first order approximation to $\frac{AZ^2}{E}\Delta x$, where E is the energy of the ion and Δx the thickness of degrader crossed, for fully stripped ions [42]. Due to this energy loss, isotopes with different Z will have different velocities after passing through the degrader. Isotopes with the same A/Z ratio will then be separated by the second dipole, in the second focal plane of the spectrometer, where a second set of slits is placed (FH43). This is equivalent to an A^3/Z^2 selection [42]. To preserve the achromatism of the system, the degrader has a wedge shape. Indeed, with a uniform wedge, since the ions have slightly different velocities, two ions sharing the same A and Z will not loose the same amount of energy. The degrader is shaped in a way that

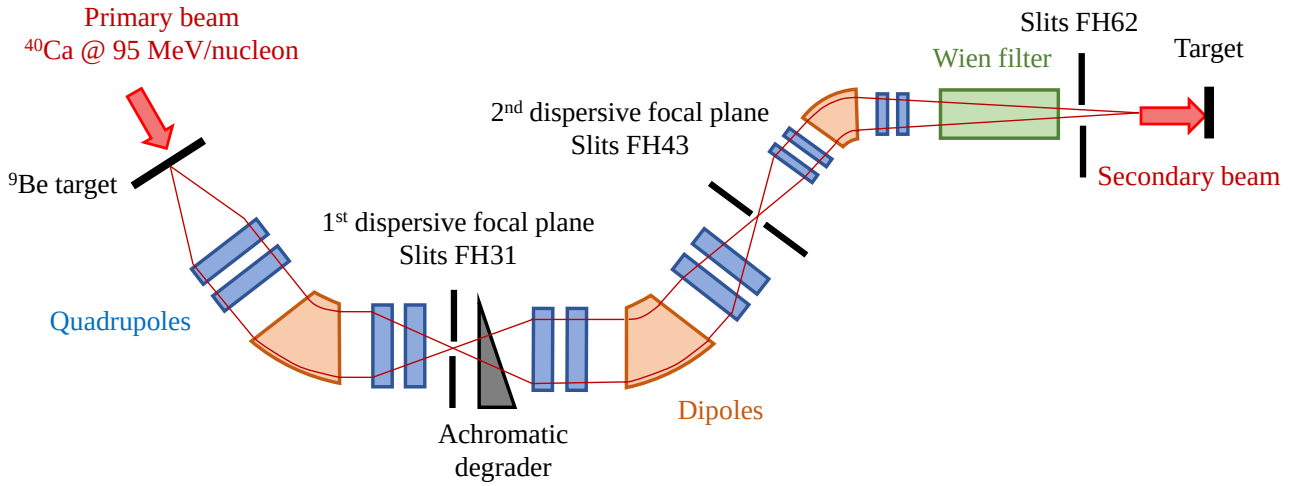

Figure 2.2: Schematic layout of the LISE spectrometer. The path of the beam for the E755 experiment is highlighted in red.

the fastest ions (the less bent by the first stage) see the thickest part of the degrader.

Finally a third stage of selection is applied using a Wien filter. A Wien filter is a combination of an electric field and a magnetic field in cross configuration. It acts as a velocity filter since the particles with a velocity different from $v_0 = -E_x/B_y$ will be deflected. To be at the maximum of its capabilities, the focus of the beam has to be done on the slits downstream of the Wien filter (FH62). This was unfortunately not achievable in our experiment, since the beam would have then be not properly focused when impinging on the LH2 target. Recently a set of quadrupoles has been installed between the final slits and the target to be able to focus the beam on both places, leading to an optimal secondary beam selection as well as an almost parallel beam optics over a long distance, up to the target.

For the E755 experiment two different settings of the spectrometer were used to optimize the production of ^{38}Ca and ^{37}Ca, which were transmitted at $B\rho$ values of 1.9860 and 1.9242 Tm, corresponding to energies of 51 and 48 MeV/nucleon at the target center, respectively.

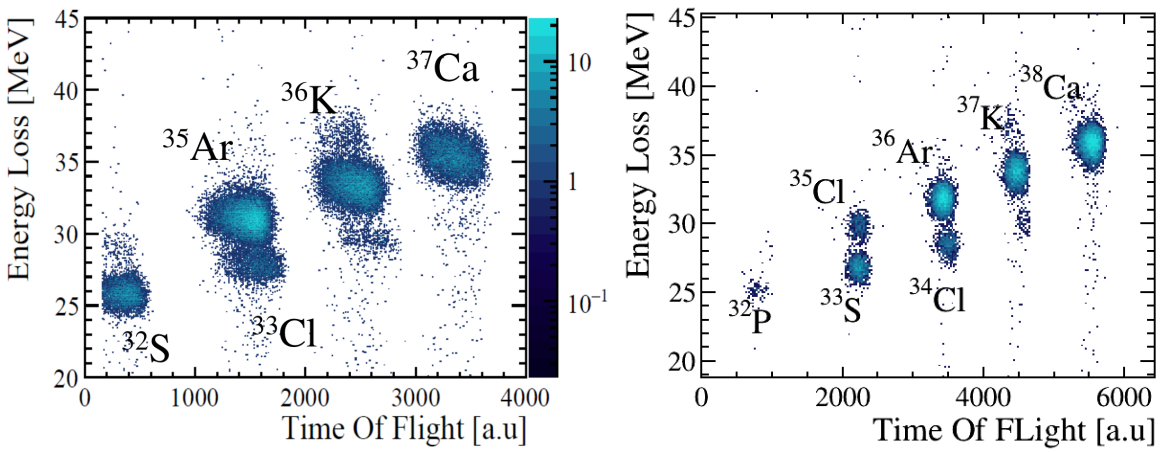

Figure 2.3: Energy loss measured in the ionization chamber at the end of the line vs. time of flight identification of the nuclei produced in the ^{37}Ca (left) and ^{38}Ca (right) cocktail beams.

The average intensity of the total beam was a few 10^5 particles per second (pps) for the ^{38}Ca setting and a few 10^4 pps for the ^{37}Ca one. The ^{38}Ca and ^{37}Ca represented respectively 28% and 20% of the total fraction of nuclei transmitted in each setting. The beam identification in the experimental area, of the two settings is shown in Fig.2.3. The identification is achieved by analyzing the correlation between the energy loss of the ions measured in the ionization chamber of the ZDD and the Time Of Flight (TOF) of the isotopes between the Hight Frenquency (HF) signal of the pulsed beam and the CATS detector. One can see in Fig.2.3 that there are still few contaminants produced along with ^{38}Ca and ^{37}Ca. Those contaminants will be very useful for the calibration of the detectors and they will not be a source of background. Indeed the TOF alone allows the separation of the Ca isotopes from other nuclei. For the ones having the same time-of-flight, the ionization chamber will be used to separate contaminants, thanks to energy loss measurement.

2 Experimental set-up

In the following, each element of the experimental setup will be presented. A schematic view of the setup is shown in Fig.2.4.

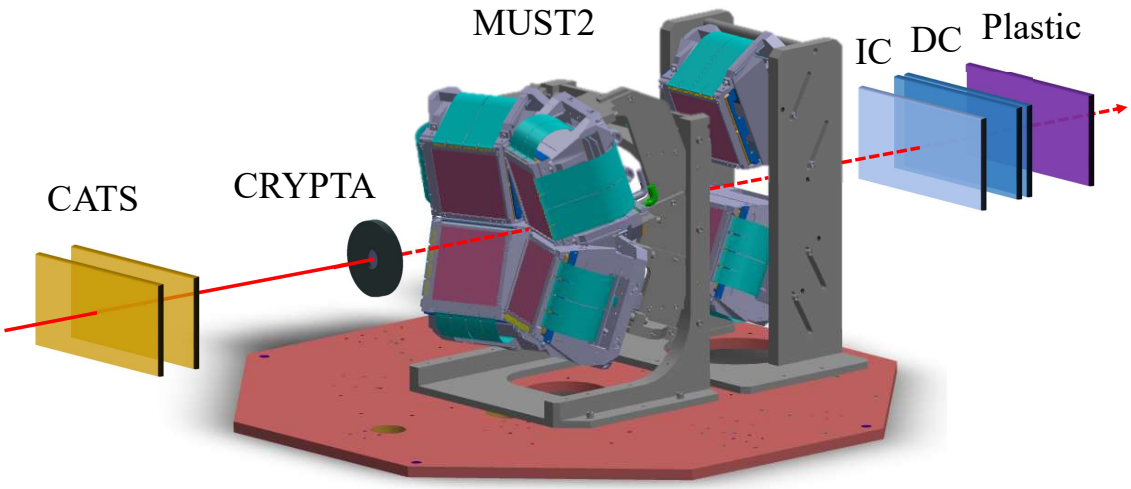

Figure 2.4: Schematic layout (not on scale) of the experimental setup. The MUST2 telescopes are represented together with the two CATS beam tracker detectors, the CRYPTA liquid Hydrogen target, the ionization chamber (IC), the drift chambers (DC), and the plastic scintillator.

2.1 Beam tracker: CATS

Radioactive beams produced by fragmentation have usually a large emittance with a position spread on the target that can reach few centimeter. However, the information of the position of the interaction vertex inside the target and of the angle of the beam is needed in order to measure the emitted angle of the light ejectile with a good precision. For this purpose, a set of two CATS detectors, located at 1188 mm and 678 mm prior to the target, was used in order to obtain a precise reconstruction of the trajectories of the beam event by event. The excellent time resolution (few hundreds of picosecond) of those detectors was used for a precise time-of-flight measurement. Finally those detectors were also used to count the number of incoming nuclei, information needed for the normalization of the cross sections.

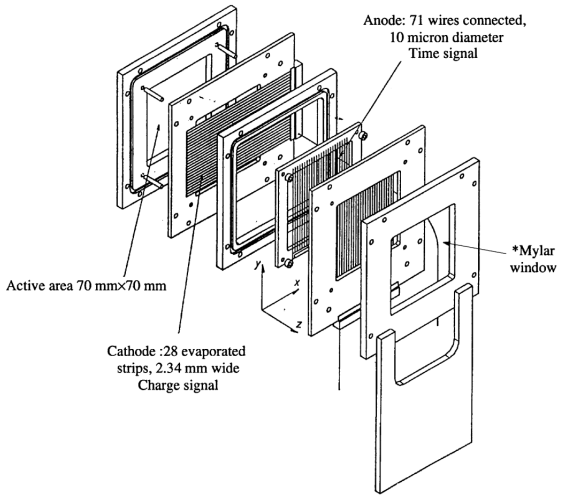

Figure 2.5: Exploded view of a CATS chamber.

CATS detectors [45] are low-pressure multi-wire proportional chambers (see a schematic view of CATS in Fig.2.5). Each detector is composed of one plane of anode wires placed between two cathode planes (active area: 70x70 mm^2), segmented into 28 vertical or horizontal strips. The anode wires deliver a time signal allowing a time of flight measurement with an accuracy of few hundreds of picoseconds. The cathode strips are individually read out and the position of incoming particles is reconstructed using a charge centroid finding methods. The trajectory is then reconstructed using the positions measurement of the two detectors. The gas used for our experiment was isobutane (C_4H_{10}) at 7 mbar and the voltage applied was 580 V. The maximum beam intensity accepted by CATS is about few 10^5 pps. If this value is exceeded, the strips could be damaged.

2.2 The liquid Hydrogen cryogenic target

To perform the one and two neutron transfer reactions, the radioactive cocktail beams impinge on a proton target. There are two main types of such target : CH_2 solid targets and cryogenic targets of liquid (or solid) Hydrogen. The choice of the target to use in an experiment depends on the resolution and the yield which are needed to study the phenomena of interest. The thicker the target is, the

higher the yield will be since it increases the number of protons with which the beam can potentially interact. But the thicker the target is, the more it will degrade the resolution since it increases the energy and angular straggling of the particles inside the target. It is the same for the volume density. To take into account both effects of volume density (ρ_v in mg/cm^3) and thickness (e in cm), nuclear physicists often use the surface density (or thickness) $\rho_s = \rho_v e$ (in mg/cm^2) to define a target.

The most common proton targets are CH_2 types. They have a typical surface density from hundreds of μg/cm^2 to few mg/cm^2, i.e. a typical thickness from 10 to 100 μm. They have the advantage to be easy to manipulate and to produce. On the other hand, the presence of carbon atoms reduces the number of hydrogen atoms per unit of length and generates large amount of contaminant reactions which are sources of background. The second type of proton target consists in liquefying Hydrogen (at temperatures between 14 K and 20 K) to reach higher densities. For a same surface density and equivalent energy straggling, cryogenic targets have five times more protons than a CH_2 target. They have the disadvantage to be much more complicated to build and to manipulate. Fig.2.6 shows the resolution obtained with simulations in excitation energy for the ground state of ^{36}Ca using the ^{37}Ca(p,d)^{36}Ca reaction. The simulation has been performed using a ^{37}Ca beam at 50 MeV/nucleons with 2% of beam energy resolution. The red curve corresponds to a simulation with a cryogenic target of liquid Hydrogen (LH_2) and the blue curve to a simulation performed with a solid target of CH_2. The thickness of the CH_2 (about 560 μm) was set to get the same number of protons in both target. The obtained resolution is almost two times better with the cryogenic target for the same obtained yield.

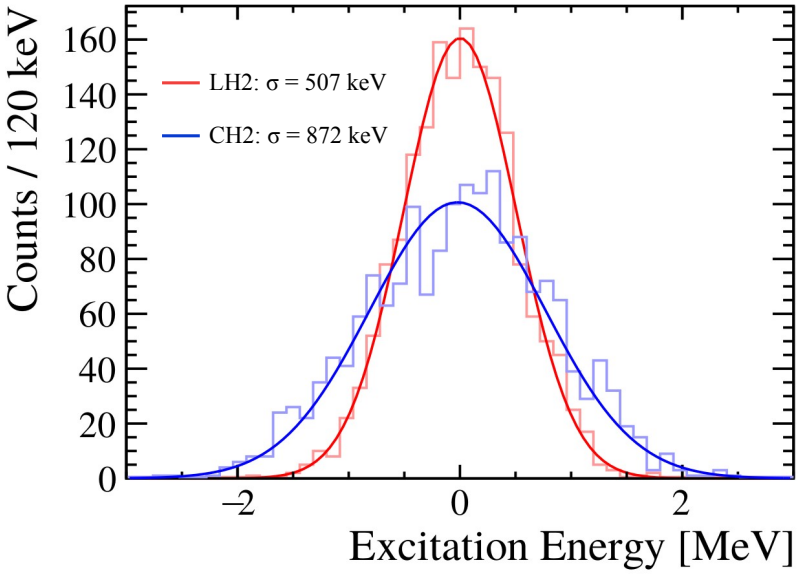

Figure 2.6: Simulated excitation energy spectra of the ^{37}Ca(p,d)^{36}Ca$_{g.s.}$ reaction. The blue curve correspond to a simulation performed with a solid CH2 target. The red curve correspond to a simulation performed with a cryogenic target of liquid Hydrogen.

For our experiment the expected yield of ^{36}Ca produced during the full experiment is a few thousands via ^{37}Ca(p,d)^{36}Ca and only a few hundreds via ^{38}Ca(p,t)^{36}Ca . To maximize these yields, without degrading the energy resolution, the use of a cryogenic target was mandatory. We used the

liquid hydrogen cryogenic target CRYPTA [46] of RIKEN.

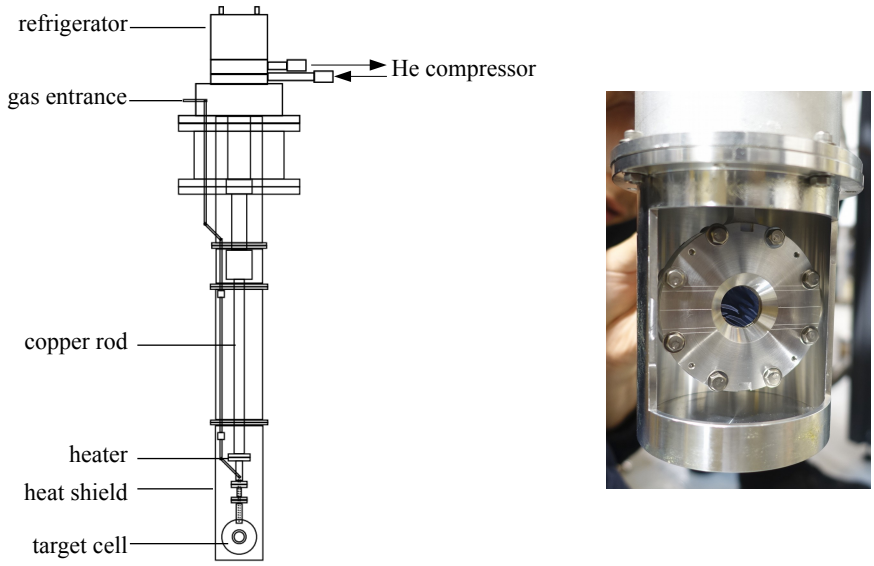

Figure 2.7: left: Schematic drawing of the cryogenic target. right: Picture of the target cell.

A schematic view of CRYPTA is shown in Fig.2.7. The cryogenic target consists in a 7.6 cm diameter target cell filled with liquid Hydrogen. The Hydrogen is liquefied by a Gifford-McMahon cycle refrigerator using gaseous Helium. The target cell is connected to the refrigerator by a copper rod. The target cell and the copper rod are surrounded by an aluminum shield, called heat shield, to protect the cold parts from thermal radiations. The whole system is placed under vacuum in the reaction chamber.

The boiling point of Hydrogen is at 20.3 K and its melting point at 14.0 K under atmospheric pressure. To maintain the temperature between these two values, a heater regulates the temperature inside the target cell. To avoid condensation of atoms of the reaction chamber on the target (which act like a hot thermostat), a vacuum level of 10^{-6} mbar is required to cool the target cell. During the experiment the target cell was cooled at 18 K at a pressure of 0.9 bar. The vacuum inside the reaction chamber was maintained at $2{\cdot}10^{-6}$ mbar.

The liquid Hydrogen was maintained between two 6.47 μm thick HAVAR foils separated by 0.5 mm. Each window has a circular aperture of 20 mm in diameter. Due to the important difference in pressure between the target cell and the reaction chamber, the filling of the target with liquid Hydrogen induced a significant deformation of the HAVAR foils. This deformation has been parameterized, using a 0.1 mm precision position measurement from a laser system. The results of the front and back surfaces are shown together in Fig.2.8. The shapes of the foils were fitted with a parabolic function. The target thickness spanned from 0.5 mm (at the edges) to 1.5 mm (at the center) corresponding to an effective surface density of 9.7 mg/cm^2. This study allows to correct from the energy loss of the particles inside the target, event by event, and therefore improve the reconstructed energy resolution.

During the experiment, gas contaminants were condensing on the heat shield, forming a layer of ice of unknown thickness and composition crossed by the light ejectiles. To minimize this effect and keep

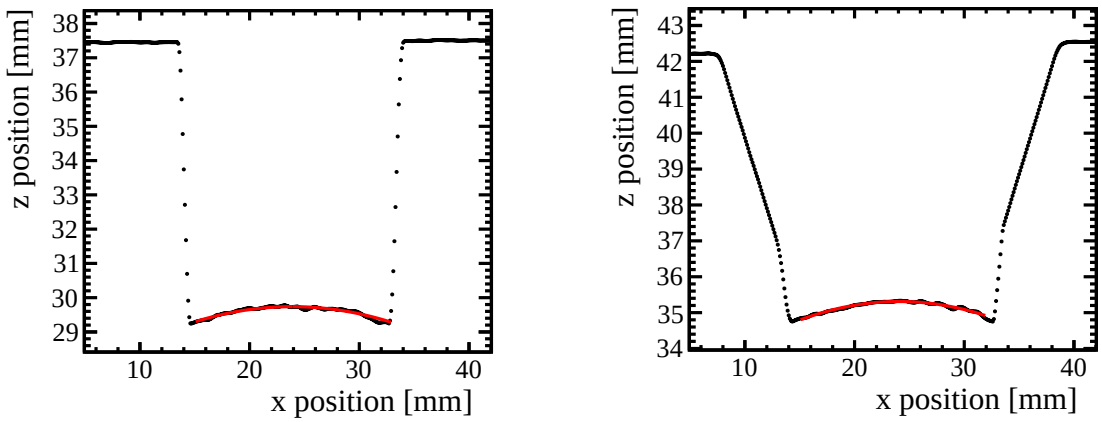

Figure 2.8: Surfaces of the upstream (left) and downstream (right) target window foils scanned by a laser sensor. The measurement were performed under vacuum (with 1 atm pressure inside the target cell) at the room temperature. One can see that the edges of the downstream window are tilted to not intercept particles scattered at large angles. The red line shows the parabolic fit of the surfaces.

the Hydrogen in a liquid phase, the target was warmed-up and cooled down three times during the 12 days of experiment in order to evaporate the ice layer. The thickness of this ice has been estimated by looking at the evolution of the position of a reference peak in excitation energy during one cycle. No significant shift was observed and the ice layer was estimated to be less than 10 μm equivalent H_2O.

2.3 Light particle detection: MUST2

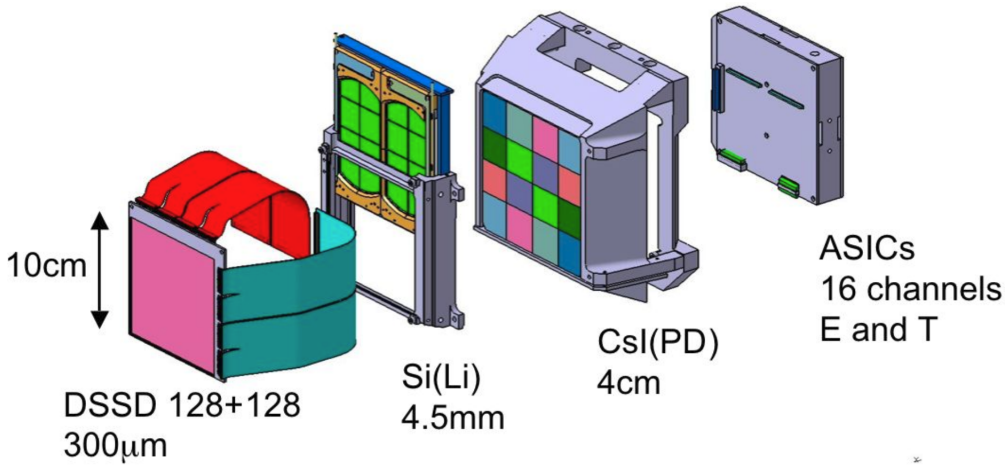

Figure 2.9: Exploded view of a MUST2 telescope.

The MUST2 telescopes [47] are dedicated to the measurement of light charged particles. A schematic view of a MUST2 telescope is shown in Fig.2.9. In our experiment, a set of 8 MUST2 telescopes was used. As explained in the beginning, the detection of light particles at small angles is crucial for this study. For this reason, the MUST2 telescopes were moved back compared to their normal configuration and two additional telescopes were added to cover very small angles. A wall

of 4 telescopes, placed at 22 cm from the target, covered angles from 5° to 37° while 2 telescopes placed downstream of the wall at 57 cm covered smaller angles from 3° to 5°. Two more telescopes were placed at large scattering angles to cover angles from 40° to 63° but they were not used for our experiment. The layout of our MUST2 set-up is shown, together with the geometrical efficiency, in Fig.2.10. Each telescope can be made of up to three detection stages:

- The first stage is a 300 μm-thick Double-sided Silicon Stripped Detector (DSSD) of 100*100 mm^2 active area. Each side of the Silicon has 128 strips (along the X axis on one side and along Y axis on the other side) with a 760 μm strip pitch and 60 μm inter-strip. Each strip is covered by a 0.4 μm-thick Aluminum foil. The typical strip resolution in energy is around 20 keV (for a 5.5 MeV α particle) and the time resolution is 500 ps. The angular resolution for the wall of 4 telescopes is about 0.2° and the one of the two placed downstream is about 0.1°. This stage provides measurement of the energy loss, time and position of the particles.

- The second is a 4.5 mm-thick Lithium-doped Silicon (Si(Li)). It composed of two sub-detectors segmented in 8 pads of 2.5x2.5 mm^2 each. The active area represents 68% of the first stage. Only the 2 telescopes at the largest angle were equipped with this stage to avoid a loss of efficiency.

- The third stage is composed of 16 40 mm-thick CsI scintillator crystals of 30x30 mm^2 read by 16 photo-diodes. Each crystal is covered by a 3 μm-thick foil of aluminized Mylar. The active area represents nearly 100% of the DSSD. Therefore the 6 telescopes at the most forward angles were equipped with this detection stage. Their typical resolution is about 5% with 5.5 MeV alpha particles and their dependency to the particle energy is given by $\sigma_{CsI} = 0.08\sqrt{E_{CsI}}$ (MeV). This stage provides measurement of the residual energy of the particles.

Since the angular range of the reactions of interest does not exceed 40°, the two telescopes at the largest angles, equiped with the Si(Li) stage of detection, were not used in the analysis.

Each MUST2 telescope is read-out by a set of two MUFEE[1] cards containing 9 MATEs[2] each. A MATE allows treating 16 channels and provides energies and time measurement. Signals are then sent to the MUVI[3] digital board installed in a VXI crate. The MUVI cards suppress the pedestals of each channel and digitize the signal to be stored in data files and produces trigger information.

2.4 Outgoing heavy ions detection: the Zero Degree Detection (ZDD)

After interaction with the target, the outgoing heavy ions were detected by means of the so-called Zero Degree Detection (ZDD) which is composed of three detectors:

- The first detector is a 100 mm thick ionization chamber filled of CF_4 gas at 250 mbar. The applied voltage was 1400 V for the anode and -1300 V for the cathode. It provides measurement of the energy loss of the outgoing heavy ions.

[1] MUST Front End Electronics
[2] MUST2 ASIC Time and Energy
[3] MUst in VxI

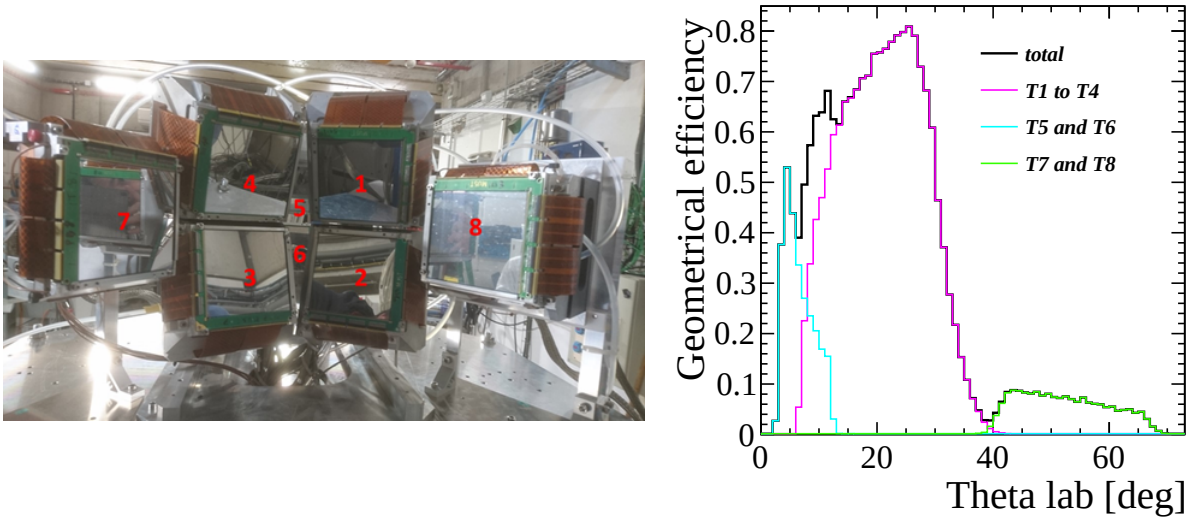

Figure 2.10: Left: Photo of the layout of the MUST2 configuration used in our experiment. The numbering of the 8 MUST2 telescopes is shown in red. Right: Geometrical efficiency of our MUST2 set-up.

- The second ensemble is a set of two XY drift chambers located at 85 cm and 103 cm downstream of the target. There were filled with isobutane at 20 mbar. The applied voltage was 450 V for the anode and the wires and -250 V for the cathode. Each drift chamber provides a measurement of the position of the residual nuclei via the measurement of the drift time inside the detector. Its trajectory is reconstructed using the position measurement of the 2 drift chambers.

- The third detector is a 1 cm thick plastic scintillator coupled to a photo-multiplier with an applied voltage of 1600 V. This detector measures the residual energy and the time of the outgoing heavy ions. Since this detector was intercepting the beam, the plastic was burned during the first day of the experiment degrading strongly its energy resolution. Therefore this detector was only used for time measurement.

To avoid a big loss of efficiency due to pile-up at high beam intensity, the ZDD was read-out by NUMEXO2 digitizer. NUMEXO2 uses a trapezoidal filter to determine the amplitude of the signal and determine if there were in pile-up. The time of the plastic scintillator acted as time reference for the ZDD acquisition system. A picture of the experimental area with the M2C chamber and the ZDD is shown in Fig.2.11.

3 Trigger

The GMT[1] module was collecting the trigger signals from different ensemble of detectors (MUST2, CATS, plastic ...), and generating a common acquisition time window of 100 ns for the whole acquisition. To avoid a big loss of efficiency due to dead time it is necessary to trigger the acquisition only

[1]Ganil Master Trigger

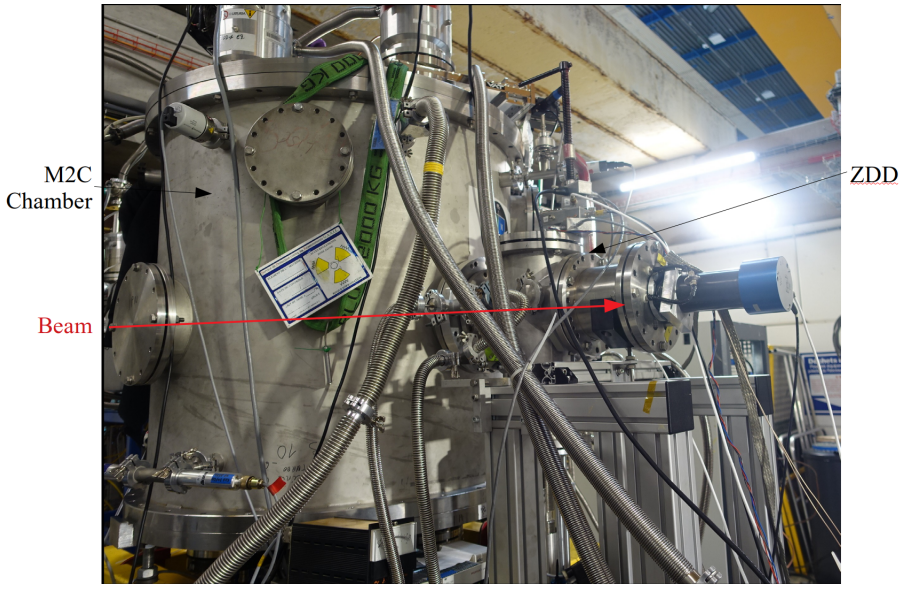

Figure 2.11: Picture of the experimental area. The beam is going from left to right. One can see the reaction chamber and the ZDD going out from the chamber.

on the events of interest. Therefore the main trigger of the acquisition was the OR of the MUST2 telescopes. In our experiment a beam intensity of $2{\cdot}10^5$ pps corresponds to a trigger rate of about 300 Hz for each MUST2 telescope. To count the total number of nuclei which were impinging on the target, a trigger of CATS was also present but divided by 30000 in order not to overload the acquisition. Here is the list of the triggers:

- Logic signals from the 8 MUST2 telescopes.
- Logic signals from the 2 CATS detectors divided.
- Logic signals from the plastic scintillator divided.

The global dead time was about 20% during the ^{38}Ca beam setting and about 10% during the ^{37}Ca beam setting.

3 Analysis

Sommaire

This chapter presents the data processing from raw data to physical observables. The calibration of the CATS detectors and the reconstruction of the trajectories of the incoming nuclei will be presented in Section 1. The energy calibration of the MUST2 telescopes and the identification of light outgoing particles will be presented in Section 2. The Zero Degree Detection (ZDD) data treatment will be presented in Section 3. Finally, the extraction methods for the physics observables will be presented in Section 4. The analysis and the simulations presented in the following have been performed using the NPTool package [48].

1 Beam tracking with the CATS detectors

In order to determine the position and the direction of the beam particles on the target, we use a set of two CATS detectors placed at 1188 mm and 678 mm upstream of the target (see Section 2.1). The analysis method of this detector is presented in the following.

1.1 Strips alignment

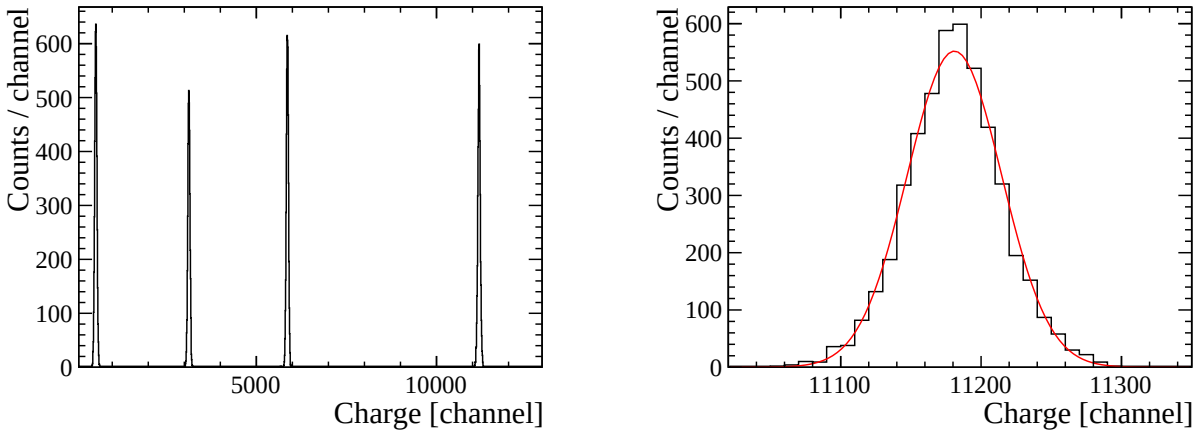

Figure 3.1: Left: Charge distribution obtained with the pulser for strip 9 of CATS 1 X. Right: Gaussian fit of one pulser peak.

The position of the beam is determined from the charge distribution along the X and Y cathode strips in CATS. Each strip has its own electronic channel with its own gain and pedestal. Therefore, to obtain an exploitable charge distribution, the gain of each strip has to be adjusted to reconstruct a correct centroid position. To this purpose, a pulse generator was used to inject a signal on the anode wires. The induced charges on the cathode wires by capacitive coupling has been measured. The amplitude of the pulse was changed to obtain series of peaks covering the useful range of the detector. Fig. 3.1 shows the charge distribution of one strip of one detector obtained after this operation. The top part of Fig. 3.2 shows the charge distributions obtained in CATS1 as a function of the strip number.

Each time a single strip receives a signal, all the strips are read out. Strips that didn't receive any electric pulse contains only a very weak signal which is coded at the position of the pedestal corresponding to the zero of the electronic. Each peak (including the pedestals) is fitted by a Gaussian

distribution (as shown in Fig. 3.1) in order to measure its position and width. To align the gain of the strips, the charge of the 12^{th} one, named Q_{ref}^{cal} in the following, was chosen as an arbitrary reference. The relation between the reference charge distribution Q_{ref}^{cal} and the one of the strip to align Q_i^{raw}, is fitted with a second order polynomial. Then each strip is aligned to the reference strip with the relation:

$$Q_i^{cal} = a_i(Q_i^{raw} - P_i)^2 + b_i(Q_i^{raw} - P_i) + c_i, \tag{3.1}$$

where, for the strip number i, Q_i^{raw} is the raw charge (in channel), Q_i^{cal} is the raw aligned charge (in arbitrary units) and P_i the pedestal position. The coefficients a, b, c are the parameters of the polynomial fit. The pedestal is subtracted so that the zero of the electronic matches the zero of the charge distribution. The charge distribution obtained after alignment is shown in the lower part of

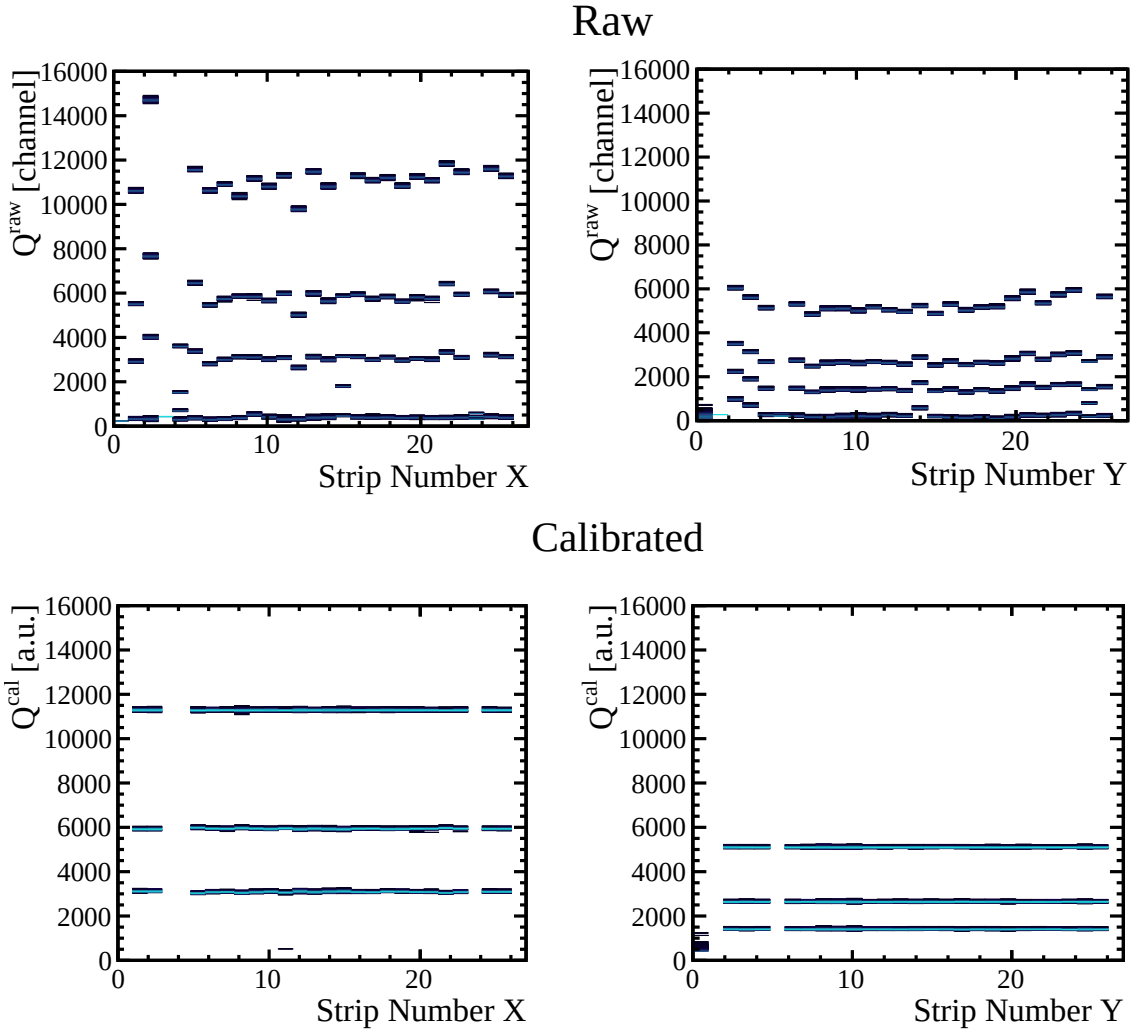

Figure 3.2: Charge distribution of the calibration pulses in CATS 1 for X (left) and Y (right) positions as a function of the strip number. The upper part of the figure are raw data and the lower part are those obtained after alignment.

Fig. 3.2.

A threshold s_i is applied to the strip number i, in the analysis, in order to reject electronic noise. This threshold is defined from the position and the width of the pedestal as: $s_i = P_i + 3\sigma_i$, where σ_i is the sigma of the Gaussian that is used in the fit of the pedestal (see Fig. 3.1).

1.2 Reconstruction of the particle position

Now that all the strips are aligned, we can measure the position of the beam particles. When a ion passes through the CATS detector, it induces a signal on the anode wires which is used for time measurement and a signal on the cathode wires (strips) which is used for position measurement. By analyzing the shape of the charge distribution on the strips one can determine its centroid with a better precision than the size of a strip, on the position measurement. The charge distribution can be described by a squared secant hyperbolic function [45]:

$$Q(x) = \frac{a_1}{cosh^2(\frac{\pi(x-a_2)}{a_3})} \ , \tag{3.2}$$

where Q is the charge and x the position in mm. The position of the centroid a_2 can be computed from a three points evaluation using:

$$\begin{cases} a_2 = x_m + \frac{a_3}{\pi} \tanh^{-1}\left(\frac{\sqrt{Q_m/Q_{m+1}} - \sqrt{Q_m/Q_{m-1}}}{2\sinh(\pi L/a_3)}\right) \\ with \\ a_3 = \frac{\pi L}{\cosh^{-1}\left(\frac{1}{2}\left(\sqrt{Q_m/Q_{m+1}} + \sqrt{Q_m/Q_{m-1}}\right)\right)} \end{cases} \tag{3.3}$$

Here m is the strip that received the largest charge Q_m and x_m is the position of the center of this strip. Q_{m+1} and Q_{m-1} are the charges of the neighboring strips and L is the strip pitch (2.54 mm). The position is calculated if the values of Q_{m-1}, Q_m and Q_{m+1} are higher than the threshold. Otherwise, the event is rejected.

Other methods are available to reconstruct the position (fit of the charge distribution, using a Gaussian model, barycentre method...). They all give very similar results in term of resolution. Performing a fit of the charge distribution instead of using the three point estimator is supposed to provide better results in case of a missing strip but it also double the computation time. During our

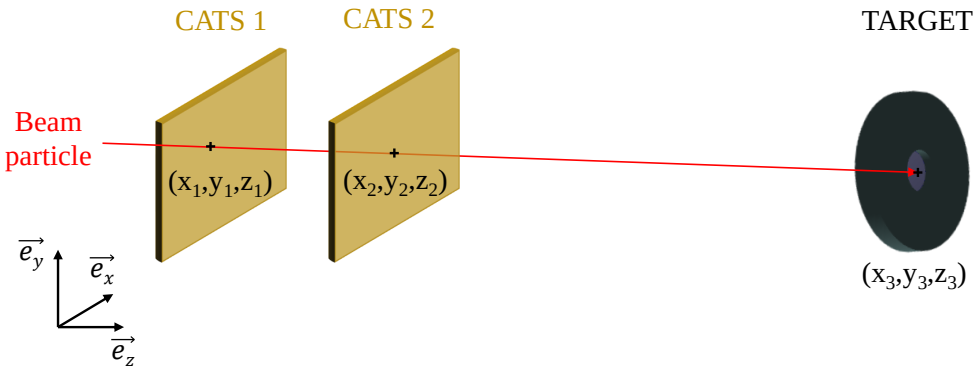

Figure 3.3: Scheme of the trajectory reconstruction of a beam particle with CATS.

experiment, all the central strips were working. Therefore, we decided to use the three point estimator as reconstruction method for the analysis.

1.3 Reconstruction in the target plane

From the knowledge of the position of the beam in two different planes, one can reconstruct the position on the interaction point of the ion with the target, event by event. The two CATS detectors provide the two position measurements $C_1 = (x_1, y_1, z_1)$ and $C_2 = (x_2, y_2, z_2)$ (see Fig. 3.3). The interaction point of the beam with the target $C_3 = (x_3, y_3, z_3)$ is given by the intersection of the vector $\overrightarrow{C_1C_2}$ with the target plane in $z_t = z_3$. The coordinate are given by:

$$\begin{cases} x_3 = x_2 + (x_2 - x_1)t \\ y_3 = y_2 + (y_2 - y_1)t \end{cases} \tag{3.4}$$

where:

$$t = \frac{z_3 - z_2}{z_2 - z_1} \tag{3.5}$$

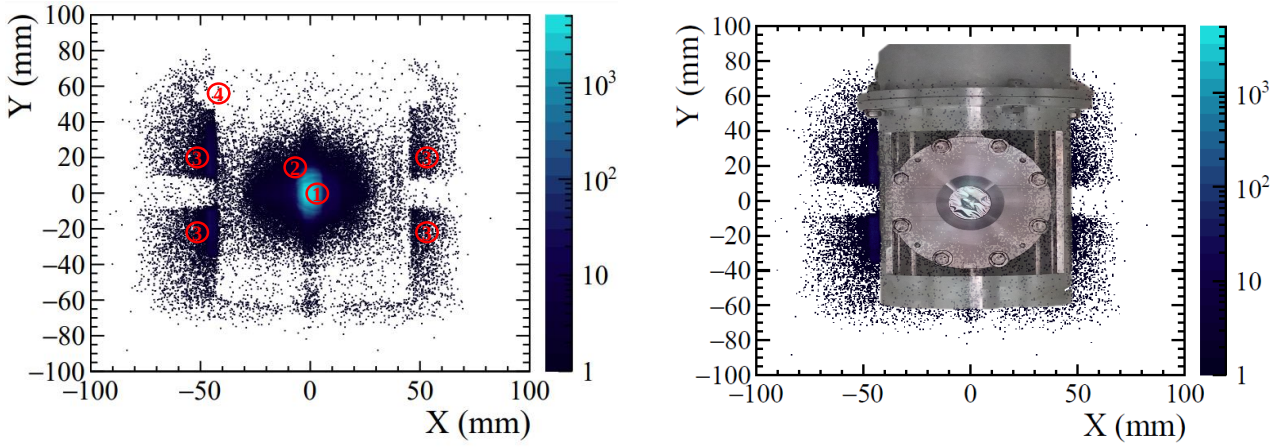

Figure 3.4: Left: Reconstruction of the beam profile in the target plane. Red numbers highlight specific areas. Area 1 corresponds to events where a beam particle made a reaction in the target cell and produced a light particle detected by MUST2. Area 2 corresponds to events where a beam particle made a reaction in the target frame. Area 3 corresponds to events where a beam particle has been deflected (generally by the CATS detectors) and reaches directly the MUST2 telescopes. Area 4 corresponds to the area where the mechanical support of the target absorbs the deflected particles. Right: Same image superimposed with a picture of the target. From the center to the borders we see the target cell (where the majority of the reactions occur), the target frame, and the heat shield.

The reconstruction of the beam position in the target plane is shown in Fig. 3.4. This plot was obtained using events triggered by MUST2 corresponding to either events where a beam particle made a reaction in the target and produced a light particle detected by MUST2, or to events where a beam particle has been deflected (generally by the CATS detectors) and reaches directly the MUST2 telescopes (if it was not absorbed by the mechanical support of the target). Therefore in this figure, we can see the structure of the target with its cell and frame. The majority of the events come

from interactions of beam particles with in the target cell. The part of the beam which is deflected by interactions inside CATS, and which is not absorbed by the mechanical support of the target, is hitting directly the MUST2 telescopes, generating two spots at X<-45 mm and X>45 mm (see the right part of Fig. 3.4). The heat shield of the target prevents the deflected beam to hit the other parts of the MUST2 telescopes.

1.4 Alignment of the detectors

In order to have the best reconstruction of the beam on the target plane, the position of the CATS detectors has to be known precisely. The X, Y and Z position of the CATS detectors were measured by the surveyor (value given in Table. 3.1) of the experiment but the Y and X are not well known because the CATS detectors can be inserted or removed during the experiment. To determine the X and Y positions, three different reference positions were used (all known from the surveyor): the position of the masks, the position of the target cell and the position of the MUST2 telescopes.

Reconstruction of the masks

Two masks were inserted, one upstream CATS and one in between the two CATS detectors. A mask consists in a metal plate, drilled with holes at known positions. The reconstruction of the image of the mask in its plane with the CATS detectors allows to tune the relative position of the two detectors. The reconstruction of the masks in their plane is shown in Fig. 3.5. The position of the CATS was shifted in the analysis procedure to reconstruct the center of the mask at the position given by the surveyor.

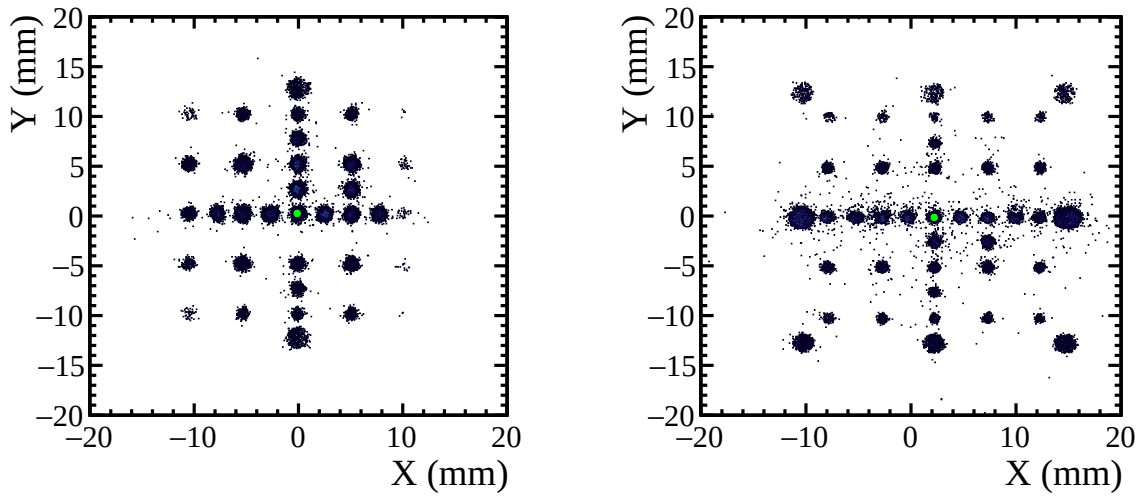

Figure 3.5: Reconstruction of the first (left) and the second mask (right) in their plane. The green point shows the measurement of the center of the mask, performed by the surveyor.

Again, the mask have been removed and re-inserted between surveyor measurements and the data taken, inducing an uncertainty on their position. Therefore we used another reference point: the position of the target cell.

Reconstruction of the target cell

The position of the center of the target cell was measured by the surveyor at $(x_t, y_t) = (3.3, 0.2)$ mm. To verify that the position of the CATS is well known relatively to the rest of the experimental setup, the position of the center of the target cell was measured using the reconstruction of the beam at the target plane, and using events triggered by MUST2, as shown in Fig.3.6. In this figure one can see the frame of the target cell (the mechanical support that surround the active area of the target, see Fig. 3.4). Indeed, the frame of the target cell offers a large amount of material with which the beam can interact. Furthermore, those events correspond to the edge of the frame since light particles, generated by interactions of the beam within the inner part of the frame, could not reach the MUST2 telescopes and trigger the acquisition. Therefore, the position of the edge of the frame of the target cell was fitted with a circle in order to measure the position of the center of the target cell. The measured center (2.9, 0.0) mm is compatible with the measurement performed by the surveyor, which confirms the good positioning of the CATS detectors.

In Fig 3.6 one can see that the beam is more spread over the Y axis than over the X axis. This effect arises from the use of the Wien filter presented in Section 1.2. Moreover the position in Y depends on the incoming nuclei. The fraction of beam that passes through the target cell is about 89%.

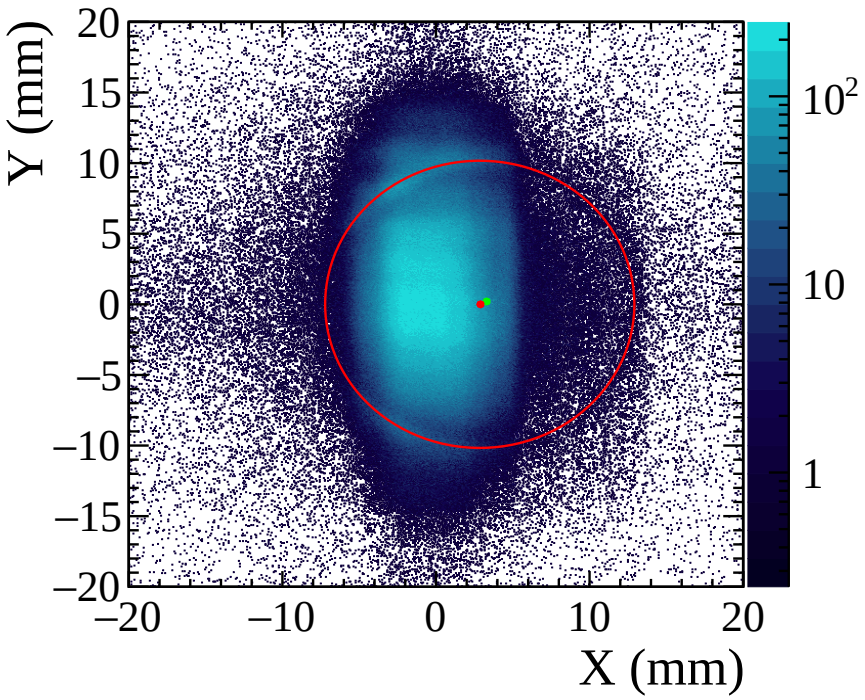

Figure 3.6: Reconstruction of the beam profile in the target plane. This figure was obtained with MUST2 trigger to look at the position of the interactions. The red circle shows the fit of the frame of the target cell. The red point (2.9,0.0) mm is the corresponding center and the green point (3.3,0.2) mm is the center given by the surveyor.

It is important to note that this method allows to confirm the X and Y position of the target but the Z position is poorly known. Indeed the cryogenic target was screwed to the top of the M2C

chamber at a distance of 80 cm from the target cell, inducing large uncertainties on the positioning of the target cell. Furthermore, the position of the target cell was measured by the surveyor when the target was at room temperature. Cooling down the target may induce significant deformations of materials that could change the position of the target cell. The Z position of the target cell was determined using the angular distributions of reference reactions. It was found that the Z position was shifted by 15 mm compared to the measurement performed by the surveyor.

Reconstruction of the position of the MUST2 telescopes

The last reference position used was that of the MUST2 telescopes. Indeed, as explained earlier, a part of the beam impinges directly on the MUST2 telescopes without passing through the target. Those events can be selected using the energy loss measured in the DSSD of the MUST2 telescopes as shown in Fig. 3.7. The position of the MUST2 detectors is known with 0.2 mm precision, from 3D position measurements performed by the surveyor. The comparison between the position of these hits determined from MUST2 only and from the beam reconstruction with CATS allows to cross check the good positioning of the CATS detectors.

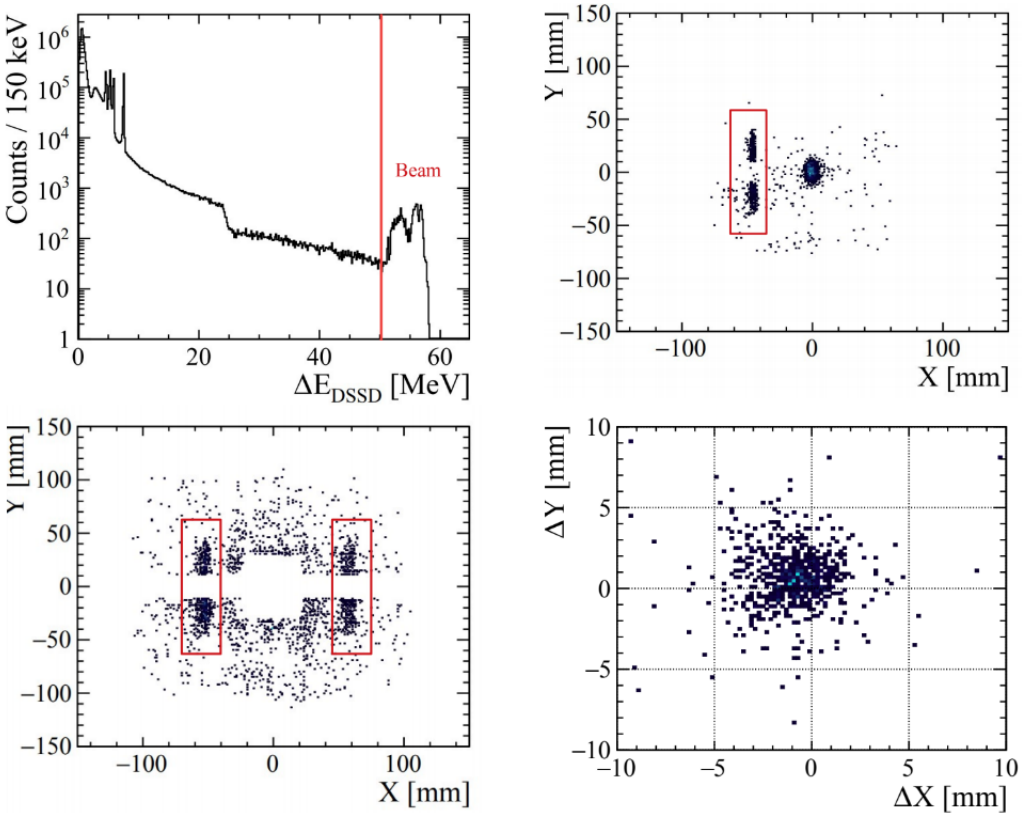

Figure 3.7: Top left: Energy loss in the DSSD of MUST2. The beam impinging directly on the MUST2 telescopes is identified at ΔE>50 MeV. Top right: Image of the beam in the target plane, reconstructed with CATS, with a gate on ΔE>50 MeV to select nuclei directly impinging on the MUST2 telescopes. Event of interest are highlighted by the red box. Bottom left: Impact matrix of the MUST2 telescopes (position of the interactions in MUST2) obtained with a gate on ΔE>50 MeV. Bottom right: Difference of the positions measured with the impact matrix of MUST2 and with the reconstruction of the beam in the MUST2 plane with the CATS. These plots were obtained with a gate on ΔE>50 MeV and on the red boxes.

	Surveyor [mm]		Analysis [mm]	
	X	Y	X	Y
CATS1	1.5	0.2	0.6	-1.1
CATS2	1.7	0.0	2.3	0.0

Table 3.1: Position of the CATS detectors measured by the surveyor and determined from the analysis.

The bottom right part of Fig. 3.7 shows the difference of the positions of the event of interest measured with CATS and MUST2. One can see on this figure that the spot centered in (-0.9,0.7) is a bit shifted from the expected (0,0) mm position. Nevertheless, this is the best result obtained since matching this spot with (0,0) degrades the results on the mask reconstruction. This method allows to estimate that the uncertainties on the position measurement with CATS is of about 1 mm in X and Y on the MUST2 plane. In the following we will consider 1 mm of uncertainties on the position determintation in the target plane with CATS, which is the typical value found in other studies [49, 50]. The final position of the CATS detectors are given in Table 3.1. Those values will be used in the rest of the analysis.

2 Light particle characterization with the MUST2 telescopes

The beam impinges on the Hydrogen target where it will produce the transfer reactions of interest. To identify and measure angles and energies of the outgoing light particles produced, the set of 6 MUST2, described in Section. 2.3, is calibrated to determine the physical information. This section describes in detail their data treatment.

2.1 Energy calibration of the DSSD

The DSSDs were calibrated, strip by strip, using a triple alpha source (^{239}Pu, ^{241}Am, ^{244}Cm) placed at the target position. The description of the source can be found in Table 3.2. For each strip, the main and satellite peaks of each nuclei were fitted using Gaussian functions. The fit of the raw spectrum of one strip is shown in Fig. 3.8. A linear fit of the correlation between raw energies and tabulated alpha energies was performed to extract the calibration parameters of the strips.

In order to determine the Aluminum dead layer, the "zero extrapolation" method was used. This method consists in varing the thickness of dead layer and perform a calibration at each iteration. The validated dead layer thickness is the one for which the zero of the electronic (the position of the pedestal) matches the zero of the calibrated energy. Precise description of this method can be found in Ref. [51]. The estimated thickness of the dead layer, that is in agreement with the nominal ones, was then used to correct the energy loss in the detector for the calibration and the analysis. Fig. 3.9 shows the energy spectra as a function of the strip number before and after the calibration.

After calibration the energy resolution was estimated from the width of the 5.48 MeV peak of the alpha source. The energy resolution of a single strip is about 20 keV while the one of the whole MUST2 telescopes is about 30 keV. The overall energy resolution of 30 keV for the 128 calibrated strips is slightly worse than the one of a typical individual strip, due to a possible slight misalignment

Nucleus	E_α [MeV]	I_α	$T_{1/2}$ [year]
^{239}Pu	5.15659(14)	70.77(14)	2.411(3) 10^4
	5.11443(8)	17.11(14)	
	5.1055(8)	11.94(14)	
^{241}Am	5.48556(12)	84.8(5)	432.2(6)
	5.44280(13)	13.1(3)	
	5.388(8)	1.66(2)	
^{244}Cm	5.80477(5)	76.40(12)	18.1(1)
	5.76264(3)	23.60(12)	

Table 3.2: Alpha energies, relative intensities and lifetimes of the source used for the DSSD calibration.

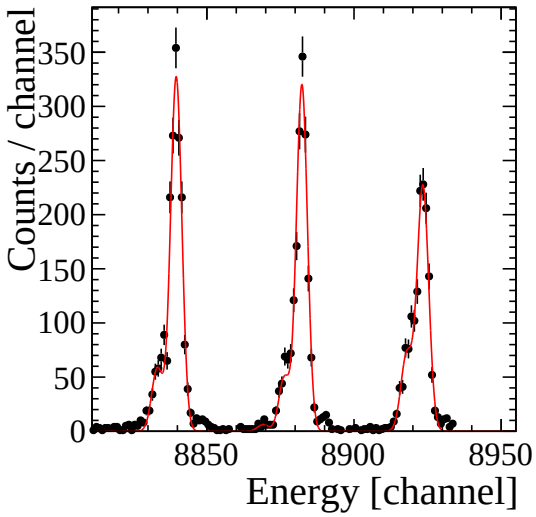

Figure 3.8: Raw energy spectra of one strip of one DSSD. This spectra was obtained after applying the data treatment presented in Section. 2.3 and keeping only multiplicity 1. The red line shows the fit of the three alpha peaks and their satellites.

of the gains and the fact some strips have a poorer resolution.

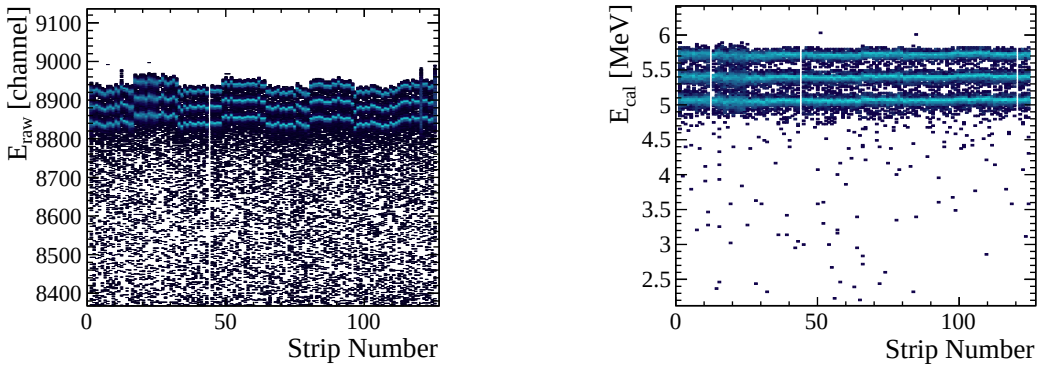

Figure 3.9: Energy measured in the DSSD of the first MUST2 telescope during the run taken with a 3-alpha source, as a function of the strip number before (left) and after (right) calibration. One can notice that some strips are missing after the calibration. Those correspond to noisy strip for which the calibration procedure could not be completed. These strips have been withdrawn from the analysis.

2.2 Energy calibration of the CsI

Most of the particles of interest (deuterons and tritons from the transfer reactions) have enough energy to punch through the DSSD (e.g. deuterons with total kinetic energy higher than 7.5 MeV). In this

case, CsI crystals are used to measure the residual energy. The response of each crystal depends on the type of the particle and it is non linear at high energy. Furthermore, the high and large energy range of interest (e.g. deuterons of interest have an energy ranging from 10 to 60 MeV) prevents from the possibility to use a source to calibrate the CsI. Therefore, the CsI crystal has to be calibrated with the beam. It is difficult to obtain a precise and absolute calibration for this detection stage. Thus, the calibration of the CsI crystals has been performed in two steps: a first rough, position sensitive calibration using the "E from ΔE" method, based on the energy deposit in the first layer, and then an absolute calibration using reference transfer reactions measured during the experiment. The calibration procedure is detailed in the following.

2.2.1 Step 1: E from Δ E

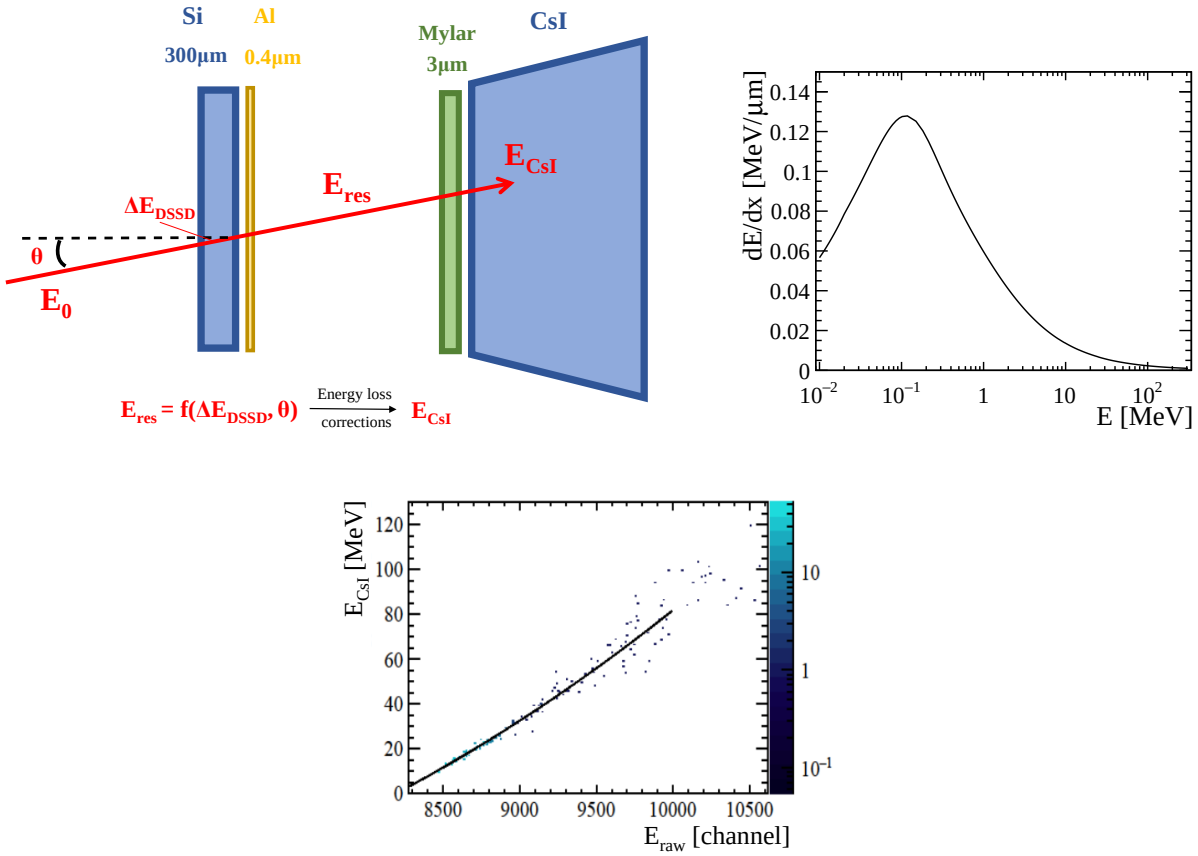

Figure 3.10: Left: Principle of the "E from ΔE" calibration method. The residual energy E_{res} of the particle is reconstructed from the energy loss measured in the DSSD. Energy loss corrections are applied to reconstruct the energy deposited by the particle in the CsI crystal. Note that in reality the CsI cristals are located just behind the DSSSD. Right: Energy loss of deuteron in Silicon per unit of thickness crossed, as a function of the energy of the particle. Bottom: Correlation between the calculated E_{CsI} and the measured raw CsI energy E_{raw}. The black line shows the second order polynomial fit performed to extract the calibration parameters. One can see that this method is not precise at high energy since a very few energy deposited in the DSSD avoids to reconstruct the energy of the incoming particle with precision.

The first step of the energy calibration of the CsI crystals relies on the E-ΔE correlation of the light

outgoing particles. Left part of Fig. 3.10 shows the principle of this method. The residual energy of the light particle is deduced from its measured energy loss ΔE and angle in the DSSD using tabulated energy loss dependency with the particle energy. Right part of Fig. 3.10 shows the energy loss of deuterons in Silicon per unit of thickness crossed, as a function of the energy of the particle. In this work we used the GEANT4 tables for energy losses calculation. Then, the energy loss corrections, shown in the left part of Fig. 3.10, are applied to reconstruct the energy deposited by the particle inside the CsI crystal E_{CsI}. This calculation is done event by event, to obtain the correlation between the reconstructed E_{CsI} and the measured raw energy of the particle in the CsI E_{raw}. This correlation is then fitted by a second order polynomial function to determine the calibrated CsI energy $E_{CsI}^{\Delta E}$:

$$E_{CsI}^{\Delta E} = p_0 E_{raw}^2 + p_1 E_{raw} + p_2 \ , \tag{3.6}$$

where p_i are the calibration parameters (a typical set of parameter being $p_0 = 5.009(11) \times 10^{-8}; p_1 = -0.0458(1)$ and $p_2 = 39.4(11)$). Bottom part of Fig. 3.10 shows the calibration plot obtained for one CsI of one telescope. The second order of the function is used to correct from non-linear effects throughout the light collection in the CsI crystals. Since the amount of scintillation light produced in a CsI crystal depends on the type of particle, this calibration procedure was performed for the protons, deuterons and tritons independently, by applying a 2D cut on the ΔE_{DSSD}-E_{raw}^{CsI} identification matrix for each CsI (see Fig.3.18).

In order to estimate the impact of the CsI calibration on the determination of the excitation energy and on the resolution, the ground state peak of ^{36}Ca reconstructed from the ^{37}Ca(p,d)^{36}Ca reaction is used as reference. The reconstruction method of the excitation energy will be detailed later in Section 4. The width of the ground state peak of ^{36}Ca was found to be 850 keV (in sigma) after the calibration. This value was higher than the value of 450 keV found in a previous study performed in very similar conditions [52]. Moreover, it was also well above the value of 500 keV sigma, found using the simulation. This suggests the need of further investigation to improve the experimental resolution.

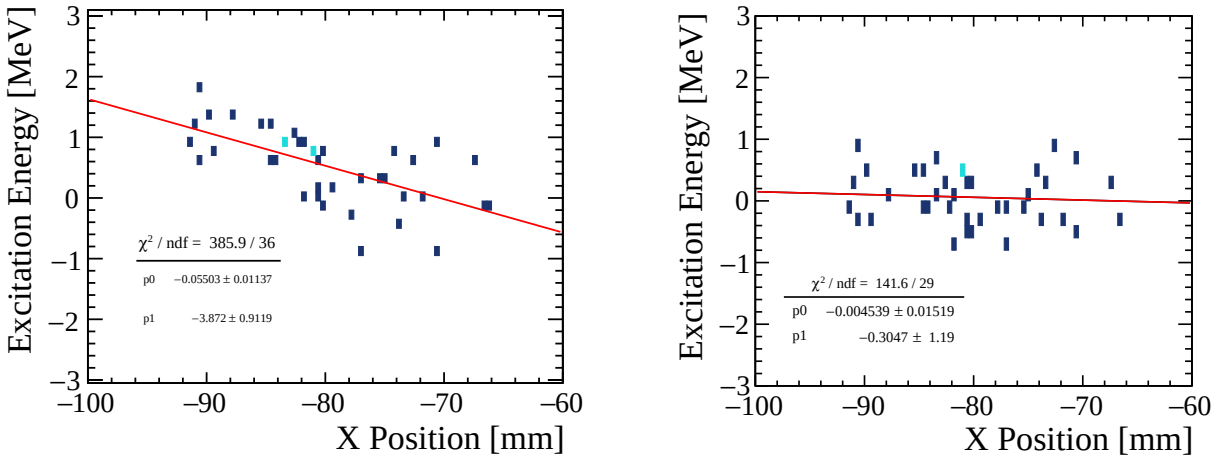

Figure 3.11: Evolution of the ground state position of ^{36}Ca in excitation energy as a function of the position in the CsI with (right) and without (left) pixel segmentation. Those plots were obtained for CsI 10 of telescope 1. Red lines shows a linear fit performed on the data.

It was found during the analysis, that there is a dependency of the excitation energy on the

vertex position of the light outgoing particle inside the CsI crystal. Left part of Fig. 3.11 shows the evolution of the ground state position of ^{36}Ca in the excitation energy spectra as a function of the X position in one CsI crystal (obtained from the information in the DSSD). There is a clear drift of the peak along the crystal that can be attributed to inhomogeneities in the light collection caused by its ageing. To correct this effect each CsI crystals was virtually divided into pixels using the position information from the DSSD. 64 pixels were used for the proton and deuteron calibrations but due to lack of statistic, only 16 pixels were used for the triton calibration. Right part of Fig. 3.11 shows the position of ^{36}Ca ground state obtained after applying the pixel calibration. This figure shows that the pixel calibration has strongly reduced the position dependency of the excitation energy peak. The resolution on the total excitation energy spectra was also improved from 850 keV to 710 keV with this pixel calibration. At the end, calibration parameters have been extracted for the 64 pixels of the 16 CsI crystals of the 6 MUST2 telescopes for 3 different type of particles making a total of 18432 independent energy calibrations.

After this first step calibration, some problems are still present. The analysis of reference reactions such as ^{38}Ca(p,d)^{37}Ca$_{g.s.}$ or ^{37}Ca(p,d)^{36}Ca$_{g.s.}$ could not reproduce the known masses of those nuclei. In other words, the measured centroid of the ground state peak in excitation energy is not compatible with zero. Furthermore, a large deviation is seen in the ground state centroid when looking at single CsI excitation energy spectra, as shown in Fig. 3.12. Those problems arise from the depth inhomogeneities of the CsI crystals but also from the uncertainties on the deformation of the target's windows foils and the inhomogeneities of dead layers which distort the energy loss corrections. To correct those effects, an absolute energy calibration procedure of the CsI crystals has been developed using reference reactions.

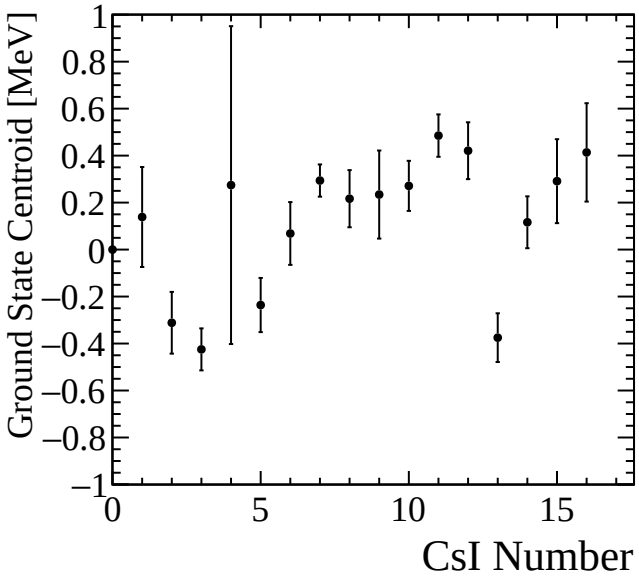

Figure 3.12: Position of the centroid of the ground state peak in the excitation energy spectra of ^{36}Ca as a function of the CsI number. This plot was obtained for telescope number 1. One can see the large dispersion of the ground state position between the CsI. Furthermore, very few of them are compatible with zero.

2.2.2 Step 2: Absolute calibration

The absolute calibration consists in adjusting the previously extracted calibration coefficients using reference reactions of well known Q-values (with less than few keV uncertainties). For the deuteron calibration the ^{38}Ca(p,d)^{37}Ca$_{g.s.}$ and the ^{35}Ar(p,d)^{34}Ar$_{g.s.}$ reactions, measured during the experiment, were used as references. Those reactions are the only ones (available among the ones present in the two cocktail beams) having enough statistics to be used for the calibration. Furthermore they well constrain the deuteron energy range of the reaction of interest, as their kinematic lines frame that of ^{37}Ca(p,d)^{36}Ca , as shown in Fig. 3.13.

Fig. 3.14 shows the principle of the calculation performed to extract the reference CsI energies from the ^{35}Ar(p,d)^{34}Ar$_{g.s.}$ reaction. Once the first step calibration has been performed, the reference reactions are analyzed using the obtained calibration coefficients. For each reference reaction, a gate is applied on the excitation energy to select events corresponding to the ground state (top left part of Fig. 3.14). This gate has been determined by fitting the ground state peak in each CsI crystal to determine the position of the centroid and by taking an interval of ±500 keV around the centroid. From those events, the measured energy in the CsI, $E^{\Delta E}_{CsI}$, is extracted, as well as the measured laboratory angle θ^{Exp}_{Lab} of the deuteron (the ΔE exponent indicates that this is the CsI energy obtained using the "E from ΔE" calibration parameters). Then, using the theoretical kinematic line of the reference reaction, the corresponding reference laboratory energy of the particle E^{Ref}_{Lab} is computed from θ^{Exp}_{Lab}. Finally, E^{Ref}_{Lab} is corrected from energy losses in dead layers and in the target (see Section 4 for details) to reconstruct the reference energy E^{Ref}_{CsI} of the particle before entering inside the CsI (with $E^{Ref}_{CsI} < E^{Ref}_{Lab}$ because of the energy loosed by the particles in dead layers).

Fig. 3.15 shows, for a single CsI crystal, the correlation between E^{Ref}_{CsI} and $E^{\Delta E}_{CsI}$ obtained for the two reference reactions and the reaction of interest. A linear fit is performed (using only the points

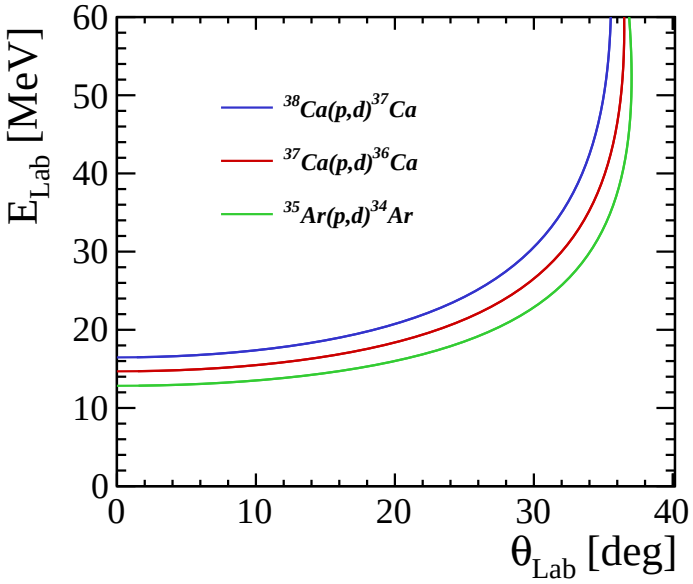

Figure 3.13: Theoretical kinematic lines of the two reference reactions compared to the one of interest.

from the two reference reactions) to extract the correction parameters c_i. Then, those correction parameters are used to compute the final CsI energy E^{Cal}_{CsI}:

$$E^{Cal}_{CsI} = c_0 E^{\Delta E}_{CsI} + c_1 = p'_0 E^2_{raw} + p'_1 E_{raw} + p'_2 \ , \tag{3.7}$$

where: $p'_0 = c_0 p_0$, $p'_1 = c_0 p_1$ and $p'_2 = c_0 p_2 + c_1$ (typical values of c_0 and c_1 being $c_0 = 1.027(9)$ and $c_1 = -0.58(9)$, given for CsI number 16 of telescope 1).

The two reference reactions used for the calibration constrain well the energy range of the deuteron of the reaction of interest as shown in Fig. 3.15. In this figure, 0 MeV, 3 MeV and 6 MeV in excitation energy in ^{36}Ca are indicated by red points. The points corresponding to the first excited state of ^{37}Ca at 1.6 MeV (yellow points) have been added on this figure to demonstrate the linear behavior of the calibration up to 6 MeV in excitation energy in ^{36}Ca (with a coefficient of determination of

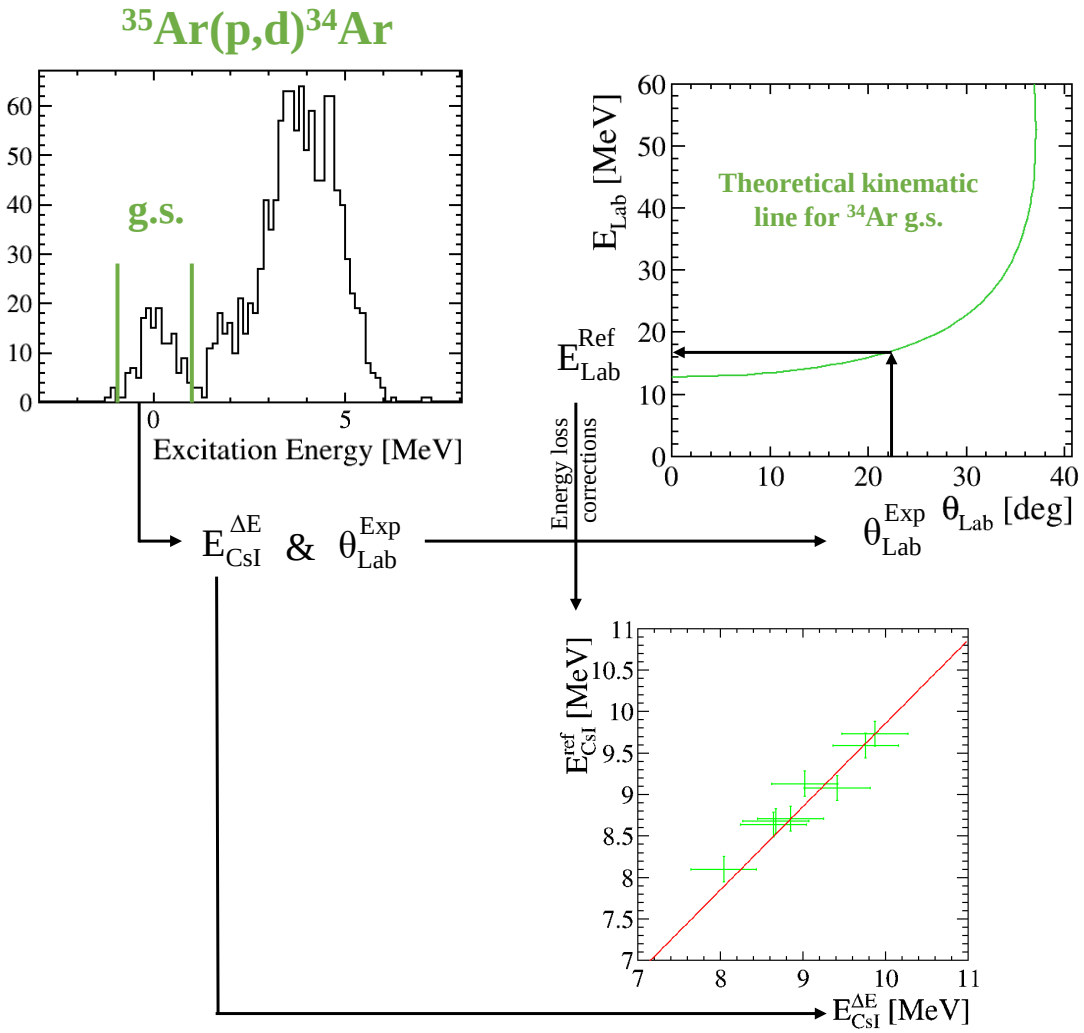

Figure 3.14: Principle of the reconstruction of the reference CsI energy for the ^{35}Ar(p,d)^{34}Ar$_{g.s.}$ reaction. Top left spectrum is the excitation energy in ^{34}Ar. Top right is the theoretical kinematic line of the reaction. Bottom part is the correlation plot between E^{Ref}_{CsI} and $E^{\Delta E}_{CsI}$ obtained for the CsI number 16 of telescope 1.

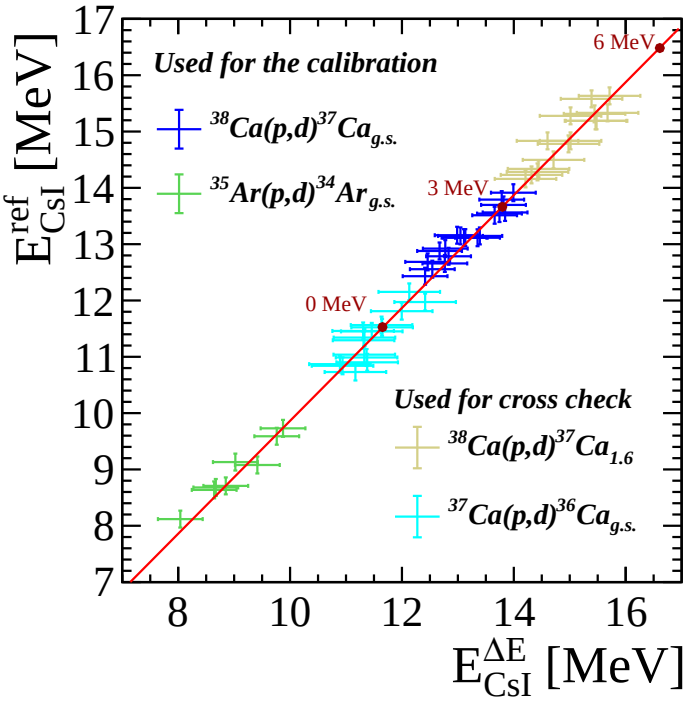

Figure 3.15: E^{Ref}_{CsI} *vs.* $E^{\Delta E}_{CsI}$ scatter plot for CsI 16 of telescope 1. The data points from the ^{38}Ca$(p,d)^{37}$Ca$_{g.s.}$ (blue), ^{35}Ar$(p,d)^{34}$Ar$_{g.s.}$ (green), ^{37}Ca$(p,d)^{36}$Ca$_{g.s.}$ (cyan) and ^{38}Ca$(p,d)^{37}$Ca$_{1.6\ MeV}$ (yellow) reactions are shown. The linear fit (red curve) was done using the ^{38}Ca$(p,d)^{37}$Ca$_{g.s.}$ and the ^{35}Ar$(p,d)^{34}$Ar$_{g.s.}$ reactions. A linear fit describes well the data points from 0 to 6 MeV in excitation energy (written in red) in ^{36}Ca (R^2 =0.992).

$R^2 = 0.992$).

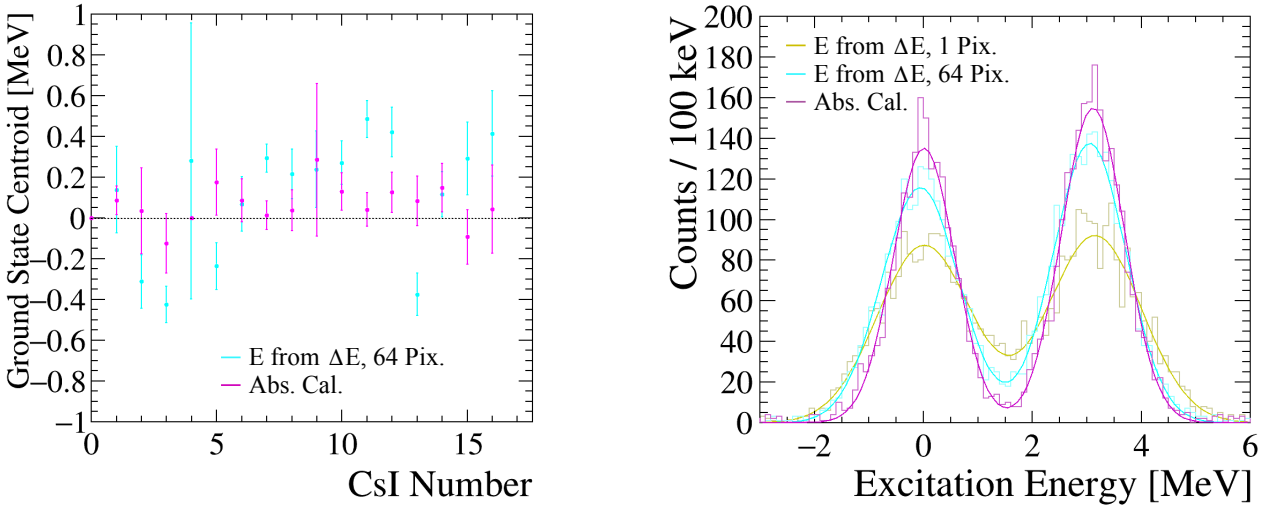

Figure 3.16: Left: Position of the centroid of the ground state peak in the excitation energy spectra of ^{36}Ca as a function of the CsI number obtained using two different calibration. Right: Excitation energy spectra of ^{36}Ca obtained with the "E from ΔE" method with 1 pixel (yellow), 64 pixels (blue) and after the absolute calibration (purple).

All the computed c_0 correction parameters are close to 1 meaning that those corrections do not affect the dependency to the particle energy. Indeed, the absolute calibration allows to correct from effects such as the depth inhomogeneities of the CsI crystals or inhomogeneities of dead layers. Those effects impact the absolute energy measurement in the CsI but not the dependency of the measurement to the energy of the particle. Left part of Fig. 3.16 compares the position of the centroid of the ground state peak in the excitation energy spectra of ^{36}Ca as a function of the CsI number obtained with the "E from ΔE" calibration method and with the absolute calibration. With the absolute calibration corrections, all the centroids are compatible with zero and the deviation is improved from 325 keV to 71 keV. This improves both the resolution of the total peak and the precision on the centroid measurement. Right part of Fig. 3.16 compares the excitation energy spectra of ^{36}Ca obtained with the three different calibrations discussed here. The resolution in excitation energy is significantly improved at each step, with a σ value of the ground state peak of 850 keV ("E from ΔE" calibration with 1 pixel), 710 keV ("E from ΔE" calibration with 64 pixel) and 560 keV (absolute calibration).

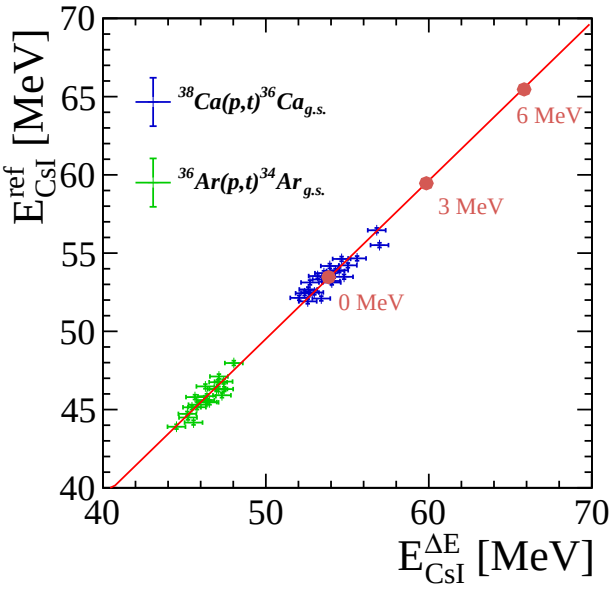

Figure 3.17: E^{Ref}_{CsI} $vs.$ $E^{\Delta E}_{CsI}$ scatter plot for CsI 16 of telescope 1. The data points from the ^{38}Ca(p,t)^{36}Ca$_{g.s.}$ (blue), ^{36}Ar(p,t)^{34}Ar$_{g.s.}$ (green) reactions are shown. The red curve shows the linear fit performed to extract the correction parameters. 0 MeV, 3 MeV and 6 MeV in excitation energy in ^{36}Ca are indicated by red points

It is important to note that, before to start this study, the mass of ^{36}Ca was known with 40 keV precision. Performing a new mass measurement on ^{36}Ca was one of the goal of the experiment. Therefore, at first, the mass of ^{36}Ca will be measured using the calibration without ^{36}Ca as reference point. Meanwhile, its mass has been more precisely measured (with 5 keV precision) by a recent Penning trap experiment [31]. Therefore, in order to achieve the best reachable resolution, this new precise ^{36}Ca mass will be used, in a second time, as a reference for the deuteron and the triton calibration.

The same method has been used to perform an absolute calibration for the tritons. The ^{38}Ca(p,t)^{36}Ca

and the ^{36}Ar(p,t)^{34}Ar$_{g.s.}$ reactions were used as reference. Fig. 3.17 shows the correlation between E_{CsI}^{Ref} and $E_{CsI}^{\Delta E}$ obtained for the tritons of the reference reactions. A linear fit has been performed to extract the correction parameters. Due to the lack of reference point for the protons, no absolute correction was performed on the proton calibration. Anyhow the reliability of the proton calibration has been confirmed by studying the one proton decay channel of reference reactions.

2.3 Data treatment procedure and multiplicity

The treatment of the data taken by the MUST2 telescopes is as follow. First, thresholds and calibrations are applied in order to suppress background and obtain physical energy measurement. The X and Y side of the DSSD are treated as independent detectors, as well as the CsI crystals. Each of them has its own multiplicity m, n and k, respectively. All the combinations of DSSD energies and positions in X and Y, and CsI energies and positions are analyzed to construct a physical event. The conditions to accept a combination between the elements i (DSSD X), j (DSSD Y) and k (CsI) (with $i \in [0,m], j \in [0,n]$ and $k \in [0,k]$) are:

1. Telescope Number (i) = Telescope Number (j) = Telescope Number (k)
2. $|E_{DSSD}^{X}(i) - E_{DSSD}^{Y}(j)| < \epsilon$, with ϵ taken as three σ of the DSSD energy resolution.
3. $(X(i),Y(j)) \in$ CsI area (k)

The final multiplicity of the event corresponds to the number of combination that has been accepted by the algorithm. An additional condition has been set to reject events in which two particles arrived in the same CsI. In this case it is impossible to match the CsI energy to the DSSD energy. Those events represent less than 1% of the total. At the end, only multiplicity one, two and three were accepted in order to get the transfer particles to bound states, one and two-proton emissions, respectively.

2.4 Particle identification

Once the calibrations and the data treatment has been performed, the sum of all MUST2 telescopes can be used for position, time, energy loss and residual energy measurement. Moreover, the combination of these information allows to identify each type of light particles. In our case all the particles of interest have sufficient energy to reach the CsI. Therefore, only the ΔE-E particle identification method was used. Fig. 3.18 shows a typical light particle identification plot obtained from the correlation of the energy loss measured in the DSSD and the residual energy measured in the CsI. The shape of the lines arises from the Beth-Bloch formula. In this plot, we can well distinguish the protons, the deuterons and the tritons.

3 Outgoing heavy ions identification with the Zero Degree Detection

In order to identify the outgoing heavy ion produced during the transfer reaction, we use the Zero Degree Detection (ZDD) composed of an Ionization Chamber (IC) a set of two Drift Chambers (DC) and a plastic scintillator. This section describes the calibrations, the characterizations and the analysis methods used for those detectors. A schematic view of the ZDD is presented in Fig. 3.19.

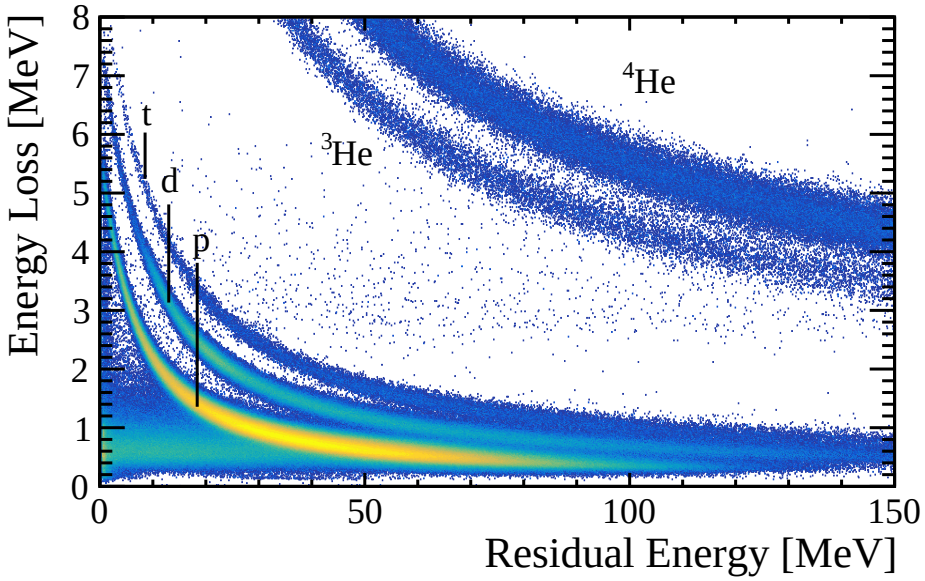

Figure 3.18: ΔE-E particle identification plot obtained with MUST2 telescopes. One can identify protons, deuterons, tritons, ^{3}He and α particles.

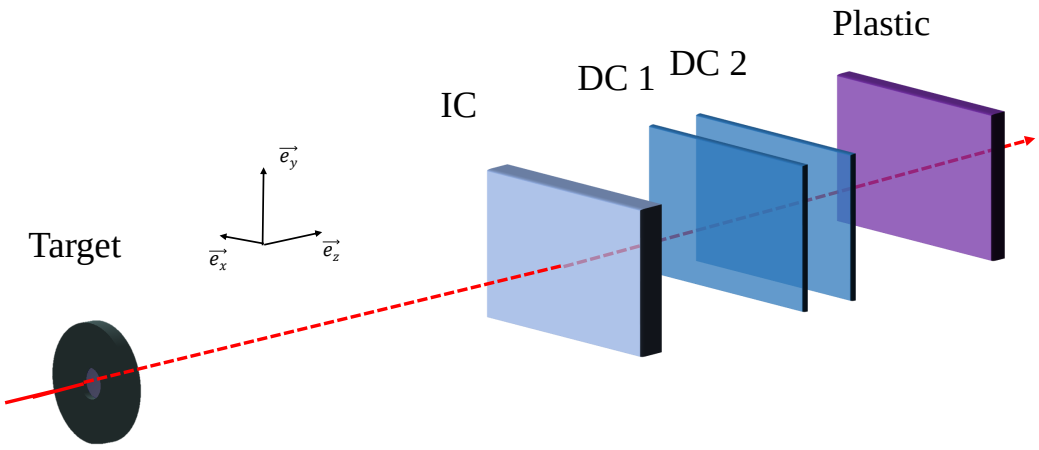

Figure 3.19: Schematic view of the ZDD composed of an Ionization Chamber (IC) a set of two Drift Chambers (DC) and a plastic scintillator. The two DC have an active area of 70×70 cm^2 and are located at 85 cm and 103 cm downstream of the target.

3.1 Calibration and characterization of the ionization chamber

The multiplicity m of an event in the ZDD is defined as the number of nuclei seen by the IC during the acquisition time. The IC provides for an event of multiplicity m, m energies and m time measurements. The NUMEXO2 read out electronics of the IC allows to measure energies and times of events that piled up, meaning that the second electric pulse arrived before the first one has fully decayed (if those pulses are separated by more than 500 ns, otherwise, the event is rejected). This way the IC can provide an energy loss measurement with high beam intensity (up to few 10^5 pps) that can be used for the identification of the outgoing heavy nuclei.

The calibration of the IC was performed using the reference nuclei present in the cocktail beam. Fig. 3.20 shows the energy loss measured in the IC during the ^{38}Ca beam setting. Given that the time-of-flight measured between the CATS detector and the HF signal delivered by the cyclotrons, provides an identification of the incoming nuclei present in the coktail beam (see Fig. 2.3 in Section 1.2), the energy loss (in channel) of each nucleus was measured independently and is shown in Fig. 3.20. One can see that for ^{38}Ca (red) and ^{37}K (green) only one peak was identified in the IC. Using the ^{36}Ar time-of-flight gate (blue) two peaks were found in the IC, the highest one corresponding to ^{36}Ar and the other one to the contaminant ^{34}Cl. For ^{33}S (purple) the contaminant was ^{35}Cl. The position of each peak was determined with a Gaussian fit. The theoretical energy loss in the IC of ^{38}Ca, ^{37}K, ^{36}Ar and ^{33}S was computed using the LISE++ software. The correlation between the theoretical energy loss and the measured one (in channel) is shown in the right part of Fig. 3.20. This distribution was fitted with a first order polynomial function to extract the calibration coefficients of the IC.

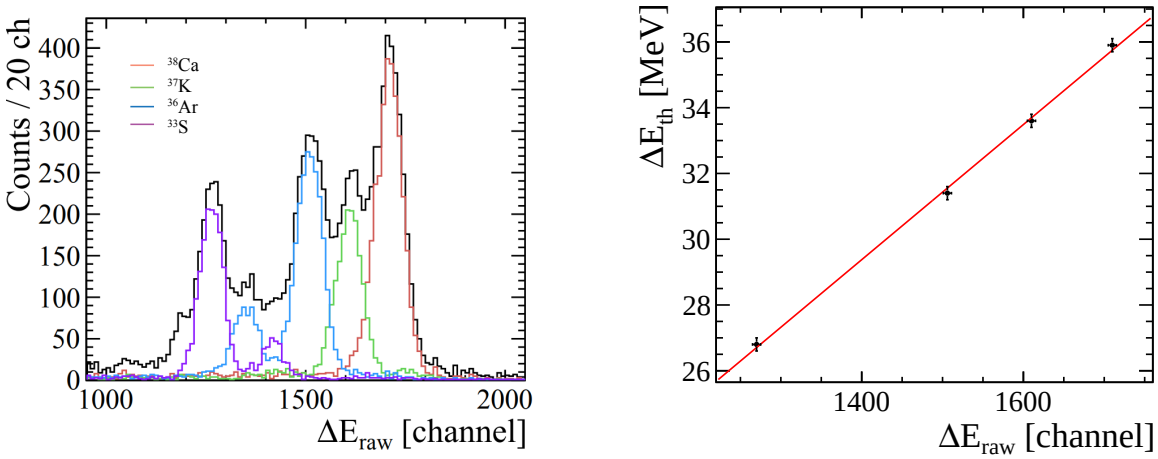

Figure 3.20: Left: Energy loss measured in the IC (in channel). The total spectrum is shown by the black line. The colored lines correspond to the spectra obtained by gating on the time-of-flight range corresponding to each contaminants (see details in the text). Righ: Calibration plot of the IC. The red line shows the linear fit performed for the calibration.

The resolution of the IC was determined by performing a Gaussian fit of the ^{38}Ca peak after applying the calibration. The sigma of the Gaussian was found to be 0.76 MeV for a centroid at 34.7 MeV corresponding to a relative resolution of 2.2%.

The intrinsic efficiency of the IC was determined by counting the number of ^{38}Ca and ^{37}Ca seen in the time-of-flight spectra CATS-HF. Selections were applied to use only events triggered by CATS (which correspond to almost 100% of unreacted beam) and colinear beam (by gating on small angles measured with CATS) that passes through the center of the target to be sure that those nuclei reach the IC. The ratio of the number of those events detected in the IC (with a non zero energy) and the total number of those events gives the IC efficiency. The efficiency was found to be 81.9% for the detection of ^{38}Ca and 98.7% for ^{37}Ca. The difference between those two numbers arises from the difference of beam intensity between the two beam settings. Indeed, the cocktail beam of ^{37}Ca was obtained at $2{\cdot}10^4$ pps and the cocktail beam of ^{38}Ca at $2{\cdot}10^5$ pps. A higher intensity increases the pile-up rate in the IC and therefore, the rate of events for which the electronics cannot disentangle

two different impulsions. This causes a loss of efficiency of the IC.

3.2 Reconstruction of the position with drift chambers

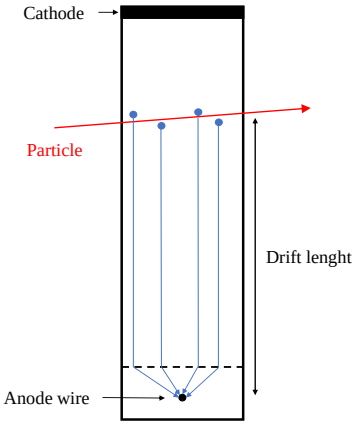

Figure 3.21: Schematic view of drift chamber. A particle that passes through the chamber will ionize the surrounding atoms. The free electrons drift toward the anode wire at a velocity of 0.05 mm/s.

A set of 4 drift chambers (DC) was used to measure the angle of the outgoing nuclei. This measurement will be used in the analysis in order to select events corresponding to a two body kinematic, with a deflected outgoing heavy ion. Each DC provides one time measurement. The drift time of the charges inside the chambers is measured relatively to a reference time given by the CATS detectors: $t_{drift} = t_{DC} - t_{CATS}$. The drift length is then computed from the drift time and the drift velocity using: $L_{drift} = \frac{t_{drift}}{v_{drift}}$ (see Fig. 3.21). The drift velocity of the ions inside C_4H_{10} gas under 20 mbar is of 0.05 mm/ns. Finally, the absolute position of the outgoing heavy ion is reconstructed from the given position and geometry of the DC. The NUMEXO2 electronics digitizes the time signal by step of 10 ns limiting the position resolution of the DC to 0.5 mm. The 4 DC were arranged to have 4 different drift directions (X, -X, Y and -Y).

The position of the DC was determined using the CATS detectors given that most of the incoming ions were not deflected. Fig. 3.22 shows the difference between the position measured by the DC and the position reconstructed by the CATS in the DC plane. The position of each DC has been set in order to center those distributions at zero. The final positions of the DC used in the analysis are given in Table 3.3. The outgoing heavy ion trajectory was then defined as a straight line between the interaction point of the ion in the target (given by CATS) and the interaction point of the ion in the DC. Since DC provides two measurements of this point, it was determined as the mean of both measurements.

The angular resolutions of the DC were determined relatively to CATS, by computing the difference of the measurement of the (θ,ϕ) angles of the unreacted beam (θ being the angle of the trajectory relatively to the Z axis in the X-Z plane and ϕ in the Y-Z plane) measured by CATS and the DC. Assuming that the angular resolution of the CATS is negligible compared to the one of the DC, the angular resolution of the DC was found to be 0.2° for both θ and ϕ angles. The efficiencies of the DC were determined for ^{37}Ca and ^{38}Ca using the method described in the previous section and are

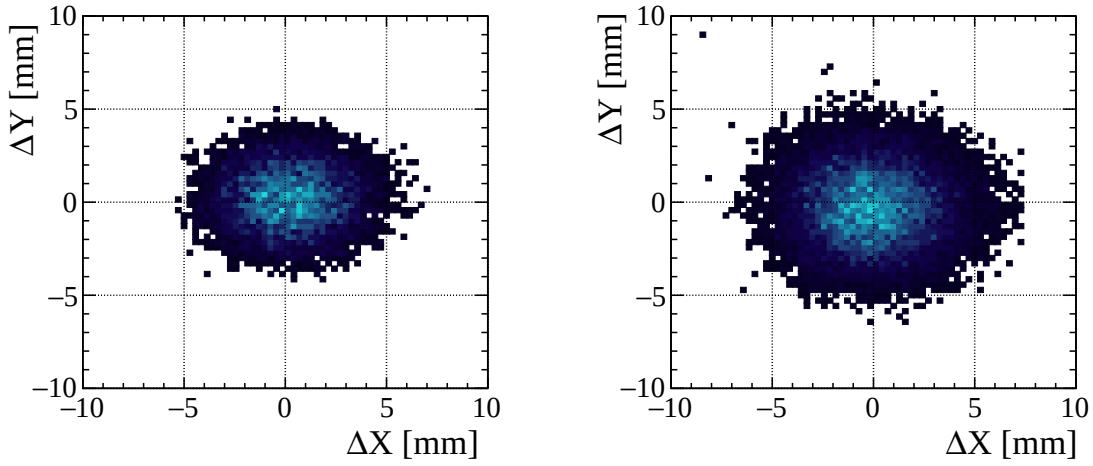

Figure 3.22: Difference of the position measured by the DC and the position reconstructed by the CATS in the DC plane. Left: First X-Y DC couple. Right: Second X-Y DC couple. The two DC couples are separated by 40 mm.

	X [mm]	Y[mm]	Z[mm]	$\epsilon(^{37}Ca)$	$\epsilon(^{38}Ca)$
DC1 (-X)	3.9	0	1000	0.78	0.62
DC2 (X)	-1.5	0	1020	0.80	0.61
DC3 (Y)	0	-2.4	1040	0.61	0.58
DC4 (-Y)	0	2.4	1060	0.81	0.61

Table 3.3: Position and efficiencies of the DC determined from the analysis.

presented in Table 3.3. As in the previous section, the efficiencies were found to be smaller during the ^{38}Ca beam setting due higher beam intensity.

3.3 Ion identification

The ZDD was used to identify the outgoing heavy ions and to study their angular correlations with the outgoing light particle. Furthermore, the IC was used to identify the nuclei present in the cocktail beam using a gate on the unreacted beam (corresponding to selection on CATS trigger only). Indeed, as presented in Section 3, the CATS detectors trigger the acquisition. Given that the majority of the beam particles do not interact with the target, by selecting only the events triggered by CATS, one can select almost only the unreacted beam and therefore study the composition of the incoming cocktail beam with the ZDD even if it is located after the target.

Fig. 3.23 shows the ion identification plot of the ^{37}Ca cocktail beam, obtained with a gate on the unreacted beam. By studying the correlation between the energy loss in the IC (depending mainly on Z) and the time-of-flight (TOF) between the cyclotrons and the CATS detectors (depending mainly on A) one can separate each isotope present in the cocktail beam. Even if only the TOF is used to gate on the incoming nuclei, this identification is very useful to look at contaminants present in the time-of-flight gate.

Then using the events triggered by MUST2, one can select only events for which the beam particle

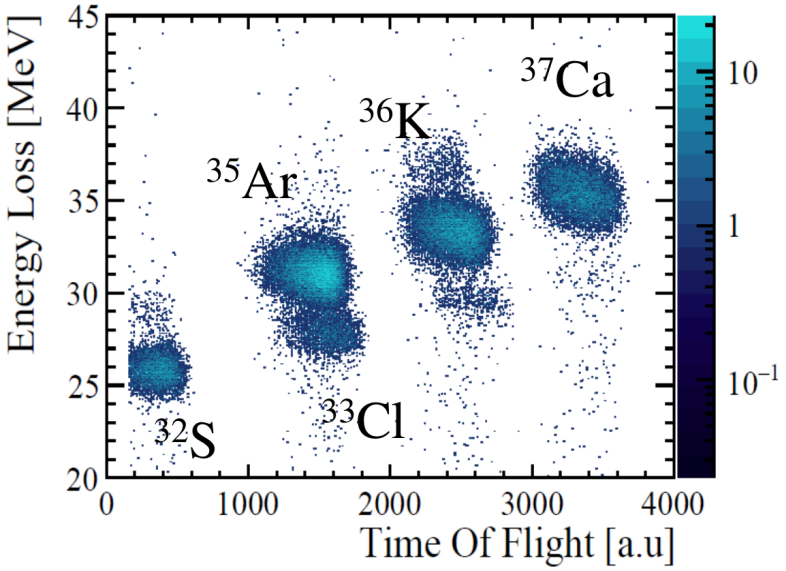

Figure 3.23: Incoming beam identification of the ^{37}Ca cocktail beam using CATS-HF time-of-flight.

made a reaction in the target. The ZDD can then be used to identify the outgoing nuclei produced after a reaction in the target. Left part of Fig. 3.24 shows the outgoing heavy ion identification obtained using a TOF gate (TOF CATS-HF) to select incoming ^{37}Ca. In this plot, the TOF was measured between CATS and the plastic scintillator at the end of the ZDD. From an incoming ^{37}Ca, many different reactions can happen in the target, leading to outgoing heavy ions going from Ca (Z=20) to Si (Z=14). The short time-of-flight basis (with about 1 m between the target and the plastic) does not allow to disentangle the isotopes in A. This plot will be used in the analysis to select the Z of the outgoing heavy ion produced in ^{38,37}Ca(p,d)^{37,36}Ca and ^{38,37}Ca(p,t)^{36,35}Ca transfer reactions, in order to study independently the one and two proton decay channels of Ca isotopes. Right part of Fig. 3.24 shows another example of outgoing heavy ion identification, obtained by selecting an incoming ^{32}S.

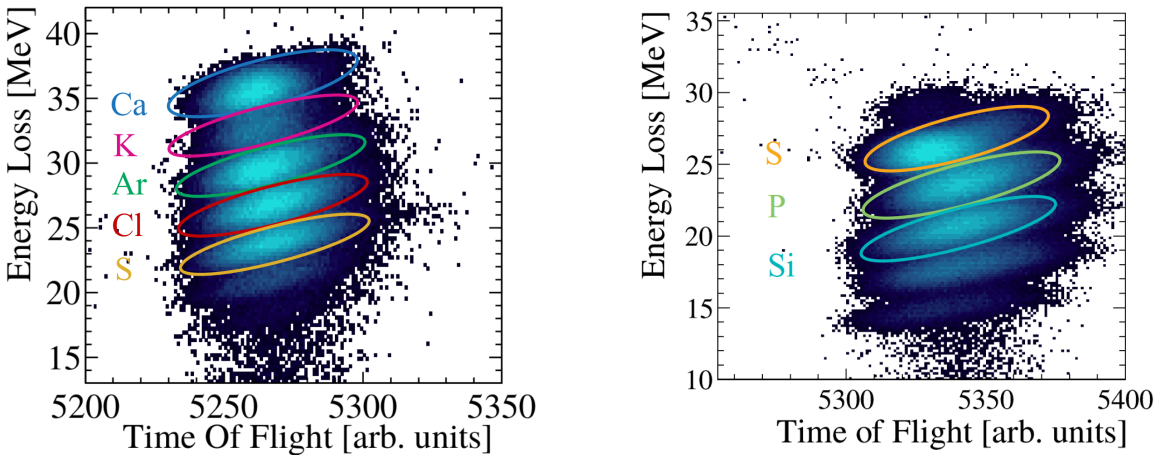

Figure 3.24: Left: Outgoing heavy ion identification using CATS-Plastic time-of-flight, obtained using a gate on ^{37}Ca incoming. Right: Outgoing heavy ion identification obtained using a gate on ^{32}S incoming.

One can identify isotopes from S to Mg in this plot. A small spot can be identified over the S events, corresponding to a small amount of ^{34}Cl contaminant present in the TOF gate. The S events, identified with the two gates S and Ca incoming, are found at slightly different values of energy loss due to the difference of kinetic energy of the incoming ^{37}Ca beam and ^{32}S beam and with a shifted TOF value arising from the difference of time-of-flight between ^{32}S and ^{37}Ca between the CATS and the target. This demonstrate the reliability of the outgoing ion identification performed with the ZDD.

4 Reconstruction of the observables of interest

4.1 The missing mass method

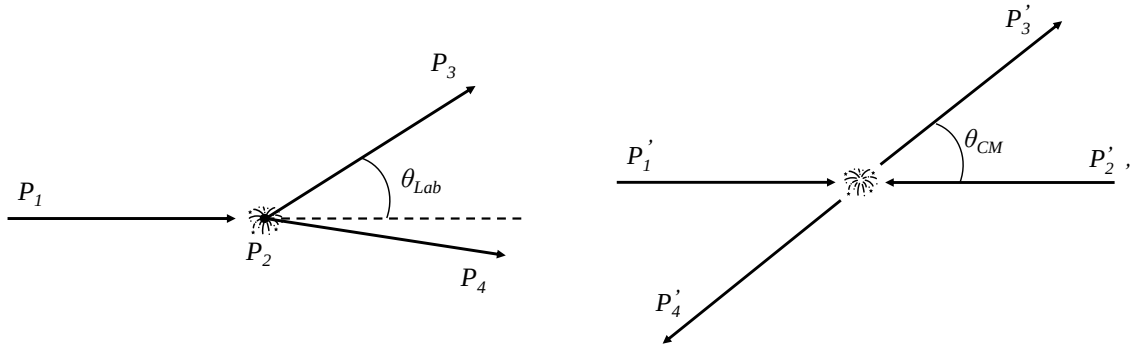

Figure 3.25: The two body kinematics in the laboratory frame (left) and in the center-of-mass frame (right).

Transfer reactions are a very powerful tool to study the structure of the nuclei. They are governed by the two-body kinematics. This allows indirect measurement of the spectroscopy of the outgoing heavy nuclei using the missing mass method. Let us consider the two body reaction:

$$1+2 \rightarrow 3+4 \ , \tag{3.8}$$

where the particle 1 represents the beam, the particle 2 is the target, 3 is the outgoing light particle and 4 the outgoing heavy ion. For a particle i, we define the momentum-energy four-vector $P_i = (E_i, \vec{p_i})$ using the natural unit convention $c = 1$, where E_i is the total energy of the particle and $\vec{p_i}$ its impulsion. In the framework of special relativity, the total energy of a particle can be expressed as a function of its kinetic energy E_k and its mass m as $E = E_k + m$ or as function of its impulsion p as $E^2 = p^2 + m^2$. Therefore, one can express the momentum-energy four-vector of our particles in the laboratory frame as:

$$\begin{cases} P_1 &= (E_{k,1}+m_1, 0, 0, \sqrt{E_{k,1}^2 + 2E_{k,1}m_1}) \\ P_2 &= (m_2, 0, 0, 0) \\ P_3 &= (E_{k,3}+m_3, sin(\theta_{Lab})\sqrt{E_{k,3}^2 + 2E_{k,3}m_3}, 0, cos(\theta_{Lab})\sqrt{E_{k,3}^2 + 2E_{k,3}m_3}) \\ P_4 &= (E_4, \vec{p_4}) \end{cases} \tag{3.9}$$

considering that the target particle is at rest in the laboratory frame, the beam particle has a straight

path along the z axis and that the reaction occurs in the (xOz) plan (which is a good approximation, since the cross-section is invariant under rotation around the beam axis).

The missing mass method consists in measuring the kinetic energy $E_{k,3}$ and the angle θ_{Lab} of particle 3 to reconstruct the momentum-energy four-vector of the particle of interest (particle 4) P_4 using energy and momentum conservation law:

$$P_4 = P_1 + P_2 - P_3. \tag{3.10}$$

In our experiment, $E_{k,1}$ was known from the $B\rho$ of the spectrometer and the masses $m_{1,2,3}$ were known from database.

4.2 Excitation energy

The excitation energy E_x of a particle can be defined as:

$$E_x = \sqrt{P^2} - m_0 \ , \tag{3.11}$$

where P is its momentum-energy four-vector and m_0 its mass at rest (or the mass of the ground state). P^2 can be seen as the internal energy of the system. In the case of a nucleus, this internal energy can take two forms: mass (including the mass of the constituents and the binding energy) and/or excitation energy (e.g. vibration, rotation, particle-hole excitation...). Considering that the masses m_i in equation (3.9) are the masses of the ground states of the particles ($m_i = m_{0,i}$), the extraction of the excitation energy for the particle of interest is straightforward:

$$E_{x,4} = \sqrt{(P_1 + P_2 - P_3)^2} - m_4, \tag{3.12}$$

where the only unknown variables are $E_{k,3}$ and θ_{Lab}. The kinetic energy of the light outgoing particle in the laboratory frame $E_{k,3}$ is usually named E_{Lab} and we use this convention in this document.

The angle of the outgoing light particle θ_{Lab} is determined using the position measurement performed by the DSSD of the MUST2 telescopes and the CATS detectors. The CATS detectors measure the direction of the beam particle $\overrightarrow{d_1}$ and the position of interaction point of this particle inside the target I_t. The MUST2 telescopes measure the position of the interaction point inside the DSSD I_{DSSD} (see Fig. 3.26). Then θ_{Lab} is given by:

$$cos(\theta_{Lab}) = \frac{\overrightarrow{d_1} \cdot \overrightarrow{I_t I_{DSSD}}}{\|\overrightarrow{d_1}\| \|\overrightarrow{I_t I_{DSSD}}\|}. \tag{3.13}$$

The energy E_{Lab} of the light particle is its energy at the time of the emission. The energy of the light particle is measured by the DSSD and the CsI of MUST2. On the way, the particle lost a part of its energy inside the target and in dead layers. Therefore, the reconstruction of E_{Lab} from the measured energy loss in the DSSD E_{DSSD} and the residual energy measured in the CsI E_{CsI} requires a precise knowledge of the thickness and the composition of the materials crossed by the particle. E_{Lab} is given by:

$$E_{Lab} = E_{CsI} + E_{DSSD} + E_{Loss}, \tag{3.14}$$

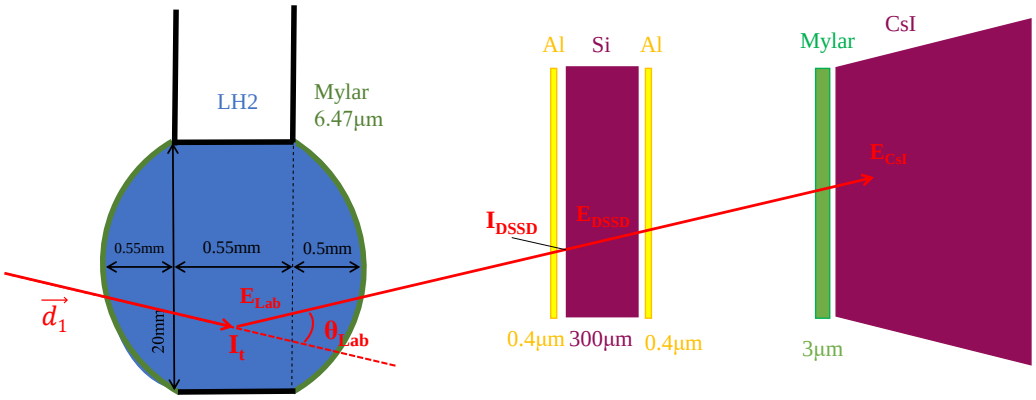

Figure 3.26: Schematic view (not on scale) of the path followed by a particle emitted inside the target and detected in MUST2. The different material crossed are represented.

where E_{Loss} represents the energy lost by the particle in the target and in dead layers. Fig. 3.26 shows a schematic view of the path followed by a particle from the emission point to the CsI crystal. For each material crossed, the energy lost in this material is computed using energy loss tables, taking into account the thickness of the material, the incident angle and the incident energy of the particle. E_{Lab} is reconstructed by starting at the end of the track and by adding, one by one, the energy lost in each material. The Z position of the vertex is not known and is supposed to be in average at the center of the target. This approximation induces a loss of resolution in excitation energy of about 3% (estimated with the simulation). One can see in Fig. 3.26 that the thickness of LH_2 crossed inside the cryogenic target can significantly vary depending on the position of the vertex. Therefore, the precise parametrization of the shape of the target windows (presented in Sec. 2.2) is very important. Anyhow, there are still uncertainties on the thickness of material crossed (e.g. the deformation of the target when cooling it down, the thickness of the Si dead layer in the DSSD...) but the absolute calibration procedure presented in Sec. 2.2 allows to correct from those effects.

4.3 Differential cross section

The differential cross section in the center-of-mass frame is given by:

$$\frac{d\sigma}{d\Omega_{CM}}(\theta_{CM}) = \frac{N(\theta_{CM})}{N_i N_{target} \epsilon(\theta_{CM}) d\Omega_{CM}(\theta_{CM})} \ , \tag{3.15}$$

with:

- $N(\theta_{CM})$: the number of light particles detected at an angle θ_{CM}
- N_i: the number of incident beam particles on the target
- N_{target}: the number of protons per cm^2 inside the target
- $\epsilon(\theta_{CM})$: the reconstruction efficiency of an event at a given angle θ_{CM}
- $d\Omega_{CM}(\theta_{CM})$: the element of solid angle in the center-of-mass frame at a given angle θ_{CM}

In practice, $N(\theta_{CM})$, $\epsilon(\theta_{CM})$ and $d\Omega_{CM}$, are computed for a slice of center-of-mass angle $\Delta\theta_{CM}$ whose width is taken to obtain enough statistics per bin of angle.

The center of mass angle θ_{CM} is computed from the measurement of E_{Lab} and θ_{Lab}. Indeed, once those quantity are extracted, one can reconstruct the momentum-energy four-vector P_3 of the light outgoing particle. Then the four-vector of the particle in the center-of-mass frame can be computed from the Lorentz transformation of P_3: $P_3' = \Lambda P_3$, where Λ is the Lorentz matrix of the center-of-mass frame. The center-of-mass angle θ_{CM} of the particle is then given by:

$$cos(\theta_{CM}) = \frac{\overrightarrow{p_1} \cdot \overrightarrow{p_3'}}{\|\overrightarrow{p_1}\| \|\overrightarrow{p_3'}\|} \tag{3.16}$$

where $\overrightarrow{p_1}$ is the impulsion of the beam particle in the laboratory frame and $\overrightarrow{p_3'}$ is the impulsion of the light outgoing particle in the center-of-mass frame (cf. Fig. 3.25). θ_{CM} is computed event by event. To obtain the angular distribution $N(\theta_{CM})$ for a state, two methods are available. Method 1: by gating on the slice of excitation energy corresponding to a state. Then the angular distribution is given by the $N(\theta_{CM})$ corresponding to a given state. Method 2: by fitting the excitation energy spectra for each slice of center-of-mass angle $\Delta\theta_{CM}$. The $N(\Delta\theta_{CM})$ will be the integral of the peak corresponding to the state of interest. The total angular distribution is then obtained by doing this operation step by step over all the angular range. The second method allows to disentangle states that overlap but is more difficult to use with low statistics.

The number of incident beam particles on the target N_i is computed from the number of incoming beam particles corresponding to a trigger CATS (divided) for which the interaction point is reconstructed inside the target cell. This number is then multiplied by the value of the division. To obtain the real number of incident beam particles, this value has to be corrected from dead time, CATS efficiency and interaction point reconstruction efficiency. But, since the same CATS efficiency is used to correct the beam counting and the number of particle detected in MUST2, this efficiency term cancels out and there is no need to apply CATS efficiency correction.

The number of protons per cm^2 inside the target N_{target} is computed using:

$$N_{target} = \frac{2\sigma_{target}\mathcal{N}_A}{M_{H_2}} \tag{3.17}$$

where σ_{target} is the surface density of the target in mg·cm^{-2}, $\mathcal{N}_A$ is the Avogadro number and M_{H_2} is the molar mass of the H_2 molecule. The value of σ_{target} is not obvious to compute due to the deformation of the target foils. Indeed $\sigma_{target} = \rho_{H_2} * e_{target}$ where ρ_{H_2} is the density of liquid H_2 in mg·cm^{-3} and e_{target} is the effective thickness of the target in mm (corresponding to the mean thickness of target crossed by unreacted beam particles). To compute e_{target}, simulations were performed with the experimental beam emittance to determine the average thickness of target crossed by the beam particles (e.g. for the ^{37}Ca beam, an effective thickness of $e_{target} = 1.3(1)$ mm was found).

Finally, the reconstruction efficiency $\epsilon(\theta_{CM})$ and the element of solid angle $d\Omega_{CM}(\theta_{CM})$ are evaluated together using the simulation as follows:

1. Perform a simulation for the reaction and state of interest (the solid angle covered by the

detectors in the center-of-mass frame can change significantly with the excitation energy).

2. Get the emitted angular distribution $N_{emit}(\theta_{CM})$
3. Reconstruct the detected angular distribution $N_{det}(\theta_{CM})$ using the same conditions as in the analysis.
4. Compute the efficiency $\epsilon(\theta_{CM}) = \frac{N_{det}(\theta_{CM})}{N_{emit}(\theta_{CM})}$.
5. Multiply the efficiency by the element of solid angle $d\Omega_{CM}(\theta_{CM}) = 2\pi sin(\theta_{CM})d\theta_{CM}$ (in practice $d\theta_{CM}$ is the size of a θ_{CM} bin).

At this step, $\epsilon d\Omega_{CM}(\theta_{CM})$ contains the geometrical, detection and reconstruction efficiencies of the simulated detectors. The ZZD was not included in the simulation. Therefore, if one wants to use the ZDD for the extraction of the differential cross section, its efficiency has to be taken into account. To determine the efficiency of the ZDD for a given reaction, the analysis was performed with and without the ZDD. Then the integrals of a reference peak (usually the ground state), obtained in both cases, were compared and the ZDD efficiency was obtained from the ratio of those integrals (e.g. for the ^{38}Ca(p,d)^{37}Ca reaction, the total ZDD efficiency was found to be of 37%. This relatively low value arises from the convolution of the individual efficiencies of each detector which was reduced due to the large counting rate of the ^{38}Ca beam setting).

4.4 Proton energy and angle in the center-of-mass

In this study, we are interested in the one and two proton decay of unbound states. The kinematic of this process is governed by the two-body decay. Let us consider the decay of the outgoing heavy particle 4 in a light particle 5 and a heavy one 6:

$$4 \rightarrow 5 + 6. \tag{3.18}$$

The reconstruction of the kinetic energy $E_{k,5}$ of the light daughter particle is done with the same method as for the excitation energy. This time the kinematic will not be invariant under the z axis (define as the direction of the beam particle 1). Therefore we have to consider the y component of the impulsion given by the $\phi_{Lab,5}$ angle. The momentum-energy four-vector of the daughter particles in the laboratory frame can the be expressed as:

$$P_5 = (E_5, sin(\theta_{Lab,5})cos(\phi_{Lab,5})p_5, sin(\theta_{Lab,5})sin(\phi_{Lab,5})p_5, cos(\theta_{Lab})p_5), \tag{3.19}$$

where $E_5 = E_{k,5} + m_5$ and $p_5 = \sqrt{E_5^2 - m_5^2}$. Then the momentum-energy four-vector of the particle in the center-of-mass frame of the particle 4 can be computed from the Lorentz transformation of P_5: $P_5' = \Lambda_4 P_5$, where Λ_4 is the Lorentz matrix of the particle 4. The energy $E'_{k,5}$ and the angle $\theta_{CM,5}$ of the particle 5 in the center of mass frame is given by:

$$\begin{cases} E'_{k,5} = E'_5 - m_5 \\ cos(\theta_{CM,5}) = \frac{\overrightarrow{p_4} \cdot \overrightarrow{p'_5}}{\|\overrightarrow{p_4}\| \|\overrightarrow{p'_5}\|} \end{cases} \tag{3.20}$$

taking the direction of the mother particle in the laboratory frame as reference to compute the center-of-mass angle. The momentum-energy four-vector of the heavy daughter particle 6 can then be eventually computed using the missing mass method.

4 Results

Sommaire

This chapter presents the results obtained on ^{36}Ca. The extraction of the excitation energy spectra and the mass measurement of ^{36}Ca using the ^{37}Ca(p,d)^{36}Ca reaction will be presented first. Then, the spectroscopy of ^{36}Ca using the ^{37}Ca(p,d)^{36}Ca will be performed. Then, the spectroscopy of ^{36}Ca using the ^{38}Ca(p,t)^{36}Ca transfer reaction will be presented. Finally, preliminary results about the study of ^{35}Ca using the ^{37}Ca(p,t)^{35}Ca reaction will be given.

1 One neutron transfer reaction: ^{37}Ca(p,d)^{36}Ca

We start here by presenting the results obtained in the analysis of the ^{37}Ca(p,d)^{36}Ca reaction. First, the extraction method of the excitation energy spectra will be presented before to show the mass measurement of ^{36}Ca. Then, the position of the excited states populated in ^{36}Ca will be determined by fitting the different excitation energy and proton energy spectra available. The transferred angular momentum L as well as the spectroscopic factors C^2S of the populated states in ^{36}Ca will then be determined using the Distorted Wave Born Approximation (DWBA) analysis of the differential cross sections. Finally, the analysis of the two-proton decay channel of ^{36}Ca will be presented.

1.1 Extraction of the excitation energy and mass measurement of ^{36}Ca

1.1.1 Selections and kinematic lines

In order to reconstruct the excitation energy of the nucleus of interest, one has first to apply conditions on the different measured quantities to select the good reaction. First, conditions are applied to select the beam particle of interest:

- ^{37}Ca as incident beam particle: using the CATS1-HF and the CATS2-HF time-of-flight measurement (see Fig. 4.1)
- Beam inside the target cell: using the reconstruction of the beam in the target plane performed by CATS (see Fig. 4.1 and Section 1.3 of Chap. 3)

Then, to select the ^{37}Ca(p,d)^{36}Ca reaction, one has to gate on a deuteron in MUST2. This condition depends on the multiplicity of the event. Indeed, if ^{36}Ca is produced in its ground state (or in a bound state), we expect an event of multiplicity 1 in MUST2. If ^{36}Ca is produced in an unbound state, we expect an event of multiplicity 2 if the decay occurs via the one-proton decay channel, or an event of multiplicity 3 if the decay occurs via the two-proton decay channel. Therefore the MUST2 conditions are applied as follow:

1. If the MUST2 multiplicity is 1: the event is accepted if the particle is a deuteron
2. If the MUST2 multiplicity is 2: the event is accepted if one particle is a deuteron and the other is a proton
3. If the MUST2 multiplicity is 3: the event is accepted if one particle is a deuteron and the two others are protons

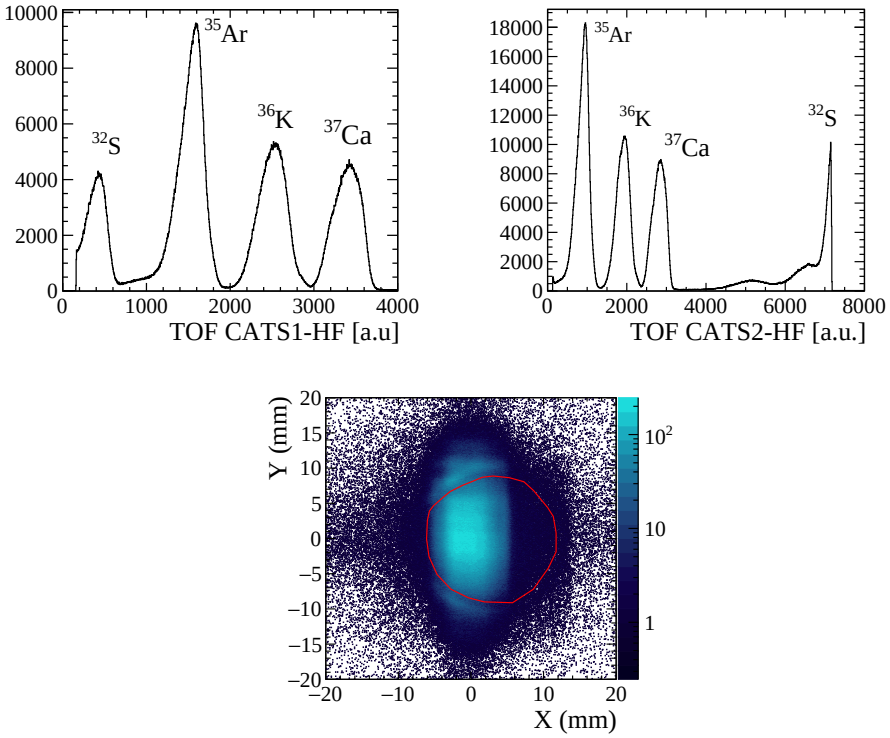

Figure 4.1: Top: Time-of-flight spectra measured between CATS1 (in the left part and CATS2 in the right part) and the High-Frequency (HF) delivered by the cyclotrons. Bottom: Graphical cut applied to select beam particles that are inside the target. The cut is adjusted to reject reactions occurring at the edge of the target cell frame.

The selection of proton and deuterons is performed using the light particle identification plot obtained with MUST2 as shown in Fig. 4.2 (see Chap. 3 Section 2.4 for details).

Finally, a condition is applied using the ZDD to select either a Ca, K or Ar outgoing heavy ions (see the identification plot in Chap. 3 Section 3.3) in order to study separately the gamma, one-proton and two-proton decay channels of the excited states of ^{36}Ca , respectively.

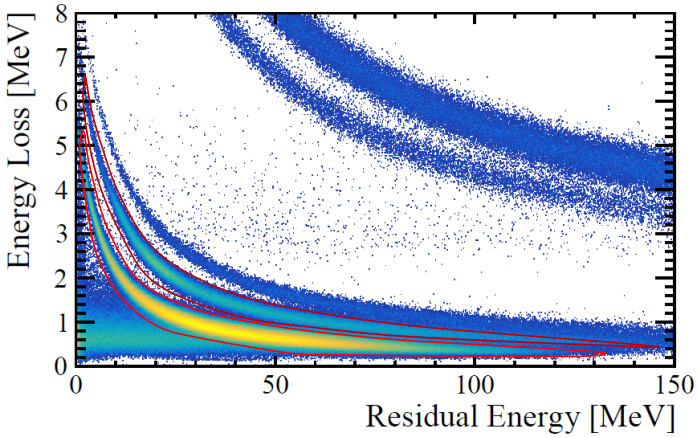

Figure 4.2: Graphical cut applied on the ΔE-E light particle identification plot obtained with MUST2. the upper red contour shows the deuteron selection and the lower one, the proton selection.

Once those conditions have been applied, one can reconstruct the kinematic lines of the reaction. They are obtained from the correlation between the energy E_{Lab} and the angle θ_{Lab} of the deuteron emitted by the transfer reaction, in the laboratory frame. To one line corresponds one state populated in ^{36}Ca. We will first focus on events obtained with a Ca outgoing in the ZDD, corresponding to the production of ^{36}Ca in its ground state or in exited states that decay via gamma emission. The kinematic lines, reconstructed for the ^{37}Ca(p,d)^{36}Ca reaction with a Ca outgoing are shown in the left part of Fig. 4.3. One can clearly see two lines, one for the ground state of ^{36}Ca and the other one for its first 2^+ excited state. The excitation energy of the 2^+ first-excited state in ^{36}Ca was measured at GANIL [35], GSI [34] and NSCL [36] by means of one-neutron knockout reactions from a ^{37}Ca secondary beam. Taking the most precise measurement, its energy was found to be 3045.0 ± 2.4 keV [36]. This value will be used as a reference for the analysis. Moreover, Fig. 4.3 shows the very low amount of background since very few counts are observed away from the expected kinematic lines.

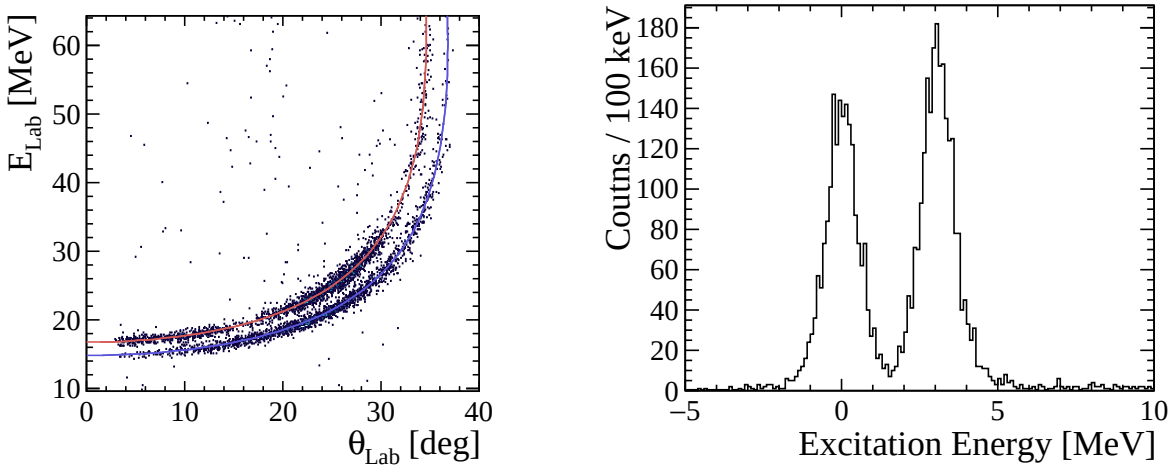

Figure 4.3: Left: Kinematic plot of the ^{37}Ca(p,d)^{36}Ca transfer reaction. This plot was obtained by gating on Ca nuclei in the ZDD. The blue line shows theoretical calculation of the kinematic line for the ground state and the red line for the known first 2^+ excited state at 3.045 MeV. Right: The corresponding excitation energy spectrum of ^{36}Ca .

From the measured energy E_{Lab} and angle θ_{Lab} of the deuteron, one can reconstruct the excitation energy spectrum in ^{36}Ca using the missing mass method (as presented in Chap. 3 Section 4). The right part of Fig. 4.3 shows the excitation energy spectrum reconstructed for the ^{37}Ca(p,d)^{36}Ca reaction with a condition on a Ca outgoing in the ZDD. One can clearly identify the two peaks in this spectrum corresponding to the two kinematic lines observed in Fig. 4.3 left. The peak around 0 MeV corresponds to the ground state and the second peak corresponds to the first 2^+ excited state. Again this spectrum displays a very small amount of background. However this background becomes non-negligible in some spectra that we will see later. Therefore, before fitting the peaks, the study of the background will be presented.

1.1.2 Background study

During the experiment, data have been taken with the empty cryogenic target, in order to study the contribution of target cell windows foils to the reconstructed excitation energy spectra. The empty target runs were taken only with the ^{38}Ca beam setting. We will make the assumption that the shape of the background does not change between the ^{38}Ca(p,d)^{37}Ca and the ^{37}Ca(p,d)^{36}Ca reactions. Left part of Fig. 4.4 shows the excitation energy spectrum obtained by analyzing the empty target runs as the ^{38}Ca(p,d)^{37}Ca reaction. This spectrum has been fitted using a combination of a second order polynomial and a logistic function:

$$f_{back} = p_0 x^2 + p_1 x + p_2 + \frac{p_3}{1 + \exp^{\frac{x+p_4}{p_5}}}, \tag{4.1}$$

where p_i are the free parameters of the function.

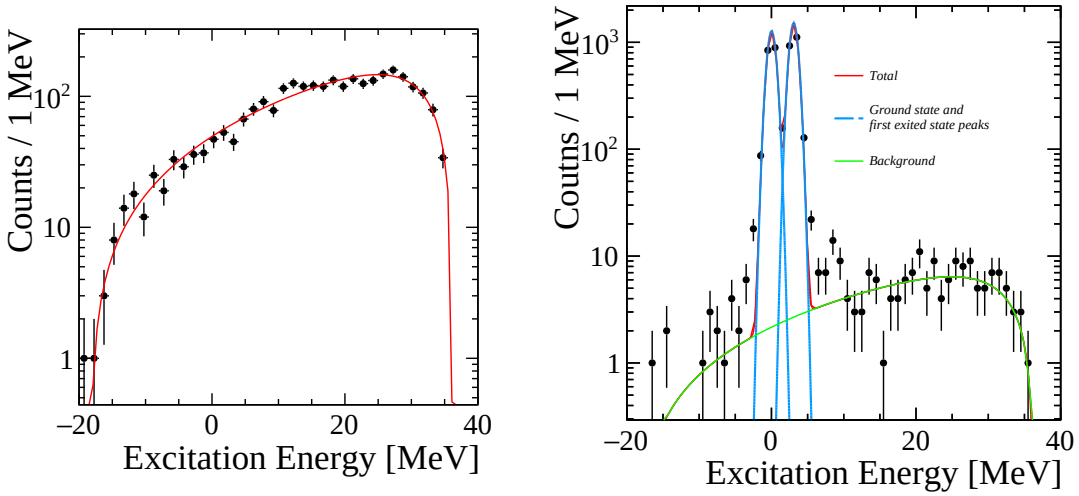

Figure 4.4: Left: Excitation energy spectrum obtained with the empty target runs. The analysis was performed as for the ^{38}Ca(p,d)^{37}Ca with a condition on a Ca outgoing. The red line shows the fit of the background. Right: Excitation energy spectrum of ^{36}Ca from the ^{37}Ca(p,d)^{36}Ca reaction. The spectra is shown in log scale to ease the background identification. The red line shows the fit performed and the blue and green lines the contributions of the states in ^{36}Ca and of the background, respectively.

Right part of Fig. 4.4 shows the excitation energy spectrum of ^{36}Ca obtained with the ^{37}Ca(p,d)^{36}Ca reaction. On this figure, the background is identified with its maximum around 25 MeV. The red line shows the fit of this spectrum performed with two Gaussians in addition to the background function f_{back}. Parameters of f_{back} are those coming from the fit performed with the empty target runs and a scaling factor was applied in order to reproduce the [20-30] MeV energy range. It is important to note that there is no phase space to consider here since we select events with a Ca outgoing, meaning that particle decay is not allowed. One can see in Fig. 4.4 that the model f_{back} reproduces well the background of the ^{36}Ca excitation energy spectrum.

Another way to separate the signal from the background is to look at the angular correlation between the light and the heavy outgoing particles. Fig. 4.5 shows the correlation plot between the

angle of the light particle θ_{light} and the heavy outgoing particle θ_{heavy} in the laboratory frame. Left part of Fig. 4.5 is obtained using the filled target. One can identify a curved line corresponding to the kinematic line of the ^{37}Ca(p,d)^{36}Ca reaction. The corresponding theoretical kinematic line is shown in red. The right part of Fig. 4.5 shows the same plot obtained with the empty target runs. For a (p,d) transfer reaction, it is expected that the more the light particle is emitted at large angle, the more the beam particle will be deflected. It is what is shown by the theoretical line in red. For the empty target runs, the ougoing heavy ion is seen most of the time at small angles ($\theta_{heavy} < 0.5°$), meaning that the beam particle has not been deflected. Therefore gating on large θ_{heavy} is a way to disantangle background from signal.

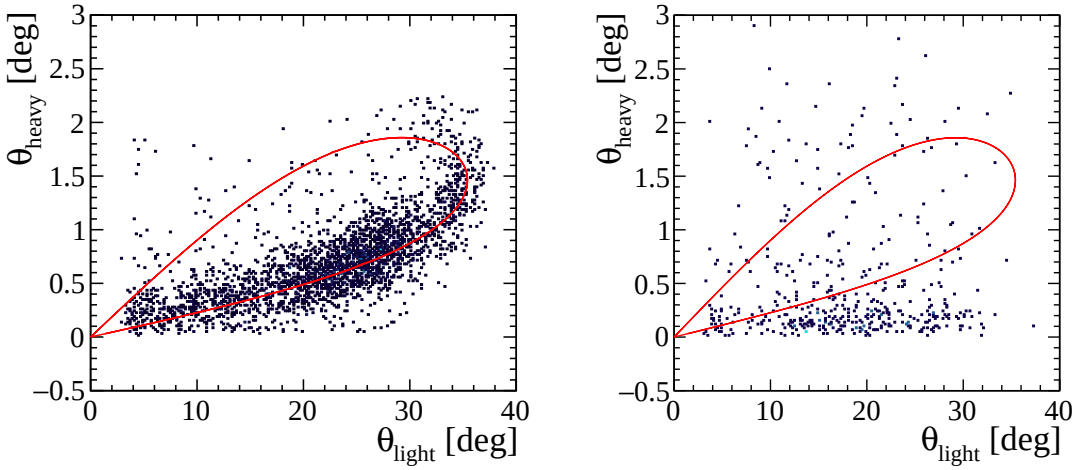

Figure 4.5: Correlation plots between the angle of the light particle $\theta_{light}$and the heavy outgoing particle θ_{heavy} in the laboratory frame. Those plots are shown for the the filled target (left) and for the empty target (right). In both plots, the theoretical line for the ^{37}Ca(p,d)^{36}Ca reaction is shown.

For the ^{37}Ca(p,d)^{36}Ca the signal-to-noise ratio obtained for the ground state peak of ^{36}Ca is of 290. The background will therefore has a negligible impact on the excitation energy spectra and on the angular distributions. Since the background has a rather flat behavior in the energy range of interest, it will be described using a constant function during the fit of the excitation energy spectra. This background will become more important when analyzing the ^{38}Ca(p,t)^{36}Ca channel. Indeed the background arises from random coincidences which rate is proportional to the beam intensity. Since the ^{38}Ca beam has been obtained with 10 times more intensity than the ^{37}Ca beam and that the cross section of the (p,t) reaction is lower than the (p,d), the signal-to-noise ratio will strongly decrease in the case of the ^{38}Ca(p,t)^{36}Ca reaction. Therefore we will come back to the background analysis in Section 2.1.2.

1.1.3 Atomic mass of ^{36}Ca

Before starting this work, the mass excess of ^{36}Ca was known experimentally to be $\Delta M = -6440(40)$ keV from one measurement performed in 1977 using the ^{40}Ca(^{4}He,^{8}He)^{36}Ca transfer reaction [30]. To re-measure its value was one of the goal of the experiment, in order to confirm (or not) the previous

measurement and to reduce its associated uncertainty. Very recently, a more precise mass excess of $\Delta M = -6483.6(56)$ keV has been obtained using a Time of Flight - Ion Cyclotron Resonance measurement technic in a Penning trap [31]. Even if the atomic mass of ^{36}Ca has now been measured with a good accuracy, it is interesting to determine its value with another method, based on transfer reactions. Indeed, even though it is less precise, this method is more generic and can also be applied to the determination of masses of unbound nuclei. Therefore, this section presents the mass measurement of ^{36}Ca without considering the recent measurement performed in [31].

The mass of a nucleus can be extracted using transfer reaction from the Q-value corresponding to its ground state if the mass of the beam particle is known with a good precision. In the case of the ^{37}Ca(p,d)^{36}Ca reaction, the mass excess of ^{37}Ca is very well known (with $\Delta M(^{37}\text{Ca}) = -13136.07(63)$ keV [53]). In practice, the reaction of interest is first analyzed considering a nominal value for the mass (either from previous measurement or from theoretical calculation). Then, the difference between the nominal value and the measured mass is then directly given by the measurement of the ground state position in the excitation energy spectrum. In the case of the ^{37}Ca(p,d)^{36}Ca reaction, the identification of the ground state peak is obvious but to identify the ground state can be more complicated in some cases, especially for odd-even or odd-odd nuclei (due to a high density of state or to a ground state to ground state transition less favored than for excited states).

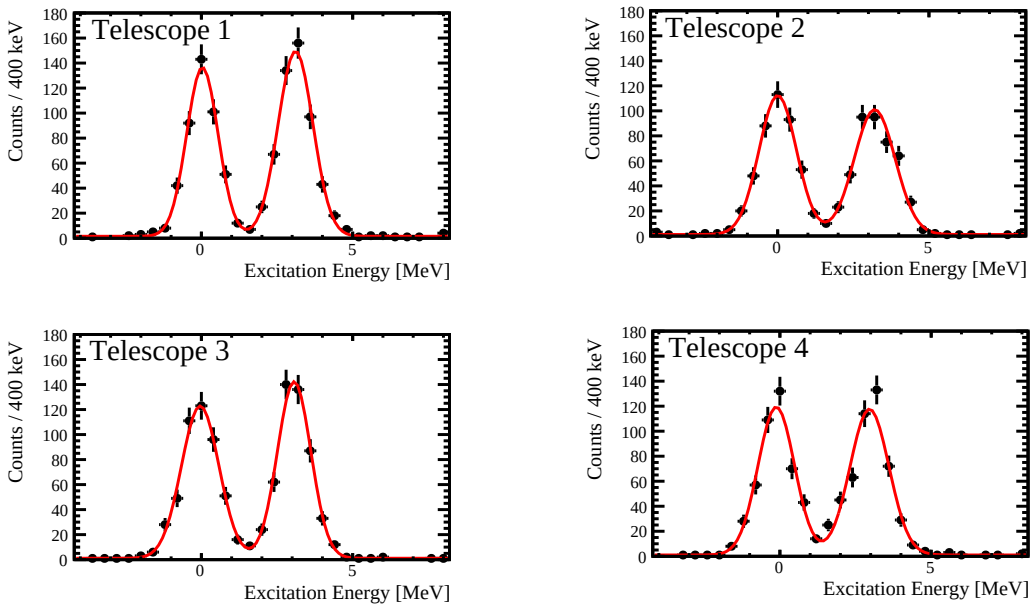

Figure 4.6: Single telescope - excitation energy spectrum of ^{36}Ca for the 4 MUST2 telescopes located at the closest distance from the target. Those plots were obtained with a condition on outgoing Ca isotopes. The red lines show the best fit obtained using a two Gaussian function.

Fig. 4.6 shows the excitation energy spectra of ^{36}Ca, for each MUST2 telescope. Only the four telescopes, located at the closest distance from the target (telescope 1 to 4) are used for the mass measurement (since the two other did not get enough statistics to be calibrated precisely). Each spectrum has been fitted using a 2 Gaussian function in order to extract the position of the ground state peak (see Section 1.2.1 for a detailed discussion about the fit and the resolution). These 4 spectra

provide 4 independent measurements of the mass. The standard deviation of these measurements is used to estimate the systematic errors and the mean value is taken as the measured mass. The total uncertainty is dominated by systematic errors arising from multiple effects such as the propagation of errors on the measured angle and energy of the deuteron and on the energy calibration of the CsI. The same method is applied to verify that the masses of the reference nuclei ^{34}Ar and ^{37}Ca are correctly reproduced. The results are given in Table 4.1.

nucleus	ΔM (keV) this work	ΔM (keV) literature
^{36}Ca	-6480(40)	-6440(40)[30]; -6483.6(56)[31]
^{37}Ca	-13141(13)	-13136.1(0.6) [54]
^{34}Ar	-18403(25)	-18378.29(0.08) [55]

Table 4.1: Mass excesses (ΔM), obtained in the present work for ^{37}Ca, ^{34}Ar, and ^{36}Ca using the (p,d) reaction are compared to other experimental works. Results from this work use the precise experimental atomic masses of ^{38}Ca [54], ^{35}Ar [53], and ^{37}Ca[54], respectively.

The error bars obtained for the reference nuclei show the best reachable precision on the mass excess measurement with this method, since they are the nuclei used for the calibration. The mass excess of ^{36}Ca, $\Delta M = -6480(40)$ keV, measured in this work, is in good agreement with the recent measurement, $\Delta M = -6483.6(56)$ keV of Ref. [31]. As expected, our uncertainty on the ^{36}Ca mass is larger than the one obtained from the Penning trap measurement, but similar to that obtained in the other transfer reaction measurement of Ref. [30]. It is interesting to note that, the same analysis performed without using the known masses of reference nuclei for the calibration (see the absolute calibration procedure Section 2.2) provides a mass measurement of ^{36}Ca of $\Delta M = -6450(160)$ keV. The absolute calibration allowed to reduce the uncertainties on the mass measurement by a factor of 3. These results demonstrate the reliability of the method.

In the following, the most precise mass measurement $\Delta M = -6483.6(56)$ keV of Ref. [31] as well as the energy of the 2^+ state, obtained from the determination of its gamma-ray energy [36], will be used as a new calibration points for the determination of the residual energy in the CsI detectors, in order to achieve the best reachable resolution in the excitation energy spectra of ^{36}Ca.

1.2 Spectroscopy of ^{36}Ca using the ^{37}Ca(p,d)^{36}Ca reaction

This section presents the spectroscopy of ^{36}Ca performed using the one-neutron transfer ^{37}Ca(p,d)^{36}Ca reaction. The upper panel of Fig. 4.7 shows the total excitation energy spectrum of ^{36}Ca, obtained without any condition on the ougoing nucleus. In this spectrum one can identify three broad peaks at about 0, 4.5 and 8 MeV. The lower pannel of of Fig. 4.7 shows the correlation between the angle θ_{cm} of the deuteron in the center-of-mass frame of the reaction and the excitation energy of ^{36}Ca. In this 2D plot, one can identify three different regimes separated by the red lines. The first one around 0 MeV displays a typical L=2 behavior, with an almost flat distribution, expected from the removal of a $d_{3/2}$ neutron in ^{37}Ca, to populate the ground state of ^{36}Ca (see Chap. 1 Section 4 for typical L=0 and L=2 distribution). The second regime, between 2 and 6 MeV, shows a typical L=0 behavior with a clear deep around 10° and an accumulation of counts at small angles, arising from the removal of a

$s_{1/2}$ neutron. The last regime, between 6 and 10 MeV corresponds to a L=2 distribution arising from the removal of a $d_{3/2}$ neutron. Therefore, one can identify the centroids of the $d_{3/2}$, $s_{1/2}$ and $d_{5/2}$ single particle orbitals at 0 MeV, 4.5 MeV and 8 MeV respectively.

The goal of this section is to identify the corresponding L=0 and 2 states populated in ^{36}Ca up to 10 MeV. The one-proton separation energy of ^{36}Ca is located at $S_p = 2599.6(61) =$ keV, meaning that all the excited state of ^{36}Ca are unbound through proton emission. Therefore, conditions on the outgoing heavy nuclei will be applied to isolate the populated excited states. The fit of the known states in the Ca gated excitation energy spectrum will be used to constrain the width of the gaussians used to fit the unexplored part of the ^{36}Ca excitation energy spectrum. Then the K gated spectrum as well as the one-proton energy spectrum will be used to extract the excitation energies of the populated state in ^{36}Ca. The extracted differential cross sections will be analyzed within the DWBA framework in order to constrain the spin of the sates and to extract neutron spectroscopic factors. Finally, the Ar gated spectrum will be used in order to study the two-proton decay of the populated states in ^{36}Ca.

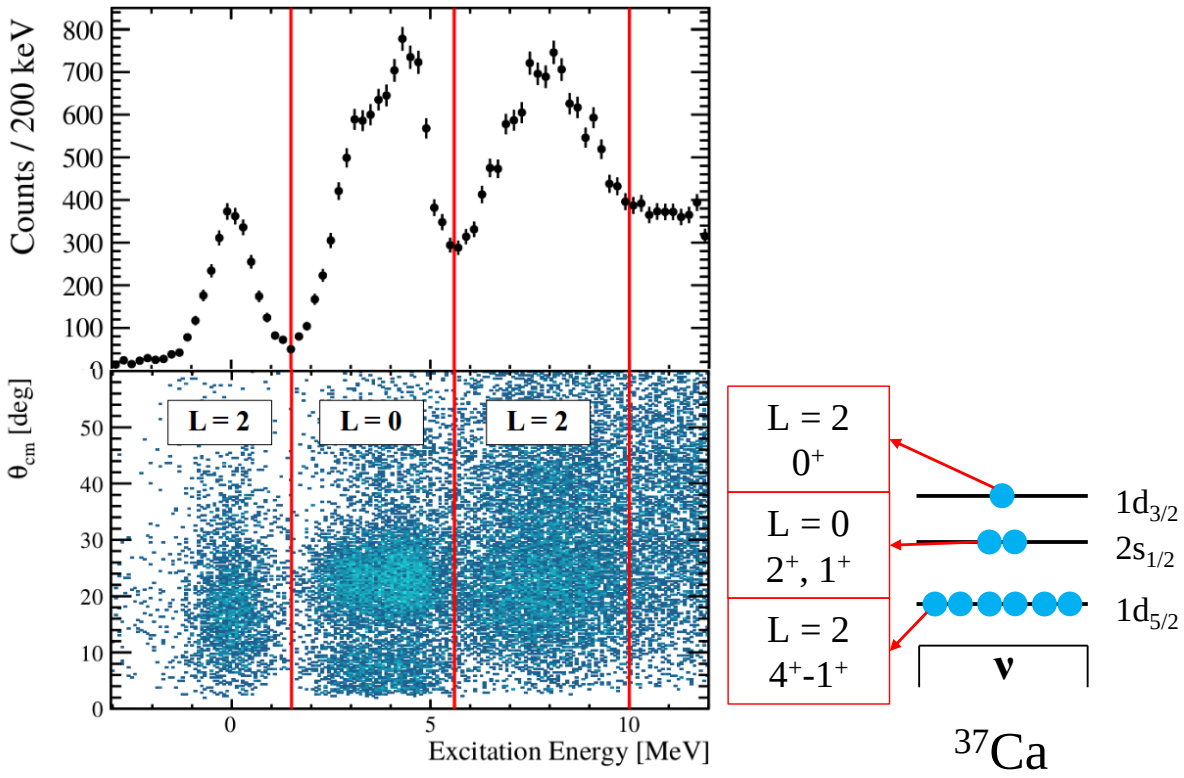

Figure 4.7: Left: The upper panel shows the total excitation energy spectrum of ^{36}Ca, obtained without any condition on the ougoing nucleus. The lower pannel shows the correlation between the angle θ_{cm} of the deuteron in the center-of-mass frame of the reaction and the excitation energy of ^{36}Ca. Right: Neutron shell structure of ^{37}Ca. The nature of the transfer and the produced states, corresponding to the orbital from which the neutron is removed, are shown in the red boxes.

1.2.1 Fit of the excitation energy spectrum with Ca outgoing gate and energy resolution study

Fig. 4.8 shows the excitation energy spectra of ^{36}Ca, reconstructed using the ^{37}Ca(p,d)^{36}Ca reaction, with the condition to have a Ca outgoing in the ZDD. In this spectrum, two peaks are identified: the first one at 0 MeV, identified as the ground state of ^{36}Ca, the second one at 3 MeV, identified as the known first 2^+ excited state of ^{36}Ca. This spectrum has been fitted with a two Gaussian function in addition to a constant function to model the background in order to extract the position of these states.

To monitor the quality of the fit, three quantities are used:

- The reduced χ^2, given by the χ^2 divided by the number of degrees of freedom. It represents the general goodness of the fit.
- The pulls, defined as the difference between the data and the fit function for a bin, normalized to the experimental error (dominated by the statistical uncertainties). They are given in units of the squared variance, σ, which corresponds to the error bars represented graphically for each bin. It represents the local goodness of the fit.
- The p-value that represents the probability to get wrong by rejecting the model used to fit the experimental data (note that the p-value should not be interpreted as the probability that the model is valid).

A fit is validated if the reduced χ^2 is lower than 2, if the p-value is higher than 0.05 and if the pulls do not exceed 2 sigma.

Fig. 4.8 shows the best fit obtained with a normalised χ^2 of 1.0 and a p-value of 0.48. The ground state is found to be at 9(14) keV. This measurement is compatible with zero which is expected since the reaction has been analysed using the precise mass measurement of Ref [31]. The first 2^+ excited state is found to be at $E_x(2^+) = 3.059(16)$ MeV. This measurement is compatible with the most precise measurement $E_x^{lit}(2^+) = 3045.0(24)$ keV of Ref. [36]. The errors are computed using ROOT and are defined as the square root of the diagonal element (corresponding to the fit parameter of interest) of the covariance matrix of the fit parameters.

The measured energy resolution for the ground state and the 2^+ excited state peak are of 565(12) keV and 557(12) keV, respectively. Simulations have been performed in order to better understand the experimental resolution. The simulation includes effects of energy and angular straggling of the light particle inside the target, which are the main limitations to the resolution. The shape of the cryogenic target has been carefully studied (see Chap. 2 Section 2.2) and included in the simulation. The intrinsic energy resolution of the CsI crystals has been set as $\sigma_{CsI} = 0.08\sqrt{E_{CsI}}$, corresponding to a relative resolution of 5% for 5.5 MeV alpha particles. The effect of the CATS reconstruction is also included, as well as the energy spreading of the incoming ions. Using a realistic differential cross section, the resolution for the ground state of ^{36}Ca, reconstructed with the ^{37}Ca(p,d)^{36}Ca reaction, is found to be 491(6) keV with the simulation. The experimental resolution is in rather good agreement with the simulated one with 74 keV of difference. This difference can arise from effects such as straggling in

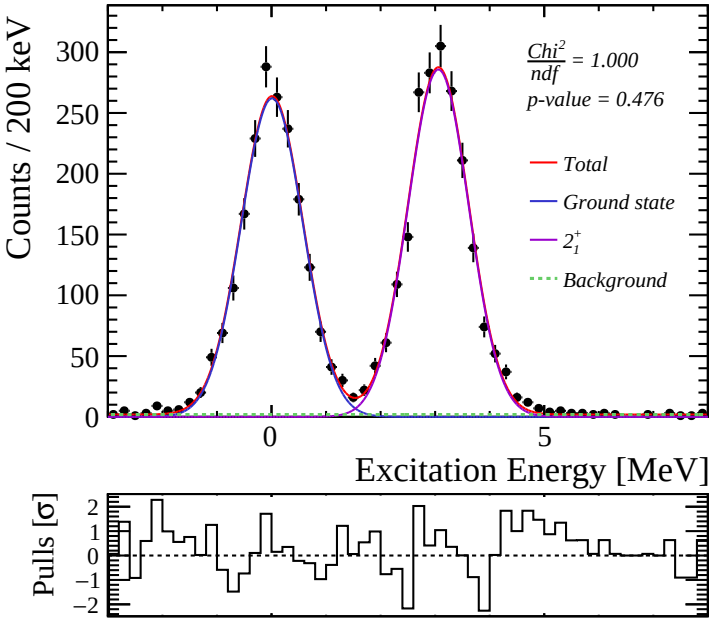

Figure 4.8: Excitation energy spectrum of ^{36}Ca reconstructed from the ^{37}Ca(p,d)^{36}Ca reaction. This plot was obtained with a condition on a Ca outgoing. The red line shows the best fit obtained. The individual components are shown in colored lines.

additional dead layers or from the misalignment in energy of the CsI crystals, which are not taken into account in the simulation.

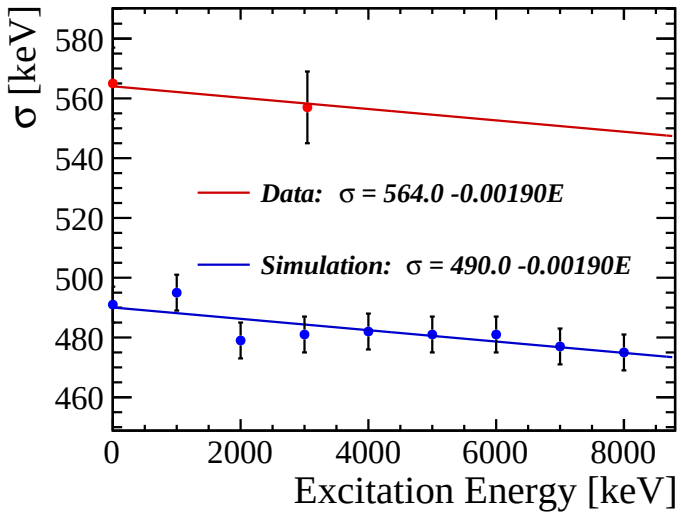

Figure 4.9: Evolution of the resolution σ of the excitation energy peak as a function of the excitation energy. The blue points are from the simulation and the red point from the experiment data. The blue line shows a linear fit performed with the blue points. The red line shows the same function scaled to match the experimental data.

A serie of GEANT4 simulations was performed with the NPTool package [48] to study the evolution

of the resolution as a function of the excitation energy, in comparison with experiment, as shown in Fig. 4.9. The behavior of the resolution can be well described by a linear model, as shown with the blue line in Fig. 4.9. After having applied the aforementioned shift in resolution energy by 71 keV, the function matches the observed resolutions of the ground and 2^+ states, hereby confirming that the excitation energy resolution is well controlled and could be applied to fit the full excitation energy spectrum as follows:

$$\sigma = 564.0 - 0.0019 \cdot E_x \pm 10 \; keV. \tag{4.2}$$

The ±10 keV of variation corresponds to the uncertainty on the measurement of the resolution σ. This technique allows to reduce the number of free parameters in the fit function, as well as the uncertainties on the centroid positions measurements of the peaks. Furthermore, it will ease the validation or the rejection of models (*i.e.* fit functions) to describe the experimental data, as it will be shown in the following.

1.2.2 Fit of the excitation energy and proton energy spectra

Excitation energy and proton energy spectra with outgoing K nuclei

In the last section, the ground state and the first 2^+ excited state of ^{36}Ca have been identified in the excitation energy spectrum, with a condition on a Ca outgoing in the ZDD. In the following, we will study the one-proton decay channel of the proton unbound states in ^{36}Ca :

$$^{37}\mathrm{Ca(p,d)}^{36}\mathrm{Ca}^* \rightarrow ^{35}\mathrm{K} + \mathrm{p} \tag{4.3}$$

using a condition on K outgoing nuclei detected in the ZDD. The left part of Fig. 4.10 shows the excitation energy spectrum reconstructed for the ^{37}Ca$(p,d)^{36}$Ca reaction with a condition on a K outgoing in the ZDD. One can notice that the ground state of ^{36}Ca has totally disappeared in this spectrum. This is expected since the ground state of ^{36}Ca is bound and that gating on a K outgoing is equivalent to gate on the unbound states of ^{36}Ca.

The proton emitted during the one-proton decay of unbound states of ^{36}Ca has been detected in the MUST2 telescopes, in coincidence with the deuteron of the reaction. Its energy in the center-of-mass frame of ^{36}Ca, has been reconstructed as explained in Chap. 3, Section 4. ^{36}Ca decays to ^{35}K which is very weakly bound. Only its ground state is bound with a one-proton separation energy of S_p=83.6(5) keV [53] (see Fig. 4.11). The first $1/2^+$ excited state of ^{35}K is unbound, with an excitation energy of 1553 (5) keV [33]. This means that if a K outgoing is observed in the ZDD, the unbound states populated in ^{36}Ca necessarily decayed to the ground state of ^{35}K by emitting one

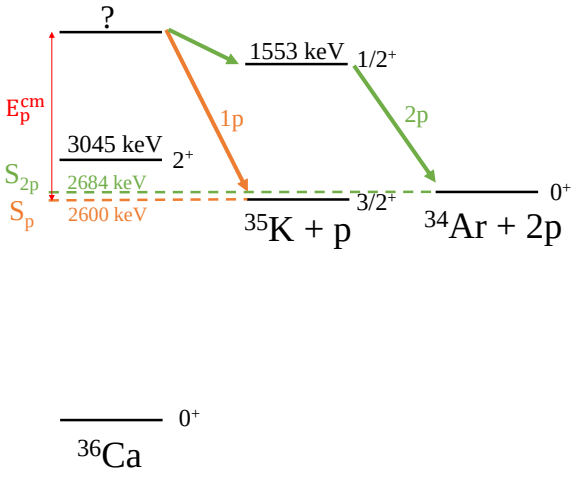

Figure 4.11: Level scheme of the known states in ^{36}Ca relative to ^{35}K and ^{34}Ar.

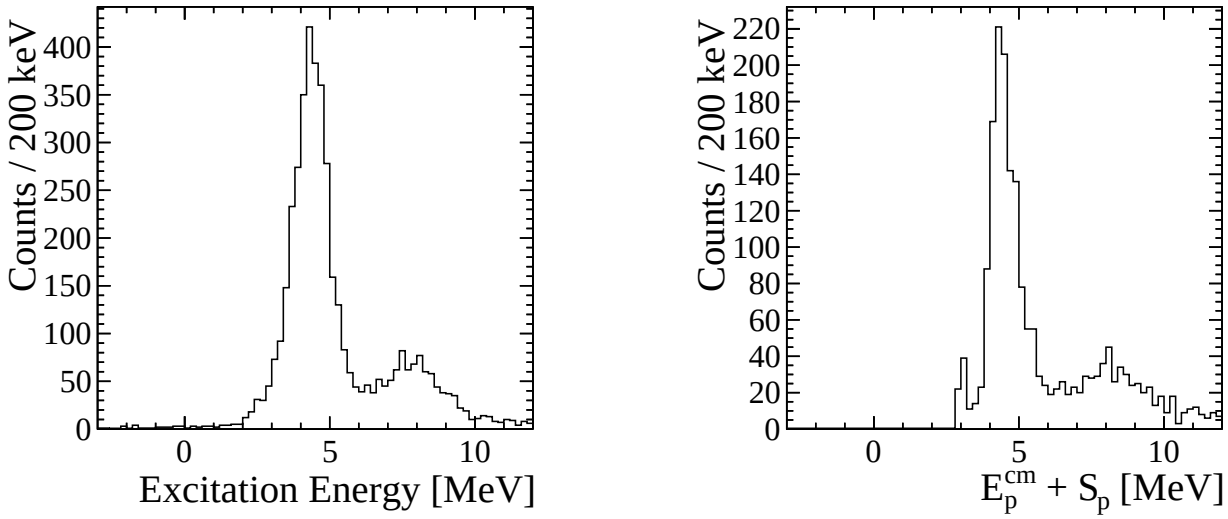

Figure 4.10: Left: Excitation energy spectrum of ^{36}Ca reconstructed from the ^{37}Ca(p,d)^{36}Ca reaction. Right: Proton energy spectrum in the center-of-mass of ^{36}Ca , in which the one-proton energy S_p = 2599.6(61) keV has been added. These plots were obtained with a gate on outgoing K nuclei.

proton. Therefore, the energy E_p^{cm} of this proton in the center-of-mass frame of ^{36}Ca, added to the one-proton separation energy of ^{36}Ca $S_p = 2599.6(61)$ keV, can be directly compared to the excitation energy spectrum of ^{36}Ca. The right part of Fig. 4.10 shows the proton energy spectrum E_p^{cm} added to the one-proton separation energy. One can notice the similarities between this spectrum and the excitation energy spectrum, in the left part of Fig. 4.10, with the same structures observed at the same positions. The difference of statistics between the excitation and the proton energy spectrum arises from the proton detection efficiency. The small peak observed at about 3 MeV in the proton energy spectrum corresponds to the first 2^+ excited state of ^{36}Ca that decays into proton emission. We will come back to the measurement of its exact position latter.

Energy resolution of the proton energy spectrum

The main difference between the excitation energy and the proton energy spectra of Fig. 4.10 resides in the energy resolution. Left part of Fig. 4.12 shows the measured resolution σ of the proton energy peak in the $E_p^{cm} + S_p$ spectrum as a function of the proton energy added to S_p (in yellow). This plot was obtained using the simulation, as explained in the previous section. The data points were fitted using a square-root parameterized function, in addition to a first order polynomial function. This behavior is expected from the typical energy resolution evolution in CsI crystals (see Section 2.3). The resolution in the excitation energy spectrum, obtained with the simulation, (see Fig. 4.9) is shown as well on this figure (in blue) for comparison. The resulting energy resolution is up to 5 times better at low excitation energy, when reconstructed with the protons than with the deuterons: 100 keV at 3 MeV and 475 keV at 8 MeV with the protons and an almost constant value around 475 keV with the deuterons. This difference has multiple origins. First, the reconstruction method is

direct for the proton energy E_p^{cm} (direct measurement of the decaying protons) and indirect for the excitation energy E_x (reconstructed from the energy and angle measurement of the deuterons using the missing mass method, see Chap. 3, Section 4). The dependency of the error on the reconstructed physical observable, to the error on the measurement of the particle energy is stronger in the indirect than in the direct case (e.g. from an equal relative error on the energy measurement of the proton and of the deuteron of 10%, it results a relative error of 64% on the excitation energy E_x and of 32% on the proton energy E_p^{cm}). However, since the reconstruction of the proton energy is direct, the dependency of the intrinsic CsI energy resolution to $\sqrt{E}$ is directly seen in the evolution of the proton energy resolution. Therefore the proton energy resolution increases quickly with the proton energy and matches the excitation energy resolution at 8 MeV. Second, the protons have higher energy in the laboratory frame compared to deuterons. Right part of Fig. 4.12 shows the simulated kinematic lines of the decaying protons compared to the one of the deuterons of the transfer reaction, for a populated state in ^{36}Ca at 3 MeV. One can see that the decaying protons have about two times more energy than the deuterons, implying about two times less energy straggling of the proton inside the target, compared to deuterons. Third, as shown in Fig. 4.12, the kinematics of the protons is more forward focused, as compared to deuterons. The proton energy spectrum is, therefore, constructed with only very few of the CsI crystals (about 4-6 CsI crystals located mainly in the two telescopes which are the closest from the beam). Furthermore, the more the proton has energy, the more its goes at large angle and the more CsI are involved in the reconstruction, which progressively degrades the proton energy resolution.

The experimental resolution for the isolated first 2^+ excited state in the proton energy spectrum is 141(20) keV. As for the excitation energy, a shift of 40 keV (corresponding to the difference between the simulated resolution 101 keV and the experimental resolution 141 keV, at 3 MeV) is applied to the

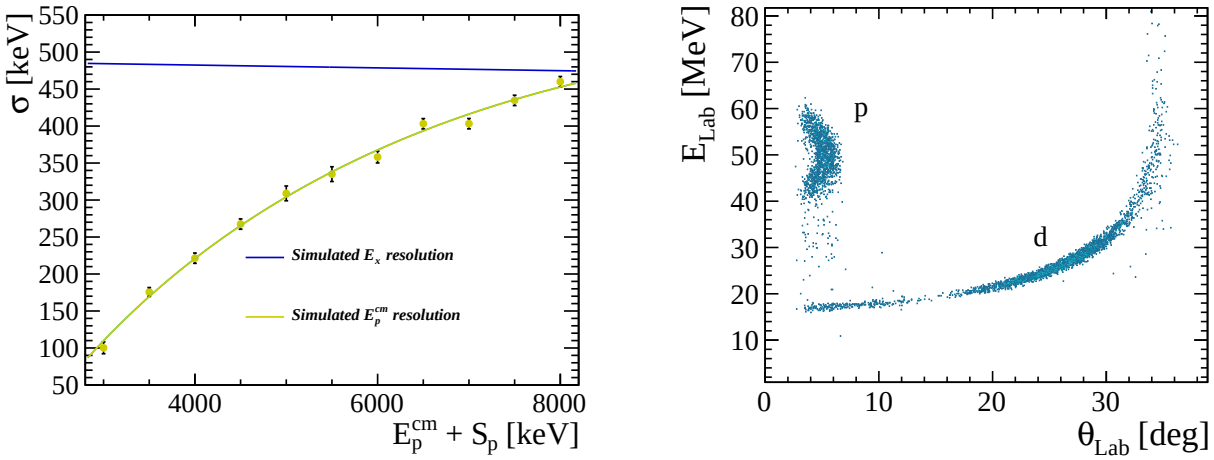

Figure 4.12: Left: Evolution of the resolution σ of the proton energy peak as a function of the proton energy. The yellow points are from the simulation. The yellow line shows a fit performed with square-root parameterized function on the yellow points. The blue line shows the resolution of the excitation energy obtained in Fig. 4.9 for comparison. Right: Simulated kinematic lines of the ^{37}Ca$(p,d)^{36}$Ca$_{3\,\mathrm{MeV}} \rightarrow {}^{35}$K + p reaction populating a state at 3 MeV. The one proton decay of this state has been simulated as well. One can identify the kinematic line of the decaying proton at about 50 MeV energy.

extracted resolution function using the simulation, to describe the experimental data. The obtained function will be used in the following to strongly constrain the resolution of the proton energy peak in the fit of the spectrum using:

$$\sigma_p = -995.9 - 0.12 \cdot E_p^{cm} + 27.6\sqrt{E_p^{cm}} \pm 10 \ keV. \tag{4.4}$$

As a result of the above discussion, the proton energy spectrum will be used in order to extract the excitation energy of the levels populated in ^{36}Ca. The fit of the proton energy spectrum has been performed using multiple Gaussian functions, assuming that the natural width of the states is much smaller than the experimental resolution (the width of the states is of the order of meV, see Section 3 of Chapter 7 for details). All the parameters of the fit are free except the energy resolution. In order to determine the number of contributions to use to describe the data (corresponding to the number of state populated in ^{36}Ca), a fit has been performed with a sum of N, N+1, N+2 ... Gaussian functions. For each assumption, the reduced Chi square, the p-value and the pulls were computed. The validated model is the one that optimized these three parameters.

Fit of the proton energy spectrum

Fig 4.13 shows the fit of the proton energy spectrum performed up to 6 MeV. Three different fits using three different assumptions on the number of contribution to consider are shown. The first hypothesis considers 3 Gaussian functions (left part of Fig. 4.13), leading to a reduced Chi square of 5.3, a p-value of 0.00 and a maximum pull value of 4 sigma. These results allow us to rule out the assumption of 3 peaks only. Indeed, given that the energy resolution of the proton spectrum is accurately determined from simulations, two states are needed between 4 and 5 MeV to achieve a good description of the spectrum. The second test consists in using 4 Gaussian functions, among which two states are used to obtain a better fit in the 4-5 energy region. A reduced Chi square of 2.4, a p-value of 0.05 and a maximum pull value of 1.5 sigma were obtained. All the criteria are fulfilled to accept this hypothesis. The use of a 5 Gaussian functions has also been tested but does not improve the goodness of the fit (with very similar pulls values). The increase of the number of degrees of freedom degrades the reduced Chi square and the p-value (of 8.7 and 0.003, respectively). Therefore, the conclusion of this study is that the second hypothesis, using two Gaussian functions to fit the 4.5 MeV region is the best and adopted one.

Left part of Fig. 4.14 shows the best fit obtained for the proton energy spectrum up to 10 MeV. A sum of 8 Gaussian functions is proposed with constrained resolution. The same procedure (described above) has been applied to determine the number of components needed to fit the 6-10 MeV part of the spectrum. All the statistical tests are fulfilled by this hypothesis (with a reduced Chi square of 1.36, a p-value of 0.16 and a maximum pull value of 1.5 sigma). The results of this fit will be commented later.

Right part of Fig. 4.14 shows the best fit obtained for the excitation energy spectrum up to 10 MeV. For this spectrum, the fit procedure was applied to determine the number of contributions needed between 1 and 6 MeV. In contrast with the proton energy spectrum, both 3 Gaussian and 4 Gaussian models were giving equivalent Chi square and p-value in the 1-6 MeV range. The discrimination

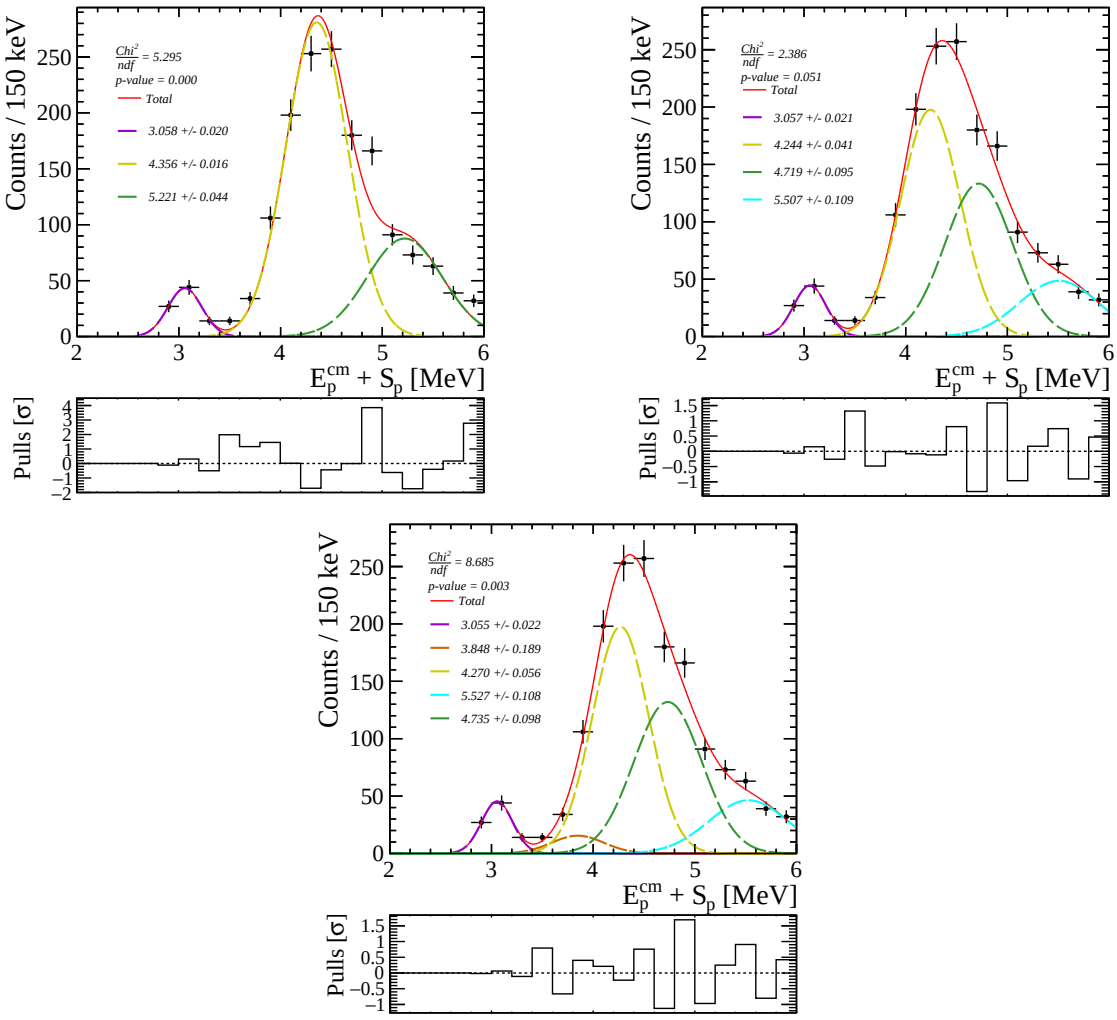

Figure 4.13: Proton energy spectra in the center-of-mass of ^{36}Ca to which the one-proton separation energy has been added. These plots were obtained with a condition on outgoing K isotopes. The red lines show the best fits obtained. The individual components are shown in different colors. The fit was performed using three different models composed of 3 (left), 4 (right) and 5 (bottom) Gaussian functions respectively.

between the two models was possible only with the proton energy spectrum. Therefore, in the fit presented in the right part of Fig. 4.14, the energies of the different contributions were constrained to be compatible with the ones of the proton energy spectrum (thus, no error are indicated in this plot because the computation method of the error matrix is meaningless for constrained parameters [56]). The amplitude of the peak at 5.4 MeV is found to be very different, compared to the proton energy spectrum. This arises from the limited resolution of the excitation energy spectrum. However, due to the very large errors obtained on the amplitudes of the Gaussian functions with the excitation energy spectrum, the relative intensities obtained in both spectra are compatible at 1 σ. Using the 4 Gaussians model, all the statistical tests are again fulfilled (with a reduced Chi square of 0.90, a p-value of 0.67 and a maximum pull value of 2 sigma). This confirms that this model describes well both the proton energy and the excitation energy spectra, obtained with a condition on outgoing K

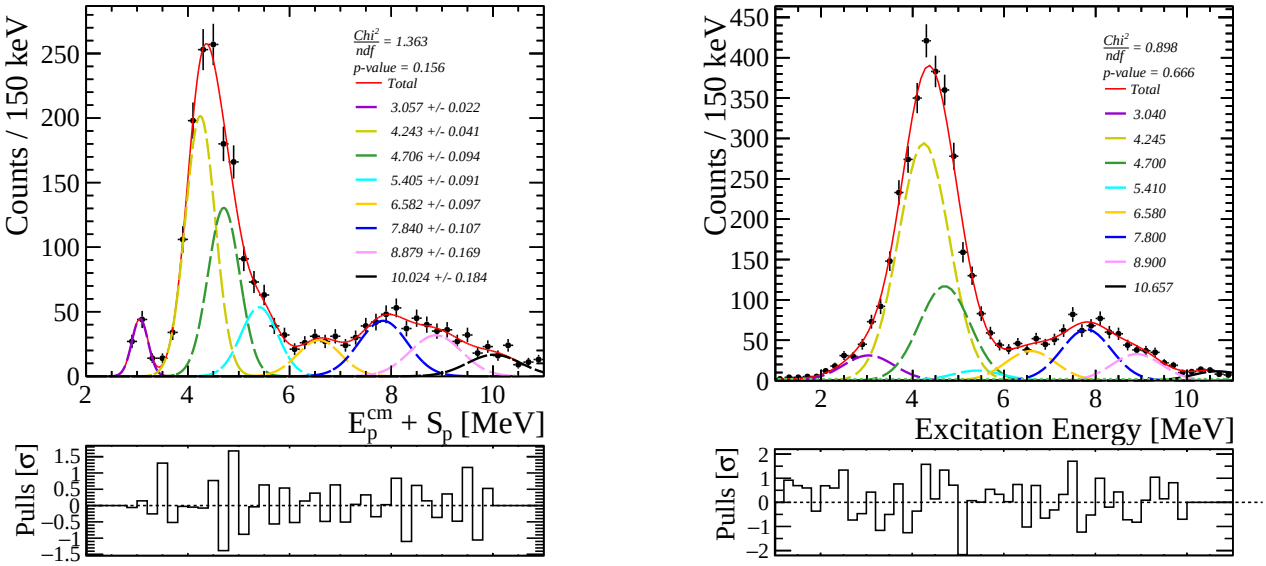

Figure 4.14: The proton center-of-mass energy spectrum, shown in the left part, has been shifted in energy by the S_p value to be compared to the excitation energy spectrum in the right. These plots were obtained with a condition on outgoing K nuclei. The red line shows the best fit obtained. The individual components are shown in different colours.

isotopes.

Fit of the total excitation energy spectrum

In order to better constrain the number of states and their position in the high-energy part (6-

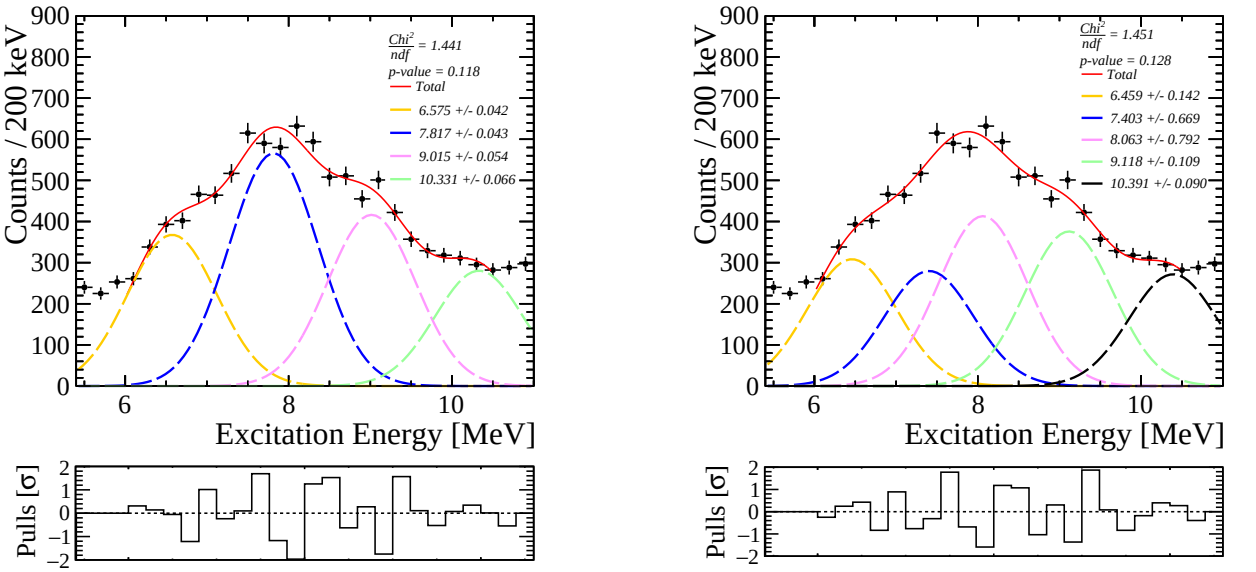

Figure 4.15: Fit of the [6-10.5] MeV range of the total excitation energy spectrum. Two fits using two different assumptions are shown: one composed of 4 Gaussian functions (left) and the other of 5 Gaussian functions (right).

10 MeV), we will study the excitation energy spectrum without any gate on the outgoing heavy ion. Fig. 4.16 shows the excitation energy spectrum of ^{36}Ca obtained without any condition on the outgoing heavy ion. One can see in this spectrum that the 6-10 MeV range has much more statistic compared to Fig. 4.14, due to the contribution of two-proton decay channel, which was not considered up to now. Moreover, to not considering the detection of the outgoing nuclei the ZDD increases the statistics as the overall efficiency of the ZDD is estimated to be about 40%. However, the background becomes non-negligible (see between -5 and -2 MeV in Fig. 4.16) and has to be considered in the fit procedure. The background function determined in Section 1.1.2 is used.

Since, the total excitation energy spectrum benefits from much more statistics in the [6-10.5] MeV range, compared to Fig. 4.14, it will be used to a more complete study of this energy range. Fig. 4.15 shows two different fits of the [6-10.5] MeV range using two different assumptions considering 4 and 5 contributions, respectively. In the first one, only one Gaussian is used to fit the 8 MeV peak, while, in the second one, two states are used to fit this peak. The two fits have very equivalent reduced Chi square (1.44 ad 1.45), p-value (0.12 and 0.13) and pulls values. It is, therefore, not possible to conclude about which model is correct and about the number of contribution to use to fit this spectrum.

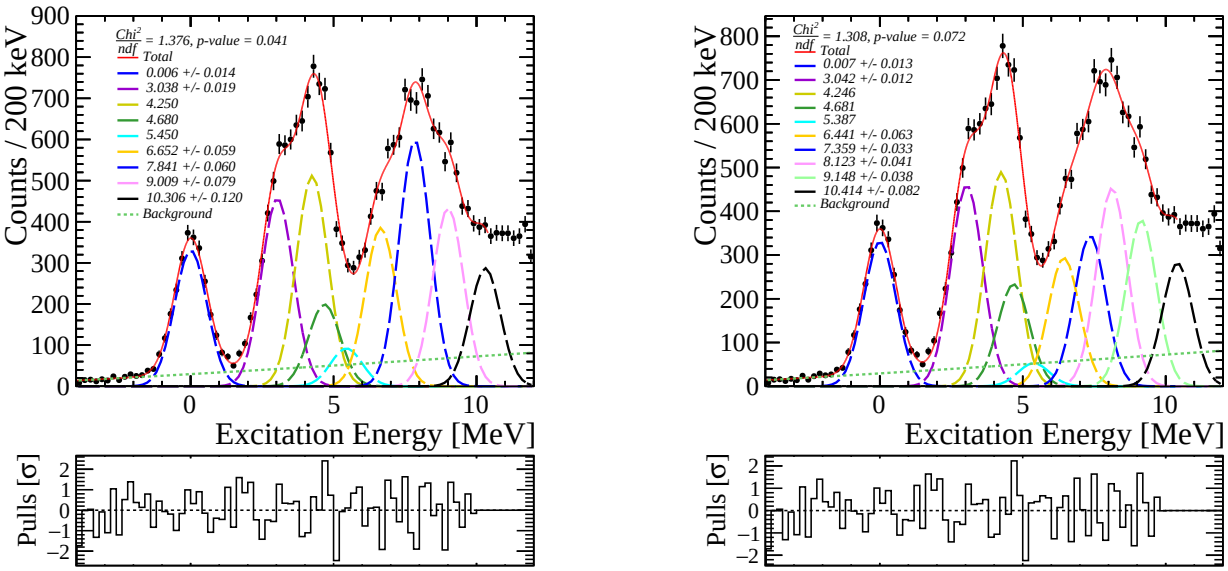

Figure 4.16: Excitation energy spectrum of ^{36}Ca . These plots were obtained without any condition on the outgoing nucleus. Two models were used to fit the spectrum: one composed of 9 Gaussian functions in addition to the background function (left) and the other composed of 10 Gaussian functions in addition to the background function (left). The red line shows the best fit obtained. The individual components are shown in colored line.

Two fits of the total excitation energy spectrum have been performed using the two different hypothesis and are shown in Fig. 4.16. The first model is composed of 9 Gaussians plus a background function (with 4 Gaussians to fit the [6-10.5] MeV range). The second model is composed of 10 Gaussians plus a background function (with the 5 Gaussians to fit the [6-10.5] MeV range). The sigma of the Gaussian functions has been strongly constrained using Eq. 4.2. A scaling factor has been applied to the background function (established in Section 1.1.2) in order to well describe the data between -5 and -2 MeV. The centroids of the peaks were derived in the 4-5.5 MeV region using the

information deduced from the proton center-of-mass energy spectrum. All the other centroids and all the amplitudes were left as free parameters. Since we cannot conclude about which hypothesis is correct, we will consider a centroid value of 6.54(14) MeV, for the orange peak, accepting measurements of the energy performed with both hypothesis, within the uncertainty, at one sigma confidence level. For the higher excited state, it is not possible to conclude about the positions of the excited states.

1.2.3 New states in ^{36}Ca populated through the ^{37}Ca(p,d)^{36}Ca reaction

The previous section allowed us to determine the energy of the new levels in ^{36}Ca from the study of the ^{37}Ca(p,d)^{36}Ca reaction, which are shown in the right part of Fig. 4.17. Their energies are compared to those of the analogue states in the mirror nucleus ^{36}S, populated in the mirror reaction ^{37}Cl(d,^{3}He)^{36}S [57]. The ^{37}Cl(d,^{3}He)^{36}S transfer reaction of Ref. [57] has been performed in direct kinematic using a 28.9 MeV deuteron beam. This corresponds to an equivalent momentum matching compared to our case with $\Delta L = 0.90$ in Ref. [57] and $\Delta L = 1.17$ in our case, at 0 MeV of excitation energy. Thus, the resulting level scheme should be similar at low excitation energy, between the two mirror reactions, assuming that the isospin symmetry is respected.

- The first 2^+ excited state:

The first 2^+ excited state of ^{36}Ca has been identified in the excitation energy spectrum with a condition on outgoing Ca and K isotopes, as well as with the proton energy spectrum. Its measured energy was found to be of 3.059(16) MeV in the Ca-gated spectrum, and of 3.057(22) MeV in the proton energy spectrum with outgoing K condition. The two measurements are compatible and in agreement with the value of 3.045(2.4) MeV from Ref. [36]. As the 2^+ state is unbound with respect to one and two proton emissions, a certain fraction of its decay occurs to the ground state of ^{35}K, allowing us to identify it both in the Ca-gated and in the K-gated spectrum. The measurement of its proton branching ratio is of astrophysical interest and will be detailed in Part. II. The left part of Fig. 4.17 shows the correlation between the center-of-mass angle θ_{cm} of the deuteron and the excitation energy of ^{36}Ca, in the lower panel. In the upper panel, the projection on the X axis, corresponding to the excitation energy is shown (together with the fit already shown in Fig. 4.16). One can identify, in the 2D plot, a clear change in the θ_{cm} distribution between the ground state and the first 2^+ state. The accumulation of counts at small angles ($\theta_{cm} < 7°$), seen between 1.5 and 5.5 MeV is typical for an L = 0 transfer, arising from the removal of a $s_{1/2}$ neutron in ^{37}Ca (see bottom part of Fig. 4.17). The particle-hole configuration $\nu(s_{1/2})^{-1}\nu(d_{3/2})^{1}$, obtained from the removal of a $s_{1/2}$ neutron in ^{37}Ca generates states of spin parity $J^\pi = 1^+$ and $J^\pi = 2^+$, in line with the $J^\pi = 2^+$ spin assignment of this state. A detailed analysis of the angular distributions will be presented in the next section.

- The 4.24 MeV state:

A new state has been observed in ^{36}Ca. From the fit of the proton energy spectrum, its excitation energy is found to be of 4.24(4) MeV. This state is observed in the same L=0 region in the θ_{cm} distribution that indicates the possibility of a $J^\pi = 1^+$ or 2^+ spin parity assignment. This assumption is confirmed by the fact that one $J^\pi = 1^+$ and two 2^+ states are populated in the same energy range in the mirror nucleus ^{36}S by means of the mirror reaction ^{37}Cl(d,^{3}He)^{36}S [57]. The isobaric analogue 1^+_1 state was measured at $E_x(1^+) = 4523.0(6)$ keV. Therefore, we tentatively assign a spin-parity of

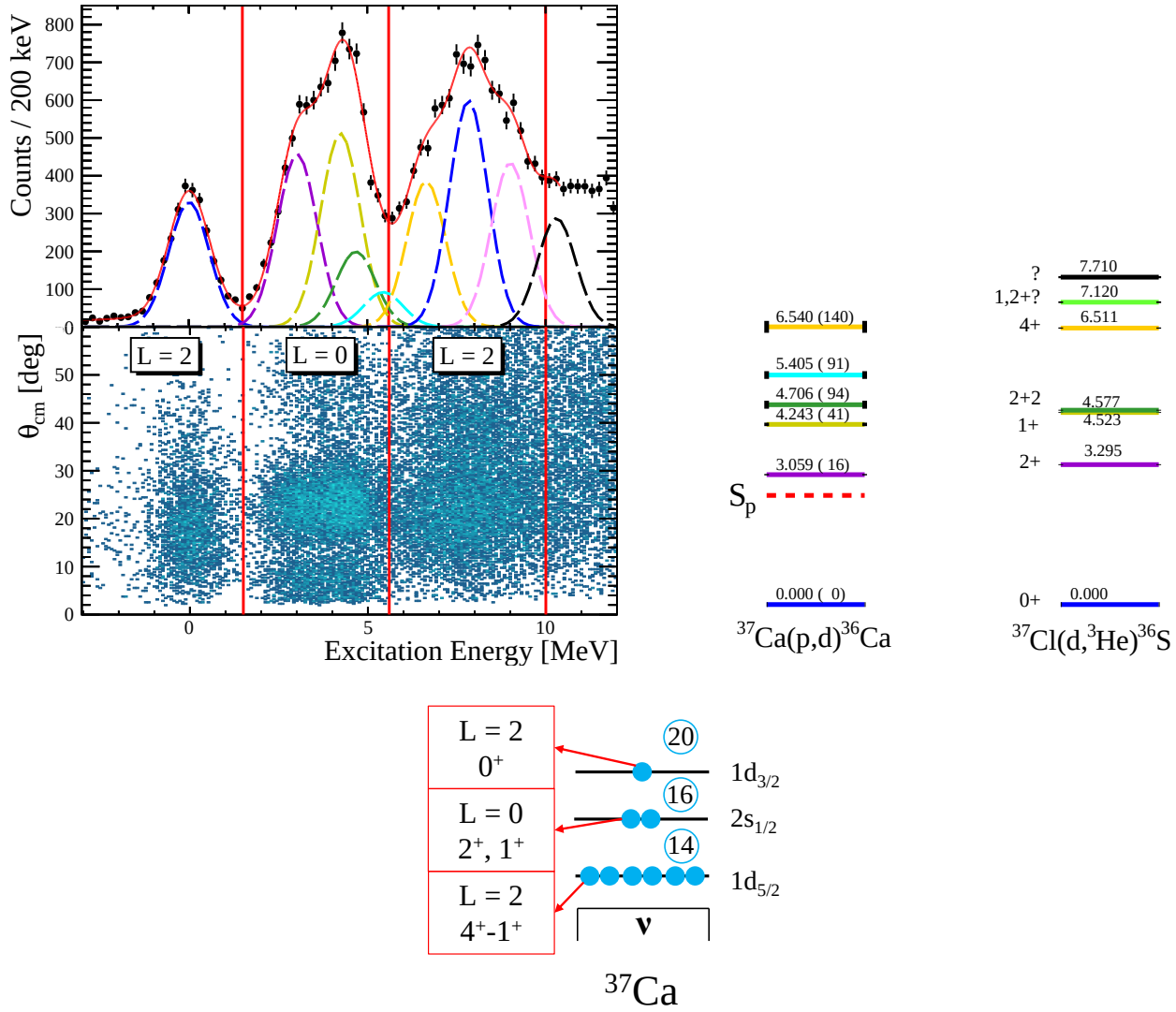

Figure 4.17: Left: Correlation between the angle θ_{cm} of the deuteron in the center-of-mass frame of the reaction and the excitation energy of ^{36}Ca . The upper pannel shows the projection on the excitation energy axis together with its fit (see Fig. 4.16). Red vertical lines highlight the changes of regimes in the θ_{cm} distributions. Right: Level scheme of ^{36}Ca obtained from the fits presented in the last section, compared to that of ^{36}S, obtained using the mirror reaction ^{37}Cl(d,^{3}He)^{36}S [57]. Bottom: Schematic neutron shell structure view of ^{37}Ca. The nature of the transfer and the produced states, corresponding to the orbital from which the neutron is removed, are shown in the red boxes.

1^+ for the excited state of ^{36}Ca at 4.243(40) MeV.

- The 4.71 MeV state:

Besides the 1^+ state at 4.24 MeV discussed above, a new excited state has been identified at E_x = 4.706(94) MeV in ^{36}Ca , using the proton energy spectrum. Again this state is observed in the L=0 region. In the mirror reaction, a 2_2^+ is populated at $E_x = 4.557$ MeV, with a relative intensity compared to the 1^+ state, equivalent to the one observed in ^{36}Ca . Therefore we tentatively assign a spin-parity of 2_2^+ to this state.

• The 5.40 MeV state:

At the border of the L=0 region, a last state has been identified at $E_x = 5.40(9)$ MeV (measured with the proton spectra and confirmed by the excitation energy spectrum). No states have been identified at this energy in ^{36}S, using the mirror reaction. This is probably due to the presence of a contaminant at the expected position of this peak (see Fig. 1 of Ref. [57]). The tentative of spin assignment for this state will therefore be discussed, with the help of angular distribution in the next section.

• The 6.54 MeV state:

At higher excitation energy, one state has been identified at $E_x = 6.54(14)$ MeV, in the proton energy spectrum and in the excitation energy spectrum. The shape of the θ_{cm} distribution between 5.5 and 10 MeV is typical for an L=2, arising from the removal of a $d_{5/2}$ neutron in ^{37}Ca. In this energy range, a high density of states is expected since the $d_{3/2} \times d_{5/2}$ excited configuration populated from this removal, generate states of spin parity from 1^+ to 4^+. A 4^+ excited state has been identified in the mirror nucleus at 6.511 MeV, using the mirror reaction. Therefore, we tentatively assign a spin-parity of 4^+ to the $E_x = 6.54(14)$ MeV state identified in ^{36}Ca .

• The [7-10] MeV range:

In the [7-10] MeV energy range, the experimental resolution of both proton energy and excitation energy peaks are of about 550 keV. It is, therefore, very difficult to conclude about the number of states needed to fit the spectra and on the exact position in excitation energy of the states. Nevertheless, it is expected that all these states arise from a $\nu(d_{5/2})^{-1}\nu(d_{3/2})^1$ configuration and the measurement of the summed $d_{5/2}$ spectroscopic factor of those state will provide the centroid of the $d_{5/2}$ strength, allowing the indirect study of the $d_{3/2} - d_{5/2}$ spin-orbit splitting in ^{36}Ca .

1.2.4 Differential cross sections and DWBA analysis

The number of counts as a function of the θ_{cm} angle $N(\theta_{cm})$ have been extracted by fitting the total excitation energy spectrum up to 10 MeV (see Fig. 4.16) for slices of θ_{cm} angle. No condition was applied on the outgoing heavy ion in order to get rid of the ZDD efficiency, which decreases the statistics. The fit has been performed with a sum of 9 Gaussian functions for which the centroids have been fixed to the energies determined in the last section. The resolutions have been fixed also, letting only the amplitudes as free parameters. Then, the differential cross sections $\frac{d\sigma}{d\Omega}$ have been determined by normalizing the number of counts extracted for each θ_{cm} slice $N(\theta_{cm})$, by the efficiencies and solid angle for the charged particle detection, the beam intensity and the target density (see Chap. 3 Section 4 for details). Fig. 4.18 shows the differential cross sections corresponding to the 8 states considered in the fit. The error of the data points are a quadratic sum of several errors: the systematic error on $N(\theta_{cm})$ (estimated from the propagation of the error of fitted parameters, mainly due to the statistical errors), the error on the beam intensity (evaluated to be 5%), the error on the target density (evaluated to be 10% with the simulation) and the error on the solid angle calculation.

In order to determine the transferred angular momentum L to light particle and the spectroscopic factors of each states, the differential cross sections have been analyzed using the Distorded Wave Born Approximation (DWBA) model. The details of the DWBA formalism can be found in Appendix A. The optical potential parameters used in the DWBA analysis are the primary ingredients of the

calculation which describes the interaction between the different particles. Different optical potential prescriptions have been tested in order to get the best description of the experimental data. The final prescriptions used for the DWBA analysis of the ^{37}Ca(p,d)^{36}Ca reaction are:

- Entrance potential describing the p + ^{37}Ca channel: Menet *et al.* global proton optical potential [58].
- Exit potential describing the d + ^{36}Ca channel: finite range adiabatic potential following the Jonhson-Tandy prescription [59] and using the Becchetti and Greenlees global optical potentials [60] for the proton and the neutron.
- The bound state wave function of the neutron in ^{37}Ca has been computed using a Wood-Saxon potential using a radius $r_0 = 1.27$ fm, a diffusivity $a_0 = 0.67$ fm and a spin-orbit potential $V_{SO} = 6$ MeV (following the prescriptions of Ref. [14]). The depth of the potential well has been adjusted to reproduce the binding energy of the orbital from which the neutron was removed.
- The bound state wave function of the neutron in the deuteron has been computed using a classical Reid soft-core potential [61]. The $\langle p|d\rangle$ vertex has been treated in finite range.

The colored lines in Fig. 4.18 show the DWBA calculations performed with the code TWOFNR [62]. Calculations have also been performed with the FRESCO code [63] to check the consistency of the results. All the calculations have been performed considering a spectroscopic factor $C^2S = 1$. Then the spectroscopic factors have been extracted by normalizing the theoretical calculations to the experimental data between $\theta_{cm} = 0°$ and 30° (since at higher angles, other channels are expected to contribute to the cross section). The obtained spectroscopic factors for each state in ^{36}Ca are given in Fig. 4.18 and summarized in Table 4.2. The influence of the choice of optical potential on the measured spectroscopic factors has been studied. It has been found that for each choice of potential, several potentials were able to fit equivalently the data (with very comparable χ^2 and p-value), but the resulting spectroscopic factor could vary up to 20% (This variation is dominated by the choice of the outgoing potential, *e.g.* both Becchetti and Greenlees potential and Chapel-Hill 89 potential in the exit channel reproduce well the experimental data with equal Chi square but the resulting spectroscopic factor for the ground state is of 1.06 and 0.87, respectively). Therefore, an additional uncertainty of 20% is considered on the spectroscopic factors, arising from the choice of the optical potentials used in the calculation. The spectroscopic factors of the analog states in ^{36}S obtained in Ref. [57] are given without uncertainties. However, the dependency of the extracted spectroscopic factor to the optical potential being the same than in our case, an uncertainty of 20% is considered on the spectroscopic factors from Ref. [57] as well (this value might be a bit under-estimated since other studies found an uncertainty of 30% for the ^{3}He potential). The error associated to the spectroscopic factors in Fig. 4.18 is the total uncertainty being the quadratic sum of the optical potential error and the fit error. In Table 4.2 these errors are given separately between parenthesis and bracket, respectively.

The ground state differential cross section is very well reproduced by the DWBA calculation, considering that the neutron has been removed from the $d_{3/2}$ orbital in ^{37}Ca. This is compatible with a $J^\pi = 0^+$ spin assignment. The spectroscopic factor $C^2S(0^+) = 1.06(22)$, is the value expected for the

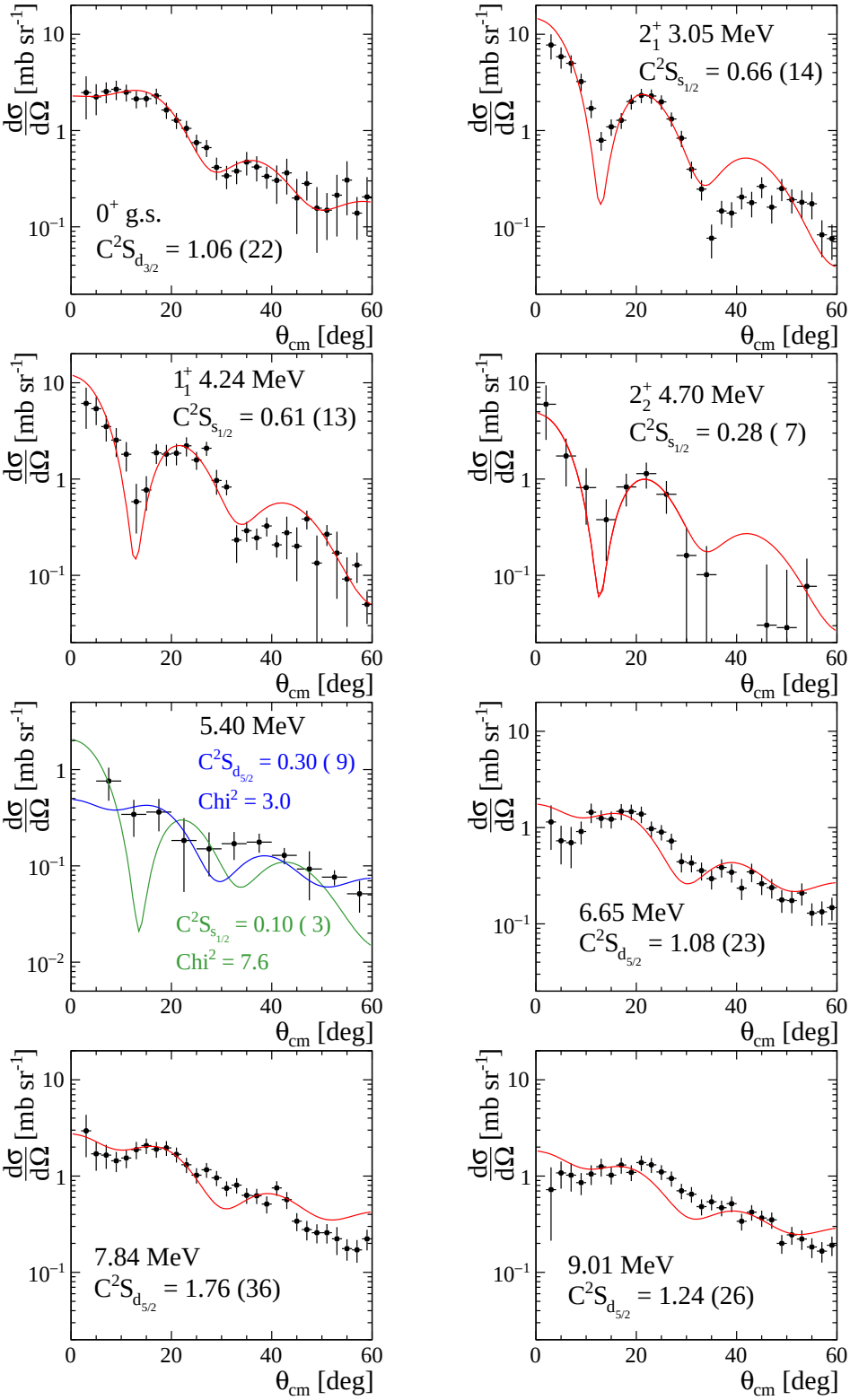

Figure 4.18: Differential cross sections of the states identified in ^{36}Ca (see Fig. 4.17). Red lines shows the DWBA calculations performed. For the 5.40 MeV state, the two blue and green lines show the calculations performed for the $d_{5/2}$ and the $s_{1/2}$ orbitals, respectively. For each calculation, the resulting spectroscopic factor is also given with its total uncertainty.

Table 4.2: Summary of the results obtained from the DWBA analysis of the differential cross sections. The results are compared to the ones of Ref. [57] obtained in the mirror nucleus, using the mirror reaction ^{37}Cl(d,^{3}He)^{36}S. For each spectroscopic factor the 20% error associated to the model is given inside the parenthesis () and the error associated to the fit is given between the bracket [].

^{37}Ca(p,d)^{36}Ca (this work)				^{37}Cl(d,^{3}He)^{36}S [57]			
E_x [MeV]	J^π	nlj	C^2S	E_x [MeV]	J^π	nlj	C^2S
0.00	0^+	$d_{3/2}$	1.06(21)[7]	0.00	0^+	$d_{3/2}$	1.06(21)
3.05	2^+	$s_{1/2}$	0.66(13)[4]	3.30	2^+	$s_{1/2}$	0.86(17)
4.24	1^+	$s_{1/2}$	0.61(12)[4]	4.52	1^+	$s_{1/2}$	0.75(15)
4.71	2_2^+	$s_{1/2}$	0.28(6)[4]	4.57	2_2^+	$s_{1/2}$	0.25(5)
5.41	$(1\text{-}4)^+$	$d_{5/2}$	0.30(6)[7]				
6.54	4^+	$d_{5/2}$	1.08(22)[7]	6.51	4^+	$d_{5/2}$	0.19(4)
7.84	$(1\text{-}4)^+$	$d_{5/2}$	1.76(35)[6]	7.12	$(1\text{-}4)^+$	$d_{5/2}$	0.44(9)
9.01	$(1\text{-}4)^+$	$d_{5/2}$	1.24(25)[8]	7.71	$(1\text{-}4)^+$	$d_{5/2}$	

total $d_{3/2}$ strength, without any quenching. The C^2S of the ground state of ^{36}Ca is equal to the one of ^{36}S found in Ref. [57].

Three L=0 distributions have been identified corresponding to the levels at 3.05, 4.24 and 4.71 MeV. The DWBA calculation has been performed considering that the neutron has been removed from the $s_{1/2}$ orbital in ^{37}Ca. These states have, therefore, a particle-hole excited configuration with one neutron on both the $d_{3/2}$ and the $s_{1/2}$ orbitals. This configuration generates states of spin parity $J^\pi = 2^+, 1^+$, as explained in the previous section. Furthermore, the feeding of the states of spin parity 1^+ and 2^+ is roughly expected to respect the rule $\frac{\Sigma C^2 S_{s_{1/2}}(2^+)}{\Sigma C^2 S_{s_{1/2}}(1^+)} = \frac{5}{3} = 1.666$, that is obtained from the degeneracy of their magnetic sub-states. With the proposed 1^+ and 2_2^+ spin assignements of the states at 4.24 and 4.71 MeV, and the extracted C^2S for 2^+, 1^+ and 2_2^+ , one finds $\frac{\Sigma C^2 S_{s_{1/2}}(2^+)}{\Sigma C^2 S_{s_{1/2}}(1^+)} = 1.54(48)$, in good agreement with the expected value. This reinforced the proposed spin assignements. These three states have a summed C^2S of 1.55(34), compared with the sum rule limit of 2 (representing the total $s_{1/2}$ strength, without quenching). The values of each states are very equivalents, within the uncertainties, to the ones obtained in the mirror nucleus, using the mirror reaction ^{37}Cl(d,^{3}He)^{36}S [57].

Four excited states have been identified with L=2 angular distributions. The state at 5.41 MeV lies in the middle of the L=0 and L=2 regions (see Fig. 4.17). Therefore, in Fig. 4.18, two calcultations are shown, one considering the removal of a $s_{1/2}$ neutron (L=0, in green) and one, a $d_{5/2}$ neutron (L=2, in blue). The experimental differential cross section is best described with an L=2 removal calculation, with a χ^2 two times better than with an L=0 one. This confirms the L=2 nature of this state. For the three other states, the $d_{5/2}$ orbital provides the best description of the experimental data as well. The states present in this energy range are, therefore, probably $d_{5/2}$ hole states with spin parity of $J^\pi = (1-4)^+$. The four L=2 contributions have a summed C^2S value of 4.38(88), compared with the sum rule limit of 6 (representing the total $d_{5/2}$ strength, without quenching). The individual values are very different from those of the mirror nucleus ^{36}S found in Ref. [57], where only a small fraction of the $d_{5/2}$ strength has been identified. The authors of Ref. [57] interpreted that "the $d_{5/2}$ strength is fragmented into many levels which were not detected". However, there is no obvious reason to have

a different fragmentation of the $d_{5/2}$ strength between the two mirror nuclei. Since the majority of the $d_{5/2}$ strength has been identified in this work at energies under 9 MeV, the reason why it has not been identified in Ref. [57] is still not understood.

1.2.5 Two-proton decay

In this section, we will focus on the study of the two-proton decay channel of ^{36}Ca. The left part of Fig. 4.19 shows the excitation energy spectrum of ^{36}Ca, obtained with a condition on a Ar outgoing in the ZDD and on multiplicity 3 in MUST2 (one deuteron and 2 protons, as explained in Section 2.3). The two-proton separation energy in ^{36}Ca is located at $S_{2p} = 2.683(6)$ MeV (shown in green on the figure). However, one can see in the Ar gated excitation energy spectrum that the two proton decay starts only at 5 MeV, meaning that the one-proton decay channel is favored for the states located between 2.7 and 5 MeV (which is shown by the K-gated excitation energy spectrum in blue). Indeed, the $J^\pi = 1^+$ and 2^+_2 states identified in the previous sections, can decay either to the $3/2^+$ ground state of ^{35}K with an angular momentum $l = 0$ (the proton and the ground state of ^{35}K being couple to spin value 1 or 2) or to its $1/2^+$ first excited state with an angular momentum $l = 2$. The probability of transmition through the centrifugal barrier favors the emission of $l = 0$ protons and therefore, the one proton decay channel for these states. The three-proton decay channel has also been investigated using a condition on outgoing Cl isotopes. It has been found that this channel starts to contribute at $E_x > 15$ MeV. No clear structure has been identified in the excitation energy or proton energy spectrum in this channel.

The right part of Fig. 4.19 shows the relative protons energy $\frac{E^{cm}_{p_i}}{E^{cm}_{p_1}+E^{cm}_{p_2}}$ (where p_1 and p_2 are the two decaying protons), as a function of the excitation energy. It is expected for a direct two-proton decay of ^{36}Ca , that the two protons are emitted with the exact same energy, within the present energy resolution of the system, giving a relative proton energy of 50%. However, a sequential decay leading to equivalent proton energies is possible too, and could generate small accumulation of counts at 50%. In the right part of Fig. 4.19, no clear enhancement is seen at 50% of relative energy which indicates that most of the two-proton decays occur in the sequential channel, passing through an intermediate resonance in ^{35}K. The more the excitation energy increases, the more channels are open, including higher excited states of ^{34}Ar. It is therefore very difficult to conclude about the decay patterns of high-energy states.

Two clear red spots can be identified in this figure at excitation energy of about 8 MeV and a proton relative energy of about 70% and 30%. The sequential decay of the state at 7.84 MeV in ^{36}Ca through a resonance at 1.55 MeV in ^{35}K to the ground state of ^{34}Ar, leads to protons with energies of 3.61 and 1.47 MeV. The corresponding relative energy of 70% and 30%, is in very good agreement with the observed value. This observation reinforced the hypothesis of the presence of the 7.84 MeV state in ^{36}Ca . The few counts observed in right part of Fig. 4.19 at about $E_x = 5.4$ MeV and 50% relative energy may correspond to the decay of the 5.4 MeV through the 1.55 MeV intermediate state in 35K, leading to two protons at almost equal energies (within the present energy resolution) of 1.25 and 1.47 MeV.

Another method to study the two-proton decay mechanism, is to look at the angular correlations

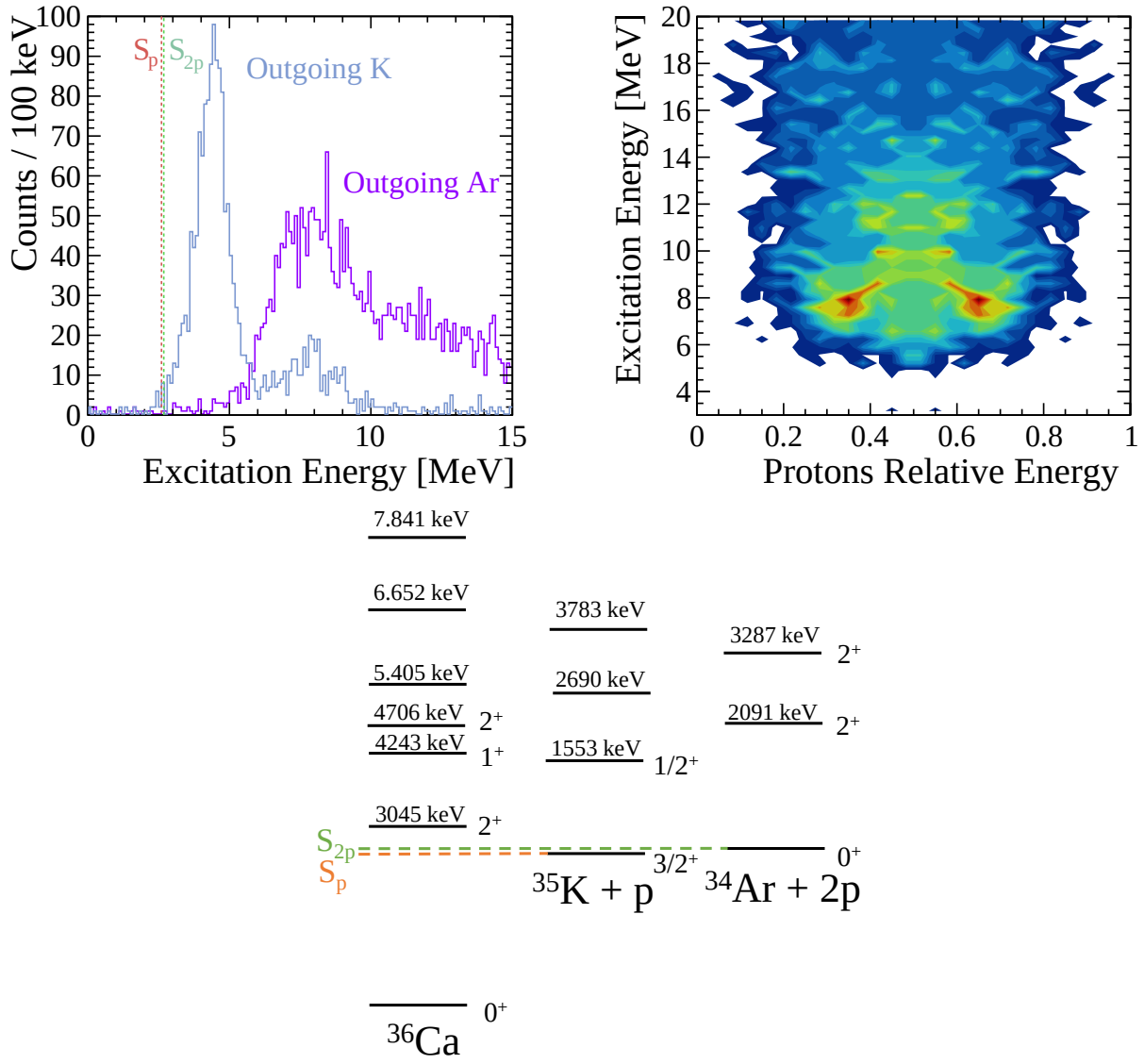

Figure 4.19: Left: Excitation energy spectrum of ^{36}Ca , obtained with a condition on outgoing Ar nuclei (in purple) and K nuclei (in blue). The one-proton and two-proton separation energies are shown by the orange and green line, respectively. Right: evolution of the protons relative energy as a function of the excitation energy. Bottom: Level scheme of ^{36}Ca , ^{35}K and ^{34}Ar. The levels of ^{36}Ca are the ones deduced from our study (see Fig. 4.17). The three first excited of ^{35}K are from Ref. [33, 64]. Other states may have not been identified as 6 excited states have been observed in this range of energy for the mirror nucleus ^{35}S. The two first excited states of ^{34}Ar are shown as well.

between the two protons and the fragment. We define here two angles θ_{pp} and $\theta_{f/pp}$ as:

$$\begin{cases} \theta_{pp} = \frac{\vec{p_1}\cdot\vec{p_2}}{\|\vec{p_1}\|\|\vec{p_2}\|} \\ \theta_{f/pp} = \frac{(\vec{p_1}-\vec{p_2})\cdot\vec{p_f}}{\|\vec{p_1}-\vec{p_2}\|\|\vec{p_f}\|} \end{cases} \tag{4.5}$$

where $\overrightarrow{p_1}$ and $\overrightarrow{p_2}$ represent the impulsions of the two protons in the center-of-mass frame of decaying nucleus and $\overrightarrow{p_f}$ is the impulsion of the residual outgoing nuclei. θ_{pp} represents the angle between the two protons and $\theta_{f/pp}$ the angle between the fragment and the relative momentum of the two protons. Since there are two ways to label the two protons, the angles are computed for the two possibilities. These plots are very powerful tool to characterize the type of decay. Indeed, a direct two-proton decay is characterized by $cos(\theta_{pp})$ distribution peaked at small angles and a rather flat $cos(\theta_{f/pp})$ distribution. Conversely, a sequential two proton decay is characterized by a flat $cos(\theta_{pp})$ distribution and by crescent-shaped bands on the $cos(\theta_{f/pp})$ distribution (which position and shape depend on the energy of intermediate resonance) [65].

Fig. 4.20 shows the two dimensional angular plots of $cos(\theta_{f/pp})$ as a function of $cos(\theta_{pp})$ obtained from data and simulations for the 7.8 MeV and the 5.4 MeV states discussed above. The top left plot

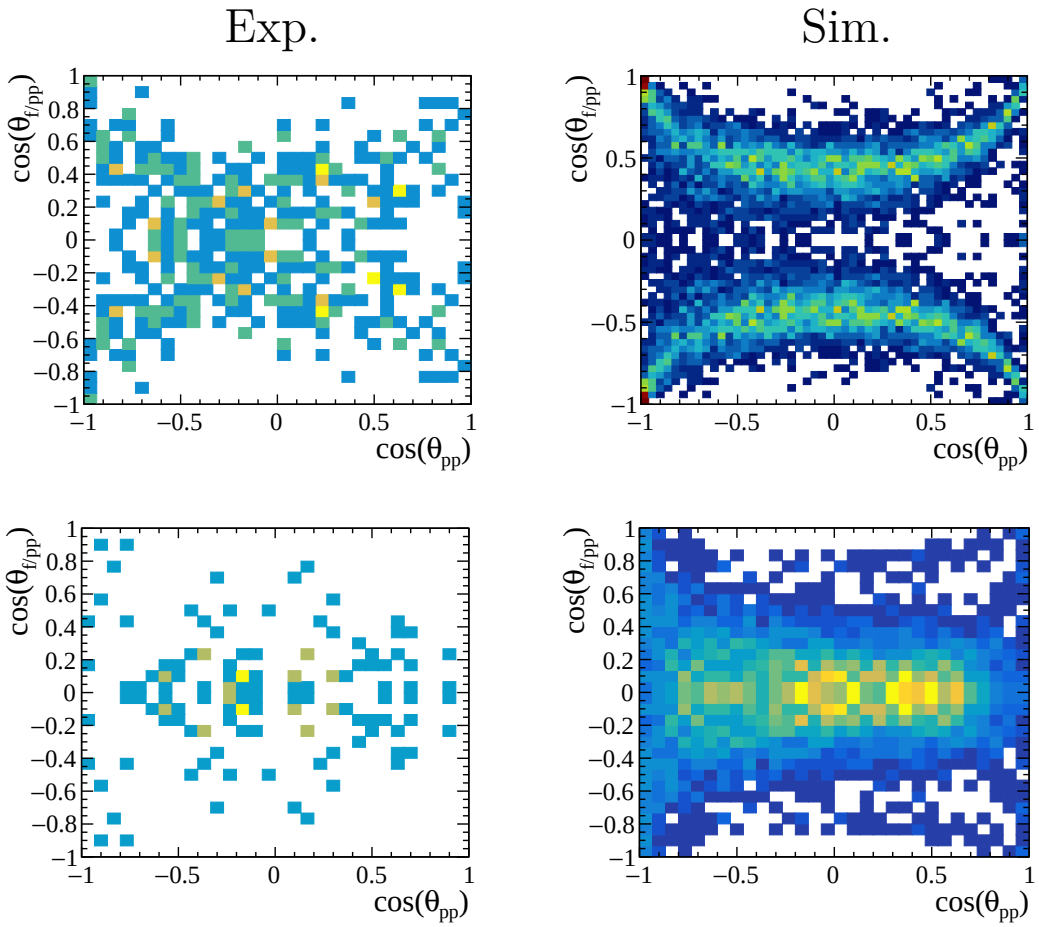

Figure 4.20: Two dimensional plots of $cos(\theta_{f/pp})$ as a function of $cos(\theta_{pp})$. The top plots are obtained for a gate on the excitation energy 7.3<E_x<8.3 MeV while the bottom ones are obtained for 4.9<E_x<5.9 MeV. Left are experimental data and right are simulation. The top right plot is obtained from a simulation of a sequential decay of a 7.84 MeV state in ^{36}Ca passing through a intermediate resonance at 1.55 MeV in ^{35}K, as described in the text. The bottom right plot is obtained from a simulation of a sequential decay of a 5.40 MeV state in ^{36}Ca passing through a intermediate resonance at 1.55 MeV in ^{35}K.

is from the experimental data for the 7.8 MeV. The presence of two bands in $cos(\theta_{f/pp})$ and the low amount of counts at small θ_{pp} angles ($cos(\theta_{pp}) = 1$) are typical from a sequential decay. A simulation has been performed considering the sequential decay of the 7.84 MeV resonance in ^{36}Ca, passing through the 1.55 MeV resonance in ^{35}K. One can clearly identify the two crescent-shaped bands in the simulated plot, in good agreement with experimental one, which confirms the sequential character of the two-proton decay of this state. The $cos(\theta_{f/pp}) = 0$ region is more filled in the experimental plot. This could indicate another decay branch to an intermediate resonance in ^{35}K (probably the 2.69 MeV state) leading to equivalent proton energies. The fact that a two-proton decay branch passing through the $J^\pi = \frac{1}{2}^+$ resonance at 1.55 MeV in ^{35}K is identified indicates a spin $J^\pi = 1^+$ for this state, since it is the only possibility allowing the emission of a $l = 0$ proton from a neutron $d_{5/2}$ hole configuration.

The same analysis is done for the 5.4 MeV state. Once again, even if the relative proton energy of 50% could account for a direct decay, the few counts at small θ_{pp} angles and the presence of a band in $cos(\theta_{f/pp})$ rule out the possibility of a direct two proton decay. Furthermore, the general shape of the experimental plot is well reproduced by a simulation performed considering the sequential decay of a 5.4 MeV state in ^{36}Ca, passing through the intermediate resonance at 1.55 MeV in ^{35}K. The angular correlations have been investigated for other excitation energies, especially in the 10 MeV region. Unfortunately the obtained experimental angular plots were very flat (but still with no count observed in the ($cos(\theta_{pp})$,$cos(\theta_{f/pp})$)=(0,-1) and (0,1) region, which is characteristic from the crescent-shaped bands of the sequential decay channel), probably due to the large number of open channels at high-energy. Therefore, no conclusion could be made on other excited states.

From the results presented in this section, we can conclude that no direct two proton decay is observed from the high-energy excited states of ^{36}Ca . For the 5.4 MeV and 7.8 MeV states in ^{36}Ca, a two-proton decay branch has been identified in the sequential channel by passing through a intermediate resonance at 1.55 MeV in ^{35}K. At higher excitation energy, the number of open channels increases, including more possible final states in ^{34}Ar. It is therefore very difficult to conclude about the decay patterns.

1.3 Summary

In this section, the results obtained on the ^{37}Ca(p,d)^{36}Ca transfer reaction have been presented. The ^{36}Ca atomic mass was measured and matches very well with previous values. Three groups of states, corresponding to the neutron removal reaction from the $d_{3/2}$, $s_{1/2}$ and $d_{5/2}$ orbitals, have been identified in ^{36}Ca ranked by increasing binding energy or by increasing excitation energy in ^{36}Ca .

The ground state of ^{36}Ca has been identified. Its differential cross section has been extracted confirming its L=2 nature, arising from the removal of the $d_{3/2}$ neutron in ^{37}Ca. A spectroscopic factor of 1.06(22) was found for this state.

Three L=0 excited states have been identified at $E_x = 3.06(2)$ MeV, $E_x = 4.24(4)$ MeV and $E_x = 4.71(9)$ MeV. Their L=0 nature has been demonstrated by the DWBA analysis of the differential cross sections, arising from the removal of a $s_{1/2}$ neutron in ^{37}Ca. This indicates a particle-hole configuration $\nu(s_{1/2})^{-1}\nu(d_{3/2})^1$ for these states. The first one corresponds to the already known 2^+ first excited state of ^{36}Ca and was found at an excitation energy compatible with the literature. The other ones

are observed for the first time in ^{36}Ca . From the comparison to the mirror nucleus ^{36}S, $J^\pi = 1^+$ and $J^\pi = 2^+_2$ spin assignments have been proposed, respectively. The majority of the $s_{1/2}$ strength has been identified with a summed spectroscopic factors for these three sates equal to $\sum C^2S(s_{1/2}) = 1.55(34)$. This value as well as the individual values of their spectroscopic factors are equivalent to what was found for the analogue in the mirror nucleus.

At higher excitation energy, four L=2 states, with $d_{5/2}$ hole configuration, have been identified. The fit performed on the excitation energy spectrum allowed us to determine the energy of the two first ones at $E_x = 5.41(9)$ and 6.54(14) MeV with proposed spin parity $J^\pi = (1-4)^+$. Due to the limited energy resolution in both proton and excitation energy spectrum at this energy, it was not possible to give a precise energy of higher excited state. A large fraction of the $d_{5/2}$ strength has been identified with a $\sum C^2S(d_{5/2}) = 4.38(88)$ up to 9 MeV.

The one-proton and two-proton decay of the excited states populated in ^{36}Ca has been investigated. The one-proton decay channel is found to be dominant up to 5 MeV. The two-proton decay channels start to contribute at $E_x > 5$ MeV and is compatible with a sequential two-proton decay. In particular, a branch of the two-proton decay of a 7.84 MeV state in ^{36}Ca has been identified by passing through a $J^\pi = \frac{1}{2}^+$ intermediate resonance in ^{35}K, which reinforced the hypothesis of a L=2 state at 7.84 MeV in ^{36}Ca .

2 Two neutron transfer: ^{38}Ca(p,t)^{36}Ca

This section presents the results obtained on ^{36}Ca, using the ^{38}Ca(p,t)^{36}Ca reaction. First, the conditions applied to reconstruct the excitation energy spectrum will be presented. Then, the analysis of the benchmark reaction ^{36}Ar(p,t)^{34}Ar will be performed. Finally, the fit of the excitation energy spectrum and the analysis of the differential cross sections will be presented.

2.1 Extraction of the excitation energy and benchmark reaction

2.1.1 Kinematic lines and excitation energy

In order to obtain the excitation energy spectrum of ^{36}Ca using the ^{38}Ca(p,t)^{36}Ca reaction, the following conditions were applied during the analysis:

- ^{38}Ca as incident beam particle: using the CATS1-HF and the CATS2-HF time-of-flight (see Fig. 4.1)
- Beam inside the target cell: using the reconstruction of the beam in the target plane performed by CATS ((see Fig. 4.1))
- Triton in MUST2 (in addition to one or two protons, depending on the multiplicity of the event, as explained in Section 1.1.1)
- Either Ca, K or Ar outgoing in the ZDD

Fig. 4.21 shows the kinematic lines and the excitation energy spectrum obtained by applying these conditions. These plots were obtained for a Ca outgoing in the ZDD. The kinematic line

corresponding to the ground state of ^{36}Ca is well identified at its expected position (shown by the blue line). The ground state peak is as well identified in the excitation energy spectrum at about 0 MeV. An accumulation of counts is seen around the theoretical kinematic line corresponding to an excited state located at about 3 MeV in ^{36}Ca (shown by the purple line in the left part of Fig. 4.21). A peak is as well found at about 3 MeV in the excitation energy spectrum.

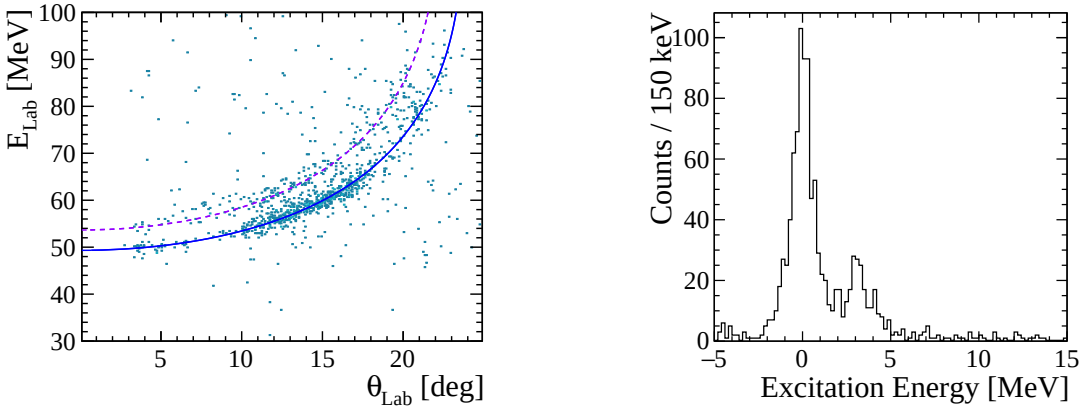

Figure 4.21: Left: Kinematic plot of the ^{38}Ca(p,t)^{36}Ca transfer reaction. This plot was obtained for Ca in the ZDD. The blue line shows theoretical calculation of the kinematic line for the ground state and the purple line for an excited state located at 3 MeV. Right: The corresponding excitation energy spectrum of ^{36}Ca .

One can see that a small amount of background is present in the excitation energy spectrum. Indeed, very few counts are observed below -2 MeV and higher than 5 MeV where no state are expected to be populated (since the one-proton threshold of ^{36}Ca is located at 2.6 MeV). Furthermore, due to the reduction of the cross section, compared to the ^{37}Ca(p,d)^{36}Ca reaction, the excitation energy spectrum has less statistics compared to what we saw in the last section. Therefore, before exploiting this spectrum, a detailed study of the background will be presented. Then, to first validate the analysis of the (p,t) reaction channel, the analysis of the ^{36}Ar(p,t)^{34}Ar will be performed.

2.1.2 Background evaluation

It is first interesting to note how the identification of the outgoing heavy nuclei in the ZDD allows to reduce the amount of background, when analyzing the (p,t) channel. Fig. 4.22 shows the excitation energy spectrum obtained with and without the ZDD. One can see that the use of the ZDD allows to improve significantly the signal to noise ratio (going from $\frac{S}{N} = 5.3$, without the ZDD, to $\frac{S}{N} = 34.1$, with the ZDD, for the ground state of ^{36}Ca).

As for the ^{37}Ca(p,d)^{36}Ca reaction, the contribution of the window foil of the target can be studied using the data taken with the empty target. Left part of Fig. 4.23 shows the excitation energy spectrum obtained from the empty target runs. The analysis has been performed for the ^{38}Ca(p,t)^{36}Ca reaction. No gate is applied on the outgoing nuclei in order to not lose statistics due to the ZDD efficiency. The contribution of the window foils to the excitation energy spectrum can be described by a Gaussian function, as shown in Fig. 4.23. The intensity of the background varies between -40 MeV to 30 MeV,

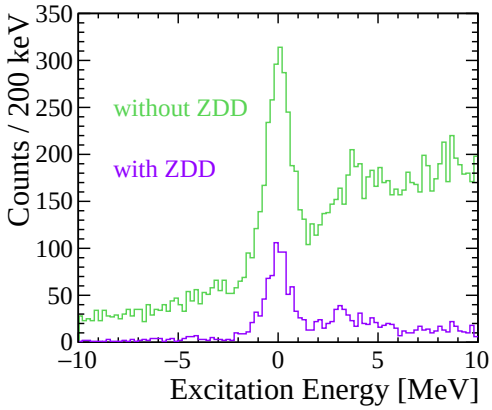

Figure 4.22: Two excitation energy spectra are superimposed. The green line correspond to the excitation energy spectrum of ^{36}Ca obtained with the ^{38}Ca(p,t)^{36}Ca reaction without using the ZDD. The purple line is the same spectrum but using the ZDD (with a condition on a Ca, K of Ar outgoing).

but in the energy range of interest (-2 MeV to 6 MeV) the background behavior is rather flat. Therefore, the background will be modeled by a simple constant function in the fit of the ^{36}Ca excitation energy spectrum. Right part of Fig. 4.23 shows the angular distribution $N(\theta_{c.m.})$ of the tritons in the center-of-mass of the reaction, obtained with the empty target runs. The angular distribution displays a maximum at about 25°. Its shape can be described by a Landau function. This parametrization will be used in the following, in order to compare the background angular distribution to the one of interest.

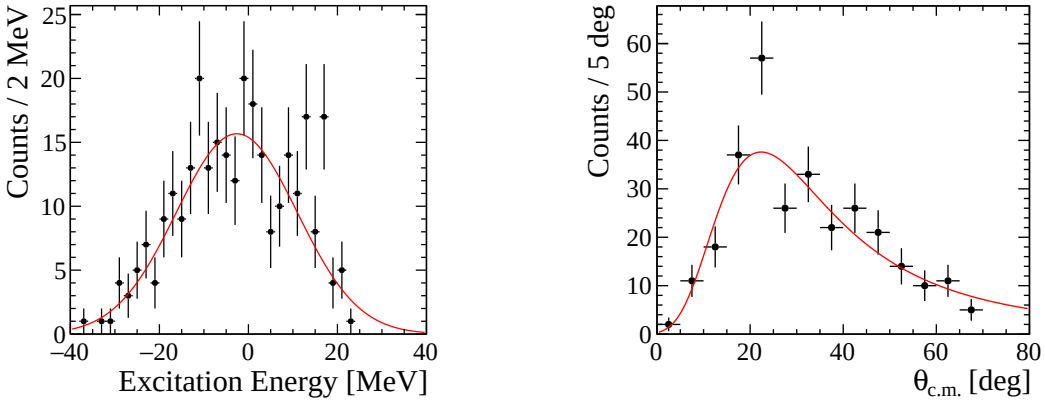

Figure 4.23: Left: Excitation energy spectrum obtained from the empty target runs, analyzed using the same procedure and cuts as for the ^{38}Ca(p,t)^{36}Ca reaction. Right: $\theta_{c.m.}$ angular distribution of the tritons obtained from the empty target runs, analyzed as the ^{38}Ca(p,t)^{36}Ca reaction.

In order to reject this background event by event, many observables have been investigated to disentangle the signal and the background events. First, from the right part of Fig. 4.23, one can see that, by selecting small $\theta_{c.m.}$ angles ($\theta_{c.m.}$<20°), one can reject 80% of the background events. On the other hand, this selection also reduces the signal events (*e.g* $\theta_{c.m.}$<20° rejects 65% of the events corresponding to the population of the ground state of ^{36}Ca). As it has been shown in Section 1.1.2, an

other way to disentangle the background from the signal is to look at the angular correlation between the light particles (triton) and the heavy outgoing nuclei. Left part of Fig. 4.24 shows the correlation between the light particle angle θ_{light} and the heavy outgoing nucleus angle θ_{heavy}. The green points in the left part of Fig. 4.24 shows the angular correlation obtained for background events (selected using $E_x < -3$ MeV). For the background events, the outgoing heavy ion is always seen at small angle, meaning that the beam particle has not been deflected. Therefore, in order to reject the background events, a graphical cut is applied on the angular correlation matrix and is shown by the red line in Fig. 4.24. The right part of Fig. 4.24 shows the excitation energy spectrum obtained with and without the cut on the angular correlation matrix. One can see that with the cut, the background between -10 and -2 MeV almost completely disappeared while the signal stay almost unchanged. In the following, this condition will be used to reject the background from the excitation energy spectrum.

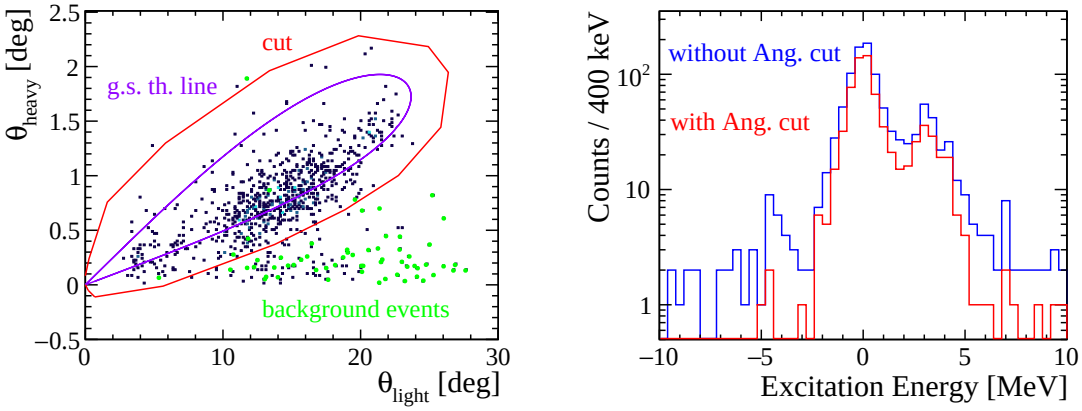

Figure 4.24: Left: Correlation between the light particle angle θ_{light} and the heavy outgoing nuclei angle θ_{heavy}. The purple line shows the theoretical prediction of the angular correlation for the ^{38}Ca$(p,t)^{36}$Ca$_{g.s.}$ reaction. Green points correspond to the background events (obtained with a condition on $E_x < -3$ MeV). The red line shows the 2D cut applied to reject the background events. Right: Excitation energy spectrum obtained with (red) and without (blue) the cut on the angular correlation.

Even if the angular correlation cut has been adjusted to keep all the good events, it is difficult to use it to extract the angular distributions since it could bias the reconstruction of the differential cross sections by inducing changes in the reconstruction efficiency. Instead, one can use the background function determined in the right part of Fig. 4.23 to study the impact of the background events on the angular distributions. The right part of Fig. 4.25 shows the angular distribution of the ground state of ^{36}Ca (obtained with a gate on the excitation energy $-1.5 < E_x < 1.5$) together with the background Landau function (see Fig. 4.23 right). A scaling factor has been applied to normalize the background function to the acquisition time and the beam intensity that differs between the empty target runs and the filled target runs. The left part of Fig. 4.25 shows the background angular distribution obtained with a condition on $-2 < E_x < 5$ MeV. One can see that the Landau function still describes well the data in the energy range of interest. By integrating the background function, we find a signal-to-noise ratio of $\frac{S}{N} = 41.6$, equivalent to the one found in the excitation energy spectrum. When extracting the angular distributions, the impact of the background on the shape of the angular distributions has been investigated by subtracting the background function from the data. It has been found that the

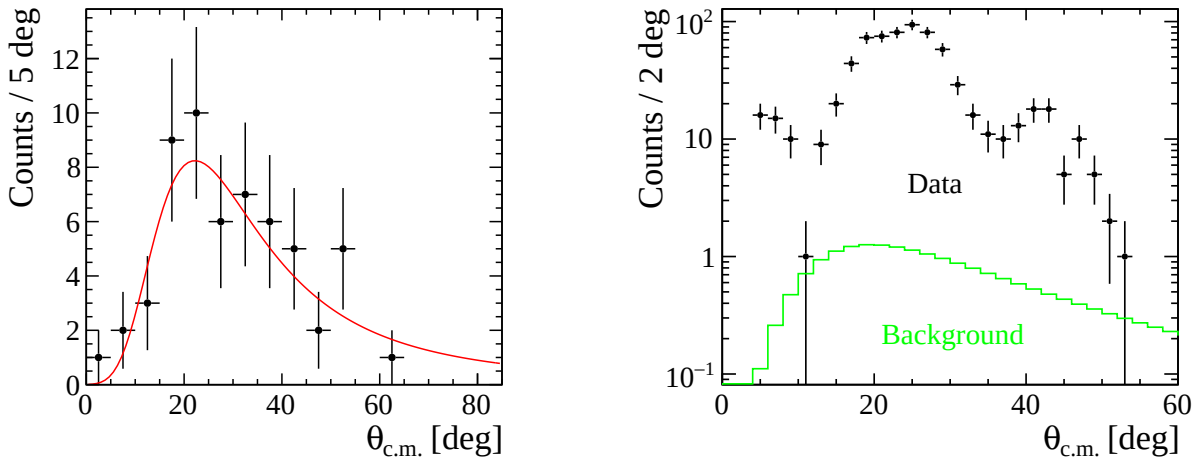

Figure 4.25: Left: $\theta_{c.m.}$ angular distribution of the tritons obtained from the empty target runs with a condition on $-2 < E_x < 5$ MeV. This condition is used to verify that the shape of the background angular distribution does not change in the energy range of interest. The red line shows a fit performed with a Landau function. Right: Angular distribution of the ground state of ^{36}Ca (in black, obtained with a gate on the excitation energy $-1.5 < E_x < 1.5$ MeV) together with the background function which has been normalized to the acquisition time (in green).

background has a negligible impact on the angular distributions.

2.1.3 Benchmark reaction: ^{36}Ar(p,t)^{34}Ar

In order to first validate the analysis of the (p,t) reaction channel and to benchmark the theoretical calculation of the two nucleon transfer differential cross sections, the analysis of the ^{36}Ar(p,t)^{34}Ar reaction has been performed, without considering the already existing results. This reaction has been already studied in direct kinematics [66], at a close beam energy (with a ^{36}Ar radioactive beam at 46.3 MeV/nucleon in this work and a 39.9 MeV proton beam in Ref. [66]).

Fig. 4.26 shows the excitation energy spectrum of ^{34}Ar reconstructed with the ^{36}Ar(p,t)^{34}Ar reaction, obtained with a condition on Ar outgoing. The angular correlation cut, presented in the last section, was used to reject the background. Still, a constant function is used to fit the few background events that survived to the cut. To fit this spectrum, the same procedure as for the ^{37}Ca(p,d)^{36}Ca reaction was used. The sigma of the Gaussian functions has been strongly constrained using the results of the simulation and the width of the ground state peak. Only the centroids and the amplitudes were left as free parameters. Different N-Gaussian functions were tested to fit the spectrum and were validated if they fulfilled the criterias presented in Section 1.2.1.

Fig. 4.26 shows the two fit functions (composed of 5 and 6 Gaussian functions, respectively, plus a background function) that provided the best results (with equivalent reduced χ^2 and p-value of about 0.70 and 0.87). Both measured the position of the ground state at 26(32) keV, compatible with zero. The first excited state is found at 2.11(10) MeV with the first model (5 Gaussians) and at 2.05(12) MeV with the second model (6 Gaussians). Since it is impossible to conclude which model is the best, we consider a mean value of 2.08(15) MeV, accepting both measurements at one sigma

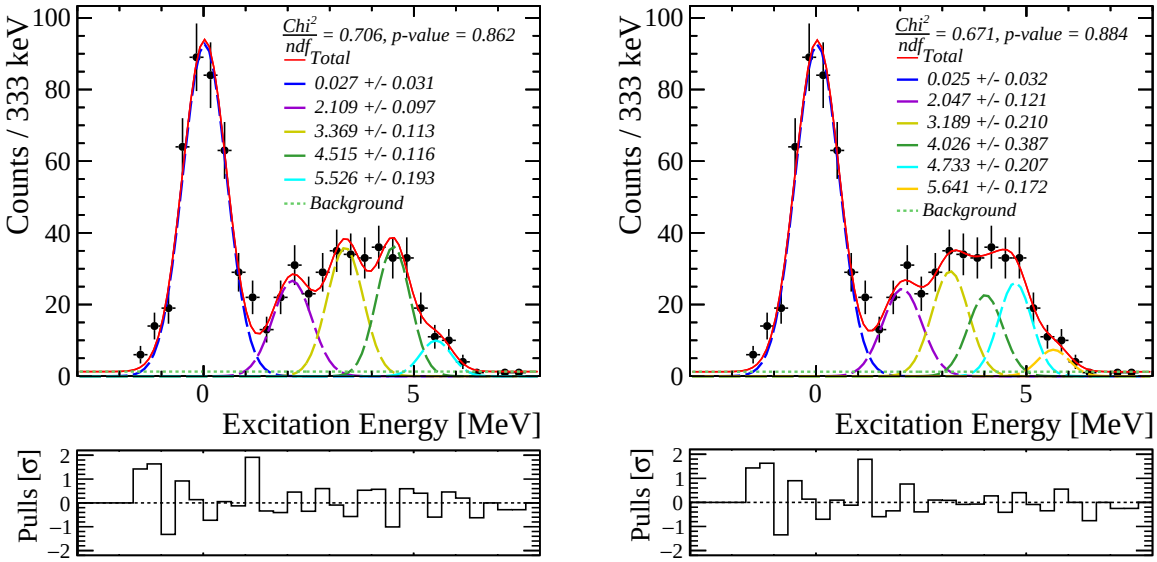

Figure 4.26: Excitation energy spectrum of ^{34}Ar reconstructed with the ^{36}Ar(p,t)^{34}Ar reaction. This plots were obtained with a condition on a Ar outgoing in the ZDD. Two fits using two different models are shown: one composed of 5 Gaussian functions in addition to the background function (left) and the other composed of 6 Gaussian functions in addition to the background function (left). The red line shows the best fit obtained. The individual components are shown in colored line.

confidence level. The next excited state identified is measured at 3.37(12) MeV with the first model and at 3.19(21) MeV with the second model. Again we will consider for this state a mean value of 3.24(26) MeV, accepting both measurements at one sigma. Both fit use a Gaussian to fit the tail at 5.57(23) MeV. In the [4-5] MeV energy range, the two fits differ. The first one uses one Gaussian at 4.51(12) MeV to reproduce the [4-5] MeV energy range while the second uses two at 4.03(39) MeV and 4.73(21) MeV. One cannot conclude about which description is correct from their χ^2 and p-values, therefore no conclusion is made about the position of the excited states in this energy range.

The angular distributions have been extracted by fitting the ^{34}Ar excitation spectrum, using the 5 Gaussian model, for each slice of θ_{cm} angle as presented for the ^{37}Ca(p,d)^{36}Ca reaction. Fig. 4.27 shows the differential cross sections obtained for the ground state and the two first excited states identified in ^{34}Ar. The differential cross sections have been analyzed using a DWBA model. The details of the DWBA formalism can be found in Appendix A. In the calculations, both single step (direct transfer) and in two steps (sequential transfer) have been considered (a more detailed study of those contributions will be presented in the next section). Different global optical potentials have been tested for the tritons. It has been found that the potential of Li *et al.* [67] provides the best description of the data (leading to the best χ^2 values when fitting the data with the results of the DWBA calculation). All the other prescriptions used are the ones used for the DWBA analysis of the (p,d) channel (see Section 1.2.4). All the calculations presented in the following have been performed using the FRESCO code [63]. The input files for the FRESCO calculations have been generated using the code FR2IN [68].

The experimental cross section for the ground state of ^{34}Ar shows a clear L=0 behavior, which supports a $J^\pi = 0^+$ spin-parity assignment for this state. The only way to obtain a L=0 distribution

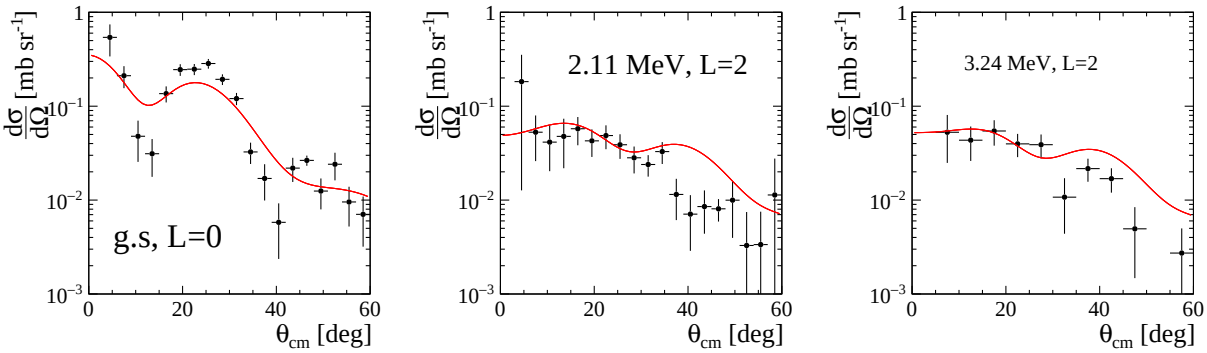

Figure 4.27: Differential cross sections of the ground state and the two first excited states identified in ^{34}Ar (see Fig. 4.26). Red lines shows the DWBA calculations which provide the best description of the experimental data, for each state.

is to couple two nucleons having the same orbital angular momentum. Since the study of ^{34}Ar was not of special interest, except to validate the analysis, no Shell-Model (SM) calculations have been performed for this nucleus. Therefore, the DWBA calculations have been performed without using any information about the structure of the states and all the two-nucleon amplitudes have been taken equal to one. The structure of the ground state of ^{34}Ar is expected to be rather well described by the single particle picture, with the neutrons filling all the orbitals up to the $2s_{1/2}$ orbital. Therefore, the calculation has been performed considering that the two neutrons are removed from the $d_{3/2}$ orbital in ^{36}Ar, without considering contributions from other orbitals. The two-nucleon amplitude for this channel is taken equal to one. The red curve in the left part of Fig. 4.27 shows this calculation. One can see that the general behavior of the cross section is well reproduced even if the calculation underestimate the amplitude of the oscillations. The amplitude of the cross section is well reproduced by this simple calculation indicating that the approximation of the $d_{3/2}$ orbital as the unique contributing channel describes already well the data. This reinforced the hypothesis made on the structure of the state. The $L = 0$ shape of the experimental cross section and the DWBA analysis supports a $J^\pi = 0^+$ spin-parity assignment for this state.

The experimental cross section of the first excited state identified in ^{34}Ar shows a rather flat behavior up to $\theta_{cm} = 20°$ which is typical from L=2 transfer. To reproduce this L=2 behavior, calculation has been performed considering the removal of one neutron from the $d_{3/2}$ orbital in ^{36}Ar and one from the $s_{1/2}$ orbital. Again, since no SM calculation has been performed for this nucleus, one considers a two-nucleon amplitude equals to one for this contribution. The result of the calculation, shown in the middle part of Fig. 4.27, reproduces very well the experimental cross section up to $\theta_{cm} = 35°$. This support a $J^\pi = 2^+$ spin-parity assignment for this state with particle-hole $d_{3/2} - s_{1/2}$ configuration. The same calculation has been performed to describe the differential cross section at 3.2 MeV. Again the general behavior and the amplitude is well reproduced by the calculation, supporting a $J^\pi = 2^+$ spin-parity assignment for this state.

Since the fit of the excitation energy spectrum did not allow us to conclude about the number of states populated between 3.7 and 5 MeV, the differential cross section of the whole energy range was extracted and is shown in Fig. 4.28. Different calculations have been performed to describe the

experimental distribution. One L=0 calculation has been performed considering that the two neutrons are removed from the $s_{1/2}$ orbital in ^{36}Ar (shown by the blue line in Fig. 4.28). One L=2 calculation has been performed considering the removal of one neutron from the $d_{3/2}$ orbital in ^{36}Ar and one from the $s_{1/2}$ orbital (shown by the green line in Fig. 4.28). In order to determine which calculation describes the best the data, the experimental distribution has been fitted using the theoretical results (the only free parameter being a scaling factor applied to the theoretical distribution). The L=0 distribution provides a better description of the data compared to the L=2 distribution (with a χ^2 and a p-value of 4.2 and 0.65 for L=0 and of 8.0 and 0.24 for L=2). This indicates the presence of a $J^\pi = 0_2^+$ state between 3.7 and 5 MeV. To get some indication about the structure of this 0^+ state, one should perform SM calculation in order to get its Two Nucleon Amplitudes (TNA). Then the amplitude of the full theoretical calculation could be compared to the data. In Ref. [66], many states have been populated in this energy range but we are not able to disentangle them, given our experimental resolution. The resulting differential cross section is therefore a sum of L=0 and L=2 contributions. In order to perform a complete analysis of this differential cross section, the sum of all possible contributions, supported by SM calculation, has to be considered in the theoretical calculations.

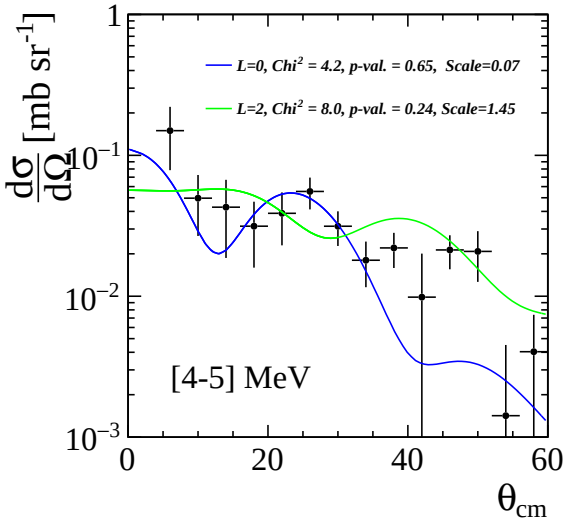

Figure 4.28: Differential cross sections of the [3.7,5] MeV energy range. It has been extracted by fitting the excitation energy spectrum using the 5 Gaussian model. The position of the Gaussian fitting this energy range (green contribution in Fig. 4.26) has been left free within the energy range considered. Red lines shows the DWBA calculations which provide the best description of the experimental data, for each state.

Table 4.3 summarizes the results obtained from the fit of the excitation energy spectrum and from the DWBA analysis of the differential cross sections. The results are compared to the ones of Ref. [66]. One can see that our conclusions for the ground state and the two first exitated states are in good agreement with the ones of Ref. [66]. In the work of Ref. [66], 6 states were observed in the 3.7-5 MeV energy region together with a 0_2^+ state has been identified unambiguously at 3.879 MeV. Due to the limited resolution in the excitation energy spectrum, it was not possible in this work

Table 4.3: Summary of the results obtained from the excitation energy spectrum and the DWBA analysis of the differential cross sections. The results are compared to the one of Ref. [66].

^{36}Ar(p,t)^{34}Ar (this work)			^{36}Ar(p,t)^{34}Ar [66]		
E_x [MeV]	J^π	L	E_x [MeV]	J^π	L
0.026(32)	0^+	0	0.00	0^+	0
2.08(15)	2^+	2	2.094(11)	2^+	2
3.24(26)	2^+	2	3.30(3)	2^+	2
4.35(65)	0^+	0	3.879(15)	0^+	0

to conclude precisely about the states between 3.7 MeV and 5 MeV. An L=0 component is clearly needed to reproduce the angular distribution gated on the (3.7-5) MeV energy range which indicates the presence of a second 0^+ state in this energy region.

These results confirm that the analysis of the (p,t) channel allows us to well distinguish between L=0 and L=2 states thanks to the differential cross sections and the two-nucleon DWBA analysis.

2.2 Spectroscopy of ^{36}Ca using the ^{38}Ca(p,t)^{36}Ca reaction

2.2.1 Fit of the excitation energy spectrum with Ca outgoing

The excitation energy spectrum of ^{36}Ca, reconstructed via the ^{38}Ca(p,t)^{36}Ca reaction, is shown in Fig. 4.29. This spectrum has been obtained with a condition on Ca outgoing in the ZDD. The angular correlation cut has been applied to reject most of the background. This spectrum has been fitted with a sum of N Gaussian plus a constant function to describe the small amount of background that is still present in the spectrum. The sigma of the Gaussian functions has been strongly constrained using the width of the ground state (being about 570 keV) and the results of the simulation. Only the centroids and the amplitudes were left as free parameters. Fig. 4.29 shows the two models that were validated by the statistical tests. The first one is composed of two Gaussian functions (left) and the second one is composed of three Gaussian functions. Both models have similar reduced χ^2 (1.06 and 0.93, respectively) and p-value (0.39 and 0.56 respectively). The description of the experimental data, made by the second model is slightly better compared to the first one due few counts at about 4 MeV that are fitted by the additional Gaussian of the second model.

The ground state of ^{36}Ca is identified and its position is measured to be 19(37) keV (taking a mean value accepting the measurement of the two models at 1σ confidence level), compatible with zero. This result is expected since the ground state of ^{36}Ca has been used as a calibration point for the triton calibration. A peak is seen at about 3 MeV. The first model measures its position at 2.86(9) MeV and the second one at 2.73(13) MeV (value slightly shifted to the low energies, due to the presence of the third Gaussian). None of these measurements is compatible with the known position of the first 2^+ excitation state at 3.045 MeV at 1σ of confidence level. It is possible that two states have been populated near 3 MeV (including the known 2^+ state) but they cannot be separated, due to the limited energy resolution of the system.

The description of the experimental data, made by the second model is slightly better compared to the first one due few counts at about 4 MeV that are fitted by the additional Gaussian of the

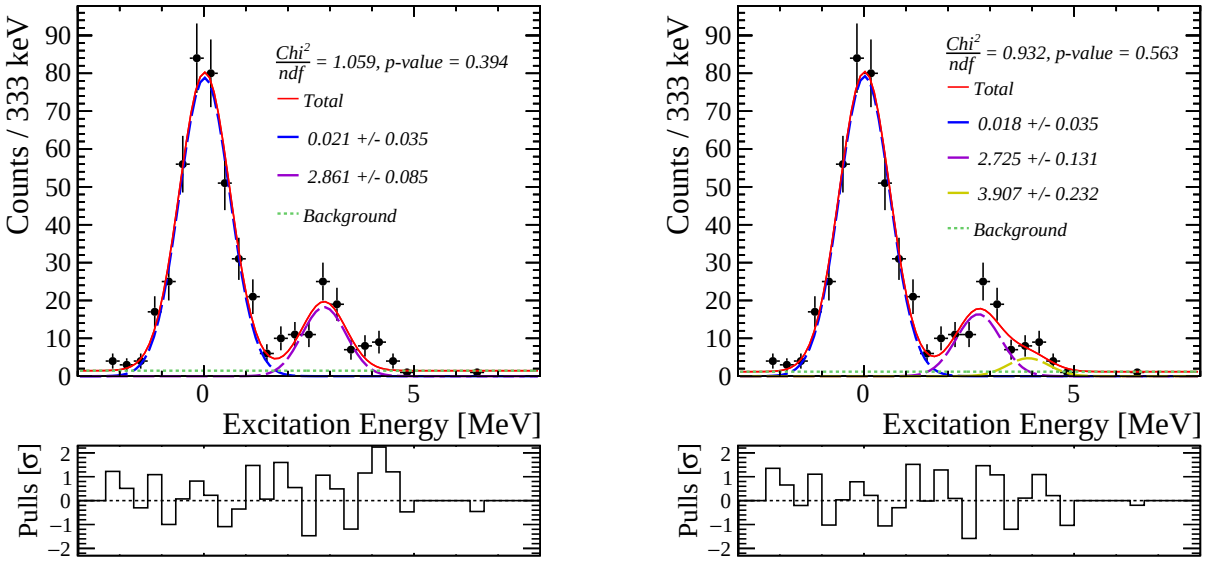

Figure 4.29: Excitation energy spectrum of ^{36}Ca reconstructed with the ^{38}Ca$(p,t)^{36}$Ca reaction, obtained with a condition on a Ca outgoing in the ZDD. Two fits using two different models are shown: one composed of 2 Gaussian functions in addition to the background function (left) and the other composed of 3 Gaussian functions in addition to the background function (left). The red line shows the best fit obtained. The individual components are shown in colored line.

second model. However, this additional contribution relies on very few counts. The integral of the 4 MeV peak in the left part of Fig. 4.29 of 17(11) events, is compatible with zero at 2 σ. Furthermore, if a state is present at 4 MeV in this spectrum, it means that it lies at 1.4 MeV above the proton emission threshold, but decays via gamma emission. This is very unlikely. Some calculations have been performed to compute the theoretical partial width of a potential 2^+ or 0^+ state at 4 MeV using reduced transition probabilities $B(E2)$ and proton spectroscopic factors computed using SM calculations. It has been found that the observation of a 2^+ or a 0^+ state at 4 MeV, in the Ca gated spectrum, is very unlikely as the calculated $\frac{\Gamma_p}{\Gamma_\gamma}$ ratio is of the order of 10^2 for a 2^+ and 10^6 for a 0^+. The possibility of some beam contaminant generating these counts has been investigated but no hint of beam contaminant has been found in the energy versus time-of-flight condition of incoming nuclei. Therefore, the possibility of the presence of a state here is excluded and will not be considered in the following. These counts probably arise from a background source that survived to the angular correlation cut. The influence of those counts on the position measurement of the first excited is taken into account by considering a mean value of 2.78(18) MeV for the measurement of the first excited state, observed in this spectrum.

2.2.2 Differential cross sections

The angular distributions have been extracted for the ground state and for the peak located at about 2.8 MeV. In the latter, it is probable that two states have been populated including the first 2^+ since the first 2^+ has been identified in the benchmark reaction ^{36}Ar$(p,t)^{34}$Ar. The angular distributions have been extracted by fitting the Ca gated excitation spectrum, using the 2 Gaussian model, by

slice of θ_{cm} angle. The sigma of the Gaussian functions have been constrained using the width of the ground state and the simulation. The centroids have been fixed at the positions obtained from the fit presented just above, letting the amplitudes as the only free parameters. The impact of the background (discussed in Section 2.1.2) on the angular distributions has been carefully studied and is found to be negligible. To check the reliability of the results, the differential cross sections have been extracted as well using the method consisting in applying a gate on the excitation energy to get the angular distributions $N(\theta_{cm})$ (see Chap. 3 Section 4). No difference is observed in the results provided by the two methods.

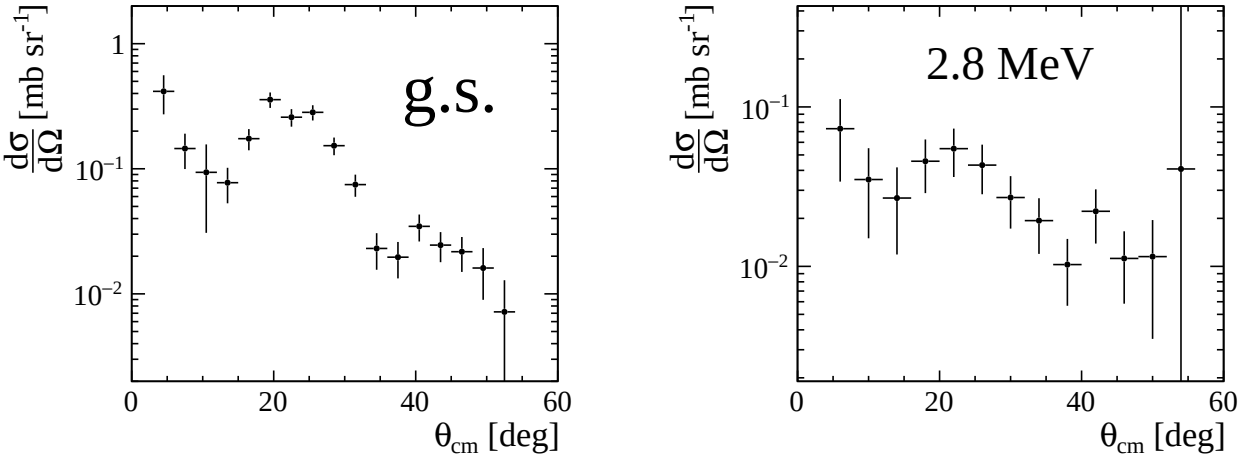

Figure 4.30: Experimental differential cross sections obtained of the ground state and the first excited state identified in the Ca gated excitation energy spectrum of ^{36}Ca , using the ^{38}Ca(p,t)^{36}Ca reaction.

The differential cross section corresponding to the ground state shows the typical behavior of a L=0 distribution. It is in perfect agreement with the $J^\pi = 0^+$ spin-parity of the ground state. The differential cross section for the excited state at 2.8 MeV displays as well a L=0 behavior. This is more surprising since the 3.045 MeV 2^+ excited state is expected to be populated in this energy range. Indeed, other (p,t) studies performed in the region (see for instance the benchmark case in Section 2.1.3) and theoretical calculations indicate that the fist 2^+ state should be populated in this reaction. From the (p,t) selection rules, the population of a state of spin-parity $J^\pi = 2^+$ should display a L=2 behavior. Therefore the shape of the angular distribution of the 2.8 MeV state indicates the observation of a new state of spin-parity $J^\pi = 0^+_2$ in ^{36}Ca .

2.2.3 TNA and DWBA calculations

In the case of a one-nucleon transfer, the cross section can be factorized in spectroscopic factors (see Appendix A). In the case of a two-nucleon transfer, the single-channel cross section can be factorized in Two-Nucleon Amplitudes (TNA), which represents the overlap between the initial wave-function plus two nucleons with the final wave-function. The definition of the TNA can be found in Appendix A.

Two-nucleon transfer DWBA calculations have been performed, using TNA's computed by Shell-Model (SM) calculations, in order to describe the experimental differential cross sections. Two different

SM calculations have been performed in the present work, one restricted to the *sd* orbitals and using the USDB interaction (performed by A. Brown), the other using the full *sdpf* valence space with sdpfu-mix plus Coulomb interaction (performed by A. Poves). The major difference between the two calculations resides in the size of their valence spaces: when restricted to *sd* shells the proton core is closed, while the use of a broader *sdpf* valence space allows proton excitations. When using the *sd* valence space, the first excited state in ^{36}Ca is found to be the 2^+ state at an energy of 3.382 MeV with a neutron particle-hole $\nu(s_{1/2})^{-1}\nu(d_{3/2})^1$. In *sdpf* valence space, the first excited in ^{36}Ca is found to be an intruder 0^+ state at 2.70 MeV with a proton 2p-2h configuration $\pi(d_{3/2})^{-2}\pi(f_{7/2})^2$ [37]. This state could not be predicted by the *sd* valence space since cross shells excitation are forbiden. A detailled discussion about the origin of this state and about the *sdpf* SM calculation can be found in Ref. [37] and in Chap. 5. The second excited state is found to be the first 2^+ state at 2.95 MeV. The TNA's have been computed for the ground state and the first 2^+ state using the two SM model calculations. The TNA's of the predicted 0_2^+ state in ^{36}Ca , computed with the *sdpf* SM calculation, can be found in Table 4.4. For a 0^+ to 0^+ two-nucleon transfer, the only possibility is to couple two nucleons having the same orbital angular momentum. Therefore, only the $d_{3/2}\otimes d_{3/2}$, $s_{1/2}\otimes s_{1/2}$ and $d_{5/2}\otimes d_{5/2}$ channels were considered for the ground state and the 0_2^+. For the 2^+ state, all the channels are allowed except the $s_{1/2}\otimes s_{1/2}$ ones which can only generate a L=0 total angular momentum. For the ground state and the 2^+ state, the *sd* and the *sdpf* calculations provides almost equal results. This is expected since the configuration of these states is of pure *sd* nature. For the ground state, one can see that the main contributing channel is the removal of the two neutrons from the $d_{3/2}$ orbital, which is in agreement with our understanding of the structure of this state. Same for the 2^+, the main contributing channel comes from the removal of one neutron from the $d_{3/2}$ and another from the $s_{1/2}$ orbital, which corresponds to the single particle picture of this state. For the second 0^+ state the main contributing channel is the removal of two neutrons from the $s_{1/2}$ orbital.

Table 4.4: Two-nucleon amplitudes for the ground state, 0_2^+ state and 2^+ state of ^{36}Ca from the two SM calculations (see text for details).

	$(nlj)_1$	$(nlj)_2$	*sd* shell	*sdfp* shells
g.s.	$d_{3/2}$	$d_{3/2}$	-0.99	-0.97
	$s_{1/2}$	$s_{1/2}$	-0.22	-0.21
	$d_{5/2}$	$d_{5/2}$	-0.19	-0.20
0_2^+	$d_{3/2}$	$d_{3/2}$		-0.05
	$s_{1/2}$	$s_{1/2}$		0.29
	$d_{5/2}$	$d_{5/2}$		-0.12
2^+	$d_{3/2}$	$d_{3/2}$	0.06	0.09
	$d_{3/2}$	$s_{1/2}$	-1.51	-1.42
	$d_{3/2}$	$d_{5/2}$	-0.06	-0.05
	$s_{1/2}$	$d_{5/2}$	0.27	0.36
	$d_{5/2}$	$d_{5/2}$	0.11	0.12

All the calculations presented in the following have been performed with the code FRESCO [63]. The input files have been generated using the FR2IN code. All the prescriptions used for the optical potentials and the bound state wave functions are the one presented in Section 1.2.4. Before presenting

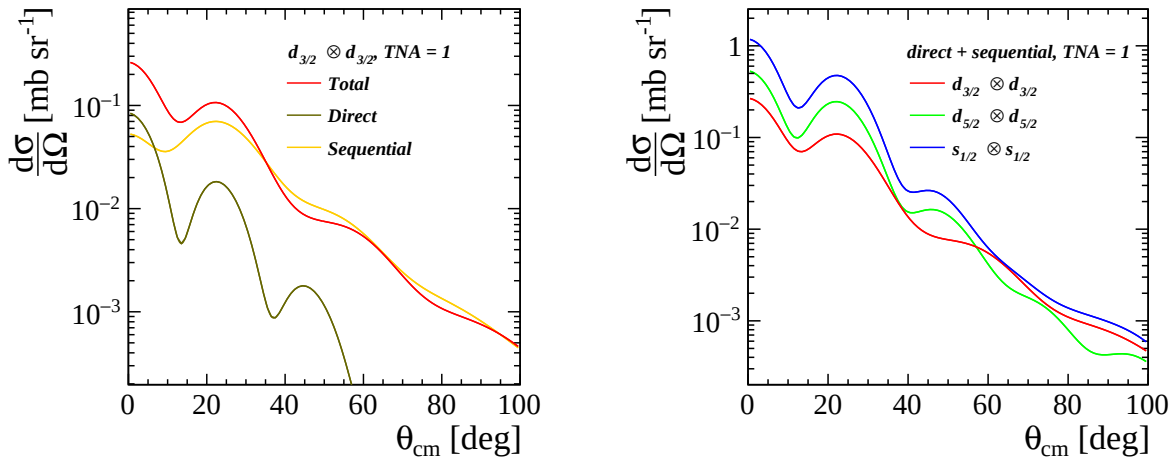

Figure 4.31: Left: Differential cross section of the ^{38}Ca(p,t)^{36}Ca reaction to the ground state of ^{36}Ca , considering only the $d_{3/2} \otimes d_{3/2}$ channel. The individual contributions of the direct transfer (in green) and of the sequential transfer (in yellow) are presented. Right: Total differential cross section of the ^{38}Ca(p,t)^{36}Ca reaction to the ground state of ^{36}Ca considering the $d_{3/2} \otimes d_{3/2}$ (red), the $s_{1/2} \otimes s_{1/2}$ (blue) or the $d_{5/2} \otimes d_{5/2}$ (green) channel. In both plots the TNA's are taken equal to one.

the results of the DWBA calculations performed with the TNA's, we will study some more simple cases to isolate effects arising from the (p,t) reaction mechanism.

Left part of Fig. 4.31 shows a calculation of the differential cross section of the ^{38}Ca(p,t)^{36}Ca reaction to the ground state of ^{36}Ca for different contributions: the direct transfer (in green) and the sequential transfer (in yellow). In this calculation, only the $d_{3/2} \otimes d_{3/2}$ channel has been considered with a TNA equal to one. In the case of a sequential transfer, no experimental information is used to describe the intermediate nucleus ^{37}Ca. One can see in the figure that the sequential transfer has a dominant contribution at large angle (θ_{cm}>10°). This is expected since the Q-value of the intermediate transfer is much lower than the direct one with a Q-value for ^{36}Ca$_{g.s.}$(t,p)^{38}Ca equal to 23.8 MeV and for ^{36}Ca$_{g.s.}$(t,d)^{37}Ca equal to 8.5 MeV (the Q-value are given in this form because the calculation is performed from ^{36}Ca to ^{38}Ca). However, the typical L=0 shape of the distribution is carried by the direct channel with a strong maximum at θ_{cm}=0°. The red line shows the total cross section obtained from the coherent sum of the two contributions. One can see that destructive interference occurs, making the total cross section inferior to the sequential contribution in some angular range ($\theta_{cm} \simeq 50$ and 80°). The right part of Fig. 4.31 shows three calculations of the ^{38}Ca(p,t)^{36}Ca$_{g.s.}$ cross section performed using either the $d_{3/2} \otimes d_{3/2}$ (red), the $s_{1/2} \otimes s_{1/2}$ (blue) or the $d_{5/2} \otimes d_{5/2}$ (green) channel. For each calculation the total cross section (direct plus sequential) is shown and the TNA has been taken equal to one. One can see on this figure that the removal of the $s_{1/2}$ neutrons is favored by the reaction mechanism. Indeed, the $s_{1/2}$ neutron does not have any centrifugal barrier to cross. Furthermore, the intermediate transfer reaction ^{36}Ca$_{g.s.}$(t,d)^{37}Ca, is well matched for small transferred angular momentum L=0 (with a maximum L transferred of $L_{max} = 0.2$ $\hbar$), which favors the removal of the $s_{1/2}$ neutrons. The $d_{5/2} \otimes d_{5/2}$ channel has a slightly higher cross section than the $d_{3/2} \otimes d_{3/2}$ one, due to the degeneracy of the magnetic sub-states of the orbitals.

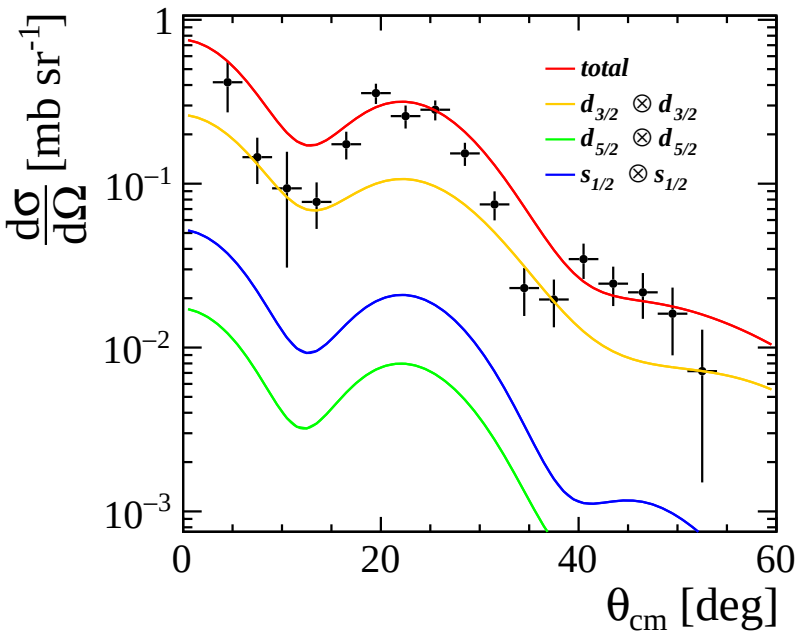

Figure 4.32: The experimental differential cross section obtained for the ground state of ^{36}Ca using the ^{38}Ca(p,t)^{36}Ca reaction are shown with the black points. The red line shows the full DWBA calculation, using the TNA's presented in Table 4.4. The colored lines show the individual contributions of the different channels considered in the calculation.

Fig. 4.32 shows the experimental differential cross section obtained for the ^{38}Ca(p,t)^{36}Ca$_{g.s.}$ reaction. It is compared to the full DWBA calculation performed considering all the channels and using the TNA values presented in Table 4.4. One can see in this figure that the L=0 behavior is well reproduced by the calculation. The amplitudes of the oscillation is underestimated by the calculations, similarly to what we found in the benchmark reaction. The amplitude of the total cross section is well reproduced by the DWBA calculation (even if the calculation slightly over-estimates the cross section at $\theta_{cm} < 15°$). From the individual contributions, one can see that the $d_{3/2} \otimes d_{3/2}$ contribution (in orange in the figure) is already enough to describe the majority of the cross section. This is expected since the ground state of ^{36}Ca is expected to have a pure configuration with two neutrons filling the $s_{1/2}$ orbital. We found a general good agreement between the experimental and the theoretical cross section. This confirms the spin-parity $J^\pi = 0^+$ of this state with a neutron $\nu(s_{1/2})^2$ configuration.

The experimental differential cross section obtained for the excited state identified in ^{36}Ca using the ^{38}Ca(p,t)^{36}Ca reaction is shown in Fig. 4.33. It is compared to the full DWBA calculations performed for the experimentally known 2^+ excited state at 3.045 MeV [36] in ^{36}Ca and for the 0^+_2 intruder state. The calculations have been performed using the TNA's presented in Table 4.4. As expected, the 0^+_2 theoretical cross section reproduces well the L=0 behavior of the experimental distribution at angles below 40°, while the 2^+ theoretical cross section displays a typical L=2 behavior with an almost constant value between 0 and 15°. The amplitude of the experimental cross section is not reproduced by any of the calculations. The 0^+_2 theoretical cross section is too low to describe the experimental

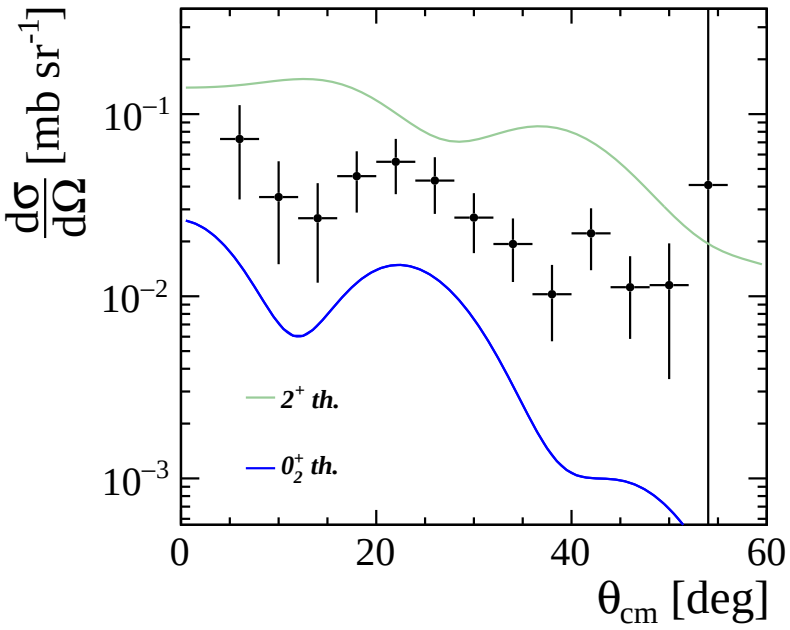

Figure 4.33: The experimental differential cross section obtained of the excited state identified in ^{36}Ca using the ^{38}Ca(p,t)^{36}Ca reaction are shown with the black points. The colored lines show the full DWBA calculation performed for the first 2^+ excited state (in green) and for the predicted 0^+_2 state (in blue).

points while the 2^+ one is too high. In order to have a more precise look at how the two theoretical calculations describe the shape of the experimental cross section, a fit of the experimental data has been performed using the results of the two calculations. The only free parameter is a scaling factor applied to the DWBA calculations. The results of the fit are shown in the left part of Fig. 4.34. The obtained χ^2 and the p-value demonstrate that the L=0 distribution obtained from the 0^+_2 theoretical cross section, describes very well the experimental one (with a χ^2 of 2.2 and a p-value of 0.97). The L=2 distribution obtained from the 2^+ theoretical cross section describes poorly the observed behavior (with a χ^2 of 12.0 and a p-value of 0.11). The resulting χ^2 is 6 times better for the 0^+_2 calculation than for the 2^+ calculation which rejects the L=2 model to describe the experimental data. Another fit has been performed using a model composed of the sum of the two theoretical cross section, each one having a scaling factor as free parameter. The result is shown in the right part of Fig. 4.34. The results of the fit shows that the L=0 contribution dominates at angles below 40° and that L=2 is very weak (starting to have a significant contribution at angles higher than 40°). A scaling factor of about 3 has been applied to the 0^+_2 calculation while a factor of 0.06 has been applied to the one of the 2^+ to obtained the best possible description of the data. This corresponds to an integrated cross section of about 1.3 mb for the 0^+_2 state and 0.3 mb for the first 2^+ state.

These results show that the behavior of the experimental cross section is well described by assuming the existence of a 0^+_2 state rather than with a 2^+. The 0^+_2 theoretical cross section is under-estimated, compared to the experimental cross section (with a scaling factor of 3 from the fit shown in left part of

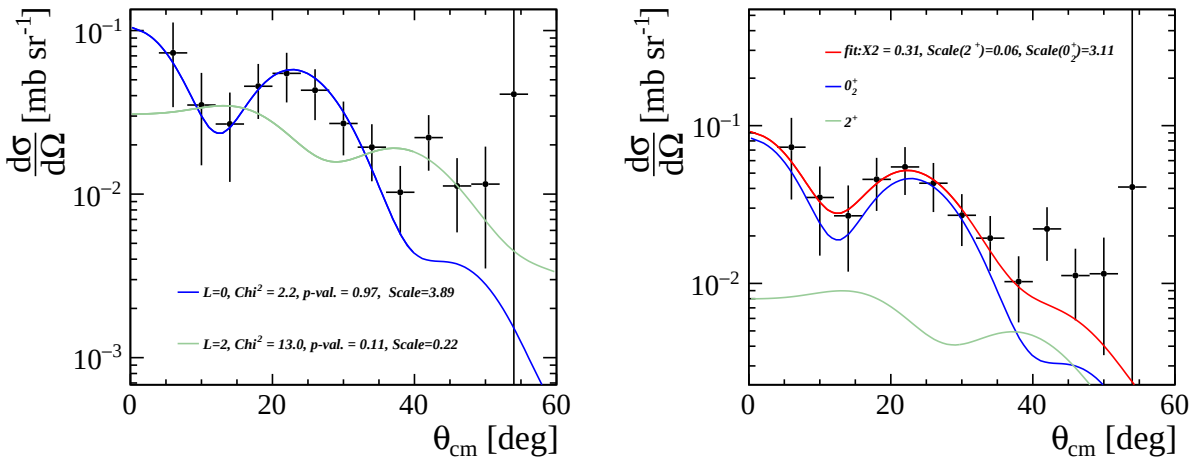

Figure 4.34: The experimental differential cross section obtained of the excited state identified in ^{36}Ca using the ^{38}Ca(p,t)^{36}Ca reaction are shown with the black points. Left: A fit of the data points is performed independently using the 0^+_2 theoretical cross section (in blue) and the 2^+ theoretical cross section (in green). The only free parameter is a scaling factor applied to the theoretical distributions. Right: A fit is performed using a function composed of the sum of the two theoretical cross sections (red). Two free parameters are considered corresponding to the two scaling factors (one for each distributions). The individual contributions of the L=2 (in green) and the L=0 (in blue) distribution, used in the fit are also shown. This fit provides a very good description of the date with a χ^2 of about 0.3.

Fig. 4.34). This might arise from the underestimation of the TNA's for the predicted 0^+_2. Conversely, the 2^+_2 theoretical cross section is largely over-estimated. From the results, only a few L=2 contribution can be used to describe the observed cross section. The origin of this over-estimation should come from the reaction mechanism, since the SM calculation successfully described the cross section of the ground state having, as the first 2^+ state, a pure *sd* configuration. Similar results were obtained using the ^{30}Mg(t,p)^{32}Mg. The second 0^+_2 state of ^{32}Mg has been strongly populated and the first 2^+ was not observed, while DWBA calculation predicted the observation of the first 2^+ excited state [69, 70]. The reason of the non-observation of these 2^+ states in two-nucleon transfer remains a mystery up to now. However, these results presented in this section provide strong evidence for the presence of a 0^+_2 state at 2.78(18) MeV in ^{36}Ca.

2.2.4 One and two-proton decay channel

This section will present the results obtained in the one and two-proton decay channels of the excited states of ^{36}Ca, using a condition on a K and Ar outgoing in the ZDD, respectively. Left part of Fig. 4.35 shows the excitation energy spectrum of ^{36}Ca obtained with a condition on K outgoing. Very few statistics is available in this spectrum. Due to the very large statistical errors and to the limited resolution of the excitation energy, it is not possible to extract anything from this spectrum. It is the same situation for the proton energy spectrum shown in the right part of Fig. 4.35. The one-proton separation energy has been added to the proton energy, reconstructed in the center-of mass of

^{36}Ca (see 4). No clear peak can be identified in this spectra (except a non negligible contribution at about 5 MeV). Furthermore, due to the very large statistical errors, many different multiple Gaussian functions can be used to fit this spectrum and therefore no conclusion could be made about the position of the populated states.

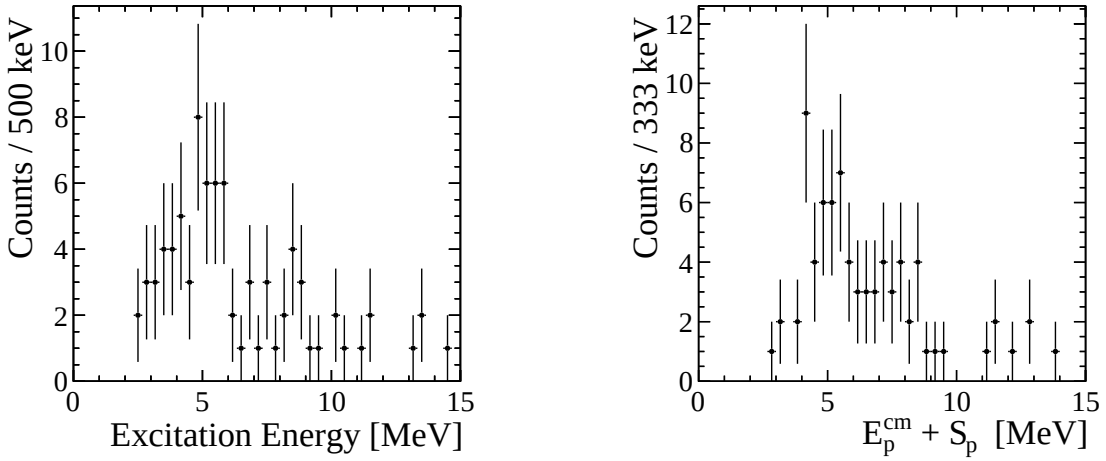

Figure 4.35: Left: Excitation energy spectrum of ^{36}Ca reconstructed from the ^{38}Ca(p,t)^{36}Ca reaction, with a condition on a K outgoing. Right: Proton energy spectrum added to the one-proton separation energy, obtained with a condition on a K outgoing. In both spectra, a contribution is identified at about 5 MeV but due to the large statistical errors, no conclusion can be made about the position of the populated states.

The two-proton decay channel benefits from more statistic compared to the one-proton decay channel. Furthermore, the coincidence with the decaying protons gives a clear signature of the excited states populated in ^{36}Ca. Left part of Fig. 4.36 shows the proton energy spectrum, reconstructed in the center-of-mass of ^{36}Ca, obtained with a condition on Ar outgoing. In this spectrum a peak is identified at 1.47 MeV. The bottom part of Fig. 4.36 shows a scheme of the sequential two-proton decay of an excited state of ^{36}Ca passing through an intermediate resonance at 1.55 MeV in ^{35}K and going to the ground state of ^{34}Ar. The decay of the first excited state of ^{35}K to the ground state of ^{34}Ar occurs through the emission of a 1.47 MeV proton. The observation of this proton in coincidence with the triton of the reaction characterizes the two-proton decay of excited state populated in ^{36}Ca . The right part of Fig. 4.36 shows the excitation energy spectrum of ^{36}Ca obtained with a condition on Ar outgoing. An additional condition is used to select events for which the triton of the transfer reaction is seen in coincidence with the proton at $E_p^{cm} = 1.47$ MeV using the gate 1 MeV $< E_p^{cm} <$ 2 MeV. In this spectrum one can clearly identify a series of four peaks. This spectrum has been fitted using a sum of 4 Gaussian functions. The coincidence between the triton, the proton and the Ar outgoing clears the spectrum from all type of background. The model describes very well the data with a reduced χ^2 of 0.65 and a p-value of 0.70. The positions of the peaks are found at 4.83(17) MeV, 6.60(14) MeV, 8.52(14) MeV and 11,14(13) MeV. Due to the limited statistics available for those states it is not possible to extract angular distributions.

It is surprising to see a peak at 4.83(17) MeV in the Ar gated excitation energy spectrum since we

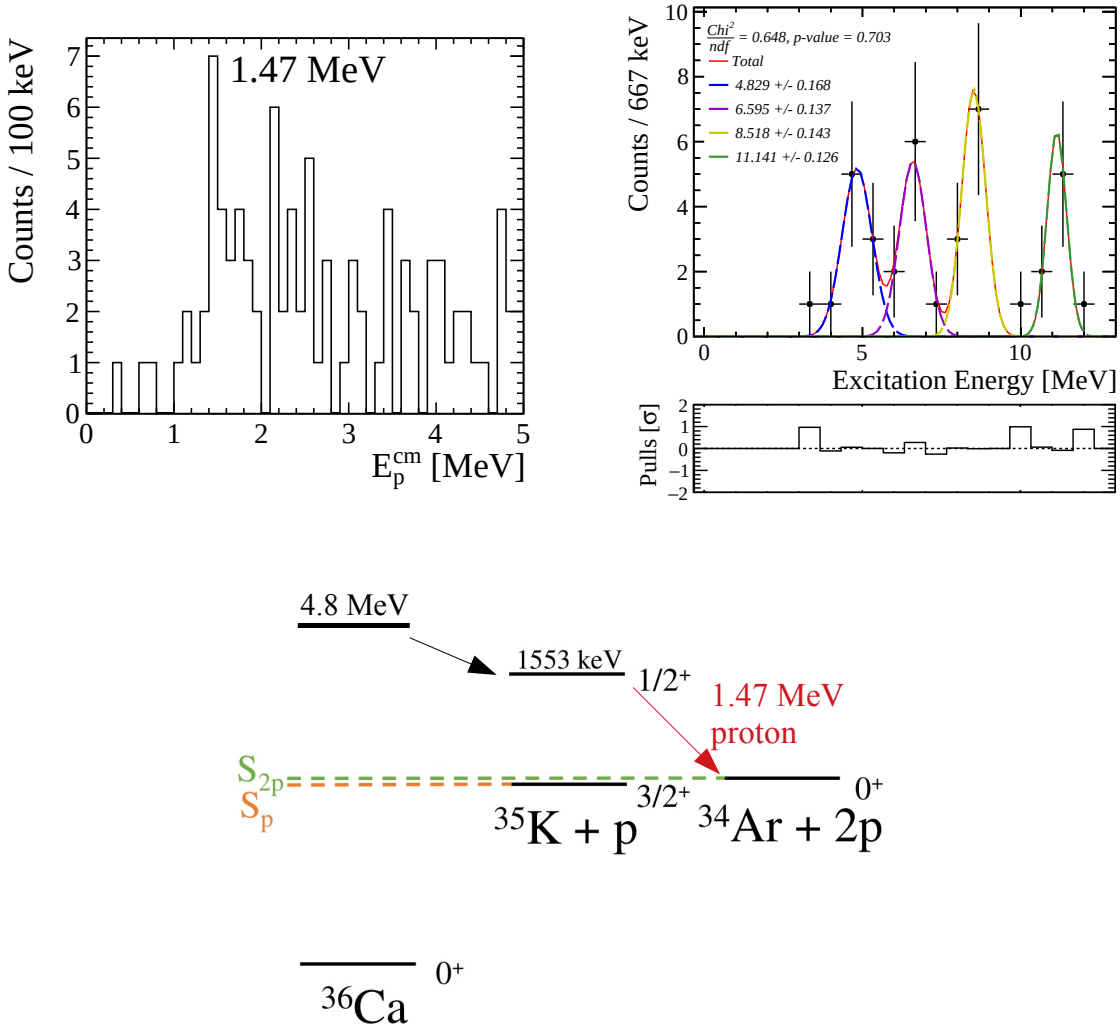

Figure 4.36: Left: Proton energy spectrum obtained with a condition on an Ar outgoing. It contains events of multiplicity 2 (one trition plus one proton) and 3 (one triton plus two protons). Right: Excitation energy spectrum of ^{36}Ca reconstructed from the ^{38}Ca(p,t)^{36}Ca reaction, with a condition on a Ar outgoing and on the proton energy 1 MeV $< E_p^{cm} <$ 2 MeV. Bottom: Scheme of the sequential two-proton decay of an excited state of ^{36}Ca passing through an intermediate resonance at 1.55 MeV in ^{35}K and going to the ground state of ^{34}Ar.

saw, in the ^{37}Ca(p,d)^{36}Ca reaction, that the two-proton channel started to contribute at 6 MeV (see Fig. 4.19 of Section 1.2.5). Indeed, a state located at an excitation energy of 4.8 MeV in ^{36}Ca can decay either directly to the ground state of ^{35}K (with a proton energy of 2.23 MeV) or to the first excited state of ^{35}K (with a proton energy of 0.68 MeV). The partial proton width for a given state λ is defined as:

$$\Gamma_{p,\lambda} = 2P_l(E_p^{cm})\gamma_{p,\lambda}^2, \tag{4.6}$$

where $P_l(E_p^{cm})$ is the penetration factor, l and E_p^{cm} are the angular momentum and the energy of the proton, respectively, and $\gamma_{p,\lambda}^2$ is the reduced proton width of the state λ [71]. The reduced width contains the information about the structure of the state while the penetration factor contains

the Coulomb barrier and centrifugal penetrability effects on the decay. From this, one can compute the ratio of the proton partial decay widths to the $\frac{3}{2}^+$ and $\frac{1}{2}^+$ states $\frac{\Gamma_{p,\lambda}(\lambda\rightarrow\frac{3}{2}^+)}{\Gamma_{p,\lambda}(\lambda\rightarrow\frac{1}{2}^+)}$, where $\Gamma_{p,\lambda}(\lambda\rightarrow\frac{3}{2}^+)$ represents the probability to decay to the ground state $J^\pi=\frac{3}{2}^+$ of ^{35}K and $\Gamma_{p,\lambda}(\lambda\rightarrow\frac{1}{2}^+)$ represents the probability to decay to the first excited state $J^\pi=\frac{1}{2}^+$ of ^{35}K. For a given state λ, this ratio is simply equal to the ratio of the the penetration factors.

Let us consider two cases: the one-proton decay of a 0^+ state at 4.8 MeV and the decay of a 2^+ state at 4.8 MeV. The 0^+ state will decay either to the ground state of ^{35}K by emitting one proton of energy $E_p^{cm}=2.23$ MeV and of angular momentum $l=2$ (due to the conservation of the total angular momentum of the decay) or to the first excited state of ^{35}K by emitting one proton of energy $E_p^{cm}=0.68$ MeV and of angular momentum $l=0$. This gives a ratio of $\frac{\Gamma_p(0^+\rightarrow\frac{3}{2}^+)}{\Gamma_p(0^+\rightarrow\frac{1}{2}^+)}=8.3\times10^2$. In the second case, the 2^+ state will decay either to the ground state of ^{35}K by emitting one proton of energy $E_p^{cm}=2.23$ MeV and of angular momentum $l=0$ or to the first excited state of ^{35}K by emitting one proton of energy $E_p^{cm}=0.68$ MeV and of angular momentum $l=2$. This gives a ratio of $\frac{\Gamma_p(2^+\rightarrow\frac{3}{2}^+)}{\Gamma_p(2^+\rightarrow\frac{1}{2}^+)}=3.1\times10^5$. From these results, one can conclude that it is very unlikely to observe a 2^+ state in the two-proton decay channel at this energy, since it has to first decay to the first $J^\pi=\frac{1}{2}^+$ excited state of ^{35}K to be observed in the two proton decay channel. Conversely, a 0^+ state could be observed in the two-proton decay channel.

A $J^\pi=0_3^+$ state with a $2p-2h$ neutron configuration $\nu(s_{1/2})^{-2}\nu(d_{3/2})^2$ is expected to be well populated using (p,t) transfer reaction. Its excitation energy has been predicted to be 4.5 MeV by the SM calculation in the *sdpf* valence space and 4.65 MeV by the SM calculation in the *sd* valence space. For these reasons, the state identified at 4.83(17) MeV, in ^{36}Ca is a good candidate for a $J^\pi=0_3^+$ state.

2.3 Summary

In this section, the results obtained on the ^{38}Ca(p,t)^{36}Ca transfer reaction have been presented. The whole analysis of the (p,t) channel has been benchmarked using the ^{36}Ar(p,t)^{34}Ar reaction. The background has been carefully studied using the empty target runs. It has been found that the majority of the background can be rejected using a cut on the light-heavy angular correlations. A new L=0 state has been identified at $E_x=2.78(18)$ MeV in ^{36}Ca . The DWBA analysis of the differential cross section has been performed using TNA's computed within the SM framework and provides strong evidence of the existence of quasi bound $L=0$ state in ^{36}Ca. From the results, a $J^\pi=0_2^+$ spin-parity is proposed for this state. A new excited state has been identified in the Ar-gated excitation energy spectrum at $E_x=4.83(17)$ MeV. The observation of this state in the two-proton decay channel favors a $J^\pi=0_3^+$ spin-parity for this state. This value being the only one allowing the observation of the proton decay of this state to the $1/2^+$ intermediate resonance in ^{35}K. This spin-assignment is also supported by the expected populated state using the (p,t) reaction and by SM calculations.

3 Study of ^{35}Ca via the ^{37}Ca(p,t)^{35}Ca reaction

The production of the ^{37}Ca radioactive beam allows the study of the weakly bound nucleus ^{35}Ca using the two neutron transfer reaction ^{37}Ca(p,t)^{35}Ca. The only information experimentaly known about this nucleus is its lifetime of 25.7 (2) ms from the measurement of its β-decay [33, 72]. In this section, the first mass measurement and the identification of the first excited state of ^{35}Ca are reported.

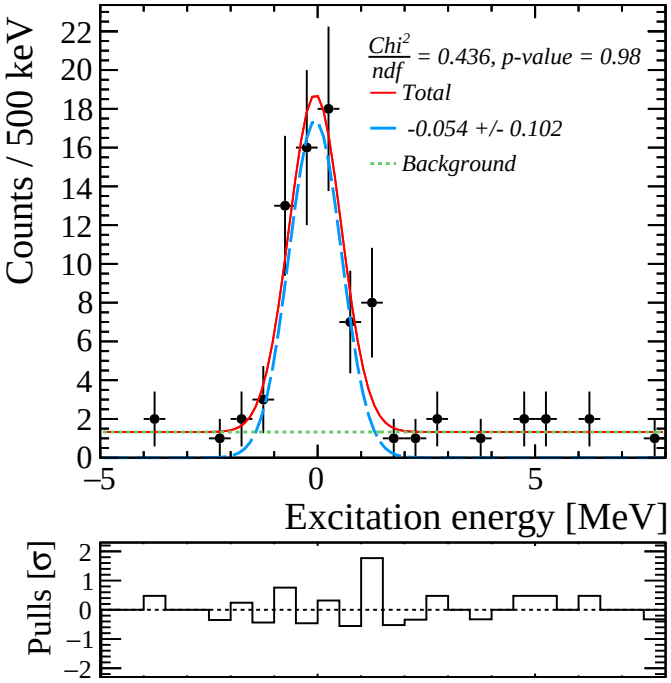

Figure 4.37: Excitation energy spectrum of ^{35}Ca reconstructed with the ^{37}Ca(p,t)^{35}Ca reaction, obtained with a condition on a outgoing Ca isotope in the ZDD. The red line shows the best fit obtained. The individual components are shown in colored line.

Fig. 4.37 shows the excitation energy spectrum of ^{35}Ca reconstructed with the ^{37}Ca(p,t)^{35}Ca reaction, obtained with a condition on Ca outgoing. One single peak is identified in this spectrum which corresponds to the ground state of ^{35}Ca. A fit of this spectrum has been performed using a fit function composed of a Gaussian function plus a constant function to describe the small amount of background present in this spectrum. The function used describes very well the data with a reduced χ^2 of 0.44 and a p-value of 0.98. The resolution is found to be about 640 keV, similarly to what was obtained in the ^{38}Ca(p,t)^{36}Ca reaction.

The identification of the ground state of ^{35}Ca allows the measurement of its atomic mass. The analysis was performed considering a nominal value of $\Delta M_{AME}(^{35}\text{Ca}) = 4790$ keV for the mass of ^{35}Ca, from the systematic study of Ref. [53]. The position of the ground state of ^{35}Ca is found at a position of -54(102) keV in the excitation energy spectrum, meaning that this measurement is in good agreement with the extrapolated value of Ref. [53]. To evaluate more accurately the systematic uncertainties on the mass measurement, the method used for the mass measurement of ^{36}Ca (described in Section 1.1.3) was used. Combining the four independent measurements performed by the four MUST2 telescopes,

located at the closest distance from the target, the ground state position was found to be located at -13(140) keV in the excitation energy spectrum. This measurement leads to a value of the mass excess of ^{35}Ca of $\Delta M_{exp}(^{35}\mathrm{Ca}) = 4805(140)$ keV. This value leads to a two-proton separation energy for ^{35}Ca of $S_{2p}(^{35}\mathrm{Ca}) = 389(180)$ keV. The mass of ^{34}K has not yet been experimentally measured, preventing the determination of the one-proton separation energy (expected to be at about 1260 keV, taking the extrapolated value of Ref. [53]). The ground state of ^{35}Ca is therefore very weakly bound and ^{35}Ca is expected to be the last bound Ca isotope.

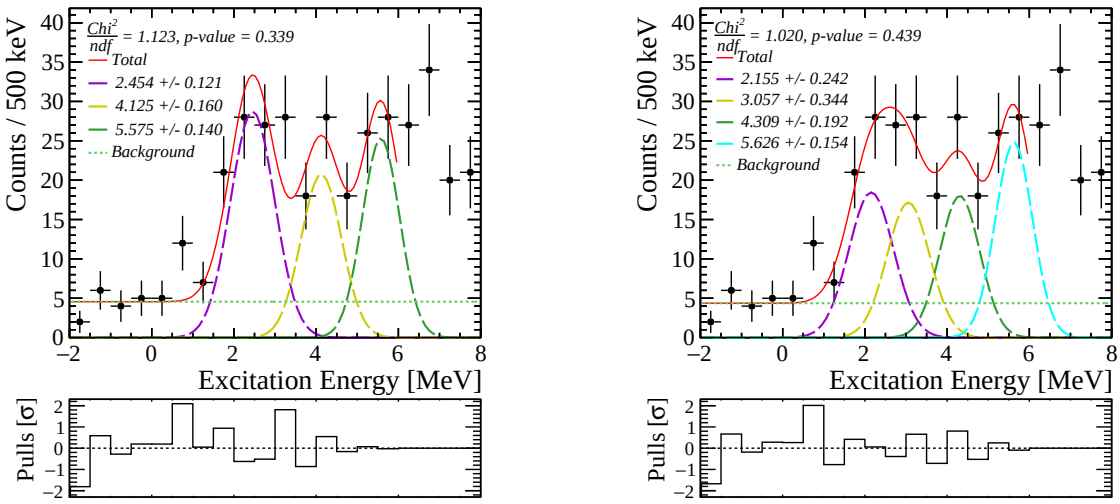

Figure 4.38: Excitation energy spectrum of ^{35}Ca obtained with a condition on outgoing Ar nuclei in the ZDD. Two fits using two different models are shown: one composed of 3 Gaussian functions in addition to the background function (left) and the other composed of 4 Gaussian functions in addition to the background function (left). The red line shows the best fit obtained. The individual components are shown in colored line.

Fig. 4.38 shows the excitation energy spectrum of ^{35}Ca obtained with a condition on outgoing Ar isotopes (note that ^{34}K is unbound and therefore no outgoing K condition can be applied). The obtained excitation energy spectrum does not exhibit a lot of statistics and displays a rather flat behavior. The mirror reaction ^{37}Cl(^{11}B,^{13}N)^{35}P has been studied in direct kinematics at about 8 MeV/nucleons [73]. Above 4 MeV of excitation energy, a high density of states has been observed and the same is expected for the ^{37}Ca(p,t)^{35}Ca reaction. It is therefore very difficult to conclude about the position of the excited states populated in ^{35}Ca, due to the limited resolution and to the flat behavior of the excitation energy spectrum. However, the clear rising edge at about 2 MeV can be used to determine the position of the first excited state of ^{35}Ca, populated in the ^{37}Ca(p,t)^{35}Ca reaction.

The fit of the spectrum has been performed between -5 and 6 MeV using different N-Gaussian plus background functions. The resolution of the Gaussian functions has been fixed using the width of the ground state peak and the simulations, as explained Section 1.2.1. Fig. 4.38 shows the two fits (using a sum of 3 and 4 Gaussian functions, respectively) providing the best results. The position of the first excited state is found at 2.45(12) MeV with the first fit and at 2.16(24) MeV with the second one. The two fits provide equivalent reduced Chi square and p-values, therefore, an average value of 2.24(33) MeV, of the two obtained energies is considered. At higher energy, the two models differ and

since one can not conclude about which one is correct, no conclusion can be made about the position of higher excited states.

In the mirror nucleus ^{35}P the ground state has a spin-parity $J^\pi = \frac{1}{2}^+$ arising from a single proton sitting on the $2s_{1/2}$ orbital. The first excited state is a $J^\pi = \frac{3}{2}^+$ located at 2.3866(5) MeV which main configuration corresponds to the promotion of the proton from the $2s_{1/2}$ to the $1d_{3/2}$ orbital. By comparison with the mirror nucleus, we propose a spin-parity assignment of $J^\pi = \frac{1}{2}^+$ for the ground state of ^{35}Ca and $J^\pi = \frac{3}{2}^+$ for its first excited state found at 2.24(33) MeV.

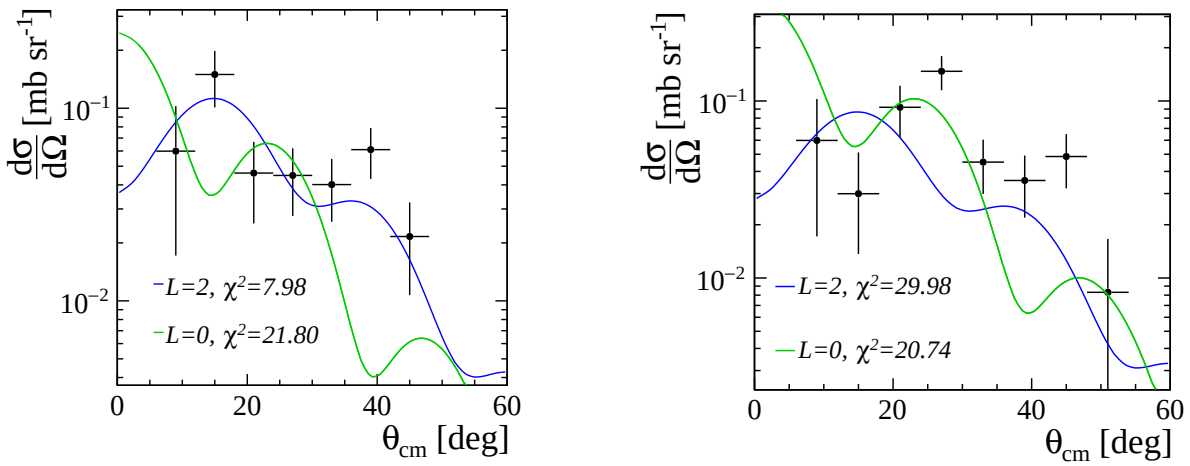

Figure 4.39: The experimental differential cross section obtained of the ground state (left) and the first excited state (right) identified in ^{35}Ca using the ^{37}Ca$(p,t)^{35}$Ca reaction are shown with the black points. A fit of the cross section is shown using the DWBA calculations performed for an L=0 (green) and an L=2 (blue) transfer.

In order to further confirm the spin-parity assignment, the differential cross sections corresponding to the ground and first excited state of ^{35}Ca have been extracted and are shown in Fig. 4.39. The angular distribution θ_{cm} of the ground state (first excited state) has been extracted using a condition on the excitation energy $-1.5 < E_x < 1.5$ MeV ($1.5 < E_x < 3.2$ MeV). Due to the lack of statistics, it is not possible to use the method consisting in fitting the excitation energy spectrum by slices of angles, as we did up to now. DWBA calculations have been performed for the ^{37}Ca$(p,t)^{35}$Ca with the code 2FNR [62] to ease the determination of the transferred angular momentum L. Two different calculations have been made, one considering an L=0 transfer by removing two neutrons from the $2s_{1/2}$ orbital in^{37}Ca, the other one considering a L=2 transfer by removing one neutron from the $1d_{3/2}$ and the other from the $2s_{1/2}$ orbital. Fig. 4.39 shows a fit of the experimental cross sections performed using the results of the DWBA calculations. For the ground state, a reduced Chi square 3 times better is obtained with the L=2 calculation than with the L=0 one. This is expected since the expected ground state configuration consists in a single neutron on the $2s_{1/2}$ orbital, obtained from a removal of neutrons from the $s_{1/2}$ and $d_{3/2}$ orbitals. This result supports the spin-parity assignment $J^\pi = \frac{1}{2}^+$ proposed for the ground state. For the first excited state, the experimental cross section exhibits an L=0 behavior. The L=0 DWBA calculation reproduces well the data up to 35° but underestimates the amplitude of the second maximum at about 45°. The obtained reduced Chi

square is better for the L=0 fit but the difference with the L=2 one is not as large as for the ground state, due to this second maximum which is better reproduced by the L=2 calculation. However the oscillations of the experimental cross section between 0 and 35° are typical from L=0 transfer, which is expected from the removal of a pair of neutron from the $s_{1/2}$ orbital in ^{37}Ca, populating the first excited state of ^{35}Ca. This supports the spin-parity assignment $J^\pi = \frac{3}{2}^+$ proposed for the first excited state of ^{35}Ca.

In summary, the weakly bound ^{35}Ca nucleus has been studied via the two neutron transfer reaction ^{37}Ca(p,t)^{35}Ca. Its atomic mass has been measured for the first time with a mass excess of $\Delta M_{exp}(^{35}\text{Ca}) = 4805(140)$ keV. From the fit of the excitation energy spectrum, the first excited state of ^{35}Ca has been identified at 2.24(33) MeV. By comparison to the mirror nucleus ^{35}P, a spin parity $J^\pi = \frac{1}{2}^+$ is proposed for the ground states, whose main configuration corresponds to a single neutron sitting on the $s_{1/2}$ orbital. For the first excited state a $J^\pi = \frac{3}{2}^+$ spin assignment is proposed consisting in the promotion of the neutron from the $s_{1/2}$ to the $d_{3/2}$ orbital. These assumptions are supported by the DWBA analysis of the experimental differential cross section obtained for these states.

5 Interpretation

Sommaire

In Chapter 4, the spectroscopy of ^{36}Ca has been performed using the ^{37}Ca(p,d)^{36}Ca and the ^{38}Ca(p,t)^{36}Ca transfer reactions. This chapter will first focus on understanding the low-lying structure of the populated states with the help of Shell Model (SM) calculations. Very large Mirror Energy Differences (MED) are observed when comparing the excitation energy of the populated states in ^{36}Ca to the one of the analogue states of the mirror nucleus ^{36}S. The mechanism from which these Colossal MED emerge will be discussed in a second part. Then, the $N = 16$ sub-shell gap will be studied using results obtained on ^{35}Ca. Finally, the $d_{5/2}$ strength in ^{36}Ca will be discussed and compared to the one of the mirror nuclei.

1 The structure of ^{36}Ca

Two different SM calculations have been performed in the present work, one restricted to the *sd* orbitals and using the USDB interaction (performed by A. Brown), the other using the full *sdpf* valence space with sdpfu-mix plus Coulomb interaction (performed by A. Poves). The major difference between the two calculations resides in the size of their valence spaces: when restricted to *sd* shells the proton core is closed, while the use of a broader *sdpf* valence space allows excitations from the *sd* to the *fp* shell.

An intruder state can be defined as a state whose configuration implies the next higher main shell, relative to the dominating shell in the vicinity of the Fermi surface, and for which the energy is comparable to the one of the ground state configuration [74]. In the case of ^{36}Ca, the ground state proton configuration corresponds to a closed *sd* shell. The intruder configuration corresponds then to the promotion of a pair of protons from the *sd* to the *pf* shell. Therefore, intruder states could not be described by the SM calculations performed in the *sd* valence space.

Fig. 5.1 shows the results of the SM calculations for excited states in ^{36}Ca, compared to the experimental results. Let's first compare the results of the two SM calculations. There is a one-to-one correspondence for the 2^+, 1^+ and 0^+_3 states between USD and $sdpfu-m$ interactions, with an energy shift of about 300 keV for the first one and 150 keV for the others. Indeed, the first 2^+ and 1^+ states have a rather pure $\nu(s_{1/2})^{-1}\nu(d_{3/2})^1$ neutron configuration which is well represented in both *sd* and *sdpf* valence space. The same stands for the 0^+_3 excited state which has a $2p$-$2h$ $\nu(s_{1/2})^{-2}\nu(d_{3/2})^2$ neutron configuration. Conversely, the 0^+_2, 2^+_2 and 2^+_3 levels, predicted by the *sdpf* SM calculations, could not be described by the SM calculations performed in the *sd* valence space, due the strong $2p$-$2h$ $\pi(d_{3/2})^{-2}\pi(f_{7/2})^2$ intruder configuration of these states. Then, the major difference between the two calculations is that the *sdpf* calculation predicts that the first excited state of ^{36}Ca is the intruder 0^+_2 state at $E_x^{sdpf}(0^+_2) = 2.70$ MeV while the *sd* calculation predicts that it is the 2^+ at about 3.4 MeV. Moreover, one can see in Fig. 5.1 that the *sdpf* SM calculation predicts a high density of intruder states in ^{36}Ca (4^+, 2^+_3, 3^+, 4^+_2,1^+_2,4^+_3) which have not been observed in this work. *A priori*, the intruder states should not be populated via neutron removal reactions since, they correspond to proton excited configurations. However, these states can still be populated through the mixing with the normal states, strongly populated in neutron removal reactions.

In Chapter 4, the spectroscopy of ^{36}Ca has been performed using the ^{37}Ca(p,d)^{36}Ca and the ^{38}Ca(p,t)^{36}Ca transfer reactions. The known first 2^+ excited state has been identified and 6 excited states have been observed for the first time in ^{36}Ca. The energies and proposed spin-parities for these

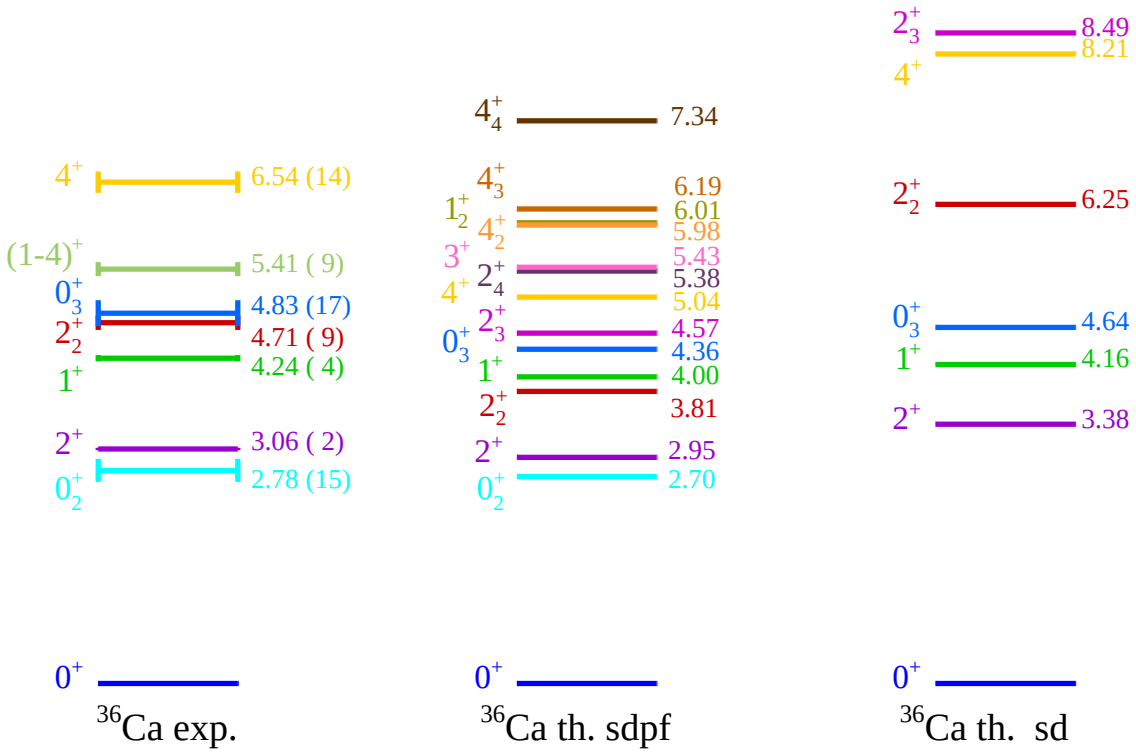

Figure 5.1: Level scheme of ^{36}Ca. The observed levels in this work are shown in the left part and the prediction of SM calculation are shown in the middle part, for the *sdpf* valence space, and in the right part for the *sd* valence space.

states are shown in Fig. 5.1 and in Table 5.1, as well as their spectroscopic factors, and are discussed in the following.

- The first 2^+ and 1^+ states

The measured energies of the 2^+_1 and 1^+_1 states agree well with the SM predictions with $E_x^{Exp}(2^+) = 3.059(16)$ MeV and $E_x^{Exp}(1^+) = 4.24(4)$ MeV, respectively. These two states share the same neutron configuration $\nu(s_{1/2})^{-1}\nu(d_{3/2})^1$. Their spectroscopic factors are given in the Table 5.1 and are compared to the results of SM calculations. For the 2^+_1, the two calculations agree very well but overestimate the observed C^2S value of 0.66. The latter is probably due to the fact the 2^+_1 has a mixed configuration with the 2^+_2 state identified in ^{36}Ca, for which an $s_{1/2}$ spectroscopic factor of 0.28 has been found. Summing up the C^2S values of the 2^+_1 and 2^+_2 states, the experimental value of 0.94(20) is closer to predictions. For the first 1^+ state, the SM calculations reproduce very well the measured C^{2}S. These two states have rather pure configuration with spectroscopic factors close to the single particle picture.

- The 0^+_3 bubble state

The 0^+_3 state has been populated via the (p,t) and not via the (p,d) reaction. This is in line with a dominant neutron $2p$-$2h$ configuration $\nu(s_{1/2})^{-2}\nu(d_{3/2})^2$ for this state. Its energy is found to be $E_x^{Exp}(0^+_3) = 4.83(17)$ MeV, in good agreement with the SM predictions, which reinforces the proposed spin-parity assignement. The non-occupancy of the $s_{1/2}$ orbital in this configuration should generate a central depletion in the neutron density, leading to a neutron bubble structure. Experimental evidences

J^π	E_x			C^2S			Config.
	Exp.	SM *sdpf*	SM *sd*	Exp.	SM *sdpf*	SM *sd*	
0^+				1.06(22)	0.91	0.94	$\pi\left((1d_{5/2})^6(2s_{1/2})^2(1d_{3/2})^4\right)$ $\nu\left((1d_{5/2})^6(2s_{1/2})^2\right)$
0_2^+	2.78(15)	2.70					$\pi\left((1d_{5/2})^6(2s_{1/2})^2(1d_{3/2})^2(pf)^2\right)$ $\nu\left((1d_{5/2})^{6/5}(2s_{1/2})^1(1d_{3/2})^{1/2}\right)$
2_1^+	3.06(2)	2.95	3.38	0.66(14)	1.01	1.16	$\pi\left((1d_{5/2})^6(2s_{1/2})^2(1d_{3/2})^4\right)$ $\nu\left((1d_{5/2})^6(2s_{1/2})^1(1d_{3/2})^1\right)$
1_1^+	4.24(4)	4.00	4.16	0.61(13)	0.71	0.71	$\pi\left((1d_{5/2})^6(2s_{1/2})^2(1d_{3/2})^4\right)$ $\nu\left((1d_{5/2})^6(2s_{1/2})^1(1d_{3/2})^1\right)$
2_2^+	4.71(9)	3.81	6.25	0.28(6)	0.10		$\pi\left((1d_{5/2})^6(2s_{1/2})^2(1d_{3/2})^2(pf)^2\right)$ $\nu\left((1d_{5/2})^{6/5}(2s_{1/2})^1(1d_{3/2})^{1/2}\right)$
2_3^+		4.57	8.49		0.03		$\pi\left((1d_{5/2})^6(2s_{1/2})^2(1d_{3/2})^2(pf)^2\right)$ $\nu\left((1d_{5/2})^{6/5}(2s_{1/2})^1(1d_{3/2})^{1/2}\right)$
0_3^+	4.83(17)	4.36	4.64				$\pi\left((1d_{5/2})^6(2s_{1/2})^2(1d_{3/2})^4\right)$ $\nu\left((1d_{5/2})^6(2s_{1/2})^0(1d_{3/2})^2\right)$
4^+	6.54(14)	7.34	8.21	1.08(23)	2.22	2.15	$\pi\left((1d_{5/2})^6(2s_{1/2})^2(1d_{3/2})^4\right)$ $\nu\left((1d_{5/2})^5(2s_{1/2})^2(1d_{3/2})^1\right)$

Table 5.1: Summary of the experimental results and the results obtained with the *sd* and *sdpf* SM calculations, for the states experimentally identified in ^{36}Ca. Proposed spin parities are given in the first row. Experimental and theoretical excitation energies are given in the second, third and fourth row. Experimental and theoretical spectroscopic factors (C^2S) for the states populated in the ^{37}Ca(p,d)^{36}Ca reaction are given in the fifth, sixth and seventh row. The given C^2S are for the $d_{3/2}$ orbital, for the 0^+ for the $s_{1/2}$ orbital for the 2_1^+, 1^+ and 2_2^+ states and for the $d_{5/2}$ orbital for the 4^+. The main configuration of these states, according to the *sdpf* SM calculation, are given in the eighth row.

for such bubble structure have been recently found in the Z=14 nucleus ^{34}Si [75]. Despite the large amount of experimental studies that have been performed in the mirror nuclei ^{36}S, the analogue proton bubble state has never been observed. The most adapted reaction to populate this state in ^{36}S should be a two proton removal reaction such as the ^{38}Ar(^{14}C,^{16}O)^{36}S reaction, which has never been studied.

- The 0_2^+ intruder state

The measured energy of the 0_2^+ state $E_x^{Exp}(0_2^+) = 2.78(18)$ MeV is in very good agreement with the predicted value of the *sdpf* SM calculation $E_x^{sdfp}(0_2^+) = 2.7$ MeV. The *sdpf* calculation predicts

that such a state has an intruder proton configuration $\pi(sd)^{-2}\pi(pf)^2$. The most adapted reaction to populate this state should be a two proton transfer such as ^{34}Ar(^{3}He,n)^{36}Ca and one could doubt about the possibility to populate it using a two neutron transfer. However, a similar intruder state has been populated in ^{38}Ca both using the ^{36}Ar(^{3}He,n)^{38}Ca and the ^{40}Ca(p,t)^{38}Ca reactions. Numerous works have studied the ^{36}Ar(^{3}He,n)^{38}Ca reaction and reported the strong feeding of the second 0_2^+ state at 3.06 MeV in ^{38}Ca [76, 77, 78] and all agree about the dominant $\pi(d_{3/2})^{-2}\pi(f_{7/2})^2\nu(d_{3/2})^{-2}$ configuration of this state. A letter of S. Kubono and collaborators [79], reported the observation of an L=0 transition to the 3.06 MeV state in ^{38}Ca populated via the ^{40}Ca(p,t)^{38}Ca reaction. The amplitude of the cross section, corresponding to the feeding of the second 0_2^+ obtained in Ref. [79], has been explained in terms of configuration mixing. Indeed, the authors considered a proton configuration of the ground state ^{40}Ca being a mixture between the $0p$-$0h$ and the $\pi(d_{3/2})^{-2}\pi(f_{7/2})^2$ configuration, allowing to populate the second 0_2^+ in ^{38}Ca through the mixing. It is very probable that the same effect is observed in this work, the 0_2^+ state in ^{36}Ca being populated via the ^{38}Ca(p,t)^{36}Ca through the mixing of the ground state of ^{38}Ca with the excited $\pi(d_{3/2})^{-2}\pi(f_{7/2})^2$ proton configuration. It is interesting to note that the intruder state is more populated, relatively to the ground state, in ^{36}Ca than in ^{38}Ca. One can find in Ref. [79] the ratio of cross sections $\frac{\sigma(g.s.\rightarrow 0_2^+)}{\sigma(g.s.\rightarrow g.s.)} \simeq 0.02$ for the ^{40}Ca(p,t)^{38}Ca while, in this work we found $\frac{\sigma(g.s.\rightarrow 0_2^+)}{\sigma(g.s.\rightarrow g.s.)} \simeq 0.2$ for the ^{38}Ca(p,t)^{36}Ca reaction. This indicates a stronger mixing of the ground state with the intruder proton configuration in ^{38}Ca than in ^{40}Ca.

- The second 2_2^+ state

The second 2_2^+ state has been identified in ^{36}Ca at an excitation energy of $E_x^{Exp}(2_2^+) = 4.71(9)$ MeV. The *sdpf* SM calculations predicts a second and a third 2^+ states at $E_x^{sdpf}(2_2^+) = 3.81$ MeV $E_x^{sdpf}(2_3^+) = 4.57$ MeV, respectively, having an intruder configuration (see Table 5.1). The *sd* SM calculation predicts the second 2_2^+ state at $E_x^{sd}(2_2^+) = 6.25$ MeV, with a $2p$-$2h$ $\nu(s_{1/2})^{-2}\nu(d_{3/2})^2$ neutron configuration coupled to $J = 2$. The closest theoretical value, as compared to the experimental one, is the one of the 2_3^+ intruder state computed in *sdpf* valence space. However, its theoretical spectroscopic factor of 0.03 is not in agreement with the observed one of 0.28(6), being closer to the C^2S value of 0.10 found for the 2_2^+ intruder state in the *sdpf* SM calculation. The comparison to the mirror nucleus ^{36}S, which is presented in the next section, may help in understanding the underlying structure of this state. Investigations about its structure are still ongoing.

- The first 4^+ state

The first 4^+ has been identified in ^{36}Ca at an energy of 6.54(14) MeV. Its large $L = 2$ spectroscopic factor is a sign of a rather pure $1p-1h$ $d_{3/2}-d_{5/2}$ neutron configuration. Its excitation energy is reproduced by none of the SM calculations: it is found at 8.21 MeV by the *sd* SM calculation and at 7.34 MeV by the *sdpf* SM calculation. The obtained spectroscopic factor in the present work is smaller than those predicted by SM calculations, which indicates a stronger fragmentation of the $d_{5/2}$ strength as compared to what is obtained in the SM calculations. This is discussed in more details in Section 4.

2 Emergence of Colossal Mirror Energy Differences

The *sdpf* SM calculation successfully reproduces the energy of most of the excited states observed experimentally in ^{36}Ca. Here we discuss how Coulomb effects play a major role in the observed excitation energies and how it generates Colossal Mirror Energy Differences (CMED) as named in Ref. [37].

The figure of Table 5.2 shows the partial level scheme of the mirror pair ^{36}S-^{36}Ca. Only the two pure *sd* states 2^+ and 1^+ and the three states having an intruder proton configuration 0^+_2, 2^+_2 and 2^+_3 are shown for ^{36}S. The corresponding levels experimentally identified are shown for ^{36}Ca. The predictions of the energies of these states made by the *sdpf* SM calculation are also shown for both nuclei. A specificity of this work, compared to other studies performed at the proton drip-line, is that the states populated by our neutron removal reactions imply very bound neutron configuration (except for the intruder states). Therefore, despite the fact that all the discussed states lie in the continuum, the presently observed energy shifts can be reproduced by the sole action of the Coulomb force. The predicted MED for the states shown in the level scheme of Fig. 5.2 are given in the table of Fig. 5.2.

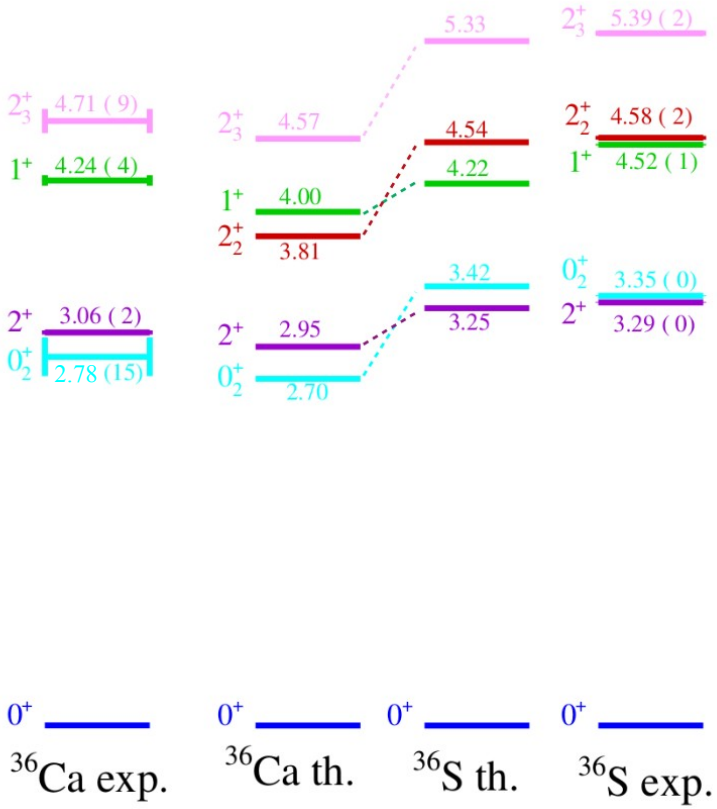

J^π	MED	
	Exp.	Th.
0^+_2	-570(180)	-720
2^+_1	-240(16)	-300
1^+_1	-280(40)	-220
2^+_2		-730
2^+_3	-680(90)	-760

Table 5.2: Left: Partial Level scheme of the mirror pair ^{36}S-^{36}Ca. Only the levels of ^{36}S relevant for the discussion are shown, together with the corresponding levels identified in ^{36}Ca . The experimental results are compared to the SM calculation performed in *sdpf* valence space. In order to ease the comparison with the *sdpf* SM results, the 2^+ state at 4.71 MeV in ^{36}Ca is labeled as 2^+_3 in this figure, conversely to Fig 5.1 and Table 5.1, in which it was labeled as 2^+_2. Right: Experimental an theoretical MED obtained for these states.

2.1 The large MED of the 2^+ and 1^+ *sd* states

The experimental Mirror Energy Difference (MED) of the first 2^+ excited state of the A=36, T=2 mirror pair is found to be $\Delta E_M(2^+) = E_x(2^+,{}^{36}\mathrm{Ca}) - E_x(2^+,{}^{36}\mathrm{S}) = -240(16)$ keV in this work (also given in the Table of Fig. 5.2), similarly to what was obtained in previous studies [34]. In the work of Ref. [34], this MED has been successfully reproduced using a USD interaction with SPE fitted on the experimental values of the A=17, T=1/2 mirror pair, which empirically account for the Thomas-Ehrman shifts and Coulomb effects. The *sdfp* SM calculation presented in this work, successfully reproduces the excitation energy of the first 2^+ excited state in both ^{36}Ca and ^{36}S (as shown in Fig. 5.2) leading to a MED of $\Delta E_M = -300$ (given in the Table of Fig. 5.2 and in Ref. [37]). Both models reproduce these large MED with the same mechanism, originating from Coulomb effect, as explained below.

In this work, a new 1^+ state has been observed at $E_x(1^+,{}^{36}\mathrm{Ca}) = 4.24$ MeV in ^{36}Ca. Its isobaric analogue state is found to be at $E_x(1^+,{}^{36}\mathrm{S}) = 4.52$ MeV in the mirror nucleus leading to a MED of $\Delta E_M(1^+) = -280\ keV$. The 1^+ state having the same structure than the 2^+_1, it is the same mechanism (described below) that produces these large MED, and it is, therefore, expected to found similar MED for these two states. As for the first 2^+ state, the *sdfp* SM calculation successfully reproduced the excitation energy of this state in the mirror pair and the MED with a theoretical value of $\Delta E_M(1^+) = -220\ keV$.

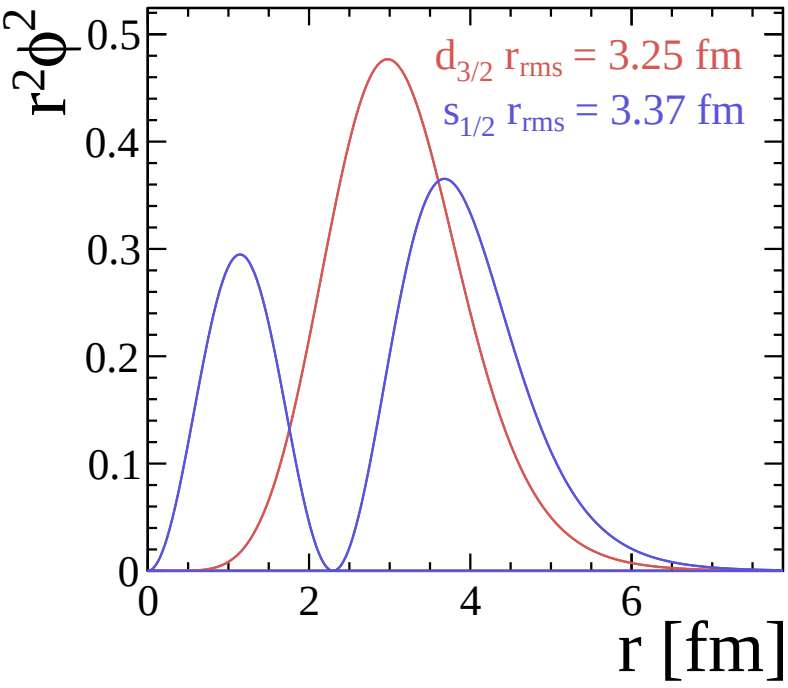

Figure 5.2: Evolution of the square of the bound-state radial wave function multiplied by squared radial distance as a function of the radial distance, shown for the $2s_{1/2}$ (in blue) and $1d_{3/2}$ (in red) neutron orbitals in ^{36}Ca.

The first 2^+ and 1^+ excited states in ^{36}Ca have a neutron configuration $\nu(s_{1/2})^{-1}\nu(d_{3/2})^1$ while the isobaric analogue states in the mirror nuclei have a proton configuration $\pi(s_{1/2})^{-1}\pi(d_{3/2})^1$. These states have a rather pure configuration with spectroscopic factors close to the single particle picture (see Section 1.2.4 of Chap. 4). Fig. 5.2 shows the radial wave functions of the $s_{1/2}$ and $d_{3/2}$ neutron orbitals in ^{36}Ca. The wave functions have been calculated with FRESCO code [63] using a Woods-Saxon potential whose depth has been adjusted to reproduce the neutron separation energy. A radius of 1.27 fm and a diffuseness of 0.67 fm have been used, following the prescription of Ref. [14]. The obtained root-mean-square radius for the $2s_{1/2}$ orbital of $r_{s_{1/2}} = 3.37$ fm is very similar to what was found in Ref. [80]. For the $1d_{3/2}$ orbital, the obtained root-mean-square radius is lower than the one of the $2s_{1/2}$ orbital with a value of $r_{d_{3/2}} = 3.25$ fm (due to the difference of principal quantum number $\Delta n = 1$). The Coulomb potential being proportional to $\frac{1}{r^2}$, a proton in the $d_{3/2}$ orbital will be more sensitive to the Coulomb repulsion than a proton in the $s_{1/2}$ orbital. Therefore, the cost in energy to promote a nucleon from the $s_{1/2}$ to the $d_{3/2}$ will be higher in the case of a proton excitation (^{36}S) than for a neutron excitation (^{36}Ca). This picture is in line with the observed higher excitation energies of the 2^+_1 and 1^+_1 states in ^{36}S than in ^{36}Ca.

One can illustrate this effect with a simple calculation. Considering the interaction of a proton in an orbital of radius r, with a core of Z protons, its coulomb energy is given by: $E_c = k_e \frac{Z}{r}$, where k_e is the Coulomb constant. Using this equation, the difference of Coulomb energy between a proton sitting on the $s_{1/2}$ orbital and an other one, sitting on the $d_{3/2}$ orbital is given by:

$$\Delta E_c = k_e Z \frac{r_{d_{3/2}} - r_{d_{1/2}}}{r_{d_{3/2}} r_{d_{1/2}}}. \tag{5.1}$$

Considering a core of $Z = 14$ protons, one obtains a difference of Coulomb energy of about 220 keV between the proton in the $s_{1/2}$ orbital and the one in the $d_{3/2}$ orbital, which already reproduces well the observe MED. In other terms, due to Coulomb effects, the $Z = 16$ gap in ^{36}S between the $s_{1/2}$ and the $d_{3/2}$ orbital is larger than the $N = 16$ gap in ^{36}Ca and the evolution of the size of the gap is directly given by the value of the MED. The MED of the first 2^+ and 1^+ states of the A=36, T=2 mirror pair, are therefore a direct probe of the shell structure of these nuclei and consequently, of the radial wave functions of the single-particle orbitals of the valence nucleons.

2.2 The Colossal MED of the 0^+_2, 2^+_2 and 2^+_3 intruder states

In this work, a second 0^+_2 excited state has been identified for the first time in ^{36}Ca at an energy of $E_x(0^+_2, ^{36}Ca) = 2.78(18)$ MeV. Its isobaric analogue state is the 0^+_2 excited state located at $E_x(0^+_2, ^{36}S) = 3.346$ MeV (see Fig. 5.2). Its main configuration corresponds to the promotion of a pair of neutron from the filled $d_{3/2}$ orbital to the $f_{7/2}$ orbital in the upper shell. This has been shown by the strong population of this state in the ^{34}S(t,p)^{36}S reaction [81]. This 0^+ intruder state has been extensively studied along the N=20 isotones leading to the discovery of the Island of Inversion (IoI) around Z=12, N=20. In this region, the reduction of the N=20 shell gap together with strong proton-neutron quadrupole correlations leads to this low-lying deformed $2p$-$2h$ intruder state to compete with the spherical $0p$-$0h$ configuration [82].

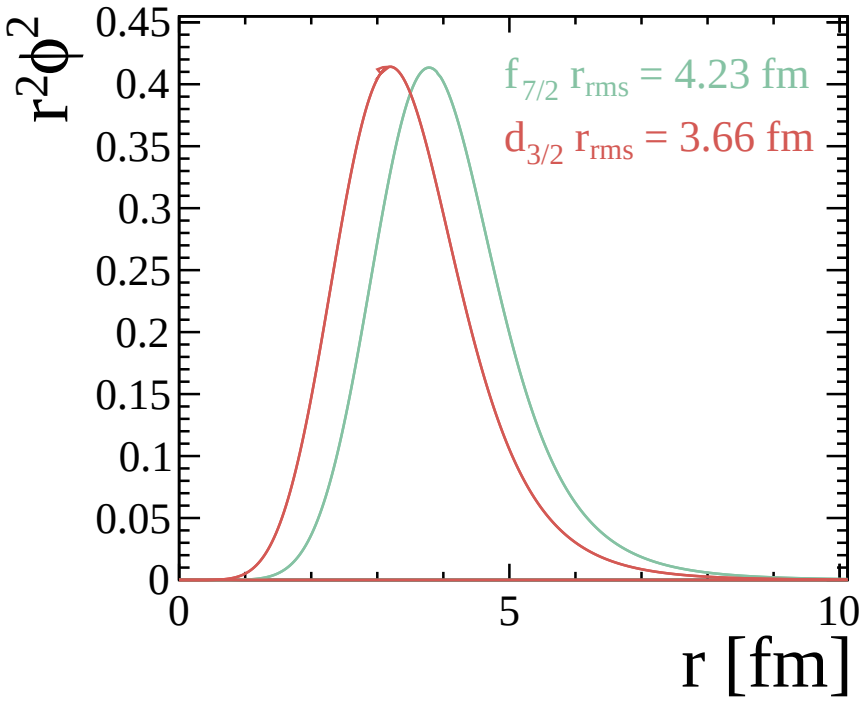

Figure 5.3: Evolution of the square of the bound-state radial wave function multiplied by squared radial distance as a function of the radial distance, shown for the $1d_{3/2}$ (in red) and $1f_{7/2}$ (in green) proton orbital in ^{36}Ca .

The 0_2^+ excited state in ^{36}Ca has the mirror configuration with a pair of proton promoted from the filled $d_{3/2}$ orbital to the $f_{7/2}$ orbital in the upper shell. Fig. 5.3 shows the bound-state radial wave functions of the proton in ^{36}Ca in the $d_{3/2}$ and the $f_{7/2}$ orbital (the wave function corresponding to the $f_{7/2}$ orbital being unbound, it has been computed using the weakly bound approximation). One can see that the proton in the $f_{7/2}$ orbital will be less sensitive to the Coulomb repulsion than in the $d_{3/2}$ orbital since the mean radius of the $f_{7/2}$ is larger. This leads to an effective reduction of the Z=20 gap as compared as the N=20 gap in the mirror nucleus ^{36}S. This is the same effect as the one discussed above for the *sd* states. It is interesting to note that this effect is already observed in the ^{38}Ca nuclei where the intruder 0_2^+ state is observed at 3.084 MeV while the isobaric analogue state is observed at 3.378 MeV in the mirror ^{38}Ar nuclei, leading to a large MED of -293 keV.

In the case of ^{36}Ca, deformation plays an important role in the explanation of the observed CMED. Indeed, the deformed nature of the intruder band, tends to mix configurations that differ by two units in angular momentum [11]. Therefore, the neutron $s_{1/2}$ and $d_{3/2}$ orbitals have a larger mixing in the intruder band than in the spherical band, leading to an important contribution of the $\nu(s_{1/2})^{-1}\nu(d_{3/2})^1$ configuration in the neutron structure of the intruder 0_2^+ state. Then, the Coulomb effect on the Z=16/N=16 gap, discussed above for the *sd* state, shall also apply to the intruder state. Both effects summed coherently lead to a CMED of -570(180) keV. In the case of ^{38}Ca, the neutron configuration $\nu(s_{1/2})^2\nu(d_{3/2})^2$ remains unchanged when going from the ground state to the 0_2^+ configuration because two neutrons are already occupying the $d_{3/2}$, $k = 1/2$ Nilsson orbital with which the $s_{1/2}$ orbital is

strongly mixed. Therefore, only the proton intruder configuration contribute to the MED of the 0_2^+ state of the ^{38}Ca-^{38}Ar mirror pair, leading to a smaller MED as compared to the one of ^{36}Ca-^{36}S.

The observed CMED of the 0_2^+ state in ^{36}Ca-^{36}S mirror pair is well reproduced, within uncertainties, by the *sdpf* calculation presented in Fig. 5.2 with a predicted value of -720 keV. Furthermore, the SM calculation predicts a CMED for the second and third 2_2^+ and 2_3^+ states of -730 keV and -760 keV respectively (see Fig. 5.2). These states are predicted by the SM calculation to belong to the same deformed intruder band than the 0_2^+ state, inducing the same Coulomb effects discussed above. The resulting 2_2^+ excitation energy is predicted to be 3.81 MeV in ^{36}Ca, while the one of the 2_3^+ is 4.57 MeV. Experimentally, a second 2^+ has been identified in ^{36}Ca at 4.71 MeV. From the above discussion, one may propose that this state is the isobaric analogue state of the 2_3^+ state at 5.391 MeV in ^{36}S, leading to an observed MED of -685(100) keV, in good agreement with the predicted value. From this picture, a 2^+ is missing in ^{36}Ca , being the analogue state of the 4.577 MeV 2^+ state in ^{36}S. It is predicted to be at an excitation energy of 3.81 MeV but no sign of this state has been seen in any of the spectra during the analysis.

J^π	C^2S	
	^{36}Ca	^{36}S
0^+	1.06(21)	1.06(21)
2_1^+	0.66(13)	0.86(17)
1^+	0.61(12)	0.75(15)
2_2^+		0.25(5)
2_3^+	0.28(6)	

Table 5.3: Experimental spectroscopic factors (C^2S) for the states populated in the ^{37}Ca(p,d)^{36}Ca and in the ^{37}Cl(d,^{3}He)^{36}S [57] reaction. The C^2S values for the ground state are given for the $d_{3/2}$ orbital and the others for the $s_{1/2}$ orbital. See section 1.2.4 for details about this values.

Finally, it is interesting to compare the values of the extracted spectroscopic factors between the two mirror nuclei. The C^2S values of the states populated in the ^{37}Ca(p,d)^{36}Ca reaction are given in Table 5.3 and are compared to the ones of the analogue states populated in the mirror nucleus ^{36}S using the mirror reaction ^{37}Cl(d,^{3}He)^{36}S. For the ground, 2_1^+ and 1^+ states, the C^2S values are equivalent in both nuclei meaning that the configuration of these states is well preserved by the mirror symmetry. Indeed, even if we are dealing with proton-unbound states in ^{36}Ca, the corresponding configurations imply deeply bound neutron orbits which are not affected by the continuum. The picture is less clear for the intruder 2^+ states. Indeed, in the discussion above, we would associate the 2^+ state at 4.71 MeV in ^{36}Ca to the third 2^+ state at 5.391 MeV in ^{36}S. However, the 2^+ state at 4.71 MeV in ^{36}Ca has been populated in the ^{37}Ca(p,d)^{36}Ca with value of spectroscopic factor of 0.28(6), very similar to the one of the second 2^+ state at 4.58 MeV in ^{36}S of 0.25(5). Moreover, as discussed in Section 1, theoretical C^2S for the third 2^+ state in ^{36}Ca is not in agreement with the observed one. The true nature of this 2^+ state at 4.71 MeV is still under investigation and remains an open question up to now.

3 The $N = 16$ gap

The enhanced excitation energy of first 2^+ excited state is a good indicator of nuclear shell gaps and is a crucial observable for the search of new magic numbers. Fig. 5.4 shows the systematics of the excitation energy of the first 2^+ excited state along the Ca isotopic chain for even-N nuclei. In this figure, one can clearly identify the $N = 20$ and $N = 28$ neutron magic numbers with a high excitation energy of about 4 MeV. Recent experimental studies proposed $N = 32$ and $N = 34$ as new magic numbers from the high excitation energies of the first 2^+ state of ^{52}Ca and ^{54}Ca [83]. At $N = 16$, a strong sub-shell closure is found through the observation of the large excitation energy $\mathrm{E}(2^+) = 3.045$ MeV [36] of the 2^+_1 excited state in ^{36}Ca. This value likely largest than the ones of ^{52}Ca and ^{54}Ca and is a sign of a sizable gap at $N = 16$.

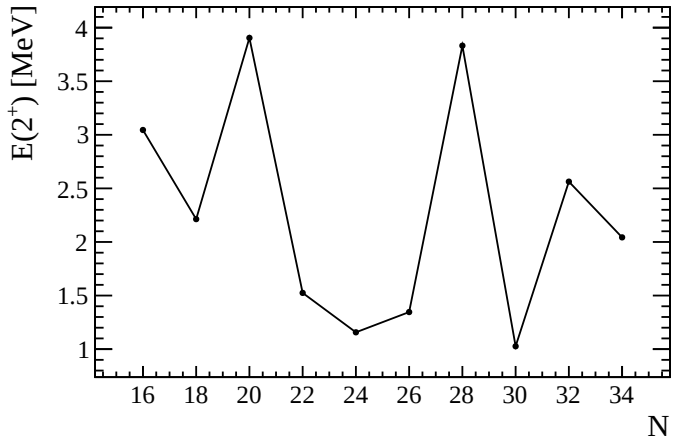

Figure 5.4: Systematics of the excitation energy of the first 2^+ excited state along the Ca isotopic chain for even-N nuclei.

The one neutron separation energy is given by the difference of binding energy between the N and $N-1$ isotopes: $S_n = B(Z,N) - B(Z,N-1)$. The binding energy encodes information of the energy gap between orbitals at the fermi surface and is therefore a crucial tool to study shell closures in exotic regions. In Chapter 4, the measurement of the mass excess of ^{35}Ca $\Delta M_{exp}(^{35}\mathrm{Ca}) = 4805(140)$ keV has been presented. This mass measurement allows to derive the one neutron separation energy of ^{36}Ca $S_n(^{36}Ca) = 19.359(146)$ MeV which is used here to study the $N = 16$ gap.

Left part of Fig. 5.5 shows the systematics of the one neutron separation energy along the Ca isotopic chain. On this figure one can see clearly when neutrons start to fill a new orbital at N=16, 20, 28, 32, and 34. Large gap, in the S_n systematics can be observed at this neutrons numbers. In order to study more in details the energy gaps between orbitals, one can look at the difference of the one-neutron separation energy between the N and $N+1$ isotopes. This is shown on the right part of Fig. 5.5. On this figure one can clearly identify the N=20 and 28 magic numbers, lying well above the odd-even staggering, which is associated to pairing correlation. Recent mass measurements performed on neutron-rich Ca isotopes established a prominent shell closure at $N = 32$ and $N = 34$ [84, 85] which can be seen to a smaller extent in this figure as well. The mass measurement of ^{35}Ca performed in this work allows to add the $N = 16$ point to the systematics. This point lies well above the odd-even

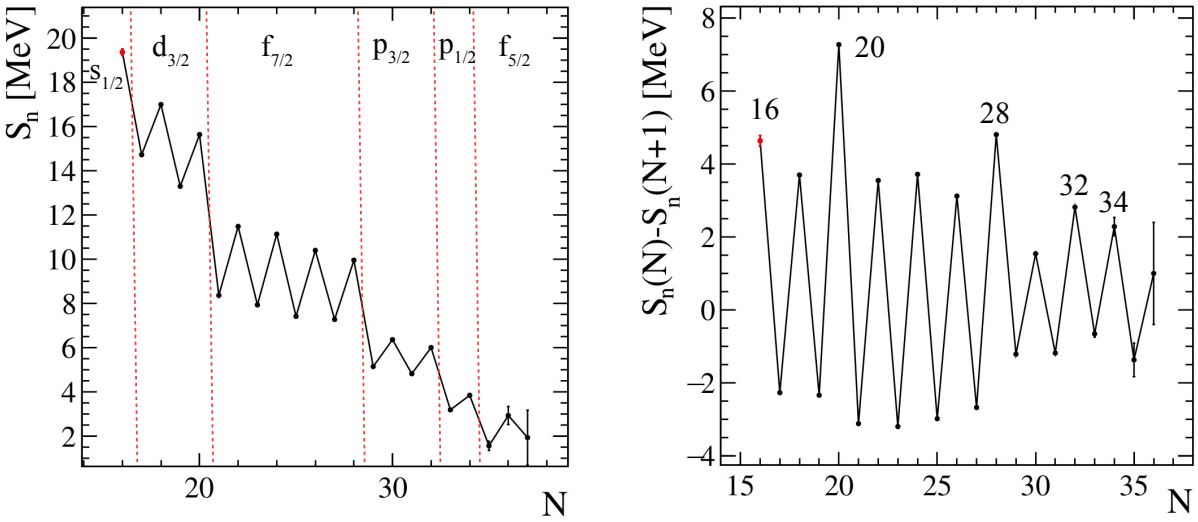

Figure 5.5: Left: Systematics of the one-neutron separation energy along the Ca isotopic chain. The neutron numbers corresponding to the shell gaps are shown by vertical red lines. The point added to the systematics by this work is highlighted in red. Right: Systematics of the difference of the one-neutron separation energy between the N and $N+1$ isotopes. The point added to the systematics by this work is highlighted in red

staggering, which is a sign of a sizable gap at $N = 16$.

Another way to look at the size of the $N = 16$ gap is to study the evolution of the first $\frac{3}{2}^+$ excited state along the $N = 15$ isotonic chain. Indeed, for the $N = 15$ isotones, the ground state configuration corresponds to a single neutron in the $s_{1/2}$ orbital. The main configuration of the first $\frac{3}{2}^+$ excited state corresponds to the promotion of the neutron from the $s_{1/2}$ to the $d_{3/2}$ orbital, which excitation energy is diretly related to the size of the $N = 16$ gap. The systematics of the excitation energy of the first $\frac{3}{2}^+$ excited state, along the $N = 15$ isotonic chain, is shown in Fig. 5.6. The emergence of the $N = 16$ magic number is clearly seen in the neutron-rich region. The high excitation energy of the $\frac{3}{2}^+$ state in ^{23}O sign for a large $N = 16$ gap. This has been interpreted as an effect of the tensor force. Indeed, by moving from ^{29}Si ($Z = 14$) to ^{23}O ($Z = 8$), one removes protons from the $d_{5/2}$ orbital. Due to the strong proton-neutron interaction $d_{5/2} - d_{3/2}$, when emptying the $\pi d_{5/2}$ the effective single particle energy of the $\nu d_{3/2}$ increases so much that it becomes near the fp shell, forming a large gap between the $\nu s_{1/2}$ and the $\nu d_{3/2}$ [86].

From the analysis of the ^{37}Ca(p,t)^{35}Ca reaction, the first $\frac{3}{2}^+$ excited state has been identified in ^{35}Ca at an excitation energy of 2.24(33) MeV. This point is added to the systematics in Fig. 5.6. One can see a clear increase of the $\frac{3}{2}^+$ excitation energy when going from ^{31}S ($Z = 16$) to ^{35}Ca ($Z = 20$). A possible interpretation of such a shift is that when going from ^{31}S to ^{35}Ca, one adds four protons to the $d_{3/2}$ orbital. The effect of the proton-neutron tensor force (which is repulsive between $l+1/2$ and $l'+1/2$ orbitals [5]) will be to increase the ESPE (see Section 1.2 in Chap. 1) of the neutron $d_{3/2}$ orbital while it will not act on the $s_{1/2}$. This effect increases the size of the gap between the $\nu s_{1/2}$ and the $\nu d_{3/2}$ orbitals making $N = 16$ a strong sub-shell closure at $Z = 20$. However, the TBME see Section 1.2 in Chap. 1) computed by Otsuka *et al.* [8] gives small and similar values of $V_{pn}(d_{3/2}, d_{3/2})$ and $V_{pn}(d_{3/2}, s_{1/2})$ which does not affect significantly the size of the $N = 16$ gap. Another explanation

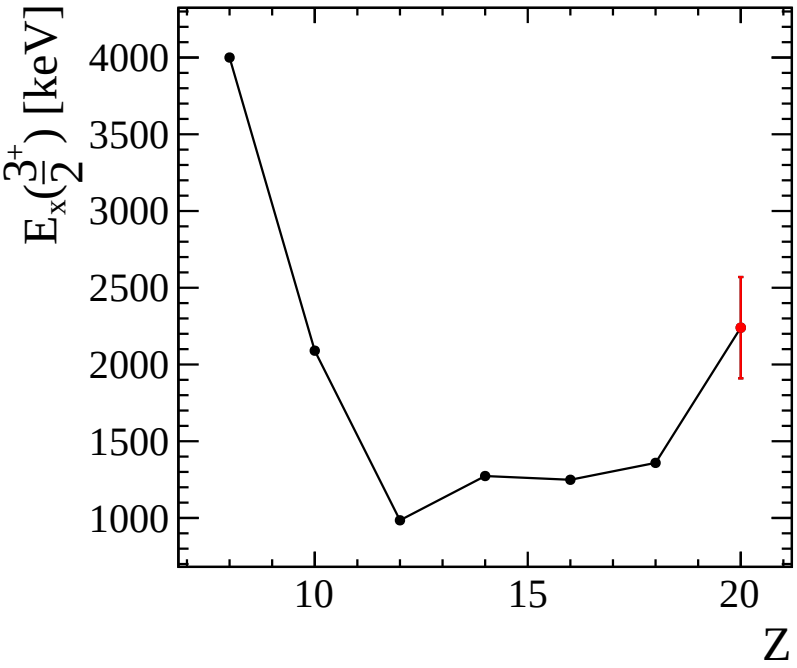

Figure 5.6: Systematics of the excitation energy of the first $\frac{3}{2}^+$ excited state along the $N = 15$ isotonic chain for even-Z nuclei. The point added to the systematics by this work is highlighted in red.

could be that the strong shell closure at $Z = 20$ enhances the excitation energy of the $\frac{3}{2}^+$ in ^{35}Ca while for the other isotones, the excitation energy is lower because protons are either in an open shell or in less sizable sub-shell closure. The interpretation of this part is still ongoing.

The magic character of $N = 16$ is also supported by the high excitation energy of the first 2^+ and 1^+ state of ^{36}Ca, which have pure $1p-1h$ neutron configuration, across the $N = 16$ gap. Moreover, several relativistic mean field calculations predicted a spherical ground state for ^{36}Ca [87, 88], which is the expected structure for a doubly magic nuclei. All these elements confirm the doubly magic nature of the $Z = 20$, $N = 16$, ^{36}Ca nucleus.

4 The $d_{5/2}$ strength

In Chap. 4 Section 1.2.4, the DWBA analysis of the differential cross section of the ^{37}Ca(p,d)^{36}Ca reaction has been presented. This analysis allowed to identify the majority of the $d_{5/2}$ strength in ^{36}Ca up to about 9.5 MeV, with a total spectroscopic factor of about 4.5. These states having a $1p-1h$ $d_{3/2}-d_{5/2}$ neutron configuration, their excitation energies are directly linked to the size of the $d_{3/2}-d_{5/2}$ neutron spin-orbit splitting and the comparison of the position of the strength between mirror nuclei allows to probe the evolution of the spin-orbit splitting under the isospin symmetry.

Fig 5.7 shows the cumulative $d_{5/2}$ strength as a function of the excitation energy for ^{36}Ca. The cumulative $d_{5/2}$ strength is obtained by summing the neutron spectroscopic factors corresponding to the $d_{5/2}$ orbital. Due to the limited resolution of the excitation energy spectrum, a precise energy centroid of the states could not be determined. The only state that has been identified without ambiguity is

the first 4^+ state at 6.54(14) MeV, which has a particle-hole neutron configuration $\nu(d_{5/2})^{-1}\nu(d_{3/2})^1$ with a $d_{5/2}$ neutron spectroscopic factor of 1.08. However, the majority of the $d_{5/2}$ strength has been collected.

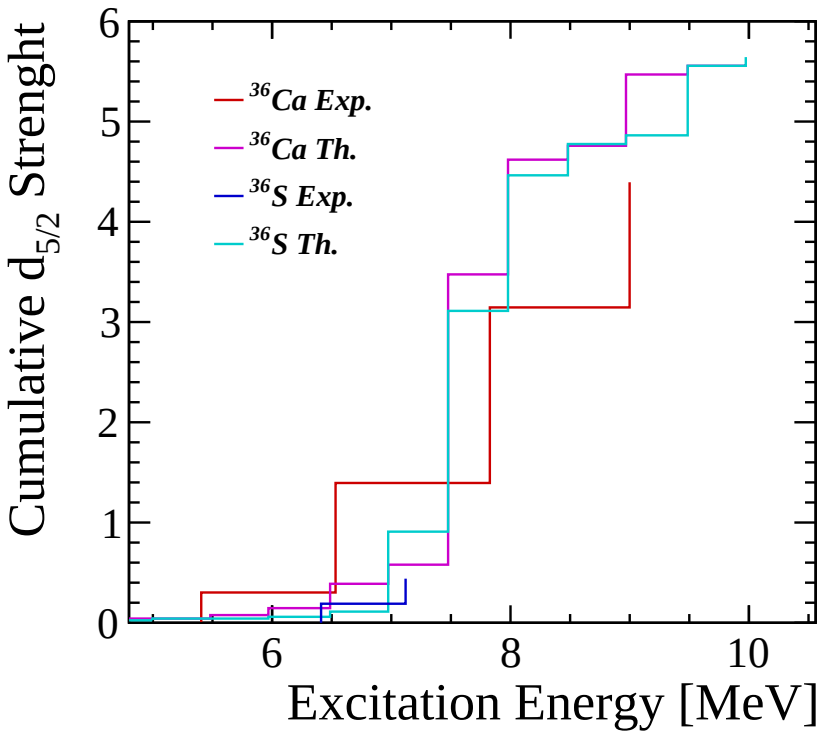

Figure 5.7: Cumulative $d_{5/2}$ strength of ^{36}Ca and ^{36}S. Experimental results are compared to SM calculations.

In the mirror nucleus ^{36}S, only a small fraction of the $d_{5/2}$ strength has been identified with a summed spectroscopic factor of 0.63 up to 7.7 MeV [57]. The experimental cumulative $d_{5/2}$ strength as a function of the excitation energy for ^{36}S is shown as well in Fig 5.7. The first 4^+ state has been also identified at 6.51 MeV with a spectroscopic factor of 0.19. One can notice the small MED observed in the energy of the 4^+ state. This is expected since this state has $1p$-$1h$ configuration between the two $d_{5/2}$ and $d_{3/2}$ orbitals. These orbitals sharing the same principal and angular momentum quantum numbers, their radial wave functions are nearly identical and no Coulomb shifts is expected to be observed using the mechanism discussed above. Conversely, a large isopin assymmetry is seen in the spectroscopic factors of this state with a factor 5 times larger observed in ^{36}Ca . In Ref. [57], the authors concluded that "the $d_{5/2}$ strength is fragmented into many levels which were not detected". Nevertheless, levels have been detected up to 8 MeV in Ref. [57] and in ^{36}Ca the summed spectroscopic factor up to 8 MeV is about 3.

SM calculations have been performed to get an insight on the expected position of the $d_{5/2}$ strength in ^{36}S. The cumulative strength for the ^{36}Ca -^{36}S mirror pair is shown as well in Fig 5.7. One can see that the overall trend and centroid of the ^{36}Ca strength function is well reproduced. The strength function of ^{36}S is found to be very similar to the one of ^{36}Ca by the SM model calculation. If so, a larger fraction of the $d_{5/2}$ strength should have been identified in Ref. [57]. Therefore, such a

difference in the observed $d_{5/2}$ strength in the mirror pair is yet not understood. A possibility could be that the $d_{5/2}$ strength is much more fragmented in ^{36}S than in ^{36}Ca , meaning that a strong isospin symmetry breaking would be observed in the residual interaction between the valence neutron in ^{36}Ca as compared to the valence protons in ^{36}S. Another explanation could be that the neutron $d_{3/2} - d_{5/2}$ spin-orbit splitting is stronger in ^{36}S than in ^{36}Ca, sending the $d_{5/2}$ strength at higher energy. Such an isospin symmetry breaking effect on the spin-orbit splitting has never been observed so far and the identification of the $d_{5/2}$ strength in ^{36}S is therefore highly desired.

Part II

Nuclear Astrophysics

6 Motivations

Sommaire

This chapter presents the astrophysics motivation of the study of ^{36}Ca. First, a general introduction about Type Ia X-ray burst will be given. Then the *rp*-process which is an nucleosynthesis process occurring in type Ia X-ray burst will be presented, as well as some sensitivity studies. Finally, the state of our knowledge about the ^{35}K(p,γ)^{36}Ca reaction rate will be given.

1 Type Ia X-ray bursts

Type-I X-ray bursts are among the most energetic events known in the universe. They are recurring thermonuclear flashes which occur in binary systems formed of a neutron star and a companion star. Fig. 6.1 shows an artistic view of the binary system. The companion star is a normal star, expected to have a similar composition to the Sun with H/He-rich material at its surface. As the sun-like star evolves, it grows, it fills its Roche lobe and it transfers material through its inner Lagrangian point to the neutron star [89]. Due of the angular momentum of the mass-losing star, the transferred material forms an accretion disc around the compact object. In this accretion disc, temperature and density can reach extreme values.

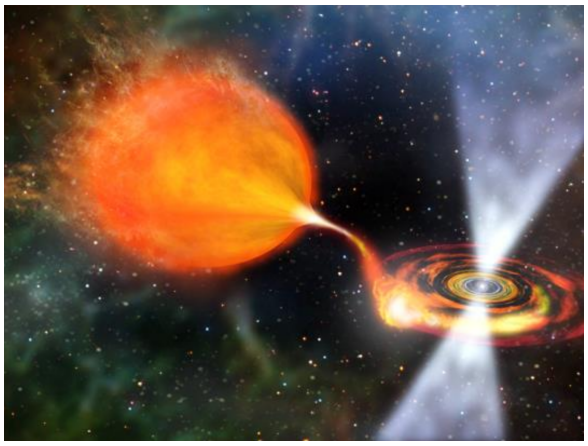

Figure 6.1: Artistic view of a binary system formed by a neutron star and a sun-like star.

Fig. 6.2 shows a schematic view of the X-ray burst mechanism. The H/He-rich material is accreted to the accretion disk of the neutron star. Friction between the inner layer and the outer layer of the disk, heats the disk and generates continuous ultraviolet and X-ray emission. Because of the friction, the accreted material transfers its angular momentum to the outer layers of the disk and fall toward the surface of the neutron star. The H material spreads over the surface and forms a shell of only about 1 m thick. The more material is accreted, the more the temperature and density increase. The H layer will then start to fuse, producing an underlying He layer, at the surface of the neutron star. Eventually, temperature and density in the He layer reach threshold values (T$\simeq 10^9$ K and $\rho \simeq 10^6$ $g cm^{-3}$) and the He starts to burn. A thermonuclear runaway occurs, triggering a chain of nuclear reactions releasing a huge amount of energy (about 10^{39} erg, corresponding to the energy released by the sun in 3 days). This thermonuclear flash heats the envelope of the star up to few 10^9 K, leading to a sharp increase of X-ray emission from the star. Thermonuclear burning spreads throughout the envelope as a convective flame, consuming most of the available fuel in about 1 s. The

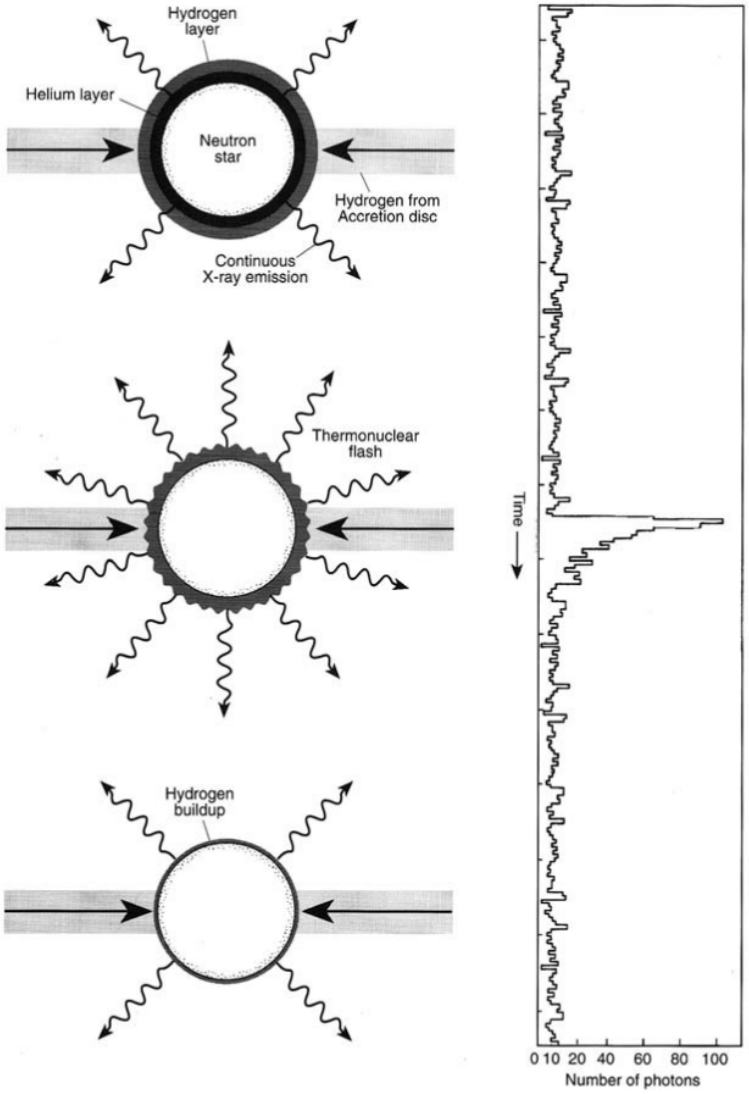

Figure 6.2: Schematic view of a X-ray burst. The time spectrum shown on the right side of the figure corresponds to the first historical observation of an X-ray burst [90]. See text for details. (Figure is from Ref. [91])

X-ray flash lasts typically between 1 and 100 s. When all the fuel is consumed, the temperature goes down. A new H layer starts to form on the surface of the neutron star and the cycle can start again. The burst recurrence time depends on the rate at which matter is being accreted and lies from hour to days. It can be very regular, as the signal shown in Fig. 6.3, or irregular.

Since the first historical observation of an X-ray burst in 1976 [90], up to 115 burst sources have been identified [94]. Numerous of long duration satellites missions reported thousands of X-ray bursts observations. A key instrument is the Proportional Counter Array on-board of the Rossi X-ray Timing Explorer (RXTE) [95]. This instrument with timing resolution of 1 μs has allowed detailed studies of spectral and timing properties of about a thousand of bursts.

One of the most important challenges in studying X-ray bursts is understanding the observed luminosity profile, which is directly related to the energy released by the nuclear reactions occurring

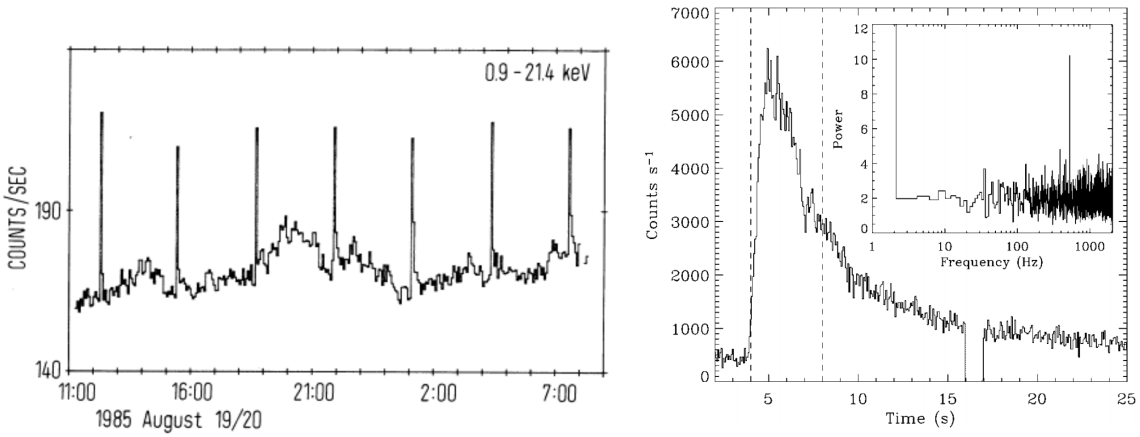

Figure 6.3: Left: X-ray burst light curve of X-ray source 4U/MXB 1820-30 in the globular cluster NGC 6624. Figure adapted from Ref. [92]. Right: Burst from the X-ray source A1744-361. The inset panel shows the power spectrum of the first 4 s interval. A peak at 530 Hz is found corresponding to the burst oscillation. Figure adapted from Ref. [93].

during the thermonuclear explosion. The comparison of the observed light curves to the X-ray burst model predictions may be used to constrain the properties of the neutron star sush as its mass, radius and spin frequency [96]. An example of such a study is shown in the right part of Fig. 6.3. It shows the X-ray burst light curve of the low mass X-ray binary system A1744-361 observed by the RXTE obtained in Ref. [93]. Since the ignition starts from a hot-spot at the surface of the neutron star, millisecond period oscillation can be observed in the rising part of the luminosity profile, due to the spin of the neutron star. A measurement of this burst oscillation frequency provides a direct measurement of the neutron star spin frequency. The insert in Fig. 6.3 left, shows the Fourier analysis of the rising part of the luminosity profile. A strong peak is observed at 530 Hz arising from the burst oscillation. The authors concluded therefore about the spin frequency of the neutron star to be 530 Hz. Furthermore, the decrease in oscillation amplitude during the rising time provides a probe of how the thermonuclear flames spread across the stellar surface. This process depends on properties of the accreted burning layer, surface fluid motions, and the surface magnetic field structure, and thus can provide insight into these stellar properties [97].

X-ray bursts can also be used to study the composition of the neutron stars. The composition of the deepest layers of the crust of accreting neutron stars is still not yet well known. Since the neutron star crust is composed of X-ray burst ashes, a precise knowledge of the final isotopic abundances of X-ray burst is needed to constrain the neutron star composition [98]. The crust parameters can also be constrained using the light curve of X-ray bursts. In Ref. [99] the authors reproduced the cooling tail of the light curve with a time-dependent cooling calculation and managed to constrain the thermal conductivity of the neutron star crust. Their results provide evidence in favor of the existence of a neutron superfluid in the inner crust.

The constraints made on the neutron star properties cited above relie on X-ray burst models which results are very sensitive to nuclear physics inputs. These inputs concern fundamental properties of nuclei such as masses and cross sections or resonances properties of the involved nuclei (resonance energies, spins, widths or spectrsocopic factors) needed to calculate the thermonuclear reaction rates

of the involved reactions. A precise knowledge of these quantities allows a better predictive power of the X-ray burst models and therefore a better precision on the determination of the neutron star parameters. There is, therefore, a crucial need of nuclear physics inputs, to better constrain the astrophysical models and to better understand the X-ray burst observables.

2 The *rp*-process and sensitivity studies

To understand the physics of X-ray burst, its light curve and final isotopic abundances, one has first to understand the underlying nuclear physics of this phenomenon. Fig. 6.4 shows the main path of the nuclear reaction flow during X-ray bursts. Prior to ignition, for temperature $T > 8 \times 10^7\ K$, hydrogen burns via the hot CNO cycle:

$$^{12}\mathrm{C}(p,\gamma)^{13}\mathrm{N}(p,\gamma)^{14}\mathrm{O}(\beta^+)^{14}\mathrm{N}(p,\gamma)^{15}\mathrm{O}(\beta^+)^{15}\mathrm{N}(p,\alpha)^{12}\mathrm{C}, \tag{6.1}$$

in which four H are consumed to produce one He [100]. The ignition starts when the temperature reaches $T \simeq 0.2$ GK. He starts to burn with the 3α-process, converting He into C via: $3\alpha \rightarrow^{12} C$. This increases the CNO abundance and allows new reactions to occur which follows the hot CNO cycle II. Once temperature reaches $T \simeq 0.7$ GK two key reactions can occur: the $^{15}\mathrm{O}(\alpha,\gamma)^{19}\mathrm{Ne}$ and the $^{18}\mathrm{Ne}(\alpha,p)^{21}\mathrm{Na}$ reactions. These reactions allow to breakout from the hot CNO cycles. This breakout paves the way for the αp-process during which a chain of (α,p) and (p,γ) reactions occurs up to the Ti region. Then, the high temperatures and the presence of H allow the *rp*-process to occur. A chain of rapid proton capture (p,γ) and of slow β-decay is achieved along the proton-drip line to reach masses up to A$\simeq$ 100. The end point of the *rp*-process lies in the SnSbTe cycle in which only α-unbound Te isotopes can be reached by the *rp*-process [89].

The path followed by this chain of reactions involves thousands of reactions and hundreds of nuclear isotopes going from the valley of stability to the proton drip-line. Most of these nuclei have never (or only partially) been studied experimentally. The needed nuclear spectroscopic information to compute the reaction rates are then adopted either from the mirror nuclei or from theoretical calculation, inducing large uncertainties.. In order to determine which uncertainties have the strongest impact on the prediction of the X-ray bursts properties, sensitivity studies have been performed.

In sensitivity studies, X-ray burst model calculations are performed, using the nominal reaction rates, to compute the X-ray burst light curve and final abundances. The nominal reaction rates are varied manually within their uncertainties (arising either from the uncertainties of the experimentaly constrained parameters or from arbitrary uncertainty factors 10 or 100 up and down, if not constrained experimentaly) and the impact of the variation on the final system is determined. Numerous sensitivity studies have been performed using different X-ray burst models and focusing on different aspects. Ref. [101] and [102] performed by Parikh *et al*. studied respectively the impact of nuclear reaction rates and reaction Q-values on the X-ray burst nucleosynthesis. Ref. [103] investigated the impact of mass uncertainties on the light curve and final abundances of X-ray burst while Ref. [104] and [105] studied the influence of reaction rate uncertainties on the constrain made on the neutron star properties and on the light curve and abundances, respectively. The models used in these various

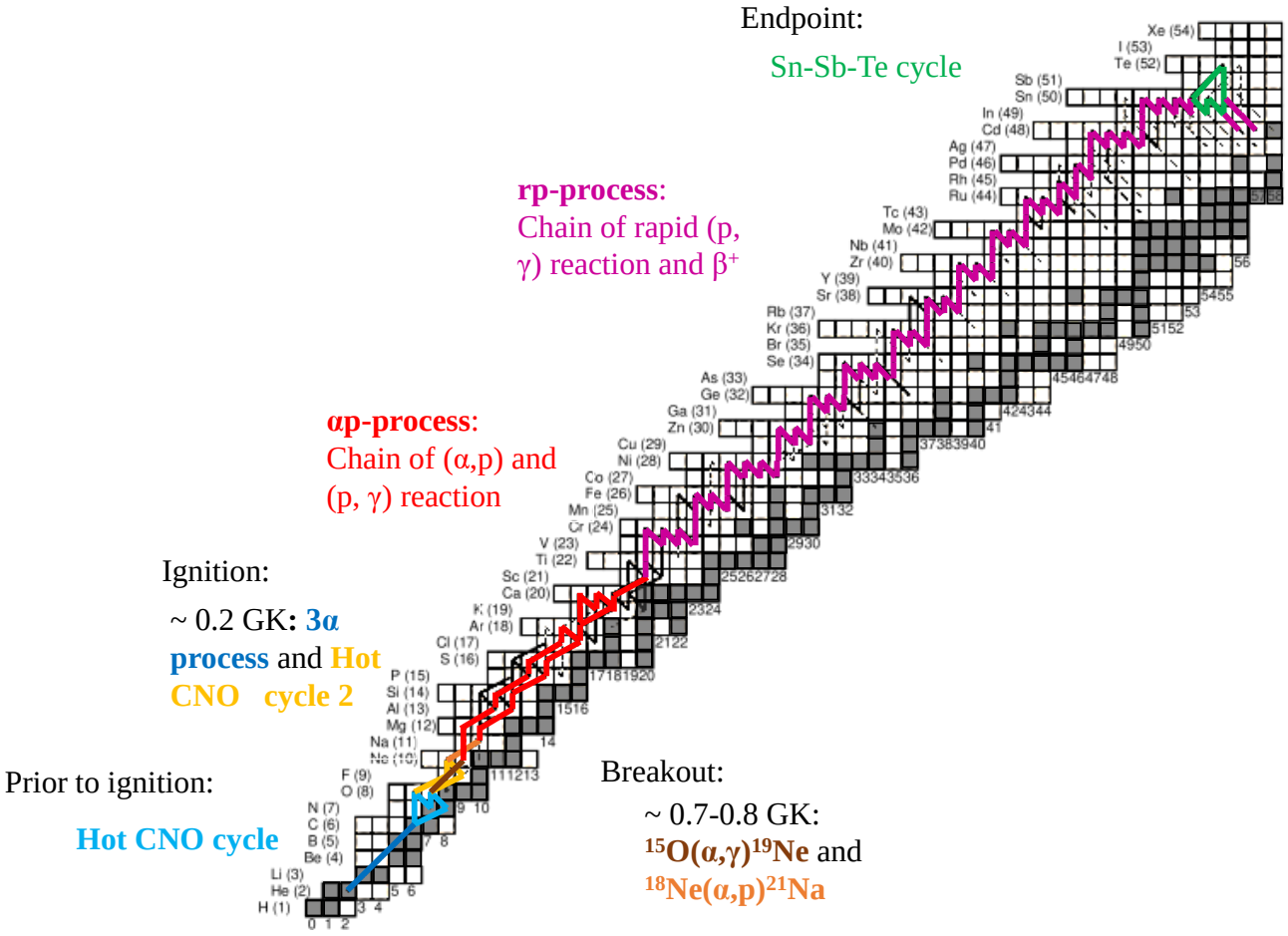

Figure 6.4: The main path of the chain of nuclear reactions occurring in X-ray bursts is shown by the colored lines. Stable nuclei are shown in grey. See text for details. This figure is adapted from Fig. 1 of Ref. [89].

studies differ. Some calculations [101, 102] used fixed temperature and density profiles which is not adequate since each reaction contributes to the energy production of the burst and therefore, to the evolution of the temperature and density during the burst. In the past decade, full 1-D multi-zone models have been developped. Multi-zone model divides the envelope of the star into zones which have independent isotopic abundances. This allows to simulate the energy transport allong the neutron star surface [105]. The recent sensitivity study of Cyburt *et al.* [105] uses a single-zone model that computes changes of temperature and density to select the most sensitive reactions. Then, the selected reactions are varied in a multi-zone model. Cyburt et al. work [105] is the first large-scale investigation of the influence of nuclear reaction rate uncertainties on X-ray burst light curves and final abundances that uses a multi-zone X-ray burst model, taking into account the evolution of temperature and density. Therefore, this study is presented in more detail in the following.

In the work of Cyburt *et al.*, the dependence of X-ray burst models on uncertainties in (p,γ), (α,γ), and (α,p) nuclear reaction rates has been investigated. For each reaction, the nominal reaction

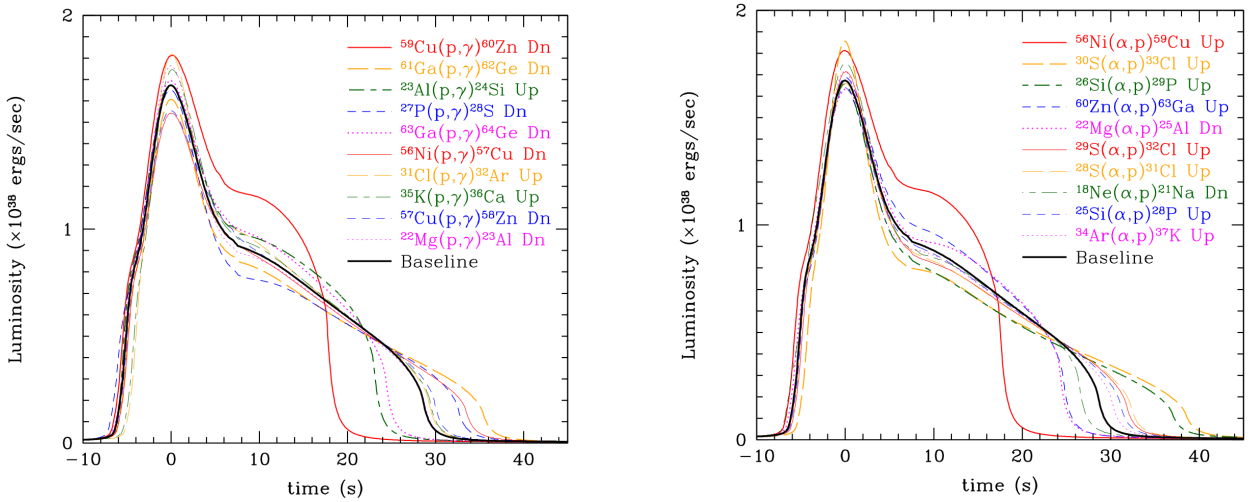

Figure 6.5: Impact of the variation of the reaction rate on the light curve, for the 10 most sensitive (p,γ) (left) and (α,p) (right) reactions. Figure adapted from Ref. [105]

rate is varied by a factor 100 up and down and the impact on the light curve and the final abundance composition is studied. They found that among the thousands of reactions involved, only a few tens of (p,γ) and (α,p) reactions have a strong impact on the light curve of the burst and the final abundances. The two breakout reactions of the hot CNO cycle are, as expected, one of them, since they set the initial conditions for the rest of the reaction chain. Fig. 6.5 shows the impact of the variation of the reaction rates on the light curve, obtained in Ref. [105], for the 10 most sensitive (p,γ) and (α,p) reactions. These reactions are the ones involving waiting points nuclei ^{22}Mg, $^{24-26}$Si ,$^{28-30}$S, ^{34}Ar, ^{56}Ni and ^{60}Zn. By definition, at a waiting point, the flow is in equilibrium with the next isotone due to a low (p,γ) Q-value (corresponding to a low one-proton separation energy in the compound nucleus and therefore, a strong (γ,p) reaction probability). This implies to await the β^+ decay, unless the (α,p) reaction is fast enough to bypass the waiting point and reach higher Z nuclei. If the proton capture reaction on the $Z+1$ isotone is fast enough, a double proton capture can compete with the (α,p) reaction in order to escape from the waiting points. One can note in Fig. 6.5 that the largest impact on the light curve comes from the ^{59}Cu(p,γ)^{60}Zn and the ^{56}Ni(α,p)^{59}Cu reactions. In this region, the presence of the NiCu cycle strongly limits the flow to heavier elements. The ^{59}Cu(p,γ)^{60}Zn allows to break out from this cycle while ^{59}Cu(p,α)^{56}Ni return to the begin of the cycle. The ratio of the (p,γ) and the (p,α) rates at ^{59}Cu then determine the strength of the cycle and has a large impact on the light curve and final abundances.

In the case of the ^{34}Ar, which is related to the reaction of interest, the Coulomb barrier that α particles have to penetrate to induce the ^{34}Ar(α,p)^{37}K reaction (see Fig. 6.6) is of 8.9 MeV, corresponding to a kinetic temperature of 7×10^{10}K. The typical temperature reached during a burst lies between 0.5×10^{9}K and 2×10^{9}K. Therefore the temperature in X-ray burst never rises sufficiently to break the Coulomb barrier and the ^{34}Ar(α,p)^{37}K reaction has therefore to occur through tunnel effect which makes the reaction rate drop. Furthermore, since the ^{34}Ar(p,γ)^{35}K has a very low Q-value of 78 keV, there is an equilibrium between the ^{34}Ar(p,γ)^{35}K rate and the ^{35}K(γ,p)^{34}Ar rate. This (p,γ)-(γ,p) equilibrium prevent a significant flow through the proton capture compound isotope ^{35}K [106]. The

third possibility to escape from the ^{34}Ar waiting point is to await for β^+ decay to occur with a lifetime of 843 ms [107].

The importance of the ^{35}K(p,γ)^{36}Ca now appears clearly. If the ^{35}K(p,γ)^{36}Ca is fast enough, the proton capture on ^{35}K can occur before the photo-disintegration of the latter. This would allow the reaction flow to continue through ^{36}Ca which would be much faster as compared to the β^+ decay path, given that the (p,γ) is order of magnitudes faster than the β^+ decay. Besides, one can see in the left part of Fig. 6.5 that if the nominal reaction rate of the ^{35}K(p,γ)^{36}Ca reaction is increased by a factor 100, the rising time of the light curve gets shorter. The ^{35}K(p,γ)^{36}Ca reaction has been identified by the work of Cyburt *et. al.* as one of the reaction having a significant influence on this reaction pathway, as well as the predicted X-ray burst light curve. However, this reaction has no influence on the final isotopic abundances of X-ray burst.

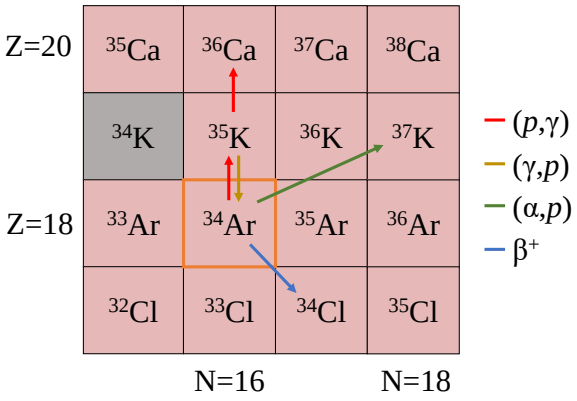

Figure 6.6: Nuclear chart around ^{34}Ar. The unbound nucleus are shown in grey. The different reaction discussed in the text are shown by the colored arrows.

3 The ^{35}K(p,γ)^{36}Ca reaction rate

It has been shown in the previous section that the ^{35}K(p,γ)^{36}Ca is of special interest to better understand the nuclear reaction flow along the *rp*-process. The sensitivity study of Cyburt *et. al.* [105] have shown that an increase by a factor 100 of the nominal value of the reaction rate will lead to a significant change in the X-ray burst light curve. Such large variation has been allowed in this study because the last estimation of the ^{35}K(p,γ)^{36}Ca reaction rate was performed with the only known resonance for which only its energy is experimentally constrained. Therefore, it is important, to re-investigate the reaction rate of ^{35}K(p,γ)^{36}Ca , as well as its associated uncertainties, in the light of the new states of ^{36}Ca observed in this work (Chapter 4) within the Gamow window of Type-I X-ray bursts and their spectroscopic properties.

3.1 Energy range of astrophysical interest for X-ray bursts

The energy range in which a capture reaction has the most probability to occurs is given by the Gamow window [$E_0-\Delta$,$E_0+\Delta$] (see Appendix B). At the typical temperature of an X-ray burst, T= 0.5-2 GK [108], the Gamow window for the ^{35}K(p,γ)^{36}Ca reaction lies between the resonance energies $E_{\text{c.m.}}$=0.37 MeV ($E_0-\Delta$ at $T=0.5$ GK) and $E_{\text{c.m.}}$=1.93 MeV ($E_0+\Delta$ at $T=2$ GK). It corresponds to excitation energies in the ^{36}Ca compound nucleus between 2.97 and 4.53 MeV. Considering the $3/2^+$ ground state (g.s.) spin value of ^{35}K and the fact that the most relevant proton captures will mostly occur through an *s*-wave ($\ell=0$), the resonances of interest in ^{36}Ca have J^π=1^+,2^+.

3.2 Status of the knowledge of the ^{35}K(p,γ)^{36}Ca reaction rate

There are mainly two techniques to determine a reaction rate: by direct measurement in which the reaction of interest is reproduced or by indirect measurement in which a different reaction is used to extract the relevant spectroscopic information to compute the reaction rate [109]. In the case of the ^{35}K(p,γ)^{36}Ca reaction, a direct measurement would be impossible with the current radioactive beam installation. Indeed, considering only a single 2^+ resonance with a resonance strength of 0.1 meV, to induce 1000 ^{35}K(p,γ)^{36}Ca reactions would require a ^{35}K radioactive beam at an intensity of 10^9 pps during 6 days, which is far from being achievable in any existing facilities. Therefore the only way to determine the ^{35}K(p,γ)^{36}Ca reaction rate is thought indirect study.

The reaction rate formalism can be found in Appendix B. We remind here the expression of the reaction rate in the case of narrow resonances:

$$\langle \sigma v \rangle = \left(\frac{2\pi}{\mu kT} \right)^{3/2} \sum_i (\omega\gamma)_i e^{-E_{r,i}/kT}, \tag{6.2}$$

where k is the Boltzmann constant, T is the temperature and μ is the reduced mass of the system. The incoherent sum over all the contributing resonances i is performed. Here, $E_{r,i}$ is the resonance energy of the resonance i and $(\omega\gamma)_i$ is its resonance strength defined as:

$$(\omega\gamma)_i = \frac{(2J+1)}{(2J_b+1)(2J_t+1)} \frac{\Gamma_a \Gamma_b}{\Gamma} \tag{6.3}$$

where the J_b and J_t are the spins of the beam and target particles, J, Γ_i and Γ are the spin, the partial decay widths (in the entrance a and the exit b channel) and the total width of the resonance, respectively.

In these equations, one can see that in order to compute the contribution of a narrow resonance to the reaction rate one has to know its energy, its spin, its partial widths or branching ratios and its total width. Therefore, to determine the ^{35}K(p,γ)^{36}Ca reaction rate one has to measure experimentally these parameters for all the resonances in ^{36}Ca that are inside the Gamow window.

Historically, owing to the lack of experimental spectroscopic information on ^{36}Ca, several studies [110, 111, 112, 113] have estimated the ^{35}K(p,γ)^{36}Ca reaction rate using either statistical model or theoretical predictions for the partial widths and the 2^+ energy either from Shell Model (SM) calculations [110] or adopted from the analog state in the mirror nucleus ^{36}S at 3.291 MeV. The reaction Q-value was derived, with about 40 keV precision, from the experimental atomic masses of ^{36}Ca and ^{35}K, known at that time from the ^{40}Ca(^{4}He,^{8}He)^{36}Ca [30] and ^{40}Ca(^{3}He,^{8}Li)^{35}K [64] transfer reactions, respectively. Since then, the excitation energy of the 2^+ first-excited state in ^{36}Ca was measured at GANIL [35], GSI [34] and NSCL [36] by means of one-neutron knockout reactions from a ^{37}Ca secondary beam. Taking the most precise measurement, its energy is found to be 3045.0 ± 2.4 keV [36] (see Chapter 4 for detailed discussion). Moreover, the mass of ^{35}K was precisely measured using a Penning trap mass spectrometer at ISOLDE [114]. Therefore, the major uncertainty on the reaction Q-value, and thereby the 2^+ resonance energy $E_r^{\text{c.m.}}$ (2^+), came from the uncertainty on the atomic mass of ^{36}Ca ($\Delta M(^{36}\text{Ca})$= -6440 ± 40 keV [30]). Very recently, a more precise mass

excess of $\Delta M(^{36}\mathrm{Ca})$= -6483.6 (56) keV has been obtained using a Time of Flight - Ion Cyclotron Resonance measurement in a Penning trap [31]. This leads to a reaction Q-value of 2599.6(61) keV and $E_r^{\mathrm{c.m.}}(2^+)$=445 ± 7 keV, combining the precise mass measurements of ^{36}Ca [31] and ^{35}K [114].

The most recent estimate of the reaction rate was made by Iliadis *et al.* [115] (which is the one used in the sensitivity study of Cyburt *et al.* [105]). This estimate takes into account a 2^+ state located at 3015 ± 16 keV [34] corresponding to a resonance energy of $E_r^{\mathrm{c.m.}}(2^+)$=459 ± 43 keV (obtained using the old mass measurement of Ref. [30]). The presence of this 2^+ state at an energy relatively close to the Gamow window induces an enhanced resonant capture component in the reaction rate, as compared to what was obtained in the previous estimates[110], using $E_r^{\mathrm{c.m.}}(2^+)$=700 keV. The partial γ and proton widths are adopted from the SM results of Herndl *et al.* [110], corrected from the excitation energy shift. For these parameters, arbitrary uncertainties of 50% have been considered.

In the following chapter, the resonance energies of the excited states of ^{36}Ca in or near the Gamow window were deduced from the measured excitation energies in this work (see Chapter 4) and their proton branching ratios were determined. SM calculation has been performed to determine the γ-width of the excited states of ^{36}Ca. This was used together with the proton branching ratios, to strongly constrain the resonances strengths of the states of interest. These relevant pieces of information are used to better constrain the $^{35}\mathrm{K}(p,\gamma)^{36}\mathrm{Ca}$ reaction rate at X-ray burst temperatures and above. This work has been recently published in PRC [116].

7 Results

Sommaire

This chapter presents the results obtained on ^{36}Ca relevant to constrain the ^{35}K$(p,\gamma)^{36}$Ca reaction rate. First a summary of the relevant resonances identified in ^{36}Ca will be presented. Then, the measurement of their proton branching ratio will be shown. Finally, the theoretical predictions for the proton and γ widths will be presented.

1 Relevant resonances identified in ^{36}Ca

In Chapter 4, the spectroscopy of ^{36}Ca has been performed using ^{37}Ca$(p,d)^{36}$Ca and ^{38}Ca$(p,t)^{36}$Ca transfer reactions. Two new states of spin-parities J^π=1^+,2^+, populated via ^{37}Ca$(p,d)^{36}$Ca reaction, have been identified in (or in the vicinity of) the Gamow window at the excitation energy Ex=4.24(4) MeV and 4.71(10) MeV respectively, in addition to the already known first 2^+ excited state located at $E_x = 3.045(24)$ MeV. Their energies have been measured in the proton energy spectrum obtained by gating on a K outgoing in the Zero Degree Detection system (ZDD). The fit of this spectrum is shown again in Fig. 7.1 (see Section 1.2.2 of Chapter 4 for details). This spectrum is particularly relevant since it corresponds to the proton decay of ^{36}Ca to ^{35}K which is the inverse reaction of ^{35}K$(p,\gamma)^{36}$Ca . An additional J^π=0^+_2 resonance has been identified in the vicinity of the Gamow window at $E_x = 2.78(18)$ MeV using the ^{38}Ca$(p,t)^{36}$Ca reaction. It is anticipated that this resonance will have a negligible impact on the reaction rate since the proton capture to this state will occur through a d-wave ($\ell = 2$).

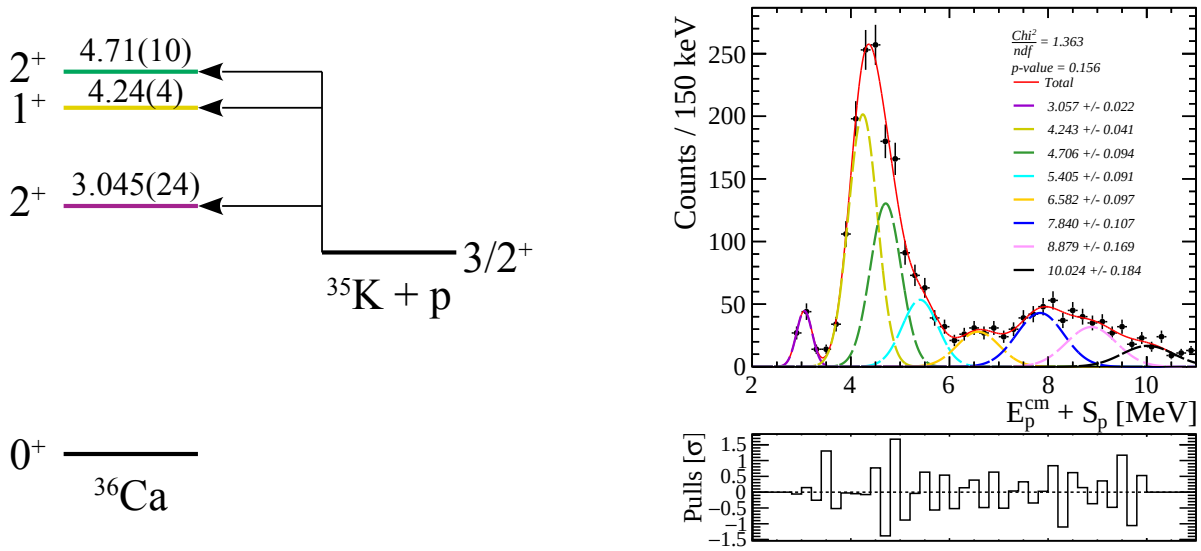

Figure 7.1: Left: Level scheme of the resonances identified in ^{36}Ca , relevant for the ^{35}K$(p,\gamma)^{36}$Ca reaction. Right: Fit of the proton energy spectrum. See Section 1.2.2 of Chapter 4 for details.

Fig. 7.2 shows the evolution of the Gamow window, in term of resonance energies $E_r^{cm} = E_x - S_p$, as a function of the temperature. The resonance energies of the three relevant state identified in ^{36}Ca are also shown. One can see that the J^π=1^+ ($l = 0$) and the J^π=2^+_2 ($l = 0$) enter in the Gamow window at $T = 2$ GK.

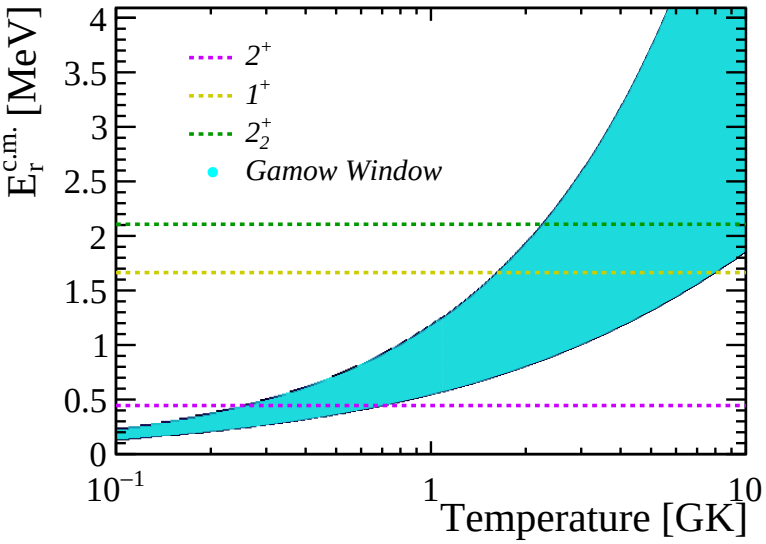

Figure 7.2: Evolution of the Gamow window (shown in Cyan), in term of resonance energies $E_r^{cm} = E_x - S_p$, as a function of the temperature. The resonance energies of the 2^+, 1^+ and 2_2^+ resonances are shown by the purple, yellow and green dashed lines, respectively.

2 Proton branching ratios measurements

In order to constrain the partial widths of the resonances, identified in ^{36}Ca , needed to calculate their resonance strength (see Eq. 8.1 in Appendix B), their proton decay branching ratio has been measured. This section presents the proton branching ratio measurements performed on the 2^+, 1^+ and 2_2^+ excited states of ^{36}Ca .

The first 2^+ excited state of ^{36}Ca at $E_x = 3.045$ MeV has been identified both in the excitation energy spectra gated by Ca and K (see Section 1.2.1 of Chapter 4), meaning that it decays through γ-ray and proton emission with respective partial widths Γ_γ and Γ_p. We propose here to determine its experimental proton branching ratio B_p=Γ_p/Γ_{tot}. Here, the assumption is made that Γ_{tot}=Γ_γ+Γ_p. This is reasonable since the only other open channel is the two-proton decay channel and these states have not been observed in the two-proton decay channel (see Section 1.2.5). Two different methods, the angular correlation method and the integral ratio method, have been used to determine the proton branching ratio of the first 2^+ excited state and only the integral ratio method for the 1^+ and 2_2^+ for the reasons that will be mentioned later.

2.1 Angular correlation method

The distribution of the angle θ_{cm} of the decaying protons, in the center-of-mass frame of the decaying nucleus, can be described by the angular correlation function $W(\theta_{cm})$. Experimentally, this function is constructed as follows:

$$W(\theta_{cm}) = \frac{N_{coinc}(\theta_{cm})}{N_{single}\epsilon(\theta_{cm})d\Omega}, \tag{7.1}$$

where, for a ^{37}Ca(p,d)^{36}Ca reaction, $N_{coinc}(\theta_{cm})$ corresponds to the number of decaying protons, detected in coincidence with the deuterons of the reaction at a given angle θ_{cm}. N_{single} corresponds to the total number of deuteron counts observed in the excitation energy peak, corresponding to the resonance of interest. $\epsilon d\Omega$ corresponds to the efficiency and solid angle corrections. The extraction method of the angular correlation function, in the case of ^{37}Ca(p,d)^{36}Ca(p)^{35}K reaction, is shown schematically in Fig. 7.3. It consists in the following steps (corresponding to the numbers in red in the figure):

1. Perform a simulation of the ^{37}Ca$(p,d)^{36}$Ca$\rightarrow^{35}$K$+p$ reaction considering a flat angular distribution $N_{simu,emit}(\theta_{cm})$ for the decaying protons (by flat we mean following a sinus law in θ_{cm}, as shown in Fig. 7.3, corresponding to a constant value of number of particles emitted by slice of solid angle).

2. Extract the angular distribution $N_{simu,coinc}(\theta_{cm})$ of simulated protons, detected in coincidence with the deuterons of the reaction as well as the total number of deuteron counts $N_{simu,single}(4\pi)$ seen in the excitation energy spectrum for a given populated state of interest.

3. Reconstruct the product of the efficiency ϵ and the portion of solid angle $d\Omega$ using: $\epsilon(\theta_{cm})d\Omega = \frac{4\pi N_{simu,coinc}(\theta_{cm})}{N_{simu,single}(4\pi)}$ (note that this expression can be used only if the simulation has been performed with a flat angular distribution for the protons, otherwise the number of proton per angle would not be proportional to the element of solid angle).

4. Extract the experimental angular distribution $N_{exp,coinc}(\theta_{cm})$ of the decaying protons, detected in coincidence with the deuterons of the reaction, for the resonance of interest.

5. Extract the total number of counts $N_{exp,single}(4\pi)$ seen in the excitation energy spectrum for the resonance of interest.

6. Reconstruct the angular correlation function using $W(\theta_{cm}) = \frac{N_{exp,coinc}(\theta_{cm})}{N_{single}\epsilon(\theta_{cm})d\Omega}$.

Fig. 7.4 shows the angular correlation function $W(\theta_{cm})$ obtained for the first 2^+ resonance in ^{36}Ca . A condition was applied on the proton center-of-mass energies ranging from 2.5 to 3.5 MeV. Errors for each point of the angular correlation are dominated by statistical uncertainties.

The angular correlation formalism has been established by J.G.Pronko and R.A.Lindgreen in Ref. [117]. It is found that the correlation function $W(\theta)$ can be described by a sum of even Legendre polynomials, $P_k(cos(\theta))$:

$$W(\theta) = \sum_{k=0}^{k_{max}} A_k P_k(cos(\theta)), \tag{7.2}$$

where A_k are coefficients that contain the nuclear structure information of the initial and final states. The sum is truncated at a maximum value of $k_{max} = min(\ell + \ell', 2J)$, where ℓ and ℓ' are the possible proton orbital angular momenta, and J is the spin of the decaying state. In the case of a 2^+ resonance decaying to the $J^\pi = \frac{3}{2}^+$ ground state of ^{35}K, the possible values for the proton angular momentum are $\ell = 0$, 2 and 4. Considering that the lowest angular momentum is favored, due to the centrifugal barrier, it is found that $k_{max} = min(\ell + \ell', 2J) = min(0+2, 4) = 2$. Therefore we expect that a sum of

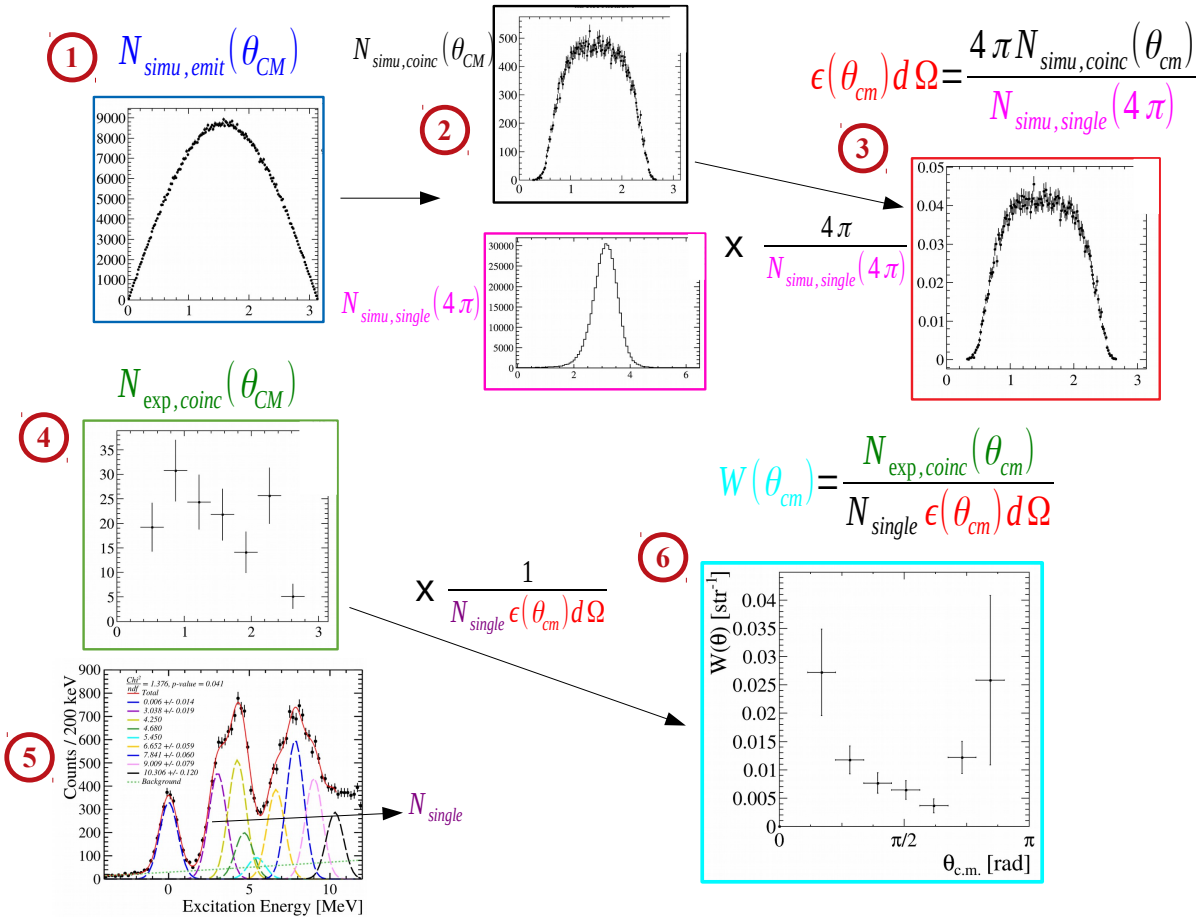

Figure 7.3: Method of extraction of the angular correlation function $W(\theta_{cm})$. See text for details.

even Legendre polynomials truncated at a maximum value of $k_{max} = 2$ well describes the experimental angular correlation function.

In practice, the A_k coefficients are determined from the fit of the experimental angular correlation function. Once these coefficients have been obtained, the proton branching ratio of the resonance is simply given by the integral of $W(\theta_{cm})$ over the full 4π solid angle:

$$\frac{\Gamma_p}{\Gamma_{tot}} = \int_0^{\pi} 2\pi sin(\theta_{cm}) W(\theta_{cm}) d\theta_{cm}. \tag{7.3}$$

Several Legendre polynomial fits, of the experimental angular correlation obtained for the 2^+ resonance (see Fig. 7.4), have been performed considering different k_{max} values of 0, 2 and 4. As expected, the best fit is obtained with $k_{max} = 2$ with a p-value of 0.58. The addition of a $P_4(cos(\theta))$ Legendre polynomial does not improve the goodness of the fit compared to the $k_{max} = 2$ value (with very similar p-value of 0.58 in both cases) and just increases the number of degrees of freedom. Therefore, the angular correlation function $W(\theta_{cm})$ with $k_{max} = 2$ was used to extract the proton branching ratio of $B_p = \Gamma_p/\Gamma_{tot} = 0.16(2)$ for the 2^+ resonance. The uncertainty results from the error propagation of the fitted parameters.

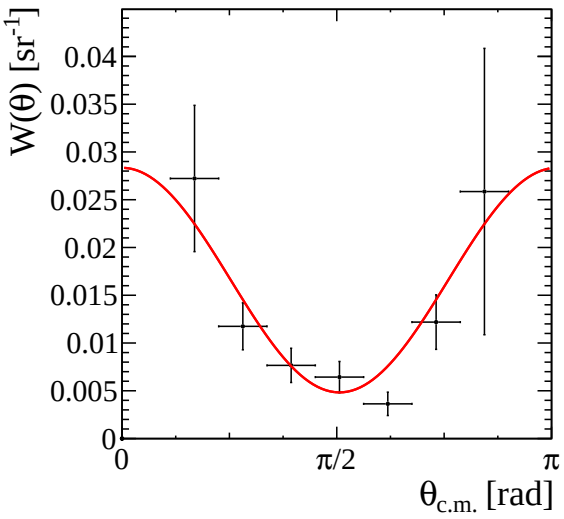

Figure 7.4: Proton-deuteron angular correlation corresponding to the 2^+_1 state as a function of the center-of-mass angle of the proton in the ^{36}Ca frame. The red line shows the best fit obtained with k_{max}=2 (p-value = 0.58).

2.2 Integral ratio method

Another method was used to extract proton branching ratios. This method allows to check the reliability of the results obtained with the angular correlation method for the 2^+ proton branching ratio. Moreover, since no counts are seen in the γ-decay branch of the 1^+ and 2^+ excited states, this method can be used to compute lower limits for their proton branching ratios.

This method consists in counting the number of events associated to the feeding of a resonance in ^{36}Ca in the K-gated and Ca-gated excitation energy spectra. This method is very easy to use since there is no difference of efficiencies between the two excitation energy spectra (except the difference of efficiency induced by the ZDD condition which is taken into account). The ratio $\frac{\Gamma_p}{\Gamma_\gamma}$ is directly given by the ratio of the integral of the Gaussian functions in the K-gated and Ca-gated spectra for a given state, corrected from the ZDD gate efficiency. Then the proton branching ratio is given by:

$$B_p = 1/(1+\Gamma_\gamma/\Gamma_p). \tag{7.4}$$

Fig. 7.5 shows the K-gated and Ca-gated excitation energy spectra, together with their fits (see Chapter 4 for details). By counting the number of events associated to the feeding of the first 2^+ excited state in the K-gated and Ca-gated excitation energy spectra, a $\Gamma_p/\Gamma_\gamma = 0.21$ (3) ratio is found, corresponding to a branching ratio of $B_p = 0.17$ (2). The uncertainty arises from the uncertainties of the fitted parameters of the Gaussian functions, as well as in the uncertainty on the Ca-gate and the K-gate in the ZDD spectrum. The proton branching ratio values for the 2^+ state derived with the two methods are in excellent agreement.

This method was applied to compute the following B_p lower limits: > 0.96 for the 1^+ state and > 0.97 for the 2^+_2 at one σ confidence level. The Ca-gated excitation energy spectrum was fitted with a 1^+ and 2^+_2 at fixed energy. The resulting integral of the two states was found to be compatible with zero.

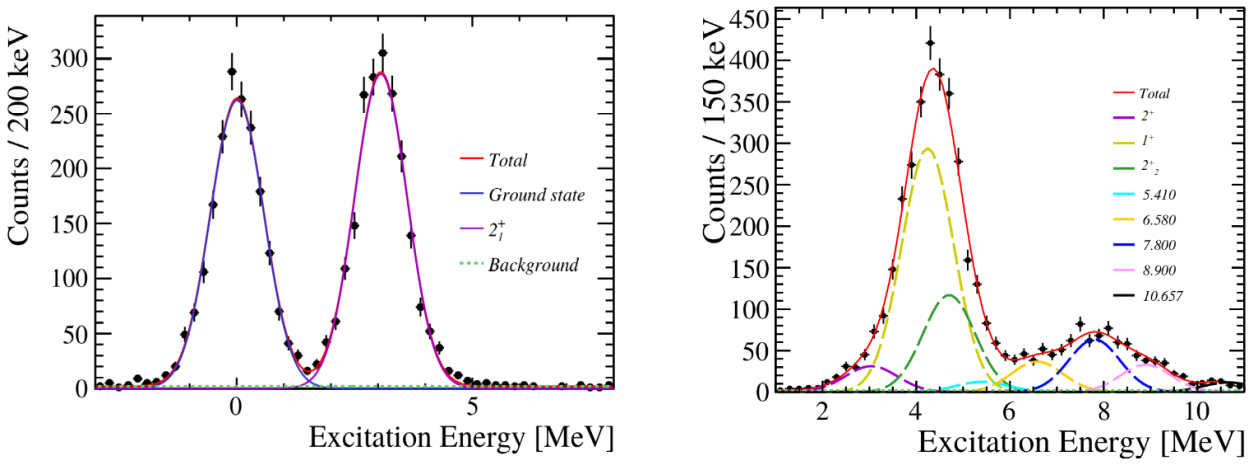

Figure 7.5: Left: Ca-gated excitation energy spectrum. Right: K-gated excitation energy spectrum. The red lines show the fits of the spectrum and the colored lines the individual contributions (see Chapter 4 for details).

The upper limits of the integrals were computed using the upper limit of the amplitudes and the widths of the Gaussian functions returned by the fit (being the central value plus the uncertainty). These upper limits on the integrals were then used in order to estimate the maximum possible contributions of the 1^+ and 2^+_2 states to the γ-decay channel.

The results for the 2^+, 1^+ and 2^+_2 proton branching ratios are summarized in Table 7.1. For the first 2^+, a weighted average value $B_p = 0.165(10)$ of the measurements using the two methods is considered.

3 Theoretical partial widths

In the previous section we measured a proton branching ratio of 0.165(10) for the first 2^+ state and a lower limit of 0.96 and 0.97 for the 1^+ and second 2^+_2 state. These values will be used to constrain the decay partial widths. Indeed, we saw in Section 3.1 that the individual values of Γ_γ, Γ_p and Γ_{tot} are needed to compute the reaction rate. Considering that $\Gamma_{tot} = \Gamma_\gamma + \Gamma_p$ and that $B_p = \frac{\Gamma_p}{\Gamma_{tot}}$, we still need the value of Γ_γ (or Γ_p) to calculate the resonance strengths and compute the reaction rate. Theoretical calculation were performed to compute these parameters and are presented in this section.

3.1 Calculated γ widths

The predicted partial gamma widths, Γ_γ, of the resonances of interest in ^{36}Ca are given in Table 7.1, expressed in meV. There were computed using the following relation [108]:

$$\Gamma_\gamma(\omega L) = \frac{8\pi(L+1)}{L[(2L+1)!!]^2}\left(\frac{E_\gamma}{\hbar c}\right)^{2L+1} B(\omega L), \tag{7.5}$$

where ω names the nature of the transition (Electric or Magnetic) and L its multipolarity. $B(\omega L)$ is the reduced transition probability for the γ decay of the resonant state (in unit of $e^2\,fm^4$ for E2 transitions

Table 7.1: The experimental and theoretical results for the resonant states in ^{36}Ca obtained in this work are presented. Tentative spins and parities J^π, measured excitation energies E_x (in keV) and proton branching ratios are listed for the three states identified in ^{36}Ca . Results of Shell Model calculations for partial γ-width (meV) and proton width (in meV) as well as their corresponding proton branching ratios are presented. Two different shell model calculations have been performed, one restricted to the *sd* orbitals and USDB interaction, the other using the full *sdpf* valence space with sdpfu-mix plus Coulomb interaction. Predicted widths, obtained for a given calculated excitation energy, have been renormalized to the experimental values given in the second column.

Exp.			*sd* shell			*sdpf* − *mix* shells		
J^π	E_x	B_p	Γ_γ	Γ_p	B_p	Γ_γ	Γ_p	B_p
(2_1^+)	3045(2.4)	0.165(10)	0.5	0.87	0.64	0.99	0.84	0.46
(1^+)	4243(40)	>0.96	37.1	2.8×10^4	≈ 1	65.4	6.3×10^4	≈ 1
(2_2^+)	4706(100)	>0.97	0.2			7.4	3.3×10^5	≈ 1

and μ_N^2 for M1 transitions) and E_γ the energy of the γ-ray transition. Shell model calculations usually predict $B(\omega L)$ and E_γ values, from which Γ_γ is calculated. However, as the experimental excitation energies of the considered excited states are known and differ from the calculated ones, the predicted partial widths Γ_γ listed in Table 7.1 are obtained from Eq. 7.5 using experimental energies and $B(E2)$ values obtained from SM calculations.

As presented in Chap. 5 Section 1, two different shell model calculations have been performed in the present work, one restricted to the *sd* orbitals and USDB interaction [118], the other using the full *sdpf* valence space with sdpfu-mix plus Coulomb interaction [119]. The reduced transition probabilities obtained in the *sdpf* and *sd* SM calculations are given in Table 7.2.

The major difference between the two shell model calculations presented here, resides in the size of their valence spaces: when restricted to *sd* shells the proton core is closed, while the use of a broader *sdpf* valence space allows proton excitations (see Fig. 7.6). When using the *sd* valence space, the 2_1^+ state in ^{36}Ca (^{36}S) is of pure neutron (proton) origin. It follows that the $B(E2)$ values of the two mirror nuclei can simply be derived from their squared neutron to proton effective charges ratio, $B(E2)(^{36}\mathrm{Ca}) = e_n^2/e_p^2\ B(E2)(^{36}\mathrm{S})$, where e_n (e_p) are the neutron (proton) effectives charges usually adopted to be 0.5 (1.5). One can see that both calculation provides equivalent results for the first 2^+ and 1^+ states, which is expected since they share the same *sd* configuration. Conversely, the results differ for the second 2_2^+ state. This arise from its expected intruder configuration which cannot be represented by the *sd* valence space. The values of the γ-decay widths obtained from these reduced transition probabilities are given in Table 7.1.

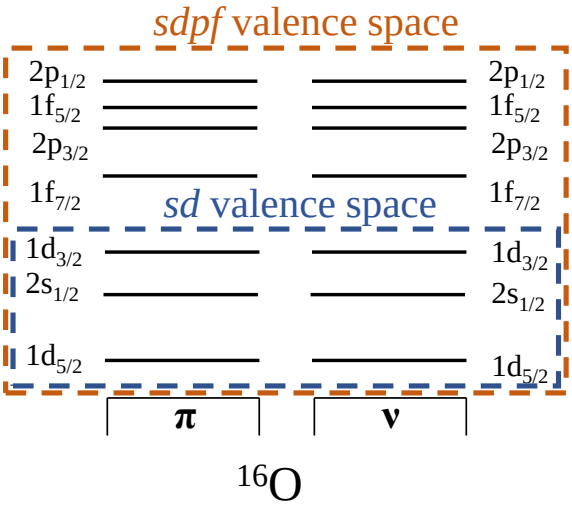

Figure 7.6: Scheme of the valence space used in the SM calculations.

Table 7.2: Reduced transition probabilities obtained in the *sdpf* and *sd* SM calculations. $B(E2)$ are given in units of $e^2\text{fm}^4$ while $B(M1)$ are given in units of μ_N^2

	J_i^π	$J_f^\pi = 0^+$		$J_f^\pi = 2_1^+$		$J_f^\pi = 1^+$	
		$B(E2)$	$B(M1)$	$B(E2)$	$B(M1)$	$B(E2)$	$B(M1)$
sdpf	2_1^+	4.71					
	1^+		0.04	1.5	1.5		
	2_2^+	0.11		29.77	0.06	0.13	0.06
sd	2_1^+	2.36					
	1^+		0.01	1.24	1.35		
	2_2^+	0.02		2.84	0.00	2.26	0.04

As the 2_1^+ state in ^{36}Ca is certainly not totally of pure neutron origin, the calculated Γ_γ using a *sd* valence space (≈ 0.5 meV) represents a lower limit. At the other extreme, a maximum Γ_γ of about 3.7 meV is obtained for ^{36}Ca when assuming the same $B(E2)$ value of 19.5 $e^2\text{fm}^4$ as in the mirror nucleus ^{36}S, after correcting from their different 2_1^+ energies. This latter assumption would imply that the 2^+ state has a very mixed (and similar) structure in both nuclei. This is very unlikely for two reasons: first, the two nuclei are likely doubly magic, at least based on the high excitation energy of their first excited states. Second, the 2_1^+ and 1^+ states in ^{36}S are very well populated by the ^{37}Cl(d,^{3}He)^{36}S proton removal reaction, with spectroscopic factors values for these states (0.86 and 0.75 respectively [57]) that are close to the single particle values, meaning it has a strong proton component rather than a mixed proton and neutron one.

3.2 Calculated proton widths

The theoretical proton widths Γ_p of the states listed in Table 7.1 are obtained by multiplying their calculated single-particle width Γ_{sp} with the SM predicted spectroscopic factor C^2S:

$$\Gamma_p = \Gamma_{sp} \times C^2S. \tag{7.6}$$

The C^2S values for the *sd* shell are obtained from the same SM calculations used to predict the γ-widths and they are given in Table 7.3. The single particle widths Γ_{sp} are calculated by using scattering phase shifts in a Woods-Saxon potential [120] which depths are adjusted to match the experimental resonance energies. The Wood-Saxon potential parameters used for the calculation can be found in page 239 of Ref. [14]. In the present work, the widths of the 2_1^+ state obtained in the *sd* and *sdpf* shell model calculations agree very well with each other, while those of the 1^+ state differ by more than a factor two.

The C^2S values (see Table 7.3) of the excited states are small and the ground state of ^{36}Ca carry out all the $d_{3/2}$ strength. The proton spectroscopic factors for the excited states are very small because they have an almost pure $1p1h$ neutron configuration, selectively populated here by the (p,d) transfer reaction, that can not be described by a proton creation operator. The C^2S values of the 2_2^+ state

Table 7.3: Proton spectroscopic factors obtained, for the *sd* shell, by the two SM calculation in *spdf* and *sd* valence space, for the ground state, and the three excited states of astrophysical interest in ^{36}Ca . The calculated single particle widths Γ_{sp} are also given in eV.

	C^2S						Γ_{sp}		
	$sdpf-mix$ shells			sd shell					
J^π	$d_{5/2}$	$s_{1/2}$	$d_{3/2}$	$d_{5/2}$	$s_{1/2}$	$d_{3/2}$	$d_{5/2}$	$s_{1/2}$	$d_{3/2}$
0^+			3.370			3.6749			
2_1^+	0.002	0.009	0.009	0.001	0.009	0.017	1.7×10^{-3}	9.2×10^{-2}	1.1×10^{-3}
1^+	0.0001	0.002	0.000	0.000	0.001	0.001	1.4×10^{3}	3.1×10^{4}	1.2×10^{3}
2_2^+	0.000	0.0003	0.000				1.3×10^{4}	1.1×10^{5}	8.6×10^{3}

could not be computed by the *sd* SM calculation since this state has an intruder proton configuration $\pi(sd)^{-2}\pi(fp)^2$. The single particle widths Γ_{sp} of the resonances of interest, calculated with the Woods-Saxon potential, are also given in Table 7.3 for the *sd* shell. One can see the effect of the centrifugal barrier in the Γ_{sp} values, with the value corresponding to the $s_{1/2}$ orbital (with no angular momentum $l=0$) which are systematically higher than the ones of the $l=2$ $d_{3/2}$ and $d_{5/2}$ orbitals.

The calculated proton widths are given in Table 7.1 as well as the calculated and experimentally determined proton branching ratios using Eq. 7.4. As shown in Table 7.1, the weighted average value $B_p = 0.165\ (10)$ for the 2^+ state is found to be significantly weaker than all theoretical predictions, while the deduced B_p lower limits for the higher 1^+ and 2_2^+ states are consistent with the predictions.

8 The ^{35}K$(p,\gamma)^{36}$Ca reaction rate

Sommaire

We now have all the information on the resonance parameters needed to compute the ^{35}K(p,γ)^{36}Ca reaction rate. This chapter presents how the calculation is performed and the results on the ^{35}K(p,γ)^{36}Ca reaction rate.

1 Ingredients of the reaction rate calculation

The ^{35}K(p,γ)^{36}Ca reaction proceeds through two processes, the resonant capture (RC) via excited states above the proton threshold in the compound nucleus ^{36}Ca and the direct capture (DC) to the ground state of ^{36}Ca . Thus the reaction rate depends on resonant capture and direct capture (DC) contributions.

1.1 Resonant capture component

In the presence of narrow resonances, as presented in Appendix B, the reaction rate can be expressed as:

$$< \sigma\nu >= \frac{1.5399 \times 10^{11}}{N_A} \left(\frac{\mu}{T_9}\right)^{3/2} \sum_i (\omega\gamma)_i e^{-11.605 E_i/T_9}, \tag{8.1}$$

where

$$(\omega\gamma)_i = \frac{2J_i+1}{(2J_p+1)(2J_{^{35}K}+1)} \frac{\Gamma_{\gamma,i}\Gamma_{p,i}}{\Gamma_i}, \tag{8.2}$$

is the resonance strength of the i^{th} resonance with $\Gamma_{\gamma,i}$, $\Gamma_{p,i}$ and Γ_i its partial γ-ray, proton and total width in MeV, respectively, E_i the resonance energy in MeV, J_i the spin of the resonance, J_p and $J_{^{35}K}$ are the proton spin (=1/2) and the g.s. spin of ^{35}K (=3/2), respectively. T_9 is the temperature in GK and μ is the reduced mass. This assumption of narrow resonance is valid as the resonant states considered here have a total width far below their resonance energies.

Three states have been indentified that could significantly contribute to the reaction rate which are the 2^+, the 1^+ and the 2_2^+. The resonance energy E_r for the 2_1^+ state has been determined from their excitation energy of Ref. [36] (being the most precise measurement performed by γ-ray spectroscopy) and the recent mass measurement of Ref. [31]. For the 1^+ and 2_2^+ states, excitation energies are those determined in the present work. The spin values used for the computation are the ones proposed in Chapter 4.

As we could only determine precisely the proton branching ratio of the 2^+ resonance in the present work (and only a lower limit for the 1^+ and 2_2^+ states), we choose to fix the Γ_γ partial widths to the predicted values using the *sdpf* shell model calculation which makes use of the broadest valence space and correctly reproduces the energy of the first 2^+ state. Once Γ_γ is fixed, Γ_p and Γ_{tot} can be derived for the 2_1^+ state using the experimental B_p value as the proton and γ decays are the only open channels.

As for the 1^+ and the 2_2^+ resonances, the proton partial width dominates the total width. It follows that the resonance strength of the Eq. 8.2 can be approximated by $\omega\gamma \simeq \frac{\Gamma_\gamma}{8}(2J_r+1)$, with J_r the spin of the resonance. All the resonance parameters needed to compute the reaction rate are listed in Table. 8.1

A central value Γ_γ of 0.99 meV was used for the 2_1^+ state with an uncertainty factor of 1.7, which corresponds to values between 0.58 and 1.7 meV at one sigma. This way, we accept the lower (0.4 meV) and upper limit (3.7 meV) of Γ_γ, discussed in Section 3.1, at about 2σ. The same uncertainty factor is assumed for the Γ_γ widths of the 1^+ and the 2_2^+ states. The uncertainty on Γ_p of the 2_1^+ is deduced from that on Γ_γ and on the experimental B_p value (of 0.165(10)), following Eq. 7.4.

Table 8.1: Resonances parameters used in this work to compute the ^{35}K(p,γ)^{36}Ca reaction rates. Resonance spin-parity value, experimental energy and calculated γ-width (using the *sdpf* valence space) are given in the three first columns. The proton-width Γ_p, derived from the calculated γ-width and the experimental proton branching ratio for the first 2^+ state, is given in the fourth column. The resonant strength of each state is listed in column five.

J^π	E_r [keV]	Γ_γ [meV]	Γ_p [meV]	$\omega\gamma$ [meV]
(2^+)	445 (7)	0.99	0.20	0.102(50)
(1^+)	1643 (41)	65.4		25 (14)
(2_2^+)	2106 (100)	7.4		4.6 (25)

1.2 Direct capture component

The DC component mostly occurs through an ℓ=2 proton capture between the ground state of ^{35}K and that of ^{36}Ca, which have $J^\pi = 3/2^+$ and 0^+, respectively. In a simplified picture, 3 protons are occupying the $1d_{3/2}$ orbital in the g.s. of ^{35}K and one more can occupy it by the direct capture process to the ground state of ^{36}Ca . The SM calculations of Ref. [110] predict a proton spectroscopic factor C^2S_p for ^{36}Ca of 3.649, while the *sdpf* shell model calculation predicts a slightly smaller value of 3.37. We propose the use of the mean value between the two (3.5) and an uncertainty of 0.15 to agree, within one sigma, with the two calculations.

The astrophysical S-factor (see Appendix B) can be computed from the spectroscopic factor using:

$$S(E_0) = \sum_i C^2 S_i \sigma_i E_0 e^{2\pi\eta}, \tag{8.3}$$

where E_0 is the centroid energy of the Gamow peak (see Appendix B) and σ_i is the single particle cross section, derived from nuclear potential model using Wood-Saxon potential [110]. The total astrophysical S-factor is obtained from the sum over all the contributing orbitals. By using a spectroscopic factor C^{2}S of 3.649 computed in Ref. [110], an astrophysical S-factor of $S(E_0) = 2.72 \times 10^{-2} MeV\,b$ is obtained. In the present work, for the direct capture reaction rate calculation (see Eq. B.7 in Appendix B), we will consider an astrophysical S-factor $S(E_0) = 2.609 \times 10^{-2} MeV\,b$ scaled from the C^{2}S mean value of 3.5.

2 Calculation of the ^{35}K(p,γ)^{36}Ca reaction rate

2.1 Monte-Carlo method

The reaction rate has been computed using the Monte-Carlo code RatesMC developped by Longland *et al.* [121], allowing a statistically meaningful evaluation of the reaction rate based on experimental and/or theoretical uncertainties. The principle of the calculation is summarized in the following.

To each nuclear physics quantity is associated a probability density function $f(x)$ defined by its expectation value E and its variance V given by :

$$E[x] = \int_{-\infty}^{+\infty} x f(x) dx, \quad V[x] = \int_{-\infty}^{+\infty} (x - E[x])^2 f(x) dx, \tag{8.4}$$

A Gaussian probability density function is assumed for the resonance energies. It is defined by:

$$f(x) = \frac{1}{\sigma\sqrt{2\pi}} e^{-\frac{(x-\mu)^2}{2\sigma^2}} \tag{8.5}$$

and have two parameters, μ and σ. μ determines the location of the distribution maximum while the σ determines the distribution width. Since it is a symmetric distribution we found $E[x] = \mu$ and $V[x] = \sigma^2$.

A log-normal distribution is used as a probability density function for γ-width and proton-width values, for the non-resonant S-factor and for the resonance strenght. A detailed discussion about the choice of probability density function associated to the different parameters can be found in Ref. [121]. The log-normal distribution is given by:

$$f(x) = \frac{1}{\sigma\sqrt{2\pi}} \frac{1}{x} e^{-\frac{(ln(x)-\mu)^2}{2\sigma^2}}. \tag{8.6}$$

Here the parameters μ and σ do not represent the mean value and standard deviation of the log-normal distribution, but of the corresponding Gaussian distribution for $ln(x)$. The expectation (or mean) value and the variance of the log-normal distribution are given in terms of these two parameters by:

$$E[x] = e^{\frac{2\mu+\sigma^2}{2}}, \quad V[x] = e^{(2\mu+\sigma^2)}(e^{\sigma^2} - 1). \tag{8.7}$$

The median value of the log-normal density function is given by e^{μ}, while for a coverage probability of 68% the lower and upper bounds are given by $e^{\mu-\sigma}$ and $e^{\mu+\sigma}$, respectively. The uncertainty factor is defined with respect to the median by $f.u. = e^{\mu+\sigma}/e^{\mu} = e^{\sigma}$. For example, an uncertainty factor of 1.7 is considered for the partial γ-widths. Therefore, the calculated value Γ_γ is taken as the median and the lower and upper bounds of the 68% coverage probability are given by $\Gamma_\gamma/1.7$ and $1.7\Gamma_\gamma$ respectively. Then the corresponding expectation value and variance are computed using Eq. 8.7 and given as input to the RatesMC code.

At a given temperature, a random value is generated for each quantity according to the corresponding probability density function, considering correlations between each quantities (*e.g.* once a random value has been chosen for the resonance energy the same value is used in order to compute

the Boltzmann factor and the penetration factor, see Appendix B). Then the total reaction rate is computed. The procedure is repeated as many times as needed to reach the required statistical precision. The log-normal distribution is used to describe the obtained distribution of the reaction rate values. Fig. 8.1 shows the results of the Monte Carlo calculation for ^{35}K(p,γ)^{36}Ca reaction rate at $T = 1$ GK for 5000 samples. One can see that the log-normal function (shown in red) describes very well the obtained distribution. The recommended reaction rate is given by the median value of the reaction rate distribution (shown by the green line). The low and high reaction rates, are defined as the 0.16 and 0.84 quantiles of the cumulative reaction rate distribution, respectively (shown by the dotted green lines). This corresponds to a coverage probability of 68 %. This procedure is repeated for temperatures ranging from 0.01 to 10 GK in order to obtain the dependency of the reaction rate to the temperature.

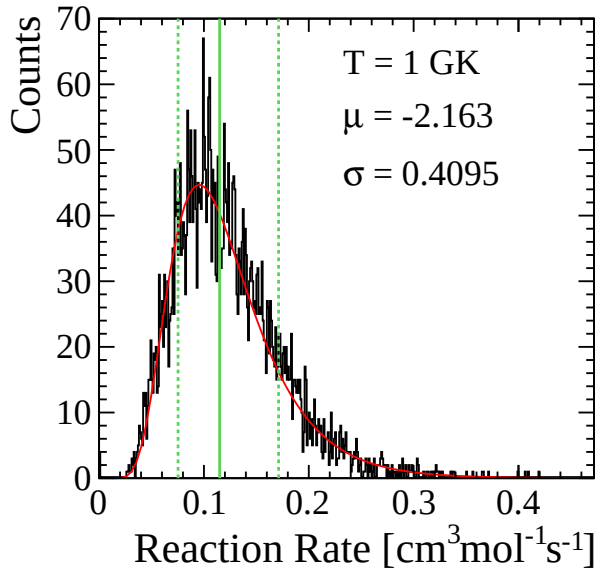

Figure 8.1: Results of the Monte Carlo calculation for ^{35}K(p,γ)^{36}Ca reaction rate at $T = 1$ GK. The reaction rate is sampled 5000 times. The red curve represent the log-normal approximation of the reaction rate which parameters are given. The vertical dotted green lines represent the low and high Monte Carlo reaction rates which are obtained from the 0.16 and 0.84 quantiles of the cumulative distribution, respectively. The vertical green line represents the median reaction rate.

2.2 Results and discussion

The evolution of the calculated rates with temperature for the ^{35}K(p,γ)^{36}Ca reaction is shown in Fig 8.2. The left part displays the results obtained in this work, for the total reaction rate as well as the contributons of the individual resonances and the direct capture component to the ground state. In this calculation, we used the resonance parameters of Table 8.1 obtained in the present work and the associated uncertainties and the astrophysical S-factor $S(E0)$ for the direct capture to the groud state as discussed in Section 1.2. The right part shows the results obtained from the work of Iliadis et al. [115], in which only the 2^+ resonance was considered (with the following parameters: $E_r = 459(43)$

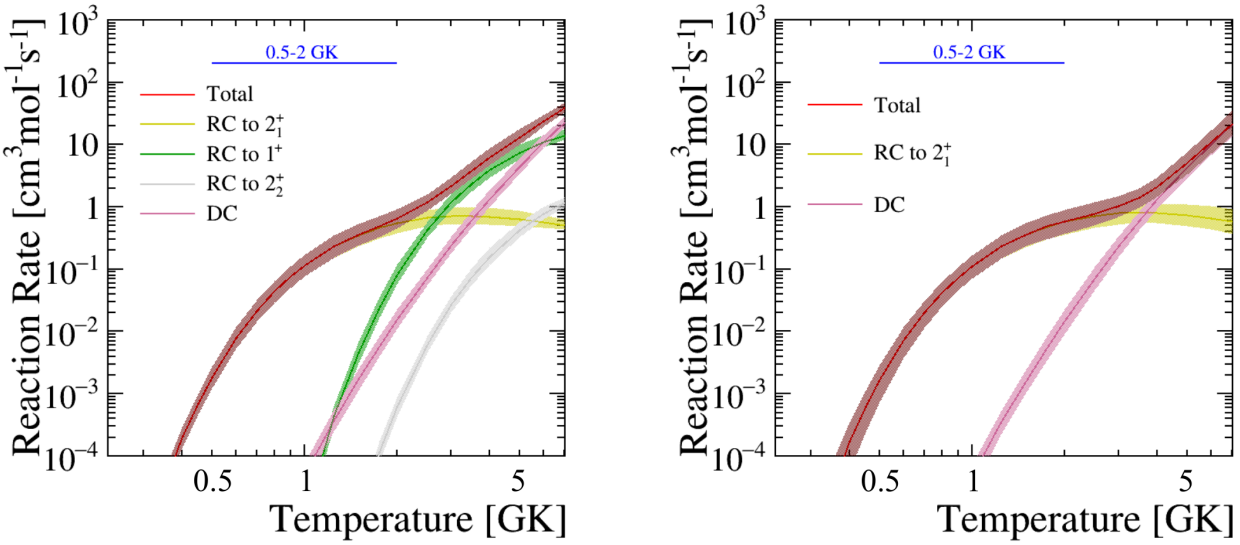

Figure 8.2: The ^{35}K(p,γ)^{36}Ca reaction rate calculated (in units of cm^3 mol^{-1} s^{-1}) in this work (left) and in [115] (right). The red curve represent the total reaction rate, which includes the contributions of resonant (RC) and direct (DC) captures. The thickness of the curves represents a coverage probability of 68%. The indicated range of 0.5 - 2 GK is typical of X-ray bursts temperatures.

keV, $\Gamma_\gamma = 0.38$ meV and $\Gamma_p = 1.4$ meV) in addition to the DC part (using the astrophysical S-factor of Ref. [110]).

As Fig. 8.2 shows, the contribution of the first 2^+ resonance dominates the total reaction rate in the temperature range of 0.5-2GK relevant for Type I X-ray bursts. One can also notice that the direct capture component on the ground state is negligible in the relevant temperature range. The major differences between our work and the one of Ref. [115] reside in the values used for the partial γ-width, the partial proton-width, the resonance energy of the 2^+ state and their associated uncertainties.

For the partial Γ_γ width, an arbitrary value of 50% was assumed in [115] with a central value of 0.4 meV for the 2^+ state. It corresponds to a log-normal confidence interval for the widths of [0.25-0.64] meV at one sigma, which partly overlaps with our current determination of the γ-ray partial width. The uncertainty on the 2^+ resonance energy considered in the present work was reduced using the very recent precise measurement of the mass of ^{36}Ca from [31] and the excitation energy from [36]. As shown in Fig. 8.2, the contributions of the 1^+ and 2^+_2 resonances to the total reaction rate, not taken into account in [115], start to be significant at temperatures above $T = 2$ GK. The resonance energy of the 2^+_2 resonance being outside of the Gamow window, its contribution to the reaction rate is found to be very small.

The ratio of the calculated reaction rate by Iliadis et al. [115] to our recommended value is shown in Fig. 8.3. The colored areas outlined by the thick/thin black lines show the uncertainty on the recommended reaction rate calculated in this work with a coverage probability of 68% and 95% respectively. The thick and dashed blue lines correspond to the reaction rate given in [115] with the associated 68% uncertainties respectively, normalized to our recommended reaction rate. For the temperature range of interest, the results are nearly similar. At temperatures higher than 2 GK, our recommended reaction rate is systematically higher due to the contributions of the 1^+ and 2^+_2

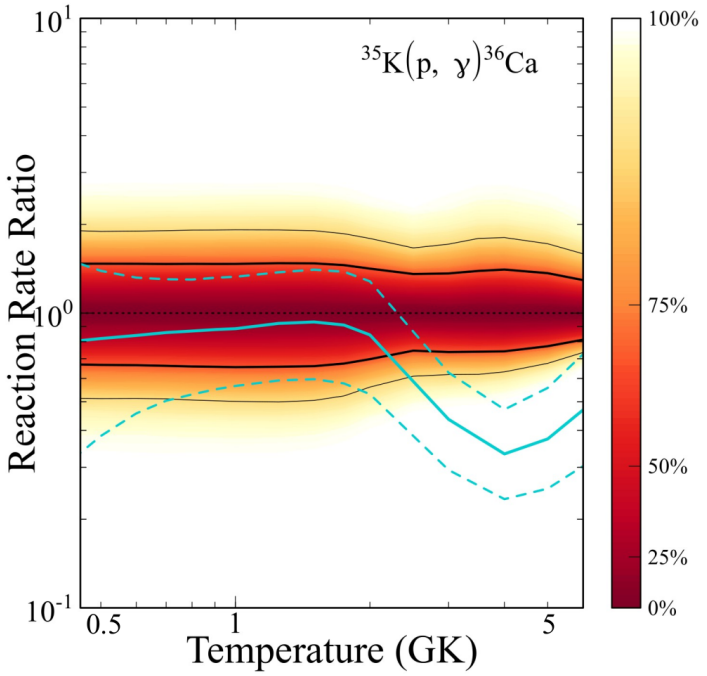

Figure 8.3: Ratio of rates normalized to our recommended reaction rate. The area delimited by the thick/thin black lines and centered around 1 represent the recommended value at the 68% and 95% confidence levels, respectively. The thick and dashed blue lines correspond to the reaction rate given by Iliadis et al. [115] and at the 68% confidence level, normalized to our recommended value.

resonances, not included in [115]. This reaction rate should, however, be considered as a lower limit, as higher-energy resonances, not observed in this work, may additionally contribute to the reaction rate beyond 2 GK. The values of the low, recommended, high reaction rates obtained in this work are given numerically in Tab. 8.2

We have also estimated the contributions coming from additional resonances. The resonant capture to the 0_2^+ ($\ell = 2$ proton capture) observed at 2.8 MeV is not considered since the 0_2^+ is the first excited state of ^{36}Ca and it cannot γ-decay to the ground state. The contribution of the 0_3^+ ($\ell = 2$ proton capture) identified at 4.8 MeV has been estimated as well as the one of the 3^- ($\ell = 1$) states, not identified here, but present in the mirror nucleus. Finally, the *sdpf* SM calculation predicted a 2^+ intruder state at 3.8 MeV, inside the Gamow window. Even if this state has not been observed, its potential contribution to the reaction rate has been investigated.

For the 0_3^+ excited state, the results of the *sdpf* SM calculation were used for the γ-width (being 1.9 μeV) and the $\omega\gamma \simeq \frac{\Gamma_\gamma}{8}(2J_r + 1)$ approximation was used. For the 3^-, we considered the γ-width of the mirror nuclei and the proton width has been set at the single particle value, considering a spectroscopic factor equal to one. For the 2^+ state at 3.8 MeV, the prediction of the SM calculation was used (being $\Gamma_\gamma = 1.8$ meV and $\Gamma_p = 291$ meV). Results of the reaction rate calculation including these states are shown in Fig. 8.4. The contribution of these states is found to be negligible as compared to the ones of the first 2^+ and 1^+ states.

We have seen in Chapter 6 that the ^{35}K(p,γ)^{36}Ca reaction is of special interest to better understand the nuclear reaction flow along the *rp*-process. The sensitivity study of Cyburt et al. [105] concluded

Table 8.2: Low, recommended and high thermonuclear rates of the ^{35}K(p,γ)^{36}Ca reaction (in units of cm^3 mol^{-1} s^{-1}) as a function of temperature. Interval between low and high rates represents a confidence level of 68% (1 σ).

T [GK]	Low	Recommended	High
0.010	3.191×10^{-51}	3.350×10^{-51}	3.516×10^{-51}
0.011	2.345×10^{-49}	2.461×10^{-49}	2.591×10^{-49}
0.012	1.051×10^{-47}	1.104×10^{-47}	1.160×10^{-47}
0.013	3.151×10^{-46}	3.316×10^{-46}	3.487×10^{-46}
0.014	6.785×10^{-45}	7.123×10^{-45}	7.487×10^{-45}
0.015	1.100×10^{-43}	1.157×10^{-43}	1.218×10^{-43}
0.016	1.407×10^{-42}	1.478×10^{-42}	1.555×10^{-42}
0.018	1.281×10^{-40}	1.346×10^{-40}	1.414×10^{-40}
0.020	6.238×10^{-39}	6.547×10^{-39}	6.886×10^{-39}
0.025	1.498×10^{-35}	1.573×10^{-35}	1.654×10^{-35}
0.030	5.656×10^{-33}	5.950×10^{-33}	6.257×10^{-33}
0.040	3.229×10^{-29}	3.393×10^{-29}	3.565×10^{-29}
0.050	1.507×10^{-26}	1.585×10^{-26}	1.665×10^{-26}
0.060	1.633×10^{-24}	1.719×10^{-24}	1.808×10^{-24}
0.070	6.881×10^{-23}	7.243×10^{-23}	7.612×10^{-23}
0.080	1.503×10^{-21}	1.581×10^{-21}	1.663×10^{-21}
0.090	2.050×10^{-20}	2.152×10^{-20}	2.262×10^{-20}
0.100	2.112×10^{-19}	2.274×10^{-19}	2.501×10^{-19}
0.110	2.632×10^{-18}	3.680×10^{-18}	5.509×10^{-18}
0.120	6.334×10^{-17}	1.066×10^{-16}	1.794×10^{-16}
0.130	1.416×10^{-15}	2.425×10^{-15}	4.077×10^{-15}
0.140	2.174×10^{-14}	3.653×10^{-14}	6.068×10^{-14}
0.150	2.322×10^{-13}	3.847×10^{-13}	6.272×10^{-13}
0.160	1.837×10^{-12}	3.007×10^{-12}	4.807×10^{-12}
0.180	5.706×10^{-11}	9.077×10^{-11}	1.426×10^{-10}
0.200	8.717×10^{-10}	1.370×10^{-09}	2.113×10^{-09}
0.250	1.116×10^{-07}	1.720×10^{-07}	2.577×10^{-07}
0.300	2.683×10^{-06}	4.073×10^{-06}	6.069×10^{-06}
0.350	2.502×10^{-05}	3.786×10^{-05}	5.595×10^{-05}
0.400	1.298×10^{-04}	1.955×10^{-04}	2.894×10^{-04}
0.450	4.570×10^{-04}	6.891×10^{-04}	1.018×10^{-03}
0.500	1.227×10^{-03}	1.856×10^{-03}	2.738×10^{-03}
0.600	5.214×10^{-03}	7.901×10^{-03}	1.163×10^{-02}
0.700	1.413×10^{-02}	2.145×10^{-02}	3.173×10^{-02}
0.800	2.911×10^{-02}	4.418×10^{-02}	6.535×10^{-02}
0.900	4.983×10^{-02}	7.581×10^{-02}	1.125×10^{-01}
1.000	7.534×10^{-02}	1.150×10^{-01}	1.712×10^{-01}
1.250	1.518×10^{-01}	2.313×10^{-01}	3.445×10^{-01}
1.500	2.356×10^{-01}	3.564×10^{-01}	5.288×10^{-01}
1.750	3.295×10^{-01}	4.886×10^{-01}	7.116×10^{-01}
2.000	4.551×10^{-01}	6.538×10^{-01}	9.253×10^{-01}
2.500	8.745×10^{-01}	$1.197\times10^{+00}$	$1.653\times10^{+00}$
3.000	$1.618\times10^{+00}$	$2.196\times10^{+00}$	$3.118\times10^{+00}$
3.500	$2.790\times10^{+00}$	$3.810\times10^{+00}$	$5.535\times10^{+00}$
4.000	$4.507\times10^{+00}$	$6.124\times10^{+00}$	$8.876\times10^{+00}$
5.000	$9.892\times10^{+00}$	$1.291\times10^{+01}$	$1.811\times10^{+01}$
6.000	$1.872\times10^{+01}$	$2.316\times10^{+01}$	$3.048\times10^{+01}$
7.000	$3.204\times10^{+01}$	$3.773\times10^{+01}$	$4.696\times10^{+01}$
8.000	$5.114\times10^{+01}$	$5.785\times10^{+01}$	$6.893\times10^{+01}$
9.000	$7.719\times10^{+01}$	$8.471\times10^{+01}$	$9.723\times10^{+01}$
10.000	$1.104\times10^{+02}$	$1.196\times10^{+02}$	$1.330\times10^{+02}$

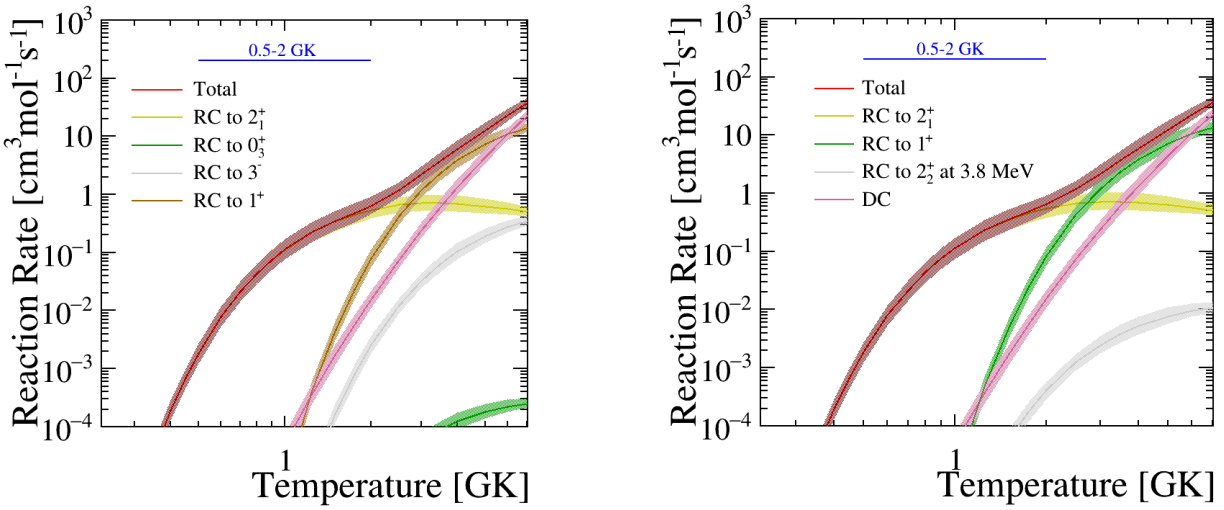

Figure 8.4: he ^{35}K(p,γ)^{36}Ca reaction rate calculated considering an additional contribution of the 0_3^+, 3^- (left) and 2_2^+ (right) state. The red curve represent the total reaction rate, which includes the contributions of resonant (RC) and direct (DC) captures. The thickness of the curves represents a coverage probability of 68%. The indicated range of 0.5 - 2 GK is typical of X-ray bursts temperatures.

that the ^{35}K(p,γ)^{36}Ca reaction would lead to a significant modification of the X-ray burst light curve if the reaction rate was a factor of one hundred higher than that of Iliadis et al. [115]. Such large variation has been allowed in the work of Cyburt et al. [105] because the last estimation of the ^{35}K(p,γ)^{36}Ca reaction rate was performed with the only one resonance (the first 2^+ excited state of ^{36}Ca) for which only its energy was experimentally constrained. Such an increase is absolutely ruled out by our study for which a factor of 2 difference is found at maximum for the reaction rate between 0.5 and 2 GK. In the temperature range relevant for X-ray burst, the potential contribution from additional resonances has been estimated and found to be negligible. Prior to this work, uncertainties in the rate of this reaction had a non-negligible influence on the results of X-ray burst model and those uncertainties are essentially eliminated by this work.

3 Conclusion

The spectroscopy of ^{36}Ca was investigated via the one neutron pick-up reaction ^{37}Ca$(p,d)^{36}$Ca in inverse kinematics, in view of determining useful information for the ^{35}K(p,γ)^{36}Ca reaction rate and compare it to earlier works such as [115]. The energy of the first 2^+ excited state was confirmed and new resonances have been reported in the vicinity of the Gamow window, at excitation energies $E_x = 4.243(40)$ and 4.706(100) MeV. Based on shell model calculations in the *sdpf* valence space and the comparison to the mirror nucleus (^{36}S), spins and parities 1^+ and 2^+ were proposed for these two new observed states, respectively.

The ^{35}K(p,γ)^{36}Ca reaction rate was investigated in the light of the spectroscopic information of ^{36}Ca extracted in Chapter 4 where new resonances have been reported in the vicinity of the Gamow window, at excitation energies $E_x = 4.243(40)$ and 4.706(100) MeV. To complete the set of information needed to compute the reaction rate, the proton branching ratio $B_p = 0.165(10)$ of the first 2^+ state

was measured with two independent methods. The lower limits, $B_p(1^+) > 0.96$ and $B_p(2_2^+) > 0.97$ were estimated for the two other resonant states. Shell model predictions of $B(\omega L)$ were used to compute the only non experimentally-constrained parameter for the resonant states: Γ_γ for which an uncertainty factor of 1.7 was considered based on nuclear structure arguments.

A Monte Carlo procedure [121], which consistently takes into account the uncertainties on the energy, spin parity, partial and total widths of the ^{36}Ca states, was then used to calculate the ^{35}K(p,γ)^{36}Ca reaction rate between 0.01 and 10 GK with its corresponding uncertainty. The factor 1.7 uncertainty associated to the Γ_γ prediction dominates the total uncertainty of the reaction rate in the X-ray burst temperature range of interest. Therefore, the determination of the gamma width (or lifetime) of the 2_1^+ state is desirable, as it would provide an almost fully experimentally-constrained reaction rate. Still this would not change significantly the results obtained in this work.

The present work provides constrains in a broad range of temperatures for the ^{35}K(p,γ)^{36}Ca reaction rate. It should be noted, however, that some additional contributions (not studied in this work) may further increase the reaction rate above 2 GK. Up to 4 GK, our recommended value is consistent, within one sigma, with the one of [115], previously used in X-ray burst models. Based on the reaction sensitivity tests of Cyburt et al. [105], our measured reaction rate is not sufficiently different from previous estimation to modify significantly the luminosity profile of X-ray burst. From the results of this work, the ^{35}K(p,γ)^{36}Ca reaction can be removed from the list of the proton radiative captures reactions having a strong impact on the light curve.

Conclusion and perspectives

In this work, the exotic nucleus ^{36}Ca has been studied using the one neutron and two-neutron transfer reactions ^{37}Ca(p,d)^{36}Ca and ^{38}Ca(p,t)^{36}Ca. The experiment has been performed at GANIL during the summer of 2018. The ^{37}Ca and ^{38}Ca radioactive cocktail beams have been produced at about 50 MeV/nucleons using the LISE spectrometer. Beam particles were tracked by two wire chambers while the light particles emitted during the transfer reactions (d or t) were detected by a set of 6 MUST2 telescopes (composed of Silicon stripped detector DSSD and CsI crystals). The Zero Degree Detection (ZDD), composed of an ionization chamber, a set of 4 drift chambers and a plastic scintillator was used to identify the Z of the outgoing nuclei, as well as their angle with respect to the beam axis. For the CsI crystals, a new calibration procedure has been developed using reference reactions present in the cocktail beams, in order to reach the best possible resolution in excitation energy and in mass measurement. The excitation energy of ^{36}Ca has been reconstructed using the missing mass method, from the measurement of the energy and angle of the light outgoing particles performed by MUST2. The differential cross sections of the populated states have been extracted and used for the determination of the transferred angular momenta L and spectroscopic factors C^2S. The one and two-proton decays of the unbound states populated in ^{36}Ca have been also studied by detecting the decaying protons in coincidence with the light particles emitted during the transfer reaction.

The atomic mass of ^{36}Ca has been re-measured as well as the energy of its first 2^+ excited state, confirming the values obtained in previous studies. Six new excited states have been observed for the first time in ^{36}Ca. The analysis of the ^{37}Ca(p,d)^{36}Ca reaction allowed the identification of states having a pure sd configuration, such as the first 1^+, 2^+ and 4^+ excited states. The DWBA analysis of the differential cross sections confirmed the $L = 0$ nature of the 1^+ and 2^+ states, arising from the removal of a $s_{1/2}$ neutron in ^{37}Ca to populate the corresponding excited configuration. The obtained spectroscopic factors for the first 2^+ and 1^+ are in line with a pure $1p-1h$ $d_{3/2}-s_{1/2}$ neutron configuration. A second 2_2^+ state has been populated as well in the ^{37}Ca(p,d)^{36}Ca reaction whose structure is still under investigation. The analysis of the ^{38}Ca(p,t)^{36}Ca reaction allowed the identification of the second 0_2^+ state at an energy of 2.78(18) MeV, below the first 2^+ state. The clear $L = 0$ shape of the differential cross section, reproduced by the DWBA calculation based on two nucleon amplitude computed by SM calculation, confirmed the $J^\pi = 0_2^+$ spin assignment. This state, which has an intruder proton configuration $(sd)^{-2}(pf)^2$, has been predicted to be the first excited state of ^{36}Ca by SM calculation performed in $sdpf$ valence space [37] and this prediction is confirmed by this work. Moreover, a state has been identified at 4.83(17) MeV in the two-proton decay channel and a spin-parity $J^\pi = 0_3^+$ is proposed for this state based on arguments of one versus two-proton

decay probability. The study of ^{35}Ca has been performed as well using the ^{37}Ca(p,t)^{35}Ca reaction. Its atomic mass as well as the energy of its first excited state, being a $\frac{3}{2}^+$ located at 2.24(33) MeV, has been measured for the the first time.

The results have been interpreted using SM calculation performed in *sdpf* valence space and the $sdpfu-mix$ effective interaction. Mirror Energy Differences (MED) are observed when comparing the excitation energies of the newly discovered states in ^{36}Ca to the ones of the analogue states in the mirror nucleus ^{36}S, and are very well reproduced by the SM calculation. Large MED are observed in the *sd* states being about -250 keV for the first 2^+ and 1^+ state, while Colossal MED (CMED) are observed for the intruder states being about -600 keV for the second 0^+ states. These CMED arise mostly from coulomb effects. Indeed, the fp shell having a larger radius and therefore, less Coulomb repulsion than the *sd* shell, the proton intruder configuration is found to be more bound than the neutron intruder configuration. This is probably the largest effect of the Coulomb interaction on the excitation energy spectrum ever observed is *sd* shell nuclei. The measurement of the mass and of the first excited state of ^{35}Ca allowed to study the size of the $N=16$ gap near to the proton drip-line. A sizable $N=16$ gap is found when comparing our value to systematic of the energy of the first $\frac{3}{2}^+$ along the $N=15$ isotonic chain. This, together with the high excitation energy and spectroscopic factor of the first 1^+ and 2^+ states in ^{36}Ca (that is likely largest than the one of ^{54}Ca recently discovered), are signatures of strong sub-shell closure at $N=16$ and of the doubly-magic nature of ^{36}Ca.

Using the relevant spectroscopic information obtained in this work about ^{36}Ca, together with SM results for the partial γ-width, the ^{35}K(p,γ)^{36}Ca reaction has been re-investigated. This reaction has been identified as one of the ten (p,γ) reactions that could significantly impact the shape of the calculated light curve emitted during Type Ia X-ray burst. A Monte Carlo procedure, which consistently takes into account the uncertainties on the energy, spin parity, partial and total widths of the states, was then used to calculate the ^{35}K(p,γ)^{36}Ca reaction rate between 0.01 and 10 GK with its corresponding uncertainty. This reaction rate is now well constrained for the use of X-ray burst models and it can be removed from the list of the proton radiative capture reactions having a strong impact on the light curve. The next logical step to pursue this work would be to investigate other reactions such as the ^{59}Cu(p,γ)^{60}Zn reaction, which have been identified as the (p,γ) reaction having the strongest impact on the light curve [105].

This work represents a step forward in our understanding of the structure of proton-rich Ca isotopes. However, some information are still missing such as the reduced transition probability of the γ transition from the first 2^+ excited to the ground state of ^{36}Ca. Its value would be a powerful probe of the doubly magic nature of ^{36}Ca and would be also useful to constrain, in a fully experimental way, the ^{35}K(p,γ)^{36}Ca reaction rate. On the mirror side, some information are missing too. Even though ^{36}S is stable and has been extensively studied, the proton $2p-2h$ state has never been observed yet and is desired to probe further the Coulomb effects observed in the MED. The most adapted reaction to populate this state in ^{36}S should be a two proton removal reaction such as the ^{38}Ar(^{14}C,^{16}O)^{36}S reaction, which has never been studied. Moreover, only a very small fraction of the neutron $d_{5/2}$ strength has been identified in ^{36}S, which is mysterious, as discussed in Chap 5. The identification of the $d_{5/2}$ proton hole states in ^{36}S would be very interesting to probe the evolution of the $d_{3/2}-d_{5/2}$ spin-orbit splitting and the fragmentation of the $d_{5/2}$ strength, under the isospin symmetry.

Another interesting physics case, present in our data, but not presented in this manuscript is the ^{37}Ca nucleus. Its spectroscopy has been performed up to 4 MeV using gamma spectroscopy and the higher excited states are still unknown. During this work, the analysis of the ^{38}Ca(p,d)^{37}Ca reaction has been performed in order to identify the neutron $d_{5/2}$ hole states populated between 4 and 10 MeV. This allows to reconstruct the energy centroid of the $d_{5/2}$ orbital and, therefore, to evaluate the $d_{3/2} - d_{5/2}$ spin-orbit splitting in ^{37}Ca. Then, the comparison of the results with the ones obtained in ^{33}S, ^{39}Ca and ^{37}Cl, allows to study the dependence of the spin-orbit coupling with the isospin. Evolutions of the spin-orbit splitting have been found. The analysis of this part is still ongoing.

The natural continuation of this study would be to go a step further toward the proton drip-line, by studying the unbound ^{34}Ca, which has never been observed yet. This nucleus is expected to be doubly magic, with $Z = 20$ and $N = 14$, and the measurement of its mass and its first excited state would allow to probe the size of the $N = 14$ gap at the proton drip-line. Furthermore, it is the mirror nucleus of ^{34}Si, in which a proton central density depletion has been observed [75] and such asymmetry in the charge densities may lead to very large mirror symmetry breaking effects or its total breakdown if ^{34}Ca would turn out to be deformed. This nucleus can be studied using the ^{36}Ca(p,t)^{34}Ca reaction and this reaction was the one of the original goals of the experiment performed for this work. However, the production of the ^{36}Ca radioactive beam being very challenging, not enough intensity for this beam was obtained in order to perform properly this study. We hope to treat this fascinating physics case in the future.

A DWBA

The theoretical description of direct reactions and of the Distorted Wave Born Approximation (DWBA) has been detailed in number of books and articles. This appendix sumurizes some important results obtained when deriving the differential cross section of a transfer reaction using the DWBA. This appendix is based on the book of N.K.Glendenning [122]. Let us consider the following reaction:

$$a + A \rightarrow b + B \tag{A.1}$$

where A is the target nucleus, a the projectile, b the ejectile and B the outgoing compound nucleus. We note α the entrance channel $a+A$ and β the exit channel $b+B$. The differential cross section of such a reaction is:

$$\frac{d\sigma}{d\Omega} = \frac{1}{(2J_a+1)(2J_A+1)} \frac{\mu_\alpha \mu_\beta}{(2\pi\hbar^2)} \frac{k_\beta}{k_\alpha} \sum_{M_\alpha M_\beta} \mid \mathcal{T}_{\alpha\beta} \mid^2, \tag{A.2}$$

where J_a and J_A are the spins of the nuclei in the entrance channel, μ_α and μ_β are the reduced masses of the entrance and exit channels and k_α and k_β are the relative momenta of the nuclei in the entrance and exit channels, respectively. $\mathcal{T}_{\alpha\beta}$ is the transition amplitude of the reaction $\alpha \rightarrow \beta$.

The Hamiltonian of the entrance and the exit channel is:

$$H = H_\alpha + T_\alpha + V_\alpha = H_\beta + T_\beta + V_\beta, \tag{A.3}$$

where $H_\alpha = H_a + H_A$ refers only to the intrinsic structure of the nuclei in the entrance channel and $H_\beta = H_b + H_B$ is the same for the exit channel. $T_{\alpha,\beta}$ is the kinetic energy operator corresponding to the relative motion of the nuclei in the entrance and the exit channel and $V_\alpha = \sum_{i\in a, j\in A} V_{ij}$ denotes the interaction between the nuclei of the channel α.

The scattering of nuclei from each other through the effect of their central field can be accounted for by an optical potential U whose parameters can be adjusted to reproduce the elastic and reaction cross section. The distorted waves $|\chi_{\alpha,\beta}\rangle$ are the eigenstates of the Hamiltonian considering only the optical potential $U_{\alpha,\beta}$ for the interaction between the nuclei in the entrance and the exit channel:

$$(H_{\alpha,\beta} + T_{\alpha,\beta} + U_{\alpha,\beta}) \, |\chi_{\alpha,\beta}\rangle = E \, |\chi_{\alpha,\beta}\rangle \, . \tag{A.4}$$

The transition amplitude can then be written in terms of distorted waves:

$$\mathcal{T}_{\alpha,\beta} = \left\langle \chi_\beta^{(-)}\phi_\beta \middle| V_\beta - U_\beta \middle| \Psi_\alpha^{(+)} \right\rangle, \tag{A.5}$$

where ϕ_α are the plane waves, solutions of the Schrödinger equation considering no interaction between the nuclei. Ψ_α is the total wave function of the incoming channel and the indexes + and − denote the incoming and outgoing boundaries conditions.

The Born Approximation states that the motion of the particles is governed by the optical potential U, representing the elastic diffusion. This is an approximation since it does not represent the possibility of a change of structure in the nuclei. This potential is a central potential depending only on the relative distance between the interacting nuclei. Usually, a Wood-Saxon potential is used, which shape reflects the density distribution of nuclei. It usually includes a Coulomb and a nuclear term, an imaginary term describing the flux lost in the other reaction channels and eventually a spin-orbit interaction term.

In the Born approximation $\Psi_\alpha \backsimeq \chi_\alpha\phi_\alpha$ and the DWBA transition can be written:

$$\mathcal{T}_{\alpha,\beta}^{DWBA} = \left\langle \chi_\beta^{(-)}\phi_\beta \middle| V_\beta - U_\beta \middle| \chi_\alpha^{(+)}\phi_\alpha \right\rangle = \left\langle \chi_\alpha^{(+)}\phi_\alpha \middle| V_\alpha - U_\alpha \middle| \chi_\beta^{(-)}\phi_\beta \right\rangle. \tag{A.6}$$

In the case of a (p,d) transfer reaction, the reaction is denoted:

$$p + A = p + (B + n) \rightarrow (p + n) + B. \tag{A.7}$$

Then from the definition of V_α we have $V_\alpha = V_{pn} + V_{pB}$. V_{pB} corresponds to the interaction of the incoming proton with the nucleus B. From the Born approximation, we assume that this interaction is dominated by the elastic scattering represented by the potential U_{pB}. Considering that $U_{pB} \simeq U_{pA} = U_\alpha$ we can neglect $V_{pB} - U_\alpha \simeq 0$ and obtains the transition amplitude:

$$\mathcal{T}_{\alpha,\beta}^{DWBA} = \int \chi_\alpha^*(\vec{r_\alpha}, \vec{k_\alpha}) \langle \phi_A | \phi_B \rangle \langle \phi_p | V_{pn} | \phi_d \rangle \chi_\beta^*(\vec{r_\beta}, \vec{k_\beta}) d\vec{r_\alpha} d\vec{r_\beta}. \tag{A.8}$$

considering $\phi_\alpha = \phi_p\phi_A$, $\phi_\beta = \phi_d\phi_B$ and that V_{pn} depends only on the relative $p-n$ distance $\vec{r}$. In the zero range approximation, V_{pn} is non zero only if the relative $p-n$ distance is zero $i.e$ $\langle \phi_p | V_{pn} | \phi_d \rangle \simeq D_0\delta(\vec{r})$. This approximation reduces the number of variable to integrate and the computational time. The calculations presented in this work do not use this approximation. They have been performed in finite range, using a radial function for the $p-n$ vertex.

In Eq. A.8, the overlap function $\langle \phi_A | \phi_B \rangle$ is called form factor and contains the nuclear structure information of the nuclei A and B. For a (p,d) reaction, the nuclear state populated in B is constructed from the removal of a neutron in A. The form factor is therefore proportional to the probability of presence of a nucleon on the orbital nlj. The spectroscopic factor C^2S (where C is the Clebsh-Gordan coefficient) then represents the occupancy of the orbital nlj and appears as a factor in the overlap function $\langle \phi_A | \phi_B \rangle$. For a ($p$,$d$) reaction where $B = A - 1$, S can be defined as:

$$S = \frac{|\left\langle \Psi_A^{J_A,M_A} \middle| a^+(nlj) \middle| \Psi_B^{J_B,M_B} \right\rangle|^2}{2J+1}, \tag{A.9}$$

where $\Psi_A^{J_A,M_A}$ denotes the total wave function of the nucleus A in the nuclear state J_A, M_A (same for $\Psi_B^{J_B,M_B}$), $a^+(nlj)$ is the creation operator of a nucleon on the nlj orbital and J is the spin of the final nuclear state created by the addition of the nlj nucleon in B. The measurement of the spectroscopic factor is therefore a direct measurement of the single-particle purity of the final state. Usually DWBA calculations are performed considering a spectroscopic factor equal to one and C^2S is then extracted experimentally from:

$$C^2S = \left(\frac{d\sigma}{d\Omega}\right)_{Exp} \left(\frac{d\sigma}{d\Omega}\right)^{-1}_{DWBA}. \tag{A.10}$$

In Eq. A.9, $\vec{j} = \vec{l} + \vec{s}$ corresponds to the total angular momentum transferred. From the conservation of the total angular momentum of the reaction, one can deduce the selection rules of a transfer reaction:

$$\begin{cases} J_B = J_A + j \\ \pi_B = \pi_A(-1)^l \end{cases} \tag{A.11}$$

The final differential cross section strongly depends on the transferred angular momentum l. The value of l can be determined by comparison of the DWBA cross section with the experimental one. The selection rules give explicit relations between initial and final angular momenta and parity of the nuclear states, such that, if those of the initial state are known, then those of the final state can be inferred.

In the case of a one-nucleon transfer, the shape of the angular distribution is determined by the transferred angular momentum l. This momentum is directly linked to the orbital angular momentum of the nucleon from (or to) which the nucleon is transferred. Therefore, one nucleon transfer probes directly the structure of the states. In the case of two-nucleon transfer, the transferred angular momentum L also characterizes the shape of the angular distribution but it is carried by the pair of nucleons. Many different configurations of the two nucleons can contribute to the resulting angular momentum. Furthermore, in the case of a one-nucleon transfer, the cross-section can be factorized into two parts, one containing the structure information (the form factor) and the other depending on the reaction mechanism. Considering only one orbital nlj, the amplitude of the cross section is then proportional to the probability that the nucleon occupies the nlj orbital from which the transfer is done (spectroscopic factor). For two nucleon transfers, the cross section is not proportional to the spectroscopic factor but to the Two-Nucleon Amplitude. Let us consider a two-nucleon transfer reaction where a nucleus $A-2$ is in an initial state J_i. Two nucleon are added to this nucleus on the orbitals $a = (nlj)_1$ and $b = (nlj)_2$ to obtain the final nucleus in a nuclear state J_f. One can shows that the final cross section will be proportional to the Two Nucleon Amplitudes (TNA) defined as:

$$TNA(f,i,a,b) = \sum_m (-1)^{J_i+J_f+\lambda}\sqrt{2\lambda+1} \begin{Bmatrix} J_f & J_i & \lambda \\ j_a & j_b & J_m \end{Bmatrix} \times \frac{\langle A, J_f | a_a^+ | A-1, J_m\rangle \langle A-1, J_m | a_b^+ | A-2, J_i\rangle}{\sqrt{1+\delta_{ab}}} \tag{A.12}$$

where J_m is the nuclear state of the intermediate nucleus $A-1$. One can identify in this equation the spectroscopic factors defined in the case of the one nucleon transfer which we cannot factorize anymore since we have to sum over all the intermediate configurations J_m. To compute a complete

two nucleon transfer cross section, all the a and b possible configurations have to be taken into account. Depending on how the two-nucleons are coupled, constructive or destructive interferences can occur for the cross sections. The extraction of spectroscopic factors with two-nucleon transfer is therefore very difficult and a precise description of the amplitude of experimental cross sections is very challenging.

In this work, the main goal of the analyis of the angular distributions obtianed with two-nucleon transfer is to determine the transferred angular momentum L, in order to constrain the spins and parities of the states produced in the (p,t) reaction. The selection rules on the transferred angular momentum L, for two-nucleon transfer are given by [123]:

$$\begin{cases} \pi_i \pi_f = (-1)^L \\ J_f = J_i + L + S \end{cases} \tag{A.13}$$

where π_i, J_i and π_f, J_f are the parities and spins of the initial and final nucleus, respectively. In the case of a (p,t) transfer, $S = 1$ in order to respect the Pauli exclusion principle. Therefore, for a spin parity $J^\pi = 0^+$ of the initial nuclei (which is the case for the ^{36}Ar(p,t)^{34}Ar and the ^{38}Ca(p,t)^{36}Ca reactions), the spin parity assignments to the final nuclear states $J_f = L$ is unambiguous once the L transferred has been determined.

B Thermonuclear reaction rates

1 Reaction rate

This section summarizes the most important features about the reaction rate formalism. The complete formalism can be found in Ref. [108]. The cross section σ of a reaction, represents the probability for the reaction to occur, expressed in units of surface. It is defined by:

$$\sigma = \frac{\mathcal{N}_r/t}{\mathcal{N}_t\mathcal{N}_b/(tA)}, \tag{B.1}$$

where $\mathcal{N}_r/t$ is the number of reaction per unit of time, $\mathcal{N}_t$ is number of target particle and $\mathcal{N}_b/(tA)$ is the number of beam particle per unit of time and surface, considering that the beam overlap with the target on the area A. The following only concerns non-photon particles in the entrance channel. The nuclear cross section σ depends on the relative velocity between the projectile and the target. In astrophysical environment, where the particles have a velocity distribution, it is more convenient to use a quantity that reflect both effect of the cross section and the relative velocity v of the interacting particles. Therefore, we define the nuclear reaction rate r as the number of reaction per unit of time and volume:

$$r = \frac{\mathcal{N}_r}{Vt} = \sigma\frac{\mathcal{N}_t\mathcal{N}_b}{VAt} = \sigma v\frac{\mathcal{N}_t\mathcal{N}_b}{V^2}. \tag{B.2}$$

By defining the $N_t = \mathcal{N}_t/V$, the density of target particle and $N_t = \mathcal{N}_b/V$, the density of beam particle, one can rewrite the reaction rate as:

$$r = N_bN_tv\sigma(v). \tag{B.3}$$

The relative velocity distribution of the beam particle and the target particle can be described by the probability function $P(v)$, with:

$$\int_0^\infty P(v)dv = 1. \tag{B.4}$$

One can therefore generalize the reaction rate expression for a relative velocity distribution with:

$$r = N_b N_t \int_0^\infty v P(v) \sigma(v) dv = N_b N_t \langle \sigma v \rangle. \tag{B.5}$$

where $\langle \sigma v \rangle$ is the reaction rate per particle pair and $N_b N_t$ is the density of pairs of beam and target particle.

In a stellar plasma (which is the environment in which X-ray bursts occur) the kinetic energy available to nuclei is that of their thermal motion. Thus the velocities of nuclei can be described by a Maxwell–Boltzmann distribution:

$$P(v)dv = \left(\frac{\mu}{2\pi kT}\right)^{3/2} e^{-\mu v^2/(2kT)} 4\pi v^2 dv, \tag{B.6}$$

where k is the Boltzmann constant, T is the temperature and μ is the reduced mass of the system. By writing the kinetic energy $E = \frac{\mu v^2}{2}$, one can replace in equation B.5 the velocity distribution by the energy distribution and obtain the following expression for the reaction rate per particle pair [108] :

$$\langle \sigma v \rangle = \left(\frac{8}{\pi\mu}\right)^{1/2} \frac{1}{(kT)^{3/2}} \int_0^\infty E\sigma(E) e^{-E/kT} \tag{B.7}$$

Thus, to compute the reaction rate one has to determine the magnitude and the energy dependency of the cross section of the reaction $\sigma(E)$. The cross section can be either measured or estimated theoretically. For an isolated resonance (meaning that resonances do not overlap), the capture cross section can be described by the one-level Breit-Wigner formula:

$$\sigma_{BW}(E) = \frac{\lambda^2}{4\pi} \frac{(2J+1)}{(2J_b+1)(2J_t+1)} \frac{\Gamma_a(E)\Gamma_b(E+Q-E_f)}{(E_r-E)^2 - \Gamma(E)^2/4} \tag{B.8}$$

where the J_b and J_t are the spins of the beam and target particles, J, Γ_i, Γ and E_r are the spin, the partial decay widths (in the entrance a and the exit b channel), the total width and the energy of the resonance, respectively. Q is the Q value of the reaction while E_f is the energy of the state in which the compound nucleus is populated in the exit channel.

The partial particle width for a given state λ and a channel c is:

$$\Gamma_{c,\lambda} = 2P_l(E)\gamma_{c,\lambda}^2, \tag{B.9}$$

where $P_l(E)$ is the penetration factor of the Coulomb and the centrifugal barriers, l and E are the angular momentum and the energy of the particle c, respectively, and $\gamma_{c,\lambda}$ is the reduced particle width of the state λ in the channel c.

The partial width for a given γ-ray transition is given by:

$$\Gamma_\gamma(\omega L) = \frac{8\pi(L+1)}{L[(2L+1)!!]^2} \left(\frac{E_\gamma}{\hbar c}\right)^{2L+1} B(\omega L), \tag{B.10}$$

where ω names the nature of the transition (Electric or Magnetic) and L its multipolarity. $B(\omega L)$ is the reduced transition probability for the γ decay of the resonant state (in unit of $e^2 fm^4$ for E2 transitions and μ_N^2 for M1 transitions) and E_γ the energy of the γ-ray transition.

Depending on the energy dependence of the cross section (given mainly by the energy dependence of the partial decay widths) to the energy, different approximations can be made in order to estimate the reaction rate. In the following we will first introduce the Gamow peak, then, three cases will be treated: non-resonant cross sections, narrow resonance cross sections and broad resonance cross sections.

2 The Gamow peak

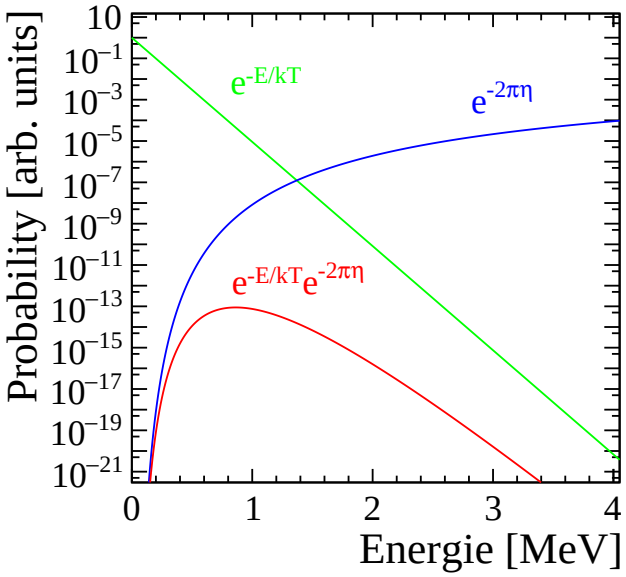

Figure B.1: Evolution of the Maxwell–Boltzmann factor (in blue) and Gamow factor (in green) as a function of the energy. The product of both, referred to as the Gamow peak, is shown by the red line.

For a charged particle, the probability of a capture reaction to occur is proportional to the transmission probability of the Coulomb barrier. In the case of a s-wave particle (with orbital angular momentum $l = 0$) with an energy well below the height of the Coulomb barrier, the transmition probability can be approximate by the Gamow factor $e^{-2\pi\eta}$ [108] (where η is the Sommerfeld parameter). In the previous section, we saw that the kinetic energy distribution of the particles in a stellar plasma can be described by a Maxwell–Boltzmann distribution which is proportional to $e^{-E/kT}$ (see Eq. B.6. Then the probability of a capture reaction to occur in a stellar plasma is proportional to the product of the Sommerfield factor and the Maxwell–Boltzmann factor $e^{-E/kT}e^{-2\pi\eta}$. This is shown in Fig. B.1 where these factors are represented together with their product. Since $e^{-E/kT}$ approaches zero for high energies and $e^{-2\pi\eta}$ tends to zero at low energies, the product of both factor is non-negligible in an energy range represented by the Gamow peak. The Gamow peak represents the energy range in which a capture reaction has the most probability to occur. The centroid E_0 and the width Δ of this peak are given by:

$$\begin{cases} E_0 = (\frac{bkT}{2})^{2/3} \\ \Delta = \frac{4}{\sqrt{3}}\sqrt{E_0 kT} \end{cases} \tag{B.11}$$

with $b = \frac{\pi e^2}{\hbar}\sqrt{2\mu}Z_1 Z_2$. T is the temperature, k is the Boltzmann constant, e the elementary charge, μ the reduced mass of the system and Z_i the charge of the nucleus i.

3 Non-resonant reaction rates

Non-resonant cross section varies smoothly with energy, if the energy is high enough to cross the coulomb barrier. For capture reactions where the direct process component is dominant, the direct capture occurs on bound states of the final nucleus, at any incident energy. Usually, the cross section is expressed in term of astrophysical S-factor $S(E)$, which expresses the nuclear part of the cross-section [108] :

$$\sigma(E) = \frac{1}{E} e^{-2\pi\eta} S(E), \tag{B.12}$$

This definition allows to removes the $1/E$ dependence of the nuclear cross sections and yo get rid of the Coulomb Barrier penetrability effect. The resulting S-factor varies far less with energy than the cross section. Therefore, the S-factor can be expand in a Taylor series around $E = 0$:

$$S(E) = S(0) + S'(0)E + \frac{1}{2}S''(0)E^2, \tag{B.13}$$

where the primes indicate derivatives with respect to E. By substituting this expression into Eq. B.7 one can solve the integral and obtain [108]:

$$\langle \sigma v \rangle_{nr} = \frac{1}{3}\left(\frac{4}{3}\right)^{3/2} \frac{\hbar}{\pi} \frac{1}{\mu Z_b Z_t e^2} S_{eff} \tau^2 e^{-\tau}, \tag{B.14}$$

where $\tau = 3E_0/(kT)$ with E_0 the maximum energy of the Gamow peak and S_{eff} is an effective S-factor depending on $S(0)$, $S'(0)$ and $S''(0)$ (see Eq. 3.94 in Ref. [108]). To compute a complete reaction rate, the direct capture contribution has to be taken into account. The more bound states are present in the compound nuclei, the more the contribution of the direct capture will be important. It can even dominate the reaction rate at low energies of for nuclei in that have a low density of states and for which the resonances are far from the Gamow window. To estimate the non-resonant contribution, one has to compute the S-factor.

4 Narrow-resonance reaction rates

A resonance can be considered as narrow if its partial widths are approximately constant over the total resonance width. This approximation can be considered correct if $E_r \gg \Gamma$. In this case, the Maxwell-Boltzmann factor $e^{-E/kT}$ of Eq. B.7 and the partial width Γ_i are considered constant over the resonance width. The one-level Breit-Wigner formula can then be written as:

$$\sigma_{BW}(E) = \frac{\lambda^2}{4\pi} \frac{(2J+1)}{(2J_b+1)(2J_t+1)} \frac{\Gamma_a \Gamma_b}{(E_r - E)^2 - \Gamma^2/4} \tag{B.15}$$

By substituting Eq. B.15 in Eq. B.7 one obtains the rreaction rate formula for narrow-resonances

[108]:

$$\langle \sigma v \rangle = \left(\frac{2\pi}{\mu kT} \right)^{3/2} \sum_i (\omega\gamma)_i e^{-E_{r,i}/kT}, \tag{B.16}$$

where the incoherent sum over all the contributing resonances i is performed. Here, $E_{r,i}$ is the resonance energy of the resonance in and $(\omega\gamma)_i$ is its resonance strength defined as:

$$(\omega\gamma)_i = \frac{(2J+1)}{(2J_b+1)(2J_t+1)} \frac{\Gamma_a \Gamma_b}{\Gamma} \tag{B.17}$$

In this equation, one can see that in order to compute the contribution of a narrow resonance to the reaction rate one has to know its energy, its spin, its partial widths or branching ratios and its total width. If these informations are not known experimentally, they can either be predicted by Shell-Modell calculation or determined from the analogue states in the mirror nucleus (if its resonances are known). Both methods induce uncertainties on the final reaction rate, the best way being to constrain these parameters experimentally.

5 Broad-resonance reaction rates

If a resonance is broad enough, the Maxwell-Boltzmann factor $e^{-E/kT}$ of Eq. B.7 and the partial width Γ_i could vary significantly along the width of the resonance. In this case, the assumption made just above are not correct anymore. Therefore the energy dependency of the partial widths have to be taken into account. If the reduced particle widths and the reduced transition probabilies of the resonances are known, this is done by substituting Eq. B.9 and Eq. B.10 in Eq. B.8. The reaction rate for broad resonances is then found by numerical integration after substituting Eq. B.8 into Eq. B.7. As in the last case this method requires to know the energy, spin, partial widths and total width of the resonance at the resonance energy.

C Résumé en Français

Sommaire

Cette annexe contient un résumé de mon travail de thèse. L'objectif de cette synthèse étant d'être consulté par un public élargi, j'ai écarté sciemment de nombreux points techniques. Pour une information complète, j'invite les personnes curieuses et anglophones à lire le manuscrit dans son intégralité.

1 Structure Nucléaire

1.1 Introduction

Le monde dans lequel nous vivons est fait de matière composée de très petits éléments appelés molécules et atomes. Pendant des siècles, les scientifiques ont pensé que les atomes étaient les briques les plus élémentaires à partir desquelles notre univers était construit. Grâce à des pionniers comme Rutherford, Bohr ou Curie, nous savons aujourd'hui qu'un atome est composé d'un nuage de particules chargé négativement, les électrons, et qu'ils orbitent autour d'un noyau chargé positivement. Le noyau atomique est lui-même composé de deux types de particules : les protons, chargés positivement, et les neutrons, qui sont neutres. Ces particules sont liées entre elles par l'interaction forte pour former un noyau. La physique nucléaire est la science qui étudie cet ensemble complexe, son comportement et ses propriétés fondamentales.

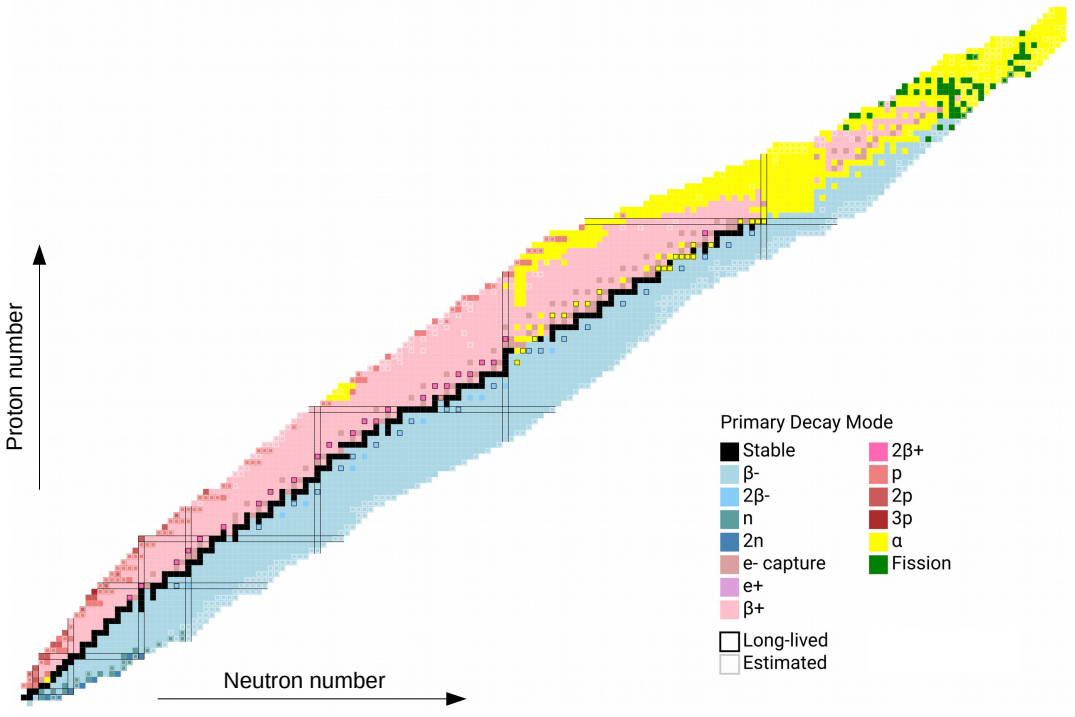

Figure C.1: La carte des nucléides. Les couleurs représentent les différents modes de décroissance (voir légende). La figure est extraite de Ref. [1].

Les noyaux atomiques sont habituellement représentés dans la carte des nucléides, présentée en Figure C.1. Dans ce tableau, chaque case représente un noyau, classé en fonction de son nombre de protons Z et de neutrons N. Aujourd'hui, 3314 noyaux sont connus expérimentalement, de l'hydrogène

(Z = 1) à l'Oganesson (Z = 118). Seuls 288 de ces noyaux sont stables, les autres sont radioactifs en raison d'un excès de protons ou de neutrons. Aujourd'hui, dans les laboratoires, on peut étudier expérimentalement des noyaux très exotiques en s'éloignant de la vallée de stabilité et ceci, avec une grande asymétrie proton-neutron. Comprendre l'évolution des propriétés nucléaires fondamentales telles que la masse, le rayon ou les énergies des états excités lors du passage de noyau stable à noyau exotique, est au cœur des études des structures nucléaires.

Pour décrire le noyau atomique, les physiciens utilisent des modèles théoriques. L'un d'entre eux, le modèle en couches a rencontré de nombreux succès dans la description de phénomènes observés expérimentalement, comme la séquence des nombres magiques. Un nombre magique est un nombre de protons ou de neutrons pour lequel un noyau atomique est particulièrement stable. Dans le modèle en couches, les nucléons (les protons et les neutrons) se placent sur des orbites (ou couches) définies par trois nombres quantiques n, l et m et une énergie. Un nombre magique correspond alors à un nombre de protons ou de neutrons pour lequel la couche est complète (ou fermée) tandis que la couche suivante est à beaucoup plus haute énergie. C'est par exemple le cas du nombre magique 20, pour lequel la couche $1d_{3/2}$ ($n = 1$, $l = 2$, $m = 3/2$) est fermée et la couche supérieure $1f_{7/2}$ ($n = 1$, $l = 3$, $m = 7/2$) est située plus haut en énergie. Cette propriété confère au noyau possédant un nombre de protons ou/et de neutrons égal à 20, une stabilité accrue.

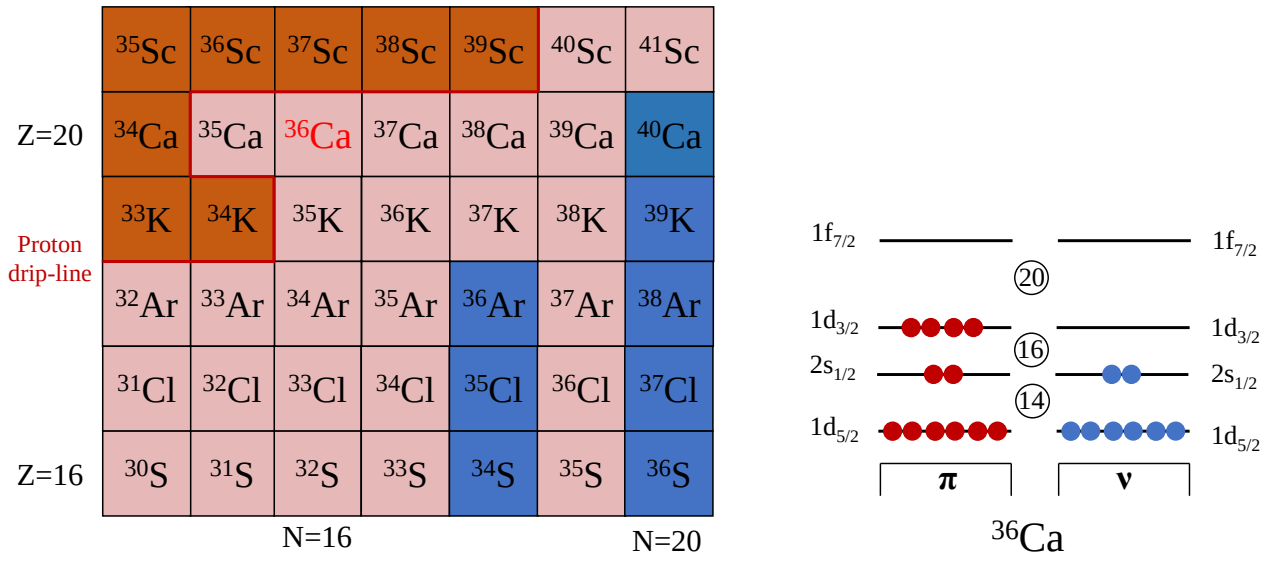

Figure C.2: Gauche: la carte des nucléides agrandie autour de ^{36}Ca. Droite : Structure de l'état fondamental de ^{36}Ca selon le modèle en couches.

L'objectif principal de ce travail est l'étude du noyau de ^{36}Ca. Le noyau de ^{36}Ca possède 20 protons et 16 neutrons. Avec 4 neutrons de moins que son isotope stable le plus proche, ^{40}Ca (voir Figure C.2), le noyau de ^{36}Ca est instable avec une durée de vie d'environ 100 ms [33]. ^{36}Ca a un nombre magique de protons, remplissant toute les couches jusqu'à la $1d_{3/2}$. Avec 16 neutrons, les couches sont remplies jusqu'à la $2s_{1/2}$, comme montré dans la partie droite de la Figure C.2. Nous disposons de peu d'informations à propos de ce noyau. Seules sont connues sa masse, sa durée de vie et l'énergie de son premier état excité, de spin-parité $J^\pi = 2^+$ à 3.045 MeV [36]. Ce dernier étant non lié, le seuil d'émission proton positionné à 2.56 MeV d'énergie d'excitation, signifie qu'il peut

décroître vers une configuration plus stable en émettant un proton. Pour autant, le noyau de ^{36}Ca possède plusieurs propriétés fascinantes liées à sa structure nucléaire. L'une d'entre elles est liée à la symétrie d'isospin (ou symétrie miroir) qui échange le nombre de protons et de neutrons. La symétrie isospin est l'une des symétries les plus fondamentales du noyau et est liée à l'indépendance de charge de l'interaction forte. Si la symétrie d'isospin est strictement respectée, les schémas de niveaux des noyaux miroirs (avec un nombre échangé de protons et de neutrons) devraient être identiques. L'interaction coulombienne brise la symétrie d'isospin car elle n'agit que sur les protons chargés positivement et elle donne lieu à un décalage de l'énergie d'excitation entre les états analogues des noyaux miroirs, appelée différence d'énergie miroir (MED). Dans le cas de la paire de noyaux miroirs ^{36}Ca-^{36}S, l'interaction Coulombienne agit comme une loupe de la structure nucléaire de leurs états excités. Les effets seront examinés dans ce travail.

1.2 Dispositif expérimental

Le noyau de ^{36}Ca a été étudié au GANIL au moyen des réactions de transfert ^{37}Ca(p,d)^{36}Ca et ^{38}Ca(p,t)^{36}Ca à partir de faisceaux radioactifs de ^{37}Ca et ^{38}Ca à environ 50 MeV/nucléons. Lors d'une réaction de transfert, un ou plusieurs nucléons sont transférés du projectile à la cible afin de produire le noyau d'intérêt (transfert d'un neutron dans le cas de la réaction (p,d) et de deux neutrons dans le cas de la réaction (p,t)). Les réactions de transfert sont un outil très puissant pour les études de structures nucléaires car elles sont très sélectives et permettent de peupler seulement les états dits de simples particules, ayant une configuration pure et très bien décrite par le modèle en couches.

Les faisceaux de ^{37}Ca et ^{38}Ca ont été produits par fragmentation, à l'aide du spectromètre LISE. Un schéma du dispositif expérimental utilisé dans cette expérience est présenté en Figure C.3. Le faisceau de noyaux incidents a été mesuré par deux ensembles de détecteurs CATS, sensibles à la position. Les noyaux interagissent ensuite avec une cible cryogénique d'hydrogène liquide CRYPTA, dans laquelle la réaction de transfert a lieu. Afin de détecter les particules légères émises lors de la réaction de transfert (particules d et t), 6 télescopes MUST2 (composés d'un étage de silicium à piste DSSD et d'un étage de cristaux de CsI) ont été utilisés. À zéro degré, un ensemble de trois détecteurs (chambre d'ionisation, chambre de dérive et scintillateur en plastique) a été utilisé pour détecter l'ion lourd dans le canal de sortie.

La détection des éjectiles légers et lourds a permis une détermination complète de la cinématique de la réaction. Grâce à la mesure de l'énergie et de l'angle d'émission de la particule légère dans la voie de sortie, l'énergie d'excitation des états peuplés dans le noyau de ^{36}Ca a été reconstruite en utilisant la méthode de la masse manquante. Les distributions angulaires de ces mêmes particules ont permis une attribution du moment angulaire transféré L de tous les états produits, afin de contraindre leurs valeurs de spin-parité J^{π}. De plus, les états excités de ^{36}Ca étant non-liés, ils décroissent en émettant un ou plusieurs protons. Ces protons sont détectés en coïncidence avec la particule de transfert dans les télescopes MUST2 et sont utilisés dans l'analyse afin de déterminer l'énergie d'excitation des états excités. La détection à zéro degré (ZDD) permet d'identifier le Z de l'ion en sortie et donc d'étudier séparément les modes de décroissance gamma, un-proton et deux-protons du ^{36}Ca, en sélectionnant respectivement un Ca, un K ou un Ar dans la ZDD. De plus, la coïncidence entre noyau incident,

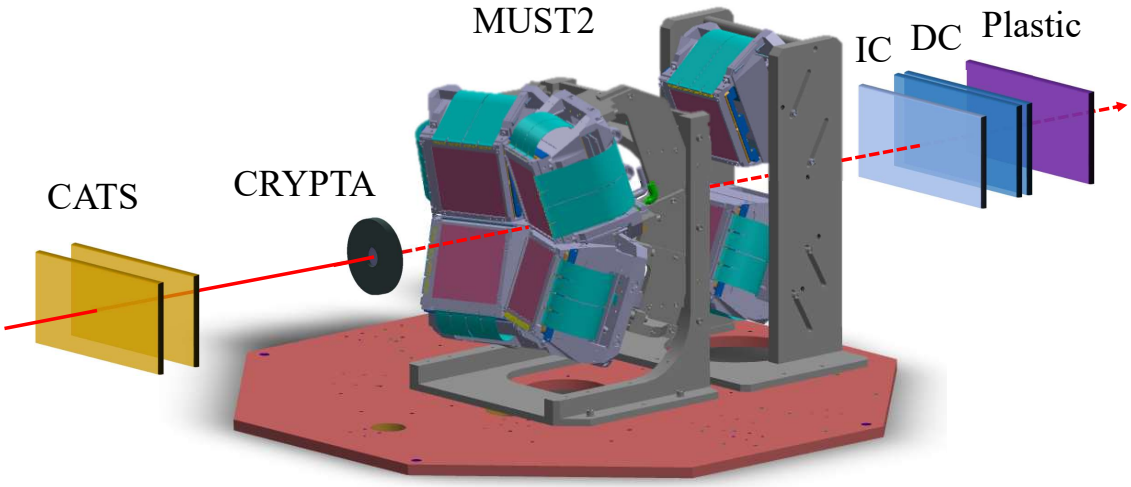

Figure C.3: Schéma du dispositif expérimental (pas à l'échelle). Les télescopes MUST2 sont représentés avec la cible d'hydrogène liquide CRYPTA, la chambre à ionisation (IC), les chambres à dérive (DC) et le scintillateur plastique.

particule de transfert et noyau lourd en sortie permet une suppression quasi totale du bruit de fond.

1.3 Résultats

L'analyse des données issues de cette expérience a permis la découverte de nouveaux états de grand intérêt dans le noyau de ^{36}Ca. La partie gauche de la Figure C.4 montre (dans le panneau supérieur) le spectre d'énergie excitation du noyau de ^{36}Ca obtenu lors de la réaction de transfert ^{37}Ca(p,d)^{36}Ca . Pour obtenir ce spectre, des conditions sont appliquées afin de sélectionner un ^{37}Ca incident, un deutéron (particule d) dans MUST2 et un noyau de Ca, K ou Ar en sortie. Ce spectre a été ajusté avec une fonction composée de plusieurs Gaussiennes et cet ajustement a été confirmé par les spectres en énergie des protons émis lors de la décroissance. Le panneau inférieur montre la corrélation entre l'angle θ_{cm} d'émission du deutéron dans le référentiel du centre de masse de la réaction et l'énergie d'excitation de ^{36}Ca. On peut voir un changement de régime dans la forme des distributions angulaires à environ 2 MeV et 6 MeV. Autour de 0 MeV et entre 6 et 10 MeV un seul maximum est observé à environ 20° ce qui est typique d'une distribution de type $L = 2$. Entre 2 et 6 MeV, 2 maximums sont observés à 0° et 25°, ce qui est typique d'une distribution de type $L = 0$.

Grâce à l'ajustement du spectre en énergie d'excitation, plusieurs états ont pu être observés et sont résumés dans la partie droite de la Figure C.4. Le premier, à 0 MeV, correspond à l'état fondamental du ^{36}Ca. Pour obtenir la configuration fondamentale du ^{36}Ca, le neutron dans ^{37}Ca doit être retiré de

la couche $1d_{3/2}$ ($l = 2$) (voir le bas de la Figure C.4). Ceci est en accord avec la forme $L = 2$ observée de la distribution angulaire (le moment angulaire transféré L provenant du moment angulaire l de l'orbital de laquelle le neutron a été retiré). Le deuxième état correspond au premier état excité 2^+, déjà connu. Notre mesure confirme sa position. Une distribution de type $L = 0$ est observée pour cet état, émergeant du retrait d'un neutron de l'orbite $2s_{1/2}$ ($l = 0$) dans ^{37}Ca. Ceci indique une configuration particule-trou pour cet état avec un neutron dans l'orbite $2s_{1/2}$ et un neutron dans l'orbite $1d_{3/2}$.

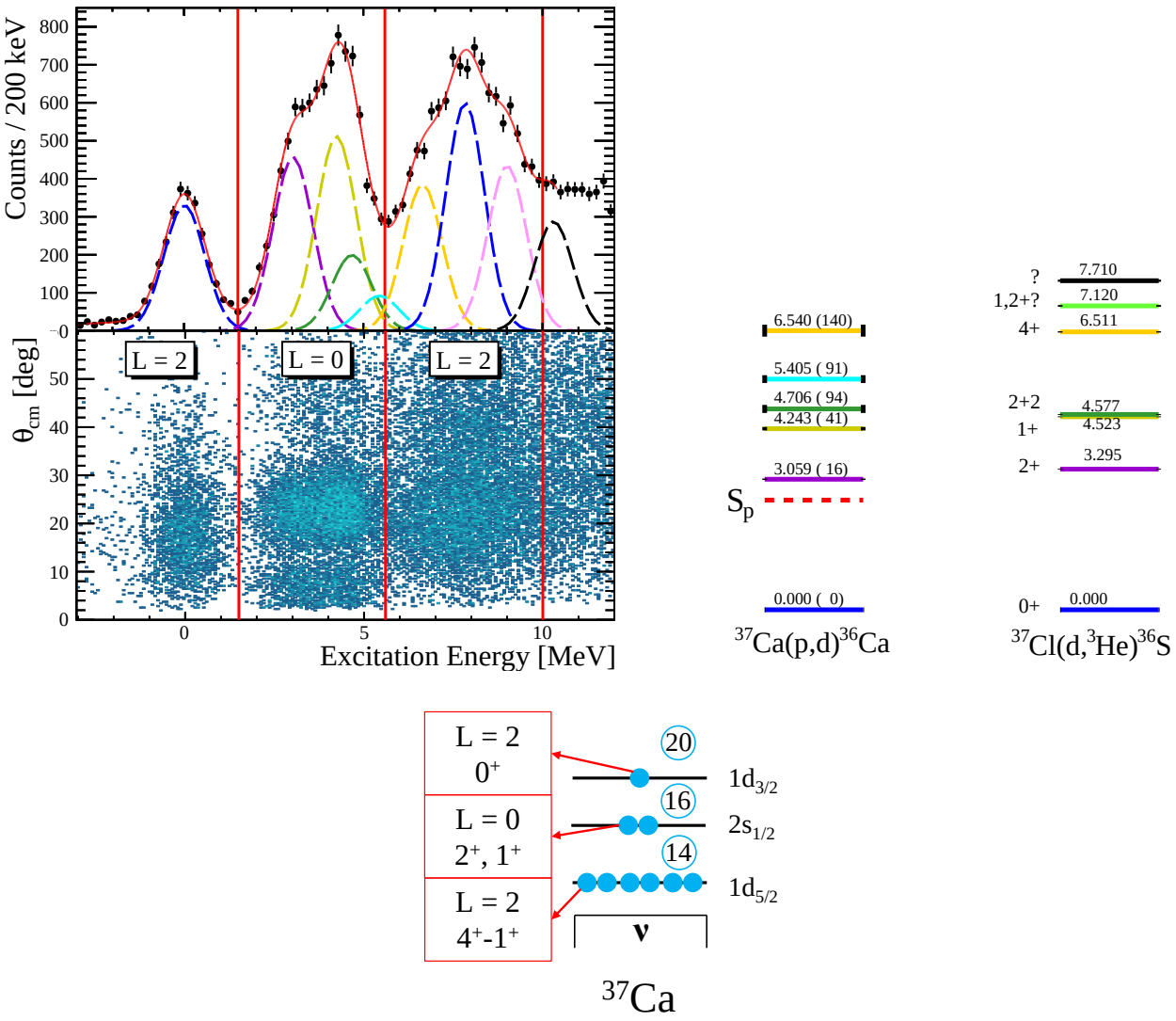

Figure C.4: Gauche : Corrélation entre l'angle θ_{cm} du deutéron dans le référentiel du centre de masse de la réaction et l'énergie d'excitation de ^{36}Ca. Le panneau supérieur montre la projection sur l'axe de l'énergie d'excitation ainsi que son ajustement. Les lignes verticales rouges soulignent les changements de régime dans les distributions de θ_{cm}. Droite : Schéma de niveau de ^{36}Ca obtenu à partir des ajustements des différents spectres d'énergie d'excitation et d'énergie protons, comparés à celui de ^{36}S, obtenu en utilisant la réaction miroir ^{37}Cl(d,^{3}He)^{36}S [57]. En bas : Vue schématique de la structure en couches des neutrons de ^{37}Ca. La nature du transfert et les états produits qui correspondent à l'orbitale de laquelle le neutron est retiré, sont indiqués dans les cases rouges.

À plus haute énergie d'excitation, 4 nouveaux états ont été identifiés pour la première fois dans le

noyau de ^{36}Ca à une énergie de 4.24, 4.71, 5.41 et 6.54 MeV. Basé sur la comparaison avec les niveaux peuplés dans la réaction miroir (montrés à l'extrême droite de la Figure C.4), sur la forme des distributions angulaires et sur des calculs théoriques de modèle en couches, nous proposons l'assignation de spin-parité 1^+, 2^+_2, 1-4^+ et 4^+ pour ces états respectivement. Les états 1^+ étant observés avec une distribution $L = 0$, ils partagent la même configuration neutrons que le premier 2^+ évoqué plus haut. Pour l'état à 5.41 MeV, l'état analogue n'a pas été observé dans la réaction miroir. La proposition 1-4^+ se base donc seulement sur la forme $L = 2$ de la distribution. À l'inverse, un état de spin-parité 4^+ a été observé dans la réaction miroir à une énergie similaire de celle observée dans ce travail.

Les sections efficaces différentielles, correspondant à chaque état peuplé, ont été reconstruites en fonction de l'angle θ_{cm} d'émission du deutéron dans le référentiel du centre de masse de la réaction et elles sont présentées en Figure C.5. Dans la Figure C.5, on peut clairement identifier les distributions $L = 0$ en vert, avec un maximum à 0° et les distributions $L = 2$, en bleu, avec un maximum à environ 20°. Les lignes de couleurs représentent les calculs théoriques des sections efficaces différentielles réalisées dans l'approximation DWBA. En normalisant les calculs aux données, nous avons extrait les facteurs spectroscopiques C^2S pour chaque état. Ce facteur est une mesure de la pureté d'un état et est proportionnel au nombre de nucléons occupant l'orbital. Par exemple, l'état fondamental 0^+ est obtenu en retirant un neutron de l'orbite $1d_{3/2}$ dans ^{37}Ca cette orbite est initialement peuplée par un seul neutron. Comme un seul niveau est généré par la configuration fondamentale de ^{36}Ca et que cet état est très pur (signifiant qu'une seule configuration contribue en grande majorité à cet état), nous observons un facteur spectroscopique de 1, représentant la totalité de la force $1d_{3/2}$ disponible. Nous pouvons constater que les calculs théoriques reproduisent très bien les formes des distributions expérimentales, confirmant les assignations de moments angulaires transférés L, données ci-dessus. De plus les valeurs de facteurs spectroscopiques élevées pour le premier 2^+ et le premier 1^+ indiquent une configuration neutron pur particule-trou. Il en va de même pour le 4^+, avec une configuration particule-trou consistant en 1 neutron sur l'orbite $d_{3/2}$ et un trou dans l'orbitale

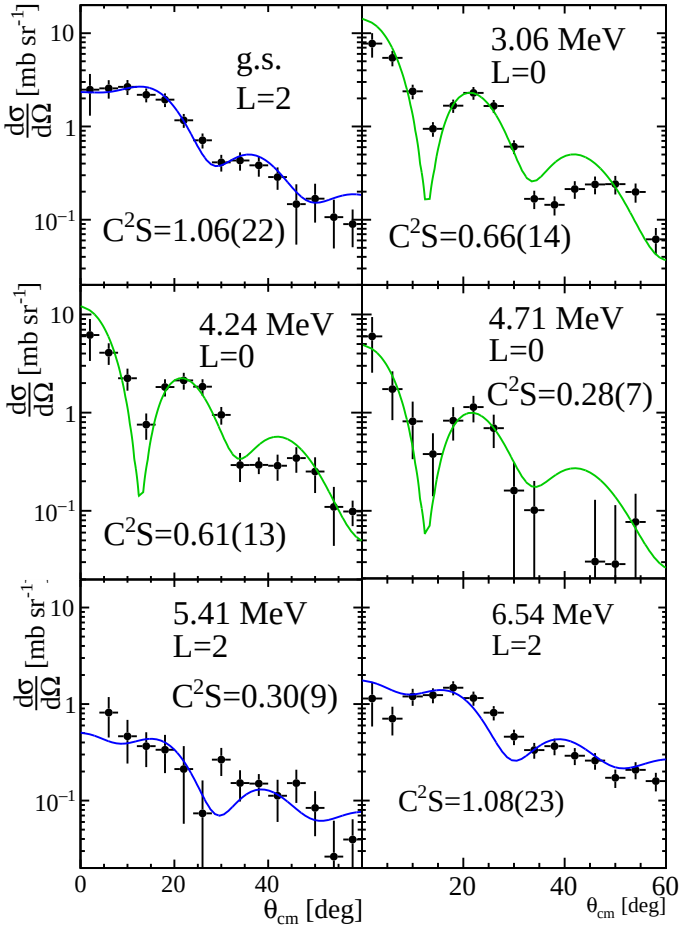

Figure C.5: Sections efficaces différentielles des états identifiés dans ^{36}Ca. Les lignes bleues (vertes) montrent les calculs théoriques DWBA effectués pour une distribution $L = 2$ ($L = 0$). Pour chaque calcul, le facteur spectroscopique résultant est également donné avec son incertitude totale.

$d_{5/2}$.

L'analyse de la voie de réaction ^{37}Ca(p,d)^{36}Ca a permis d'identifier 4 nouveaux états dans le noyau de ^{36}Ca. La seconde voie de réaction ^{38}Ca(p,t)^{36}Ca , correspondant au transfert de deux neutrons du projectile à la cible, est présentée ci-dessous. La partie gauche de la Figure C.6 montre le spectre en énergie d'excitation de ^{36}Ca, obtenu avec la réaction ^{38}Ca(p,t)^{36}Ca , et en imposant d'avoir observé un Ca dans la voie de sortie. Dans ce spectre, on peut clairement identifier l'état fondamental à 0 MeV et un second état à environ 2.8 MeV. La partie droite de la figure montre les sections efficaces différentielles obtenues pour ces 2 états ainsi que les calculs théoriques correspondants. Pour le fondamental, la distribution affiche clairement une forme $L = 0$. Dans le cas d'un transfert de deux nucléons, le moment angulaire transféré L est porté par la paire de neutrons. Pour une transition $0^+ \rightarrow 0^+$, la seule possibilité est de retirer une paire de neutrons qui provient de la même orbitale de façon à ce qu'ils se couplent dans le canal $L = 0$. Pour l'état à 2.8 MeV on trouve également une forme $L = 0$ dans la distribution expérimentale. Étant donné qu'il est attendu de peupler l'état 2^+ à 3.045 MeV dans cette région en énergie, deux calculs théoriques ont été effectués, l'un pour un état 2^+ ($L = 2$ en bleu), l'autre pour un état 0^+ ($L = 0$ en vert). On voit que la distribution expérimentale est très bien reproduite par le calcul $L = 0$ ce qui est une preuve forte de la présence d'un état excité 0^+_2 à 2.78 MeV. La raison de la non-observation de l'état 2^+ dans la voie de réaction ^{38}Ca(p,t)^{36}Ca reste une question ouverte jusqu'à présent.

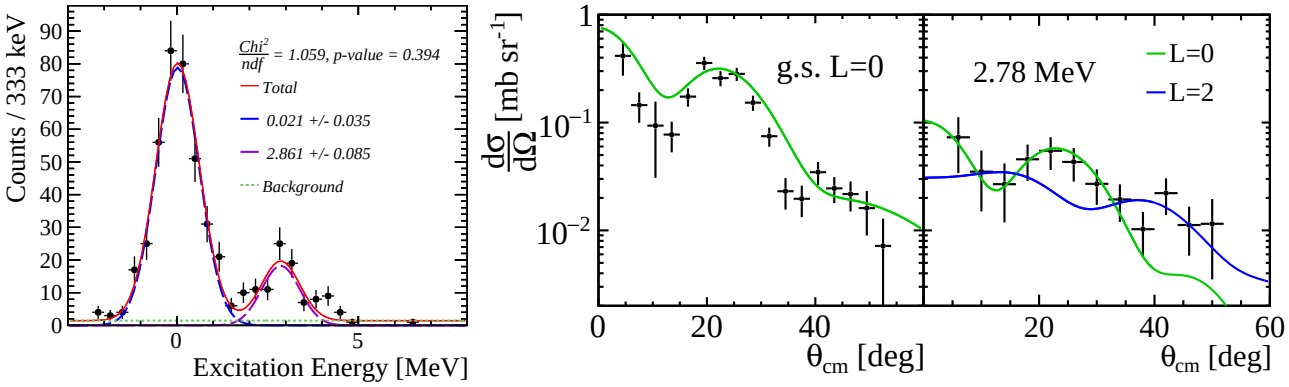

Figure C.6: Gauche: Spectre d'énergie d'excitation de ^{36}Ca obtenu avec la réaction ^{38}Ca(p,t)^{36}Ca en imposant l'observation d'un Ca en voie de sortie. La ligne rouge représente le meilleur ajustement obtenu. Droite : Sections efficaces différentielles des deux états identifiés dans ^{36}Ca avec la réaction ^{38}Ca(p,t)^{36}Ca . Les lignes bleues (vertes) montrent les calculs théoriques DWBA effectués pour une distribution $L = 2$ ($L = 0$).

1.4 Interprétation

L'analyse des voies de réactions ^{37}Ca(p,d)^{36}Ca et ^{38}Ca(p,t)^{36}Ca a permis d'identifier de nouveaux états excités dans le noyau de ^{36}Ca. En comparant ces nouveaux états aux états analogues connus dans le noyau miroir ^{36}S, il est possible d'étudier la brisure de symétrie miroir dans ce système. La Figure C.1 présente le schéma de niveau partiel de ^{36}Ca comparé à celui de son noyau miroir ^{36}Ca. Seuls les états 0^+_2, 2^+_1, 1^+ et 2^+_2 y sont montrés. Des calculs théoriques modèle en couches ont également été

réalisés afin de les comparer aux résultats expérimentaux. Les résultats de ces calculs sont également présentés dans la Figure C.1.

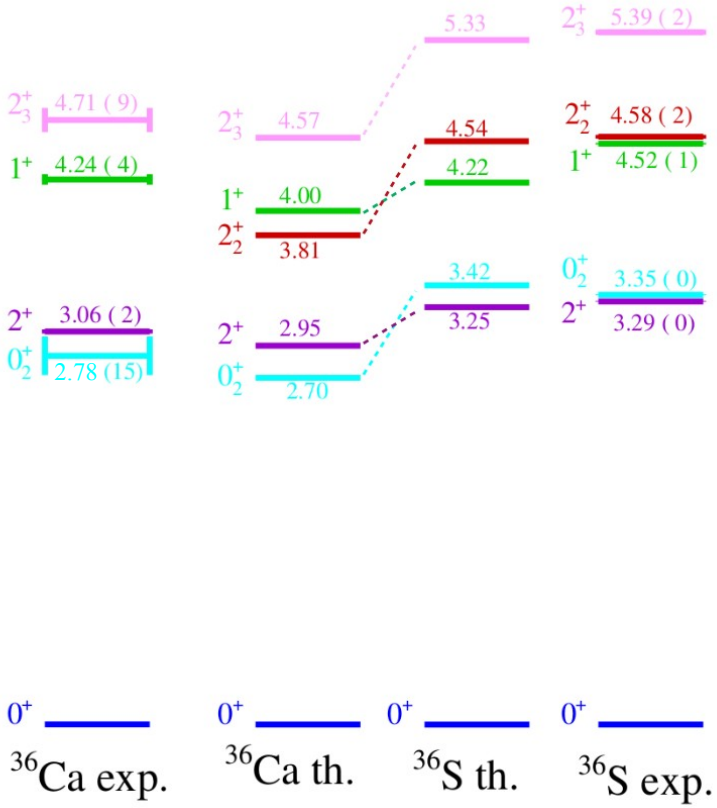

J^π	MED	
	Exp.	Th.
0^+_2	-570(180)	-720
2^+_1	-240(16)	-300
1^+_1	-280(40)	-220
2^+_2		-730
2^+_3	-680(90)	-760

Table C.1: Gauche : Schéma de niveaux partiels de la paire miroir ^{36}S-^{36}Ca. Seuls les niveaux de ^{36}S pertinents pour la discussion sont représentés, ainsi que les niveaux correspondants identifiés dans ^{36}Ca . Les résultats expérimentaux sont comparés au calcul modèle en couches effectué. Afin de faciliter la comparaison avec les résultats théoriques, l'état 2^+ à 4,71 MeV dans ^{36}Ca est étiqueté 2^+_3 dans cette figure, contrairement aux parties précédentes, dans lesquelles il était étiqueté 2^+_2. A droite : Différences d'énergie miroir expérimentales et théoriques obtenues pour ces états.

Dans la partie droite de la Figure C.1 sont données les différences d'énergie miroir (MED) expérimentales et théoriques pour les états discutés ici. On trouve expérimentalement de grandes MED d'environ 250 keV pour l'état 2^+_1 et 1^+_1. L'origine de cette différence réside dans la structure de ces états. En effet, ces 2 états partagent la même configuration avec les protons qui remplissent toutes les couches jusqu'à la $1d_{3/2}$ et une configuration neutron particule-trou avec un neutron dans l'orbite $2s_{1/2}$ et un autre sur l'orbite $1d_{3/2}$. La configuration de ces états dans le miroir ^{36}S étant obtenue en échangeant le nombre de protons et de neutrons. De plus ces états ont une configuration pure, comme le montrent les valeurs des facteurs spectroscopiques proches de la vision particule indépendante. Ceci est confirmé par les calculs théoriques qui reproduisent convenablement l'énergie de ces états. Les MED de ces états s'expliquent alors seulement en considérant les effets de la force Coulombienne. En effet, dans ^{36}S, le proton dans l'orbite $1s_{1/2}$ ressent moins de répulsion Coulombienne que celui dans l'orbite $2d_{3/2}$ (par interaction avec le cœur de proton) car le rayon moyen de l'orbite $1s_{1/2}$ est plus grand que celui de l'orbite $2d_{3/2}$. Ceci a pour effet d'augmenter de façon effective le gap en

énergie entre les deux orbites, comparé au gap entre les orbitales neutrons, sur lesquelles l'interaction Coulombienne n'a aucun effet. On trouve donc une énergie plus grande pour le 2_1^+ et le 1^+ dans le ^{36}S (excitation proton) que dans le ^{36}Ca (excitation neutron).

Dans le cas de l'état excité 0_2^+ la MED observée est encore plus grande avec une valeur de -570 keV, aussi bien reproduite par la théorie. Une fois encore, cette MED peut s'expliquer par les seuls effets Coulombiens. L'état 0_2^+ a une configuration dite intruse. Dans le cas du ^{36}Ca les protons ne sont pas dans leurs configurations fondamentales. Une paire de protons est excitée, passant de l'orbite $1d_{3/2}$ à la première orbite de la couche suivante : l'orbite $1f_{7/2}$. Le rayon moyen de cette dernière étant plus grand que celui de l'orbite $1d_{3/2}$, les protons excités ressentent moins de répulsion Coulombienne que ceux qui restent dans l'orbite $1d_{3/2}$ ce qui a pour effet de réduire effectivement l'écart en énergie entre ces deux orbites, comparé à celui des orbitales neutrons. À cet effet de configuration intruse s'ajoute un second effet de mélange de configurations. En effet, la configuration intruse décrite précédemment a pour effet de déformer le noyau et d'augmenter le mélange entre les orbitales s et d. De ce fait, il est énergétiquement favorable pour les deux neutrons de l'orbite $2s_{1/2}$ (configuration de l'état fondamental de ^{36}Ca) de se répartir entre l'orbite $2s_{1/2}$ et l'orbite $1d_{3/2}$, donnant une configuration similaire à celle discutée. Dans le cas de l'état 2_1^+ et 1^+. L'effet Coulombien dû à la configuration intruse et à la configuration particule-trou s'ajoute et donne une très grande différence d'énergie miroir. La différence d'énergie miroir pour l'état 0_2^+ est si grande qu'il en vient à passer en dessous du 2_1^+ dans ^{36}Ca, devenant le premier état excité de ce noyau. Une telle brisure de symétrie miroir est un exemple rare dans la carte des noyaux et son explication n'invoquant que des effets Coulombiens rendent ce cas de physique particulièrement remarquable.

2 Astrophysique Nucléaire

2.1 Introduction

La première étape de ce résumé était concentré sur la partie structure nucléaire de l'étude mais nous avions également une autre motivation pour analyser ce noyau de ^{36}Ca et cet intérêt est lié à l'astrophysique nucléaire. En effet, l'étude de noyaux exotiques tels que ^{36}Ca est très intéressante pour l'astrophysique car ces noyaux interviennent lors de processus de nucléosynthèses explosives, donnant lieux à la création de nouveaux éléments. Ces processus ont lieux dans les novæ classiques, les novæ à effondrement de cœur, les fusions d'étoiles à neutrons ou les sursauts de rayons X, ces derniers étant le site astrophysique d'intérêt pour cette étude.

Les sursauts de rayons X correspondent à une augmentation rapide et périodique de la luminosité dans le domaine des rayons X. Ce phénomène a lieu dans un système binaire composé d'une étoile à neutron et d'une étoile de type solaire. Au fil du temps, l'étoile de type solaire évolue et grossit et après avoir dépassé une certaine taille, elle commence à transférer de la matière à son étoile compagnon, plus dense. Se forme alors un disque d'accrétion autour de l'étoile à neutrons, dont une vue d'artiste est présentée dans la Figure C.7. Dans ce disque d'accrétion la température et la densité de matière peuvent atteindre des valeurs extrêmes. Une fois que suffisamment de matière a été accrété et lorsque les conditions de température et de densité sont réunies, une chaîne de réactions nucléaires se déclenche,

libérant une énorme quantité d'énergie. La surface de l'étoile à neutrons s'enflamme alors, menant à une forte augmentation de l'émission de rayons X durant entre 1 et 100 s. Une fois que tout le carburant a été consommé, la flamme s'éteint. La matière continue d'être accrétée jusqu'à ce que les conditions de l'explosion soient à nouveau réunies et que le cycle recommence.

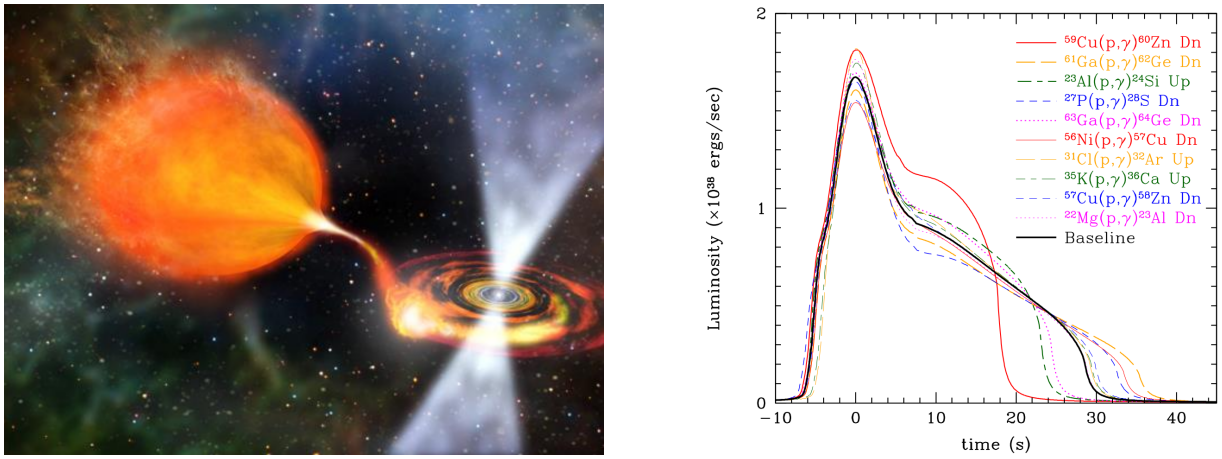

Figure C.7: Gauche: Vue d'artiste d'un système binaire formé par une étoile à neutrons et une étoile de type solaire. Droite: Impact de la variation du taux de réactions sur la courbe de lumière, pour les 10 réactions (p,γ) les plus sensibles. Figure adaptée de Ref. [105]

La chaîne des réactions nucléaires ayant lieu lors d'un sursaut X, elle implique des centaines de réactions et de noyaux différents. Ce processus est connu sous le nom de processus *rp* et consiste en une chaîne de réactions de capture de protons et de désintégrations β. Certaines de ces réactions peuvent avoir une grande influence sur les résultats des sursauts X que sont, sa courbe de lumière et les abondances isotopiques des noyaux produits pendant ce processus. Afin d'identifier les réactions ayant le plus grand impact sur ces éléments, les physiciens réalisent des études de sensibilité. Ces études consistent à faire varier les taux de réactions (*i.e.* la probabilité que la réaction se produise) un à un, de calculer la courbe de lumière ou les abondances isotopiques correspondantes et d'identifier quelles variations ont le plus fort impact sur l'observable d'intérêt. La Figure C.7 présente l'une de ces études réalisées par R.H. Cyburt *et.al* [105]. Dans cette étude, la réaction ^{35}K$(p,\gamma)^{36}$Ca a été identifiée comme l'une des 10 réactions (p,γ) pour lesquelles les incertitudes sur notre connaissance de son taux de réactions implique le plus d'incertitudes sur le calcul de la courbe de lumière des sursauts X. Il est donc important de contraindre précisément le taux de réactions de la réaction ^{35}K$(p,\gamma)^{36}$Ca afin que les modèles théoriques qui décrivent la courbe de lumière des sursauts gagnent en pouvoir prédictif. Ces modèles sont également cruciaux pour les études d'astrophysique car ils permettent de contraindre les paramètres de l'étoile à neutrons (tels que sa masse, son rayon ou sa vitesse de rotation) à partir de l'observation d'un sursaut X.

Les calculs du taux de réactions nécessitent de connaître la masse des noyaux impliqués, ainsi que les énergies, spin-parités et largeurs de décroissances partielles des états du noyau de la voie de sortie, présents dans la fenêtre de Gamow. La fenêtre de Gamow étant la plage en énergie dans laquelle la capture a le plus de probabilité de se produire. Dans la gamme de température d'intérêt pour les sursauts de rayons X (0.5-2 GK), la fenêtre de Gamow s'étend d'environ 3 MeV à environ 4.5 MeV,

en énergie d'excitation dans le noyau de ^{36}Ca. Avant cette étude, un seul état excité était connu dans ^{36}Ca, son premier 2^+ à 3.045 MeV [36]. L'objectif de cette étude est donc de réévaluer le taux de réactions de la réaction ^{35}K(p,γ)^{36}Ca , basé sur les résultats obtenus lors de notre expérience.

2.2 Résultats

Dans la partie précédente nous avons identifié 5 nouveaux états excités dans le noyau de ^{36}Ca. Parmi eux, 2 reposent dans la fenêtre de Gamow: le 1^+ à 4.24 MeV et le 2^+_2 à 4.71 MeV. À ces deux niveaux s'ajoute le premier 2^+ à 3.05MeV. Dans la partie précédente nous avons déterminé l'énergie et les spin-parités de ces états. Il reste donc à déterminer les largeurs de décroissance partielle de ces états avant de pouvoir calculer le taux de réactions.

En faisant l'approximation que seules les voies de décroissance gamma et un proton sont ouvertes, la largeur totale d'un état peut s'écrire : $\Gamma = \Gamma_p + \Gamma_\gamma$ où Γ est la largeur totale, Γ_p la largeur proton et Γ_γ la largeur gamma. La mesure du rapport de branchement de la voie de décroissance permet alors de contraindre les largeurs partielles, étant donné que le rapport de branchement peut s'écrire : $B_p = 1/(1+\Gamma_\gamma/\Gamma_p)$. Le rapport Γ_γ/Γ_p a été mesuré directement dans notre expérience. En effet, pour un état peuplé un nombre donné de fois, ce rapport correspond au nombre de décroissances γ sur le nombre de décroissances protons de cet état. Ce rapport a donc été calculé pour les 3 états d'intérêts en calculant le rapport du nombre d'événements vus en utilisant une condition Ca en sortie (voie γ) et K en sortie (voie proton). Les rapports de branchements ont également été mesurés avec une seconde méthode dite de corrélation angulaire et elle a fourni des résultats équivalents.

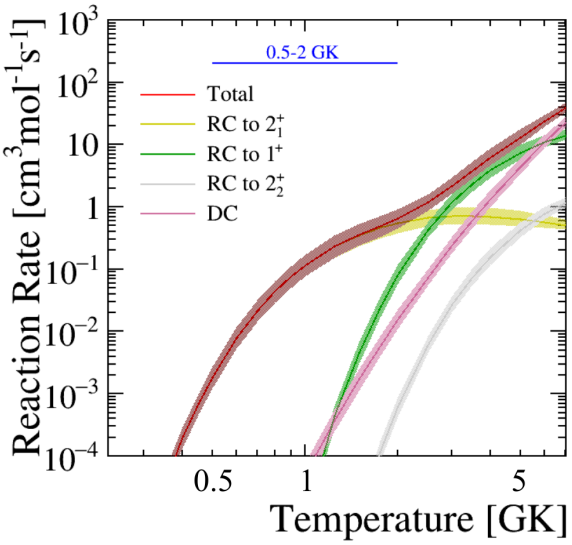

Figure C.8: Le taux de réaction de ^{35}K(p,γ)^{36}Ca calculé (en unités de cm^3 mol^{-1} s^{-1}) dans ce travail. La courbe rouge représente le taux de réaction total, qui inclut les contributions des captures résonantes (RC) et directes (DC). L'épaisseur des courbes représente une probabilité de couverture de 68%. La plage indiquée de 0,5 - 2 GK est typique des températures des sursauts de rayons X.

La mesure de rapport de branchement permet de contraindre expérimentalement les valeurs de largeurs partielles mais une information est toujours manquante pour calculer le taux de réaction. Nous avons donc choisi d'utiliser les résultats théoriques des calculs modèle en couches pour fixer la

valeur de largeur gamma Γ_γ. Combinés avec les résultats expérimentaux, tous les ingrédients sont réunis pour calculer le taux de réaction. Le résultat du calcul est présenté en Figure C.8. On peut voir dans cette figure que le taux de réaction est dominé par la capture résonnante sur le premier 2^+ du ^{36}Ca (en jaune). Les nouveaux états découverts dans ce travail commencent à contribuer au taux de réaction à partir de 2 GK. Les incertitudes associées au taux de réaction ont été calculées en considérant les incertitudes expérimentales pour tous les paramètres sauf pour la largeur γ pour laquelle un facteur 2 d'incertitude a été considéré. Dans la gamme de température typique des sursauts X (0.5-2GK) le calcul réalisé dans ce travail représente la meilleure contrainte sur le taux de réaction de ^{35}K(p,γ)^{36}Ca . Ce taux est maintenant bien déterminé pour l'utiliser dans des modèles de sursauts X.

3 Conclusion

Lors de cette étude, le noyau exotique ^{36}Ca a été étudié au GANIL en utilisant les réactions de transfert d'un neutron et de deux neutrons ^{37}Ca(p,d)^{36}Ca et ^{38}Ca(p,t)^{36}Ca. De nouveaux états ont été identifiés pour la première fois et ont été utilisés pour étudier les effets de brisure de symétrie miroir. De grandes différences d'énergie miroir ont été trouvées en comparant l'énergie des niveaux dans ^{36}Ca à celles des niveaux analogues dans le noyau miroir ^{36}S. Ces grandes différences ont été expliquées à l'aide de calculs modèle en couches, en considérant seulement les effets de l'interaction Coulombienne ainsi que la structure des états. Les résultats obtenus ont également été utilisés pour réévaluer le taux de la réaction ^{35}K(p,γ)^{36}Ca . Cette réaction étant identifiée comme l'une des 10 réactions (p,γ) dont les incertitudes ont le plus d'impacts sur la courbe de lumière des sursauts X. Le taux calculé dans ce travail représente l'estimation la plus robuste disponible dans la littérature et il pourra être utilisé dans des modèle théoriques de sursauts X. Comme indiqué en préambule, ceci est un résumé de mon manuscrit de thèse. Afin de ne pas le surcharger, de nombreux points ont été éludés, comme la procédure complexe de calibration, les nouvelles mesures de masses ou bien la première spectroscopie du noyau ^{35}Ca. L'intégralité du manuscrit est disponible en anglais pour les lecteurs qui souhaitent prendre connaissance de l'ensemble de mon travail.

Bibliography

[1] URL https://people.physics.anu.edu.au/~ecs103/chart/.

[2] Michael Thoennessen. Discovery of nuclides project. URL https://people.nscl.msu.edu/~thoennes/isotopes/.

[3] Hideki Yukawa. On the Interaction of Elementary Particles. I. Progress of Theoretical Physics Supplement, 1:1–10, 01 1955. ISSN 0375-9687. doi: 10.1143/PTPS.1.1. URL https://doi.org/10.1143/PTPS.1.1.

[4] N. Ishii, S. Aoki, and T. Hatsuda. Nuclear force from lattice qcd. Phys. Rev. Lett., 99:022001, Jul 2007. doi: 10.1103/PhysRevLett.99.022001. URL https://link.aps.org/doi/10.1103/PhysRevLett.99.022001.

[5] Takaharu Otsuka, Alexandra Gade, Olivier Sorlin, Toshio Suzuki, and Yutaka Utsuno. Evolution of shell structure in exotic nuclei. Rev. Mod. Phys., 92:015002, Mar 2020. doi: 10.1103/RevModPhys.92.015002. URL https://link.aps.org/doi/10.1103/RevModPhys.92.015002.

[6] K. Heyde. Basic Ideas and Concepts in Nuclear Physics An Introductory Approach, Third Edition. Fundamental and applied nuclear physics series. CRC Press, 2020. ISBN 9781420054941.

[7] A. Messiah. Mécanique quantique. Number vol. 1 in 2e cycle universitaire. Dunod, 1995. ISBN 9782100024261. URL https://books.google.fr/books?id=k_bcAQAACAAJ.

[8] Takaharu Otsuka, Toshio Suzuki, Michio Honma, Yutaka Utsuno, Naofumi Tsunoda, Koshiroh Tsukiyama, and Morten Hjorth-Jensen. Novel features of nuclear forces and shell evolution in exotic nuclei. Phys. Rev. Lett., 104:012501, Jan 2010. doi: 10.1103/PhysRevLett.104.012501. URL https://link.aps.org/doi/10.1103/PhysRevLett.104.012501.

[9] Steven C. Pieper. Quantum monte carlo calculations of light nuclei. Nuclear Physics A, 751:516–532, 2005. ISSN 0375-9474. doi: https://doi.org/10.1016/j.nuclphysa.2005.02.018. URL https://www.sciencedirect.com/science/article/pii/S0375947405001247. Proceedings of the 22nd International Nuclear Physics Conference (Part 1).

[10] N. Smirnova. Shell structure evolution and effective in-medium nn interaction. In Ecole Internationale Joliot Curie"Interaction forte dans la matiere nucleaire : nouvelles tendances", Lacanau, France, September 2009. URL http://hal.in2p3.fr/in2p3-00438311.

[11] R. Casten. Nuclear structure from a simple perspective. Oxford studies in nuclear physics. Oxford University Press, New York, 1990. ISBN 978-0-19-504599-4.

[12] Maria Goeppert Mayer. On closed shells in nuclei. ii. Phys. Rev., 75:1969–1970, Jun 1949. doi: 10.1103/PhysRev.75.1969. URL https://link.aps.org/doi/10.1103/PhysRev.75.1969.

[13] Otto Haxel, J. Hans D. Jensen, and Hans E. Suess. On the "magic numbers" in nuclear structure. Phys. Rev., 75:1766–1766, Jun 1949. doi: 10.1103/PhysRev.75.1766.2. URL https://link.aps.org/doi/10.1103/PhysRev.75.1766.2.

[14] Aage Niels Bohr and Ben R Mottelson. Nuclear Structure (In 2 Volumes). World Scientific Publishing Company, 1998.

[15] E. Caurier, G. Martínez-Pinedo, F. Nowacki, A. Poves, and A. P. Zuker. The shell model as a unified view of nuclear structure. Rev. Mod. Phys., 77:427–488, Jun 2005. doi: 10.1103/RevModPhys.77.427. URL https://link.aps.org/doi/10.1103/RevModPhys.77.427.

[16] N.A. Smirnova, B. Bally, K. Heyde, F. Nowacki, and K. Sieja. Shell evolution and nuclear forces. Physics Letters B, 686(2):109–113, 2010. ISSN 0370-2693. doi: https://doi.org/10.1016/j.physletb.2010.02.051. URL https://www.sciencedirect.com/science/article/pii/S0370269310002388.

[17] Takaharu Otsuka, Toshio Suzuki, Rintaro Fujimoto, Hubert Grawe, and Yoshinori Akaishi. Evolution of nuclear shells due to the tensor force. Phys. Rev. Lett., 95:232502, Nov 2005. doi: 10.1103/PhysRevLett.95.232502. URL https://link.aps.org/doi/10.1103/PhysRevLett.95.232502.

[18] Takaharu Otsuka, Rintaro Fujimoto, Yutaka Utsuno, B. Alex Brown, Michio Honma, and Takahiro Mizusaki. Magic numbers in exotic nuclei and spin-isospin properties of the *NN* interaction. Phys. Rev. Lett., 87:082502, Aug 2001. doi: 10.1103/PhysRevLett.87.082502. URL https://link.aps.org/doi/10.1103/PhysRevLett.87.082502.

[19] B. Bastin, S. Grévy, D. Sohler, O. Sorlin, Zs. Dombrádi, N. L. Achouri, J. C. Angélique, F. Azaiez, D. Baiborodin, R. Borcea, C. Bourgeois, A. Buta, A. Bürger, R. Chapman, J. C. Dalouzy, Z. Dlouhy, A. Drouard, Z. Elekes, S. Franchoo, S. Iacob, B. Laurent, M. Lazar, X. Liang, E. Liénard, J. Mrazek, L. Nalpas, F. Negoita, N. A. Orr, Y. Penionzhkevich, Zs. Podolyák, F. Pougheon, P. Roussel-Chomaz, M. G. Saint-Laurent, M. Stanoiu, I. Stefan, F. Nowacki, and A. Poves. Collapse of the $n = 28$ shell closure in ^{42}Si. Phys. Rev. Lett., 99:022503, Jul 2007. doi: 10.1103/PhysRevLett.99.022503. URL https://link.aps.org/doi/10.1103/PhysRevLett.99.022503.

[20] E. K. Warburton, J. A. Becker, and B. A. Brown. Mass systematics for a=29–44 nuclei: The deformed a∼32 region. Phys. Rev. C, 41:1147–1166, Mar 1990. doi: 10.1103/PhysRevC.41.1147. URL https://link.aps.org/doi/10.1103/PhysRevC.41.1147.

[21] O. Sorlin. Shell Evolutions and Nuclear Forces. EPJ Web Conf., 66:01016, 2014. doi: 10.1051/epjconf/20146601016.

[22] K Heyde and J L Wood. Intruder states and shape coexistence in the region n = 20, z = 12. Journal of Physics G: Nuclear and Particle Physics, 17(2):135–143, feb 1991. doi: 10.1088/0954-3899/17/2/007. URL https://doi.org/10.1088/0954-3899/17/2/007.

[23] W. Heisenberg. Über den bau der atomkerne. i. Zeitschrift für Physik, 77:1–11, 21932. doi: 10.1007/BF01342433. URL https://doi.org/10.1007/BF01342433.

[24] J. Chadwick. Possible Existence of a Neutron. Nature, 129:312, 1932. doi: 10.1038/129312a0.

[25] M.A.Bentley S.M.Lenzi. Isospin symmetry breaking in mirror nuclei, 2010.

[26] A. P. Zuker, S. M. Lenzi, G. Martínez-Pinedo, and A. Poves. Isobaric multiplet yrast energies and isospin nonconserving forces. Phys. Rev. Lett., 89:142502, Sep 2002. doi: 10.1103/PhysRevLett.89.142502. URL https://link.aps.org/doi/10.1103/PhysRevLett.89.142502.

[27] Silvia M Lenzi. Coulomb energy differences in mirror nuclei. Journal of Physics: Conference Series, 49:85–90, oct 2006. doi: 10.1088/1742-6596/49/1/019. URL https://doi.org/10.1088/1742-6596/49/1/019.

[28] M. A. Bentley, C. Chandler, M. J. Taylor, J. R. Brown, M. P. Carpenter, C. Davids, J. Ekman, S. J. Freeman, P. E. Garrett, G. Hammond, R. V. F. Janssens, S. M. Lenzi, C. J. Lister, R. du Rietz, and D. Seweryniak. Isospin symmetry of odd-odd mirror nuclei: Identification of excited states in $n = z - 2$ ^{48}Mn. Phys. Rev. Lett., 97:132501, Sep 2006. doi: 10.1103/PhysRevLett.97.132501. URL https://link.aps.org/doi/10.1103/PhysRevLett.97.132501.

[29] B.H. Wildenthal and E. Newman. 39k(d, 3he)38ar and the s-d shell structure of 38ar. Nuclear Physics A, 118(2):347–360, 1968. ISSN 0375-9474. doi: https://doi.org/10.1016/0375-9474(68)90341-2. URL https://www.sciencedirect.com/science/article/pii/0375947468903412.

[30] R. E. Tribble, J. D. Cossairt, and R. A. Kenefick. Mass of Ca 36. Physical Review C, 15 (6):2028–2031, June 1977. ISSN 0556-2813. doi: 10.1103/PhysRevC.15.2028. URL https://link.aps.org/doi/10.1103/PhysRevC.15.2028.

[31] J. Surbrook, G. Bollen, M. Brodeur, A. Hamaker, D. Pérez-Loureiro, D. Puentes, C. Nicoloff, M. Redshaw, R. Ringle, S. Schwarz, C. S. Sumithrarachchi, L. J. Sun, A. A. Valverde, A. C. C. Villari, C. Wrede, and I. T. Yandow. First penning trap mass measurement of ^{36}Ca. Phys. Rev. C, 103:014323, Jan 2021. doi: 10.1103/PhysRevC.103.014323. URL https://link.aps.org/doi/10.1103/PhysRevC.103.014323.

[32] J. Äystö, M. D. Cable, R. F. Parry, J. M. Wouters, D. M. Moltz, and Joseph Cerny. Decays of the $T_z = -2$ nuclei ^{20}Mg, ^{24}Si, and ^{36}Ca. Phys. Rev. C, 23:879–887, Feb 1981. doi: 10.1103/PhysRevC.23.879. URL https://link.aps.org/doi/10.1103/PhysRevC.23.879.

[33] Study of the β decays of ^{37}ca and ^{36}ca. Nuclear Physics A, 620(2):191 – 213, 1997. ISSN 0375-9474. doi: https://doi.org/10.1016/S0375-9474(97)00163-2. URL http://www.sciencedirect.com/science/article/pii/S0375947497001632.

[34] Doornenbal *et al*. The T=2 mirrors 36Ca and 36S: A test for isospin symmetry of shell gaps at the driplines. Physics Letters B, 647(4):237–242, April 2007. ISSN 03702693. doi: 10.1016/j.physletb.2007.02.001. URL https://linkinghub.elsevier.com/retrieve/pii/S0370269307001499.

[35] A. *et al*. Bürger. Cross sections for one-neutron knock-out from ^{37}ca at intermediate energy. Phys. Rev. C, 86:064609, Dec 2012. doi: 10.1103/PhysRevC.86.064609. URL https://link.aps.org/doi/10.1103/PhysRevC.86.064609.

[36] A.M.Amthor. Experimental and theoretical study of nuclear reaction rates in the rp-proces. PhD thesis, Michigan State University, 2009.

[37] J. J. Valiente-Dobón, A. Poves, A. Gadea, and B. Fernández-Domínguez. Broken mirror symmetry in ^{36}S and ^{36}Ca. Phys. Rev. C, 98:011302, Jul 2018. doi: 10.1103/PhysRevC.98.011302. URL https://link.aps.org/doi/10.1103/PhysRevC.98.011302.

[38] Blank, B., Thomas, J. -C., Ascher, P., Audirac, L., Bacquias, A., Cáceres, L., Canchel, G., Daudin, L., de Oliveira Santos, F., Didierjean, F., Gerbaux, M., Giovinazzo, J., Grévy, S., Kurtukian Nieto, T., Matea, I., Munoz, F., Roche, M., Serani, L., Smirnova, N., and Souin, J. Half-life and branching ratios for the ay of 38ca. Eur. Phys. J. A, 51(1):8, 2015. doi: 10.1140/epja/i2015-15008-1. URL https://doi.org/10.1140/epja/i2015-15008-1.

[39] M Lindroos. Review of ISOL-type Radioactive Beam Facilities. page 5, 2004.

[40] Y Blumenfeld, T Nilsson, and P Van Duppen. Facilities and methods for radioactive ion beam production. Physica Scripta, T152:014023, January 2013. ISSN 0031-8949, 1402-4896. doi: 10.1088/0031-8949/2013/T152/014023. URL https://iopscience.iop.org/article/10.1088/0031-8949/2013/T152/014023.

[41] Clement Delafosse. Etude des dérives monopolaires neutron au-delà du ^{78}Ni par spectroscopie gamma avec BEDO à ALTO et AGATA au GANIL. Theses, Université Paris-Saclay, July 2018. URL https://tel.archives-ouvertes.fr/tel-01848718.

[42] R. Anne, D. Bazin, A.C. Mueller, J.C. Jacmart, and M. Langevin. The achromatic spectrometer lise at ganil. Nuclear Instruments and Methods in Physics Research Section A: Accelerators, Spectrometers, Detectors and Associated Equipment, 257(2):215 – 232, 1987. ISSN 0168-9002. doi: https://doi.org/10.1016/0168-9002(87)90741-8. URL http://www.sciencedirect.com/science/article/pii/0168900287907418.

[43] Y. Jacob. GANIL, Matière à Histoire. Technical report, 2001. URL http://hal.in2p3.fr/in2p3-01002049.

[44] Thomas Baumann. Minicourse on experimental techniques at the nscl: Fragment separators, August 2001.

[45] S. Ottini-Hustache, C. Mazur, F. Auger, A. Musumarra, N. Alamanos, B. Cahan, A. Gillibert, A. Lagoyannis, O. Maillard, E. Pollacco, J.L. Sida, and M. Riallot. Cats, a low pressure multiwire proportionnal chamber for secondary beam tracking at ganil. Nuclear Instruments and Methods in Physics Research Section A: Accelerators, Spectrometers, Detectors and Associated Equipment, 431(3):476 – 484, 1999. ISSN 0168-9002. doi: https://doi.org/10.1016/S0168-9002(99)00380-0. URL http://www.sciencedirect.com/science/article/pii/S0168900299003800.

[46] S. Koyama, D. Suzuki, M. Assié, N. Kitamura, L. Lalanne, M. Niikura, H. Otsu, T. K. Saito, and O. Sorlin. Liquid hydrogen target for radioactive beam experiments with missing mass method. to be submitted to NIM A, 2020.

[47] E Pollacco, D Beaumel, P Roussel-Chomaz, E Atkin, P Baron, JP Baronick, E Becheva, Y Blumenfeld, A Boujrad, A Drouart, et al. Must2: A new generation array for direct reaction studies. In The 4th International Conference on Exotic Nuclei and Atomic Masses, pages 287–288. Springer, 2005.

[48] A Matta, P Morfouace, N de Séréville, F Flavigny, M Labiche, and R Shearman. NPTool: a simulation and analysis framework for low-energy nuclear physics experiments. Journal of Physics G: Nuclear and Particle Physics, 43(4):045113, mar 2016. doi: 10.1088/0954-3899/43/4/045113. URL https://doi.org/10.1088%2F0954-3899%2F43%2F4%2F045113.

[49] Freddy Flavigny. Détermination de facteurs spectroscopiques absolus par réactions de knockout et de transfert. page 157.

[50] Benjamin Le Crom. Étude de l'appariement neutron-proton dans les noyaux instables N=Z par réactions de transfert. page 159.

[51] Adrien Matta. Etude du noyau très riche en neutrons 10He par réaction de transfert d'un proton 11Li(d,3He). page 140.

[52] D. Suzuki. Missing mass spectroscopy on oxygen isotopes beyond the proton-drip line: mirror symmetry of nuclear shell evolution. The European Physical Journal A, 48(9):130, September 2012. ISSN 1434-6001, 1434-601X. doi: 10.1140/epja/i2012-12130-6. URL http://link.springer.com/10.1140/epja/i2012-12130-6.

[53] Meng Wang, G. Audi, F. G. Kondev, W.J. Huang, S. Naimi, and Xing Xu. The AME2016 atomic mass evaluation (II). Tables, graphs and references. Chinese Physics C, 41(3):030003, March 2017. ISSN 1674-1137. doi: 10.1088/1674-1137/41/3/030003. URL https://iopscience.iop.org/article/10.1088/1674-1137/41/3/030003.

[54] R Ringle, T Sun, G Bollen, D Davies, M Facina, J Huikari, E Kwan, DJ Morrissey, A Prinke, J Savory, et al. High-precision penning trap mass measurements of ca 37, 38 and their contributions to conserved vector current and isobaric mass multiplet equation. Physical Review C, 75(5):055503, 2007.

[55] F. Herfurth, J. Dilling, A. Kellerbauer, G. Audi, D. Beck, G. Bollen, H.-J. Kluge, D. Lunney, R. B. Moore, C. Scheidenberger, S. Schwarz, G. Sikler, J. Szerypo, and ISOLDE Collaboration. Breakdown of the isobaric multiplet mass equation at $A = 33$, $T = 3/2$. Phys. Rev. Lett., 87: 142501, Sep 2001. doi: 10.1103/PhysRevLett.87.142501. URL https://link.aps.org/doi/10.1103/PhysRevLett.87.142501.

[56] Fred James and Matthias Winkler. MINUIT User's Guide. 6 2004.

[57] W.S. Gray, P.J. Ellis, T. Wei, R.M. Polichar, and J. Jänecke. Study of the structure of 36s and 38ar. Nuclear Physics A, 140(3):494 – 522, 1970. ISSN 0375-9474. doi: https://doi.org/10.1016/0375-9474(70)90576-2. URL http://www.sciencedirect.com/science/article/pii/0375947470905762.

[58] J. J. H. Menet, E. E. Gross, J. J. Malanify, and A. Zucker. Total-reaction-cross-section measurements for 30-60-mev protons and the imaginary optical potential. Phys. Rev. C, 4:1114–1129, Oct 1971. doi: 10.1103/PhysRevC.4.1114. URL https://link.aps.org/doi/10.1103/PhysRevC.4.1114.

[59] R.C. Johnson and P.C. Tandy. An approximate three-body theory of deuteron stripping. Nuclear Physics A, 235(1):56–74, 1974. ISSN 0375-9474. doi: https://doi.org/10.1016/0375-9474(74)90178-X. URL https://www.sciencedirect.com/science/article/pii/037594747490178X.

[60] F. D. Becchetti and G. W. Greenlees. Nucleon-nucleus optical-model parameters. Phys. Rev., 182:1190–1209, Jun 1969. doi: 10.1103/PhysRev.182.1190. URL https://link.aps.org/doi/10.1103/PhysRev.182.1190.

[61] Roderick V Reid. Local phenomenological nucleon-nucleon potentials. Annals of Physics, 50 (3):411–448, 1968. ISSN 0003-4916. doi: https://doi.org/10.1016/0003-4916(68)90126-7. URL https://www.sciencedirect.com/science/article/pii/0003491668901267.

[62] J. A. Tostevin. J. a. tostevin, university of surrey version of the code twofnr (of m. toyama, m. igarashi and n. kishida) and code front (private communication). URL http://nucleartheory.eps.surrey.ac.uk/NPG/code.htm.

[63] Ian J Thompson. Coupled reaction channels calculations in nuclear physics. Computer Physics Reports, 7(4):167–212, 1988.

[64] W. Benenson, A. Guichard, E. Kashy, D. Mueller, and H. Nann. Mass of ^{35}K. Phys. Rev. C, 13:1479–1482, Apr 1976. doi: 10.1103/PhysRevC.13.1479. URL https://link.aps.org/doi/10.1103/PhysRevC.13.1479.

[65] Aldric Revel. Nuclear forces at the extremes. PhD thesis, Grand Accélérateur National d'Ions Lourds, France, 2018.

[66] RA Paddock. (p, t) reaction on even-even n= z nuclei in the 2 s 1 d shell. Physical Review C, 5(2):485, 1972.

[67] Xiaohua Li, Chuntian Liang, and Chonghai Cai. Global triton optical model potential. Nuclear Physics A, 789(1):103–113, 2007. ISSN 0375-9474. doi: https://doi.org/10.1016/j.nuclphysa.2007.03.004. URL https://www.sciencedirect.com/science/article/pii/S0375947407002291.

[68] B.A.Brown. Fr2in. URL https://people.nscl.msu.edu/brown/reaction-codes/.

[69] K. *et al*. Wimmer. Discovery of the shape coexisting 0^+ state in ^{32}Mg by a two neutron transfer reaction. Phys. Rev. Lett., 105:252501, Dec 2010. doi: 10.1103/PhysRevLett.105.252501. URL https://link.aps.org/doi/10.1103/PhysRevLett.105.252501.

[70] K.Wimmer. Discovery of the shape coexisting 0^+ state in ^{32}Mg. PhD thesis, Technische Universitat Munchen, Physik-Department E12, 2010.

[71] Richard Longland, Christian Iliadis, Art Champagne, Joe Newton, Claudio Ugalde, Alain Coc, and Ryan Fitzgerald. Charged-Particle Thermonuclear Reaction Rates: I. Monte Carlo Method and Statistical Distributions. Nuclear Physics A, 841(1-4):1–30, October 2010. ISSN 03759474. doi: 10.1016/j.nuclphysa.2010.04.008. URL http://arxiv.org/abs/1004.4136. arXiv: 1004.4136.

[72] J. Äystö, D. M. Moltz, X. J. Xu, J. E. Reiff, and Joseph Cerny. Observation of the first $T_z = -\frac{5}{2}$ nuclide, ^{35}Ca, via its β-delayed two-proton emission. Phys. Rev. Lett., 55:1384–1387, Sep 1985. doi: 10.1103/PhysRevLett.55.1384. URL https://link.aps.org/doi/10.1103/PhysRevLett.55.1384.

[73] N.A. Orr, W.N. Catford, L.K. Fifiekd, T.R. Ophel, D.C. Weisser, and C.L. Woods. Heavy-ion reaction studies of 35,36p. Nuclear Physics A, 477(3):523–540, 1988. ISSN 0375-9474. doi: https://doi.org/10.1016/0375-9474(88)90355-7. URL https://www.sciencedirect.com/science/article/pii/0375947488903557.

[74] Bengtsson R. Intruder States and Low Energy Nuclear Spectroscopy In: Vergnes M., Sauvage J., Heenen PH., Duong H.T. (eds) Nuclear Shapes and Nuclear Structure at Low Excitation Energies. Springer, Boston, MA, 1992. doi: https://doi.org/10.1007/978-1-4615-3342-9_10.

[75] A.Mutschler et al. A proton density bubble in the doubly magic 34si nucleus. Nature Physics, 12:152–156, Oct 2017. doi: 10.1038/nphys3916. URL https://doi.org/10.1038/nphys3916.

[76] W.P. Alford, P. Craig, D.A. Lind, R.S. Raymond, J. Ullman, C.D. Zafiratos, and B.H. Wildenthal. Structure of 22mg, 26si, 34ar and 38ca via the (3he, n) reaction. Nuclear Physics A, 457 (2):317–336, 1986. ISSN 0375-9474. doi: https://doi.org/10.1016/0375-9474(86)90381-7. URL https://www.sciencedirect.com/science/article/pii/0375947486903817.

[77] M.H. Shapiro, C. Moss, and W.M. Denny. A study of the 36ar(3he, n)38ca reaction. Nuclear Physics A, 128(1):73–80, 1969. ISSN 0375-9474. doi: https://doi.org/10.1016/0375-9474(69)90979-8. URL https://www.sciencedirect.com/science/article/pii/0375947469909798.

[78] W. Bohne, K.D. Büchs, H. Fuchs, K. Grabisch, D. Hilscher, U. Janetzki, U. Jahnke, H. Kluge, T.G. Masterson, and H. Morgenstern. The reactions 36, 38, 40ar(3he, n)38, 40, 42ca and 40, 42ca(3he, n)42, 44ti. Nuclear Physics A, 284(1):14–28, 1977. ISSN 0375-9474. doi: https://doi.org/10.1016/0375-9474(77)90682-0. URL https://www.sciencedirect.com/science/article/pii/0375947477906820.

[79] S. Kubono, S. Kato, M. Yasue, H. Ohnuma, and K. Ogawa. Anomalous l = 0 transition observed in the reaction 40ca(p,t)38ca. Physics Letters B, 49(1):37–39, 1974. ISSN 0370-2693. doi: https://doi.org/10.1016/0370-2693(74)90574-7. URL https://www.sciencedirect.com/science/article/pii/0370269374905747.

[80] R. Shane, R. J. Charity, L. G. Sobotka, D. Bazin, B. A. Brown, A. Gade, G. F. Grinyer, S. McDaniel, A. Ratkiewicz, D. Weisshaar, A. Bonaccorso, and J. A. Tostevin. Proton and neutron knockout from ^{36}ca. Phys. Rev. C, 85:064612, Jun 2012. doi: 10.1103/PhysRevC.85.064612. URL https://link.aps.org/doi/10.1103/PhysRevC.85.064612.

[81] J. W. Olness, W. R. Harris, A. Gallmann, F. Jundt, D. E. Alburger, and D. H. Wilkinson. Levels of s^{36} from $s^{34}(t,p)s^{36}$. Phys. Rev. C, 3:2323–2344, Jun 1971. doi: 10.1103/PhysRevC.3.2323. URL https://link.aps.org/doi/10.1103/PhysRevC.3.2323.

[82] K Heyde and J L Wood. Intruder states and shape coexistence in the region n approximately 20, z approximately 12. Journal of Physics G: Nuclear and Particle Physics, 17(2):135–143, feb 1991. doi: 10.1088/0954-3899/17/2/007. URL https://doi.org/10.1088/0954-3899/17/2/007.

[83] D. Steppenbeck, S. Takeuchi, N. Aoi, P. Doornenbal, M. Matsushita, H. Wang, H. Baba, N. Fukuda, S. Go, M. Honma, J. Lee, K. Matsui, S. Michimasa, T. Motobayashi, D. Nishimura, T. Otsuka, H. Sakurai, Y. Shiga, P.-A. Söderström, T. Sumikama, H. Suzuki, R. Taniuchi, Y. Utsuno, J. J. Valiente-Dobón, and K. Yoneda. Evidence for a new nuclear 'magic number' from the level structure of 54Ca. Nature, 502(7470):207–210, October 2013. ISSN 0028-0836, 1476-4687. doi: 10.1038/nature12522. URL http://www.nature.com/articles/nature12522.

[84] F. Wienholtz et al. Masses of exotic calcium isotopes pin down nuclear forces. Nature, 498 (7454):346–349, 2013. doi: 10.1038/nature12226.

[85] S. Michimasa, M. Kobayashi, Y. Kiyokawa, S. Ota, D. S. Ahn, H. Baba, G. P. A. Berg, M. Dozono, N. Fukuda, T. Furuno, E. Ideguchi, N. Inabe, T. Kawabata, S. Kawase, K. Kisamori, K. Kobayashi, T. Kubo, Y. Kubota, C. S. Lee, M. Matsushita, H. Miya, A. Mizukami, H. Nagakura, D. Nishimura, H. Oikawa, H. Sakai, Y. Shimizu, A. Stolz, H. Suzuki, M. Takaki, H. Takeda, S. Takeuchi, H. Tokieda, T. Uesaka, K. Yako, Y. Yamaguchi, Y. Yanagisawa, R. Yokoyama, K. Yoshida, and S. Shimoura. Magic nature of neutrons in ^{54}Ca: First mass

measurements of $^{55--57}$Ca. Phys. Rev. Lett., 121:022506, Jul 2018. doi: 10.1103/PhysRevLett.121.022506. URL https://link.aps.org/doi/10.1103/PhysRevLett.121.022506.

[86] Z. *et al* Elekes. Spectroscopic study of neutron shell closures via nucleon transfer in the near-dripline nucleus ^{23}O. Phys. Rev. Lett., 98:102502, Mar 2007. doi: 10.1103/PhysRevLett.98.102502. URL https://link.aps.org/doi/10.1103/PhysRevLett.98.102502.

[87] D. SINGH and G. SAXENA. Study of two-proton radioactivity within the relativistic mean-field plus bcs approach. International Journal of Modern Physics E, 21(09):1250076, 2012. doi: 10.1142/S0218301312500760. URL https://doi.org/10.1142/S0218301312500760.

[88] A. Shukla and S. Åberg. Deformed bubble nuclei in the light-mass region. Phys. Rev. C, 89:014329, Jan 2014. doi: 10.1103/PhysRevC.89.014329. URL https://link.aps.org/doi/10.1103/PhysRevC.89.014329.

[89] H. Schatz and K.E. Rehm. X-ray binaries. Nuclear Physics A, 777:601 – 622, 2006. ISSN 0375-9474. doi: https://doi.org/10.1016/j.nuclphysa.2005.05.200. URL http://www.sciencedirect.com/science/article/pii/S0375947405008791. Special Issue on Nuclear Astrophysics.

[90] J. Grindlay, H. Gursky, Herbert Schnopper, D. Parsignault, John Heise, A. Brinkman, and J. Schrijver. Discovery of intense x-ray bursts from the globular cluster ngc 6624. Astrophys. J., 205, 06 1976. doi: 10.1086/182105.

[91] Frederick D. Seward and Philip A. Charles. Exploring the X-ray Universe. Cambridge University Press, 2 edition, 2010. doi: 10.1017/CBO9780511781513.

[92] F. Haberl, L. Stella, Nicholas White, Manfred Gottwald, and W. Priedhorsky. Exosat observations of double-peaked bursts with radius expansion from 4u/mxb 1820-30. The Astrophysical Journal, 314:266–271, 02 1987. doi: 10.1086/165056.

[93] Sudip Bhattacharyya, Tod E. Strohmayer, Craig B. Markwardt, and Jean H. Swank. The discovery of a neutron star with a spin frequency of 530 hz in a1744-361. The Astrophysical Journal, 639(1):L31–L34, feb 2006. doi: 10.1086/501438. URL https://doi.org/10.1086/501438.

[94] Duncan K. Galloway, Jean in 't Zand, Jérôme Chenevez, Hauke Wörpel, Laurens Keek, Laura Ootes, Anna L. Watts, Luis Gisler, Celia Sanchez-Fernandez, and Erik Kuulkers. The multi-INstrument burst ARchive (MINBAR). The Astrophysical Journal Supplement Series, 249(2):32, aug 2020. doi: 10.3847/1538-4365/ab9f2e. URL https://doi.org/10.3847/1538-4365/ab9f2e.

[95] Keith Jahoda, Jean H. Swank, Alan B. Giles, Michael J. Stark, Tod Strohmayer, William W. Zhang, and Edward H. Morgan. In-orbit performance and calibration of the Rossi X-ray Timing Explorer (RXTE) Proportional Counter Array (PCA). In Oswald H. W. Siegmund and Mark A. Gummin, editors, EUV, X-Ray, and Gamma-Ray Instrumentation for Astronomy VII, volume

2808, pages 59 – 70. International Society for Optics and Photonics, SPIE, 1996. doi: 10.1117/12.256034. URL https://doi.org/10.1117/12.256034.

[96] Nättilä, J., Miller, M. C., Steiner, A. W., Kajava, J. J. E., Suleimanov, V. F., and Poutanen, J. Neutron star mass and radius measurements from atmospheric model fits to x-ray burst cooling tail spectra. A&A, 608:A31, 2017. doi: 10.1051/0004-6361/201731082. URL https://doi.org/10.1051/0004-6361/201731082.

[97] Sudip Bhattacharyya and Tod E. Strohmayer. Thermonuclear flame spreading on rapidly spinning neutron stars: Indications of the coriolis force? The Astrophysical Journal, 666(2):L85–L88, aug 2007. doi: 10.1086/521790. URL https://doi.org/10.1086/521790.

[98] Andrew W. Steiner. Deep crustal heating in a multicomponent accreted neutron star crust. Phys. Rev. C, 85:055804, May 2012. doi: 10.1103/PhysRevC.85.055804. URL https://link.aps.org/doi/10.1103/PhysRevC.85.055804.

[99] Edward F. Brown and Andrew Cumming. MAPPING CRUSTAL HEATING WITH THE COOLING LIGHT CURVES OF QUASI-PERSISTENT TRANSIENTS. The Astrophysical Journal, 698(2):1020–1032, may 2009. doi: 10.1088/0004-637x/698/2/1020. URL https://doi.org/10.1088/0004-637x/698/2/1020.

[100] Compact Stellar X-ray Sources. Cambridge Astrophysics. Cambridge University Press, 2006. doi: 10.1017/CBO9780511536281.

[101] Anuj Parikh, Jordi José, Fermín Moreno, and Christian Iliadis. The effects of variations in nuclear processes on type i x-ray burst nucleosynthesis. The Astrophysical Journal Supplement Series, 178(1):110–136, sep 2008. doi: 10.1086/589879. URL https://doi.org/10.1086/589879.

[102] A. Parikh, J. José, C. Iliadis, F. Moreno, and T. Rauscher. Impact of uncertainties in reaction q values on nucleosynthesis in type i x-ray bursts. Phys. Rev. C, 79:045802, Apr 2009. doi: 10.1103/PhysRevC.79.045802. URL https://link.aps.org/doi/10.1103/PhysRevC.79.045802.

[103] H. Schatz and W.-J. Ong. Dependence of x-ray burst models on nuclear masses. The Astrophysical Journal, 844(2):139, aug 2017. doi: 10.3847/1538-4357/aa7de9. URL https://doi.org/10.3847/1538-4357/aa7de9.

[104] Zach Meisel, Grant Merz, and Sophia Medvid. Influence of nuclear reaction rate uncertainties on neutron star properties extracted from x-ray burst model–observation comparisons. The Astrophysical Journal, 872(1):84, feb 2019. doi: 10.3847/1538-4357/aafede. URL https://doi.org/10.3847/1538-4357/aafede.

[105] R. H. Cyburt, A. M. Amthor, A. Heger, E. Johnson, L. Keek, Z. Meisel, H. Schatz, and K. Smith. Dependence of X-Ray Burst Models on Nuclear Reaction Rates. The Astrophysical Journal, 830(2):55, October 2016. ISSN 1538-4357. doi: 10.3847/0004-637X/830/2/55. URL http://arxiv.org/abs/1607.03416. arXiv: 1607.03416.

[106] Jacob Lund Fisker, Friedrich-Karl Thielemann, and Michael Wiescher. The nuclear reaction waiting points: 22 mg, 26 si, 30 s, and 34 ar and bolometrically double-peaked type i x-ray bursts. The Astrophysical Journal, 608(1):L61–L64, may 2004. doi: 10.1086/422215. URL https://doi.org/10.1086/422215.

[107] V. E. Iacob, J. C. Hardy, J. F. Brinkley, C. A. Gagliardi, V. E. Mayes, N. Nica, M. Sanchez-Vega, G. Tabacaru, L. Trache, and R. E. Tribble. Precise half-life measurements for the superallowed β^+ emitters ^{34}Ar and ^{34}Cl. Phys. Rev. C, 74:055502, Nov 2006. doi: 10.1103/PhysRevC.74.055502. URL https://link.aps.org/doi/10.1103/PhysRevC.74.055502.

[108] Christian Iliadis. Nuclear Physics of Stars. 01 2007. ISBN 9783527406029. doi: 10.1002/9783527618750.ch4.

[109] Faïrouz Hammache and Nicolas de Séréville. Transfer reactions as a tool in nuclear astrophysics. Frontiers in Physics, 8:630, 2021. ISSN 2296-424X. doi: 10.3389/fphy.2020.602920. URL https://www.frontiersin.org/article/10.3389/fphy.2020.602920.

[110] H. Herndl, J. Görres, M. Wiescher, B. A. Brown, and L. Van Wormer. Proton capture reaction rates in the *rp* process. Physical Review C, 52(2):1078–1094, August 1995. ISSN 0556-2813, 1089-490X. doi: 10.1103/PhysRevC.52.1078. URL https://link.aps.org/doi/10.1103/PhysRevC.52.1078.

[111] Thomas Rauscher and Friedrich-Karl Thielemann. Astrophysical Reaction Rates From Statistical Model Calculations. Atomic Data and Nuclear Data Tables, 75(1-2):1–351, May 2000. ISSN 0092640X. doi: 10.1006/adnd.2000.0834. URL https://linkinghub.elsevier.com/retrieve/pii/S0092640X00908349.

[112] Christian Iliadis, John M D'Auria, Sumner Starrfield, William J Thompson, and Michael Wiescher. Proton-induced thermonuclear reaction rates for a= 20–40 nuclei. The Astrophysical Journal Supplement Series, 134(1):151, 2001.

[113] L. van Wormer, J. Goerres, C. Iliadis, M. Wiescher, and F.-K. Thielemann. Reaction rates and reaction sequences in the rp-process. The Astrophysical Journal, 432:326, September 1994. ISSN 0004-637X, 1538-4357. doi: 10.1086/174572. URL http://adsabs.harvard.edu/doi/10.1086/174572.

[114] C. Yazidjian, G. Audi, D. Beck, K. Blaum, S. George, C. Guénaut, F. Herfurth, A. Herlert, A. Kellerbauer, H.-J. Kluge, D. Lunney, and L. Schweikhard. Evidence for a breakdown of the isobaric multiplet mass equation: A study of the A = 35 , T = 3 / 2 isospin quartet. Physical Review C, 76(2):024308, August 2007. ISSN 0556-2813, 1089-490X. doi: 10.1103/PhysRevC.76.024308. URL https://link.aps.org/doi/10.1103/PhysRevC.76.024308.

[115] Christian Iliadis, Richard Longland, Art Champagne, Alain Coc, and Ryan Fitzgerald. Charged-Particle Thermonuclear Reaction Rates: II. Tables and Graphs of Reaction Rates and Probability Density Functions. Nuclear Physics A, 841(1-4):31–250, October 2010. ISSN 03759474. doi: 10.1016/j.nuclphysa.2010.04.009. URL http://arxiv.org/abs/1004.4517. arXiv: 1004.4517.

[116] L. Lalanne, O. Sorlin, M. Assié, F. Hammache, N. de Séréville, S. Koyama, D. Suzuki, F. Flavigny, D. Beaumel, Y. Blumenfeld, B. A. Brown, F. De Oliveira Santos, F. Delaunay, S. Franchoo, J. Gibelin, V. Girard-Alcindor, J. Guillot, O. Kamalou, N. Kitamura, V. Lapoux, A. Lemasson, A. Matta, B. Mauss, P. Morfouace, M. Niikura, J. Pancin, A. Poves, T. Roger, T. Saito, C. Stodel, and J-C. Thomas. Evaluation of the ^{35}K$(p,\gamma)^{36}$Ca reaction rate using the ^{37}Ca$(p,d)^{36}$Ca transfer reaction. Phys. Rev. C, 103:055809, May 2021. doi: 10.1103/PhysRevC.103.055809. URL https://link.aps.org/doi/10.1103/PhysRevC.103.055809.

[117] J.G. Pronko and R.A. Lindgren. Angular correlations of sequential particle decay for aligned nuclei. Nuclear Instruments and Methods, 98(3):445–449, February 1972. ISSN 0029554X. doi: 10.1016/0029-554X(72)90226-1. URL https://linkinghub.elsevier.com/retrieve/pii/0029554X72902261.

[118] B. Alex Brown and W. A. Richter. New "usd" hamiltonians for the *sd* shell. Phys. Rev. C, 74: 034315, Sep 2006. doi: 10.1103/PhysRevC.74.034315. URL https://link.aps.org/doi/10.1103/PhysRevC.74.034315.

[119] E. Caurier, F. Nowacki, and A. Poves. Merging of the islands of inversion at $n = 20$ and $n = 28$. Phys. Rev. C, 90:014302, Jul 2014. doi: 10.1103/PhysRevC.90.014302. URL https://link.aps.org/doi/10.1103/PhysRevC.90.014302.

[120] A. Brown. https://people.nscl.msu.edu/brown/reaction-codes/wspot.for, 2011. URL https://people.nscl.msu.edu/brown/reaction-codes/.

[121] R. Longland, C. Iliadis, A.E. Champagne, J.R. Newton, C. Ugalde, A. Coc, and R. Fitzgerald. Charged-particle thermonuclear reaction rates: I. monte carlo method and statistical distributions. Nuclear Physics A, 841(1):1 – 30, 2010. ISSN 0375-9474. doi: https://doi.org/10.1016/j.nuclphysa.2010.04.008. URL http://www.sciencedirect.com/science/article/pii/S0375947410004185. The 2010 Evaluation of Monte Carlo based Thermonuclear Reaction Rates.

[122] Norman K Glendenning. Direct Nuclear Reactions. WORLD SCIENTIFIC, 2004. doi: 10.1142/5612. URL https://www.worldscientific.com/doi/abs/10.1142/5612.

[123] Norman K. Glendenning. Nuclear spectroscopy with two-nucleon transfer reactions. Phys. Rev., 137:B102–B113, Jan 1965. doi: 10.1103/PhysRev.137.B102. URL https://link.aps.org/doi/10.1103/PhysRev.137.B102.

université PARIS-SACLAY

ÉCOLE DOCTORALE
Particules, hadrons, énergie et noyau : instrumentation, imagerie, cosmos et simulation (PHENIICS)

Titre: Étude du ^{36}Ca : structure nucléaire et implications astrophysiques

Mots clés: évolution des couches, Astrophysique nucléaire, réactions directes, radioactivité 2 protons, symétrie d'isospin, X-ray burst

Résumé: Le noyau de ^{36}Ca possède plusieurs propriétés fascinantes liées à la structure nucléaire, avec l'étude des effets de brisure de la symétrie d'isospin et de l'évolution de l'espacement des couches à la limite de non-liaison. De plus, l'énergie et la structure de ses états excités ont un intérêt astrophysique notamment pour l'étude de la réaction ^{35}K(p,γ)^{36}Ca qui est impliquée dans le processus *rp* se produisant dans les sursauts X.

La symétrie isospin est l'une des symétries les plus fondamentales du noyau et est liée à l'indépendance de charge de l'interaction forte. Si la symétrie d'isospin est strictement préservée, les schémas de niveaux des noyaux miroirs (avec un nombre échangé de protons et de neutrons) devraient être identiques. L'interaction coulombienne brise la symétrie d'isospin et donne lieu à un décalage de l'énergie d'excitation entre les états analogues des noyaux miroirs, appelé différence d'énergie miroir. Dans le cas de la paire miroir ^{36}Ca-^{36}S, l'interaction coulombienne agit comme une loupe de la structure nucléaire, dont les effets sont examinés dans ce travail.

La motivation d'astrophysique nucléaire est liée à la mesure indirecte du taux de la réaction ^{35}K(p,γ)^{36}Ca afin de mieux comprendre le profil de luminosité émis lors des sursauts X de Type Ia. En effet, cette réaction a été identifiée comme l'une des dix réactions (p,γ) qui pourraient avoir un impact significatif sur la forme de la courbe de lumière calculée des sursauts X. La présente expérience vise à étudier l'énergie, les valeurs de spin, les facteurs spectroscopiques protons et les largeurs des états excités d'intérêt astrophysique dans le ^{36}Ca. Les informations spectroscopiques pertinentes sont utilisées pour réexaminer le taux de la réaction ^{35}K(p,γ)^{36}Ca et ses incertitudes correspondantes et déterminer son impact sur la courbe de lumière des sursauts X.

Le ^{36}Ca a été étudié au GANIL au moyen des réactions de transfert ^{37}Ca(p,d) et ^{38}Ca(p,t) à environ 50 MeV/nucléons. Des faisceaux radioactifs de ^{37}Ca et ^{38}Ca, produits avec le spectromètre LISE, ont été mesurés par deux ensembles de détecteurs sensibles à la position avant d'interagir avec une cible cryogénique d'hydrogène liquide. 6 télescopes MUST2 (cristaux de silicium DSSD et CsI) ont été utilisés pour identifier et mesurer les particules légères émises pendant la réaction de transfert. Un ensemble de trois détecteurs (chambre d'ionisation, chambre de dérive et scintillateur en plastique) ont été utilisés pour détecter l'ion lourd sortant dans le canal de sortie. La détection des éjectiles légers et lourds a permis une détermination complète de la cinématique de la réaction, une attribution du moment angulaire transféré L de tous les états produits, et une réduction significative du bruit de fond.

La spectroscopie complète du ^{36}Ca a été obtenue et de nouveaux états excités ont été identifiés. De très grandes différences d'énergie miroir ont été observées dans les nouveaux états intrus du ^{36}Ca. La corrélation des protons, vue à partir de la désintégration en deux protons des états hautement excités, a également été étudiée. Grâce aux résultats expérimentaux et aux calculs de modèles en couche, le taux de réaction ^{35}K(p,γ)^{36}Ca a été réévalué et fortement contraint avec une incertitude statistique pertinente. Outre le ^{36}Ca, la première étude de la spectroscopie du ^{35}Ca (y compris la mesure de sa masse) sera également présentée.

Title: Study of ^{36}Ca: nuclear structure and astrophysical implications

Keywords: Shell evolution, Nuclear astrophysics, direct reactions, 2 proton radioactivity, Isospin symmetry, X-ray burst

Abstract: The ^{36}Ca nucleus has several fascinating properties linked to nuclear structure, with the study of isospin symmetry breaking effects and shell gap evolution at the proton drip-line. Moreover, the energy and structure of its excited states have an astrophysical interest in particular for the study of the key reaction ^{35}K(p,γ)^{36}Ca involved in the *rp*-process occurring in X-ray bursts.

Isospin symmetry is one of the most fundamental symmetries in nuclei and is related to charge independence of the strong interaction. If the isospin symmetry is strictly preserved, the level schemes of mirror nuclei (with exchanged number of protons and neutrons) should be identical. The Coulomb interaction breaks the isospin symmetry and gives rise to shift in excitation energy between analogue states in mirror nuclei called Mirror Energy Differences (MED). In the case of the mirror pair ^{36}Ca-^{36}S, the Coulomb interaction act as a magnifying glass of the nuclear structure, which effects are scrutinized in this work.

The nuclear astrophysics motivation is linked to the indirect measurement of the ^{35}K(p,γ)^{36}Ca reaction rate to better understand the luminosity profile emitted during Type Ia X-ray burst. Indeed, this reaction has been identified as one of the ten (p,γ) reactions that could significantly impact the shape of the calculated X-ray burst light curve. The present experiment aims at studying the energy, spin values, proton spectroscopic factors and widths of the excited states of astrophysical interest in ^{36}Ca. These relevant spectroscopic information are used to reinvestigate the ^{35}K(p,γ)^{36}Ca reaction rate and its corresponding uncertainties and determine its impact on the X-ray burst's light curve.

^{36}Ca was studied at GANIL by means of the ^{37}Ca(p,d) and ^{38}Ca(p,t) transfer reactions at about 50 MeV/nucleons. Radioactive beams of ^{37}Ca and ^{38}Ca, produced with the LISE spectrometer, were tracked by two sets of position-sensitive detectors before impinging on a liquid Hydrogen cryogenic target. 6 MUST2 telescopes (Silicon DSSD and CsI crystals) were used to identify and measure light particles emitted during the transfer reaction. An assembly of three detectors (ionization chamber, drift chamber and plastic scintillator) were used to detect the outgoing heavy ion in the exit channel. The detection of both light and heavy ejectiles ensured a complete determination of the kinematics of the reaction, an assignment of the transferred angular momentum L of all states produced, and a very reduced amount of background.

The full spectroscopy of ^{36}Ca has been obtained and new excited states have been identified. Colossal MED have been observed in the newly discovered intruder states of ^{36}Ca. The proton correlation, viewed from the two-proton decay of highly excited states, has been also studied. With the experimental results and the help of shell-model calculations, the ^{35}K(p,γ)^{36}Ca reaction rate has been re-evaluated and constrained with meaningful statistical uncertainty. Besides ^{36}Ca, the first study of the spectroscopy of ^{35}Ca (including its mass measurement) will also be presented.

Université Paris-Saclay
Espace Technologique / Immeuble Discovery
Route de l'Orme aux Merisiers RD 128 / 91190 Saint-Aubin, France